

Ultramicroscopy of complex pharmaceutical materials



Natalia Anna Koniuch

School of Chemical and Process Engineering

University of Leeds

Thesis submitted in accordance with the requirements for the degree of

Doctor of Philosophy

September 2023

The candidate confirms that the work submitted is her own, except where work which has formed part of jointly authored publications has been included. The contribution of the candidate and the other authors to this work has been explicitly indicated below. The candidate confirms that appropriate credit has been given within the thesis where reference has been made to the work of others.

The work in **Chapter 4** of the thesis has been published in the following journals:

S'ari, M., **Koniuch, N.**, Brydson, R., Hondow, N. and Brown, A. 2020. High-resolution imaging of organic pharmaceutical crystals by transmission electron microscopy and scanning moiré fringes. *Journal of Microscopy*. **279**(3), pp.197-206.

The candidate carried out part of the experiment work (Figures 3 and 4). Mark S'ari was responsible for the majority of the experimental work, data analysis and writing in the manuscript. The other authors contributed to the analysis and writing of the manuscript.

The work in **Chapter 6** of the thesis is under review in the following journals:

Pham, T. S., **Koniuch, N.**, Wynne, E., Brown, A. and Collins, S. M. (2023). Microscopic crystallographic analysis of dislocations in molecular crystals, *under review in Nature Materials (arXiv pre-print shown here)*.

The candidate carried out part of the experiment work (Figures 4, Supplementary Figures 14 and 15). Sang T. Pham was responsible for the majority of the experimental work, data analysis and writing in the manuscript. The other authors contributed to the analysis and writing of the manuscript.

The work in **Chapter 7** of the thesis has been published in the following journals:

Koniuch, N., Ilett, M., Collins, S.M., Hondow, N., Brown, A., Hughes, L. and Blade, H. 2023. Structure of polymeric nanoparticles encapsulating a drug - pamoic acid ion pair by scanning transmission electron microscopy. *Heliyon*. **9**(6), pe16959.

The candidate was responsible for carrying out the experiment work and data analysis. The manuscript was written by N. Koniuch with a contribution from A. Brown. The other authors contributed to writing the manuscript.

The candidate contributed also to the collaborative publication:

Ilett, M., S'Ari, M., Freeman, H., Aslam, Z., **Koniuch, N.**, Afzali, M., Cattle, J., Hooley, R., Roncal-Herrero, T., Collins, S.M., Hondow, N., Brown, A. and Brydson, R. 2020. Analysis of complex, beam-sensitive materials by transmission electron microscopy and associated techniques. *Philosophical Transactions. Series A, Mathematical, Physical, and Engineering Sciences*. **378**(2186), p20190601.

This copy has been supplied on the understanding that it is copyright material and that no quotation from the thesis may be published without proper acknowledgement.

Acknowledgements

I would like to express my deepest gratitude to my main supervisor, Prof. Andy Brown, for all his invaluable support, guidance, patience and encouragement on all stages of the project. Your immense knowledge and overall insights in this field have made this an inspiring experience for me. I would like to express my sincere gratitude to my supervisor, Dr Nicole Hondow, for her support, guidance and enthusiasm to assist in any way throughout this research project. I would also like to thank my co-supervisor, Prof. Rik Brydson, for providing advice regarding analysis and overall insights in this field. I would like to say a special thank you to my external supervisors from AstraZeneca, Dr Helen Blade and Dr Les Hughes, whose insight and knowledge from an industrial perspective steered me through this research.

I would like to thank everyone from the LEMAS and School of Chemical and Process Engineering I've worked with and from whom I've learned so much. I would like to especially thank Dr Sean Collins for his help with the scanning electron diffraction data acquisition and all the thoughtful comments on this project, Dr Mark S'ari for his dedicated support and guidance during TEM training, Dr Zabeada Aslam for her kind help and technical support, Dr Martha Ilett for her help during cryo experiments and electron energy loss spectra acquisition, Dr Steph Foster for her support during a heating in-situ experiment, Dr Sang T Pham for all invaluable discussion and his support during data processing in Python, Stuart Micklethwaite and John Harrington for their help during focussed ion beam sample preparation. I would also like to thank all the PhD students in the LEMAS group: Emily, Jess, Dario and especially Maryam for always being supportive.

I am grateful to the ePSIC team from Diamond Light Source, especially to Dr Mohsen Danaie, Dr Tom Slater and Dr Chris Allen for their help and support in data collection.

I would like to acknowledge AstraZeneca and EPSRC for the iCASE studentship that allowed me to conduct this thesis.

Last but not least, I would like to thank my wonderful children, the greatest motivation there is, for their love and patience. I also wish to thank my family and friends, especially my mother, brother, sister and grandparents for their unbreakable faith and support throughout this time.

Abstract

Transmission electron microscopy (TEM) is a promising tool for the analysis of pharmaceutical therapeutics because it can probe key interfaces, drug distribution, phase type, stability and defects. This work explores parallel beam and focussed probe, scanning (S)TEM for the analysis of four model pharmaceutical compounds. First, and for each compound analysed, the characteristic or critical electron fluence for irradiation-induced fading of an electron diffraction pattern is established. Any further data are acquired within this electron budget to minimize specimen alteration. The results demonstrate that STEM imaging and elemental analysis can provide information on performance parameters such as defect type and concentration, composition, strain, phase transformation pathways and barriers to the release of a drug.

Specifically, scanning electron diffraction (SED) and scanning moiré fringe (SMF) methods image the crystal lattice and identify defects in a small molecule drug, furosemide; highlighting that strain in furosemide (001) crystal planes is less than for (010). Scanning electron microscopy (SEM) and STEM lattice imaging with energy-dispersive X-ray spectroscopy (EDX), reveal a decrease in micrometre particle size and loss of shape, surface contamination by silicate nanoparticles, and a lowering of Na⁺ content on protonation of a development batch of a model K⁺ cation exchanger, sodium zirconium silicate. SED shows that hydrate formation from theophylline anhydrous form II is solution-mediated, dissolution-re-precipitation phase transformation. TEM and SED show that vacuum and thermal dehydration of theophylline monohydrate begins at particle surfaces with exposed water channels undergoing surface etching (first step), and then, water is removed from deeper in particles via diffusion along water channels (second step), to produce anhydrous form III before thermally induced reconstruction to anhydrous form II. Finally, multi-modal cryogenic (S)TEM of new modality, polymeric nanoparticles imaged in the frozen, hydrated state, reveals a multi-layer particle structure that indicates release of API from the 50 nm cores is through a 9 nm thick, layer of polylactic acid - polyethylene glycol co-polymer.

Table of Contents

Acknowledgements	iii
Abstract	iv
Table of Contents	v
List of Tables	ix
List of Figures	x
Abbreviations	xxiii
Chapter 1 Introduction	1
1.1 Background.....	1
Chapter 2 Literature Review	4
2.1 Problems of Pharmaceutical Product Development.....	5
2.2 Different Types of Drug Products and The Main Challenges That Can Be Addressed by (S)TEM.....	7
2.2.1 Small Molecule Drugs - Monitoring Crystal Defects and the Potential Impact on Dissolution	7
2.2.2 Microporous Inorganics - Monitoring the Compositional Changes and Ion Distribution Upon Cation Exchange	11
2.2.3 Channel Hydrates – Monitoring Hydration and Dehydration of Organic Compounds	13
2.2.4 New Modalities – Monitoring API Loading in Polymeric Nanoparticles	17
2.3 Common Bulk Characterisation Techniques.....	20
2.4 Transmission Electron Microscopy (TEM)	22
2.5 Electron Beam Damage in TEM.....	23
2.6 Mitigating of Radiolytic Damage of Organic and Inorganic Crystals under TEM Analysis	25
2.7 Scanning Transmission Electron Microscopy (STEM)	28
2.8 Recent Development Electron Microscopy of Pharmaceutical Compounds	35
2.9 Summary	41
2.10 Project Aim	42
2.11 Objectives	42
Chapter 3 Materials and Methods	43
3.1 Materials	44
3.2 Electron Microscopy.....	46
3.2.1 Basics	46
3.2.1.1 Electron.....	46

3.2.1.2 Resolution Limits and Lens Aberration	47
3.2.1.3 Electron Source	50
3.2.1.4 Optics and Apertures	51
3.2.2 Scanning Electron Microscopy (SEM).....	51
3.2.3 Transmission Electron Microscopy (TEM)	52
3.2.3.1 Basics of Transmission Electron Microscopy.....	52
3.2.3.2 Contrast Mechanism.....	55
3.2.3.3 Selected Area Diffraction Pattern (SAED).....	57
3.2.3.4 Energy Dispersive X-Ray Spectroscopy (EDX / EDS)	58
3.2.3.5 Electron Energy Loss Spectroscopy (EELS).....	59
3.2.4 Scanning Transmission Electron Microscopy (STEM)	60
3.2.4.1 Basics of Scanning Transmission Electron Microscopy....	60
3.2.4.2 Scanning Moiré Fringes (SMFs)	62
3.2.4.3 Scanning Electron Diffraction (SED).....	64
3.2.5 Cryogenic - (Scanning) Transmission Electron Microscopy (Cryo- (S)TEM)	65
3.3 Powder X-Ray Diffraction (pXRD).....	67
Chapter 4 Moving from TEM to STEM: Low-dose Techniques to Acquire Structural Information of Furosemide Form I	68
4.1 Background.....	69
4.2 Materials and Methods.....	70
4.2.1 Sample Preparation	70
4.2.2 (S)TEM Operating Condition.....	71
4.2.3 Data Analysis	71
4.3 Critical Fluence Measurement	72
4.4 Phase-Contrast Lattice Imaging.....	77
4.5 Scanning Electron Diffraction – General Defect Identification.....	80
4.6 Scanning Moiré Fringes and Attempts to Correlate Strain to Dissolution Rate	84
4.6.1 Standard Sample - Crocidolite	84
4.6.2 SMF of (001) Plane of Furosemide	88
4.6.3 SMF of (010) Plane of Furosemide	92
4.6.4 Summary	96
4.7 Chapter Summary.....	99
Chapter 5 Investigation of Microporous Structure of Sodium Zirconium Cyclosilicate Hydrate	101
5.1 Commercial Product Background	102

5.2 Materials and Methods.....	105
5.2.1 Sample Preparation	105
5.2.2 (S)TEM Operating Condition.....	106
5.2.3 SEM and FIB	106
5.2.4 Data Analysis	107
5.3 Chemical Composition Modifications and Pore Structure Investigation of Test Samples	108
5.3.1 Provision of Test Samples and Powder XRD.....	108
5.3.2 Pore Structure Simulation	112
5.4 Crystal Morphology Observation and Particle Size Distribution Analysis by SEM	114
5.5 Critical Fluence Measurements	120
5.6 Direct Comparison Between Experimental and Theoretical Predictions of Sodium Content by STEM EDX.....	122
5.6.1 Standard – Albite	122
5.6.2 Effect of Sample Preparation Method on STEM-EDX Measurement	127
5.6.3 Investigation of AZ1-2 Surface Particles	134
5.6.4 EDX Conclusions	135
5.7 Lattice Imaging and Strain Analysis.....	135
5.8 Chapter Summary.....	146
Chapter 6 Investigation of Structural Changes During Hydration and Dehydration of a Model Channel Hydrate, Theophylline	148
6.1 Background.....	149
6.2 Materials and Methods.....	152
6.2.1 Sample Preparation	152
6.2.2 Powder X-Ray Diffraction.....	154
6.2.3 (S)TEM Operating Condition.....	155
6.2.4 Polarised Light Microscopy	156
6.2.5 Data Analysis	156
6.3 Crystallisation of Anhydrous Theophylline Form II and Theophylline Monohydrate	156
6.4 Critical Fluence Measurement	162
6.5 Lattice Imaging.....	165
6.6 Investigation of Structural Changes During Hydration	176
6.7 Investigation of Structural Changes During Dehydration	182
6.8 Chapter Summary.....	196

Chapter 7 Investigations into the Physical and Chemical Structure of Tumour-Targeted Polymeric Nanoparticles	198
7.1 Background.....	199
7.2 Sample Preparation and Methods of Analysis	200
7.2.1 Nanoparticles and Suspension Preparation	200
7.2.2 Cryo Sample Preparation.....	201
7.2.3 Cryo-(S)TEM Analytical Microscopy	201
7.2.4 Data Processing and Analysis	201
7.3 Results and Discussion.....	202
7.3.1 Imaging Condition Optimisation	202
7.3.2 Physical Characterisation	209
7.3.3 Chemical Characterisation.....	214
7.3.4 Identifying Impurities and Non-Standard Particles	221
7.3.5 Discussion	223
7.4 Chapter Summary.....	226
Chapter 8 Final Conclusions and Future Work	228
8.1 Conclusions	228
8.2 Final comments.....	230
8.3 Future Work	231
Appendix A Methods of Data Acquisition and Data Analysis	234
A.1 Apparatus	234
A.2 Calculation of Critical Fluence (C_F).....	234
A.3 Acquisition of Scanning Moiré Fringes	238
A.4 Image Filtering of lattice (phase contrast) images.	240
A.5 SED Data Processing.....	241
A.6 EDX Absorption Correction	243
Appendix B XRD plots of AZ1 and AZ1-2	245
B.1 XRD plot of AZ1.....	245
B.2 XRD plot of AZ1-2	246
Appendix C SED of Theophylline Form IIIb	247
References.....	249

List of Tables

Table 3.1 Electron wavelength as a function of accelerating voltage. ...	53
Table 4.1 Mean C_F and standard deviation (\pm SD) of each measurement calculated from diffraction pattern data.	77
Table 5.1 AZ1 and AZ1-2 structure parameters (calculated in CrystalMaker from the .cif files supplied by Helen Blade, AstraZeneca).	111
Table 5.2 The average particle size distribution parameters.	118
Table 5.3 Size and shape parameters of AZ1 and AZ1-2 (\pm SD).	119
Table 5.4 STEM-EDX of FIB-TEM wedge sample of albite. Na/Si is calculated without and with absorption correction based on the sample thickness at each range. Grey backgrounds indicate accurate Na/Si prediction.	125
Table 5.5 Measured Na/Si ratio of albite standard sample (\pm SD).	127
Table 5.6 Experimental Na/Si ratio of AZ1 and AZ1-2 acquired using a total electron fluence of $\sim 17 \times 10^3 \text{ e}/\text{\AA}^2$ (\pm SD).	131
Table 5.7 Elemental composition of areas selected on STEM-EDX mapping.	135
Table 6.1 Type of samples used in the experiments.	153
Table 6.2 Crystallographic parameters for anhydrous theophylline form II (REF code: BAPLOT01), monohydrate (REF code: THEOPH01 and from Paiva et al. (2021)) and metastable forms III (from Paiva et al. (2021)).	155
Table 6.3 Mean critical fluence (\pm SD) and optimal total electron fluence for d -spacing ranges of $> 2 \text{\AA}$, $< 2 \text{\AA}$ and an average C_F calculated from the series of electron diffraction pattern data.	165
Table 7.1 Measurement of corresponding particle diameter from close to focus and $4 \mu\text{m}$ under-focus images. A two-tail P-test was performed on both datasets.	206
Table A.1 Calculated electron fluence in STEM mode using 5 pA probe current.	240

List of Figures

Figure 2.1 Potential causes and effects of structural changes in pharmaceutical compounds.	5
Figure 2.2 Electron beam damage mechanism (adapted from Egerton (2005)).	24
Figure 2.3 Example of an electron diffraction pattern time series of griseofulvin, acquired using an electron flux of $0.02 \text{ e}^-/\text{\AA}^2\text{s}$. Taken from S'ari et al. (2018).	25
Figure 2.4 Beam propagation in (a) TEM and (b) STEM mode. Taken from Wolf and Elbaum (2019).	29
Figure 2.5 Schematic representation of the formation of artificial moiré fringes. Taken from Murakami et al. (2015).	31
Figure 2.6 Schematic representation of STEM for scanning electron diffraction (SED; LHS) and the need for a low convergence angle to keep the diffraction disks from overlapping (RHS).	32
Figure 2.7 Schematic of analytical scanning transmission electron microscopy showing image detector configurations and a typical HAADF image of polymer nanoparticles in vitreous ice. STEM can be coupled with an electron energy loss (EEL) spectrometer and an energy-dispersive X-ray (EDX/EDS) detector.	34
Figure 2.8 Cryo-STEM-EDX and cryo-STEM-EEL spectra of polymeric nanoparticles in vitreous ice (see Chapter 7). The improved spectral resolution of EELS is evident however the red arrows in the cryo-STEM-EELS spectrum show the multiple scattering regions due to the thickness of the ice in the cryo-sample and indicate the reduced sensitivity (peak-to-background ratio) for elements such as N and F.	35
Figure 2.9 Scanning moiré fringes of furosemide form I (a) SAED of [110] zone axis, (b) BFSTEM image of SMFs produced by using a pixel size of 1.32 nm and $1.50 \pm 0.10 \text{ nm}$ d -spacing. The Fourier-filtered image from within the red box highlights a defect seen within (100) planes of the crystal (red lines). Taken from S'ari et al. (2019).	37
Figure 2.10 (a) Simulated atomic packing structure of the TiO_6 - SiO_4 zeolite, (b) HAADF-STEM image of the corresponding structure. Some stacking faults are visible in the bottom right of the image (red arrow). Images taken with electron fluence of $\sim 1000 \text{ e}^-/\text{\AA}^2$. Taken from Mayoral et al. (2015).	39
Figure 2.11 Scanning electron diffraction of a paracetamol-theophylline co-crystal. (a) Spatially averaged diffraction pattern, (b) individual diffraction pattern from near the tip of the rod, (c) Dark-field images formed by plotting the intensity within the disks marked in (a) as a function of probe position. Taken from Johnstone et al. (2019).	40

- Figure 2.12 Cryo-TEM images of PEG-b-PLGA block copolymer nanoparticles taken in (a) low and (b) high magnification of the area marked in red square in (a). White arrows show the ‘halo’ around some nanoparticles indicating the PEG layer. Red arrows indicate the bubble formation due to extensive beam damage of some nanoparticles. This allows the differentiation of particles without API (more beam-sensitive due to the presence of polymer blocks only) and with API. Reproduced from Han et al. (2015).41**
- Figure 3.1 Schematic of the ray diagram representing image formation using thin lens approximation.....48**
- Figure 3.2 2D profile and representation of Airy disks when two objects (a) can be resolved, (b) are on the resolution limit defined by the Rayleigh criterion and (c) cannot be resolved due to overlapping discs.49**
- Figure 3.3 Schematic representation of spherical and chromatic aberration in electromagnetic lens.50**
- Figure 3.4 Illustration showing various interactions of an incident high-energy electron beam with a thin specimen in TEM, which results in a range of signals that can be emitted and collected.....54**
- Figure 3.5 Schematic diagram of a TEM operating in two modes: imaging and diffraction. Taken from Braidy et al. (2020).55**
- Figure 3.6 Different contrast mechanisms in TEM: (A) mass/thickness (example of theophylline form II, results Chapter 6), (B) diffraction (example of furosemide form I, results Chapter 4) and (C) phase (example of theophylline, results Chapter 6).56**
- Figure 3.7 (a) Geometry representation of incident, transmitted and diffracted electron beams in a crystalline specimen that satisfies the Bragg condition. (b) Geometry representation of the Ewald sphere showing the equivalence of the Laue condition and satisfying Bragg’s law.58**
- Figure 3.8 (a) Principle of Energy Dispersive X-Ray Spectroscopy (EDX). (b) example of EDX spectrum of silica mineral, albite (see Chapter 5).59**
- Figure 3.9 (a) Excitation mechanism in the specimen. (b) Example EEL spectrum with features from various loss mechanisms. The vertical scale is enlarged for the higher energy loss peak (above 250 eV) due to their intensity being much lower than the zero-loss and plasmon peaks.60**
- Figure 3.10 (a) Schematic of translational and general moiré fringes created by a scanning lattice (d_s) and crystal lattice (d_l) of similar sizes. (b) SAED of furosemide form I oriented to [110]. (b) BF-STEM image of SMFs produced by using a pixel size of 1.32 nm and 1.50 ± 0.10 nm d -spacing. Fourier Fourier-filtered image from within the red box highlights a defect seen within the crystal. Taken from S’ari et al. (2019).63**

- Figure 3.11 Schematic representation of the impact of (a) large and (b) small convergence semi-angle α on the size of the diffraction discs.65
- Figure 3.12 Schematic representation of cryo-EM sample preparation: (a) the drop of suspension is loaded onto the EM grid and blotted (A) and then the grid is rapidly plunge frozen into liquefied ethane (B) and (b) transferred into a cryo-transfer holder under liquid nitrogen. (c) Cryo-EM thin film of dispersion can be then analysed via cryo-(S)TEM techniques. (d) examples of cryo-TEM images of polymeric nanoparticles taken in low and higher magnification (see results Chapter 7).66
- Figure 4.1 (A) Molecular and (B) crystal structure of furosemide form I.70
- Figure 4.2 Example of an electron diffraction pattern time series of furosemide form I, initially orientated close to [100] zone axis, acquired at 200kV using an electron flux of $0.047 \text{ e}^-/\text{\AA}^2\text{s}$ and obtained after (a) 120, (b) 167, (c) 182, (d) 208, (e) 226, and (f) 256 s exposure time to electron irradiation.....73
- Figure 4.3 Diffraction pattern series of a furosemide crystal orientated close to [001] zone axis. (a)-(c) The diffraction pattern changes to a systematic row, and then reflections gradually reduce in intensity as the electron fluence accumulates until it completely disappears, indicating loss of crystallinity. (d)-(f) Difference in the intensity profiles of marked spots (i)-(iii).75
- Figure 4.4 Example of an electron diffraction pattern time series of furosemide form I, initially orientated close to [131] zone axis, acquired at 300 kV and using an electron flux of $0.059 \text{ e}^-/\text{\AA}^2\text{s}$, after 55, 171 and 252 s after initial exposure.....76
- Figure 4.5 (a) BF-TEM image of furosemide form I particle and (b) SAED pattern of the region imaged in (a) indexed to [231]. Disruptions in the bend contour are marked by red arrows in (a).78
- Figure 4.6 (a) BF-TEM image of furosemide form I crystals and (b) SAED indexed to [432] and taken from the area marked by the yellow circle in (a). (c) cropped phase-contrast lattice image of the area marked by the red square in (a). The blue square in (a) indicates a sacrificed area for focusing. (d) FFT from the area in (c) showing 0.46 nm d -spacing indexed to (102) lattice plane.....79
- Figure 4.7 (a)-(b) Cropped raw phase-contrast lattice image from the area in Figure 4.6c. The lattice spacing of 0.46 nm is marked by blue lines in (b). (c) FFT from (a) show clearly 0.46 lattice spacing corresponding to (102) lattice plane. (d) line profile from the yellow box in (b) showing that the 0.46 nm d -spacings are present in the image.80

- Figure 4.8 (a)-(c) ADF-STEM image of furosemide form I particle and SED reveals two orientations: (i) [201] and (ii) [301] from areas marked by red and yellow boxes in (a). (d) Virtual ADF-STEM images formed by plotting the intensity within the red disks from orientation (i). (e)-(f) Virtual ADF-STEM images formed by plotting the intensity within the yellow disks from orientation (ii), (f) Virtual ADF-STEM images formed by plotting the intensity within the yellow disks from orientation without (010) and (010) lattice planes. (g) molecular orientation between area (i) and (ii) revealing (010) common plane. (h) BFDH morphology orientation between area (i) and (ii) suggesting the presence of twin boundary (mirror symmetry).....82**
- Figure 4.9 (a) SED pattern from the crystal area (i) in Figure 4.8a with marked diffraction disks and (b)-(f) Virtual DF-STEM images formed by plotting the intensity within the specific disks (i)-(vi) marked in the SED pattern as a function of probe position. Disruptions in the bend contour are marked by red lines and arrows. The slip plane is marked by a blue line.....83**
- Figure 4.10 Table of phase contrast TEM images with inset FFTs taken over a range of electron fluxes and fluences. It was possible to resolve 8.9 Å spacing at an electron fluence of 10 e⁻/Å² with an electron flux of 10 e⁻/Å²s. Taken from S'ari et al. (2019).85**
- Figure 4.11 (a) High magnification BF-STEM lattice image of crocidolite and (b) corresponding FFT from the area (a) resolving 0.86 nm d-spacing and indexed as (020) lattice plane. (c) the cropped area marked by a red square in (a). The crystal lattice is marked by orange lines and a line defect is highlighted by a red circle.86**
- Figure 4.12 (a) Experimental BF-STEM SMFs of crocidolite with corresponding (b)-(c) FFTs from area (i) – blue square and area (ii) – red square. Variations in the size and ϕ of the SMF are labelled.88**
- Figure 4.13 (a) BF-TEM image of longitudinal crystals of furosemide form I and (b) SAED pattern initially oriented close to [110] and exhibiting largest atomic spacing of 1.5 nm corresponding to (001) lattice plane.89**
- Figure 4.14 BF-STEM SMF image of the particle presented in Figure 4.13 with selected (i)-(iii) regions and corresponding FFTs. Variations in the size and ϕ of the SMF are labelled.....91**
- Figure 4.15 (a) BF-TEM image of furosemide form I recrystallized from ethanol and (b) SAED pattern initially oriented close to [001] and exhibiting different atomic spacing of 0.96 nm corresponding to (010) lattice plane.....92**
- Figure 4.16 (a) BF-STEM SMF image of the particle presented in Figure 4.15 with (b) selected (i)-(iii) regions and corresponding FFTs. Variations in the size and ϕ of the SMF are labelled.95**
- Figure 4.17 Correlation between predicted (calculated) and measured value of SMFs.....97**

- Figure 4.18 Comparison of the corresponding crystal faces to the values of the dissolution rate from Adobes-Vidal et al. (2016) and the observed variations. Δ of SMF spacing and orientation in images of the (001) and (010) furosemide form 1 lattice planes....98**
- Figure 5.1 Stick-and-ball (left) and polyhedral (right) unit cell structural model of the microporous sodium zirconium cyclosilicate hydrate. Red = zirconium, green = silicon, blue = oxygen atoms. Counter cations (Na^+ and H^+). Taken from European Medicines Agency (2018).103**
- Figure 5.2 Diameters (\AA) of monovalent and divalent cations (both unhydrated and hydrated). Taken from Stavros et al. (2014).....104**
- Figure 5.3 Mechanism of ion exchange system in sodium zirconium cyclosilicate hydrate. Potassium K^+ ions are preferentially trapped in pores due to the size of the pore matching the unhydrated ion diameter. Other cations, e.g. Na^+ , have smaller unhydrated diameters, therefore, require more energy to shed their hydration shell than K^+ and this action is energetically unfavourable. Taken from Skoyles et al. (2017).....104**
- Figure 5.4 Preparation of FIB-TEM lamella: (a) thick lamella attached to the TEM grid via Pt deposition, (b) two windows were further milled until a desired thickness was reached i.e. (c) usually below 100 nm (marked by orange arrows), (d) BF-TEM of the fabricated lamella.107**
- Figure 5.5 Measured (green) and simulated (black) pXRD patterns of AZ1. A minor peak shift is marked by red arrows.....109**
- Figure 5.6 Measured (orange) and simulated (black) pXRD patterns of AZ1-2.....110**
- Figure 5.7 Superimposed experimental pXRD patterns for AZ1 and AZ1-2. The dashed lines correspond to the characteristic (002) peak position.....111**
- Figure 5.8 Model of (a) a single pore opening in AZ1, (b) selected three connected internal pores and (c) pores across a unit cell of AZ1 simulated in Mercury software. Red spheres = oxygen atoms; blue spheres = zirconium atoms; yellow spheres = silicon atoms. Counter cations are not pictured.113**
- Figure 5.9 Simulated model of sodium sites and cavities (unoccupied sites/pores) of AZ1 for single and extended (2x2) crystal units along (a-b) [111] and (b-c) [010] directions, respectively.113**
- Figure 5.10 SEM micrographs of crystal morphology of (a)-(b) AZ1 and (c)-(d) AZ1-2 taken at 10 kX and 100 kX magnification, respectively. Yellow arrows indicate micro-cracks on the crystal surface in both AZ1 and AZ1-2. Blue arrows indicate the additional spherical particles on the surface of AZ1-2.115**
- Figure 5.11 FIB cross-sections of (a) AZ1 and (b) AZ1-2 demonstrating no evidence of the internal pore structure.116**

Figure 5.12 Examples of different AZ1 particle morphology. Inset shows the EDX elemental map (Na-K) of the particle.116

Figure 5.13 (a)-(b) SEM images of AZ1 and AZ1-2 taken at 1 kX with (c)-(d) corresponding histograms of the particle size distribution of AZ1 and AZ1-2, respectively. The inset in (c)-(d) shows the cumulative average of the maximum Feret's diameter.....118

Figure 5.14 Mean C_F and standard deviation of each measurement calculated from diffraction pattern series of AZ1 and AZ1-2 (\pm SD).122

Figure 5.15 (a) Wedge-shaped FIB-TEM section of reference mineral, albite, with measured thickness in (b).124

Figure 5.16 (a) HAADF-STEM of albite, (b) typical EDX spectra from isolated particle, (c) sodium and (d) silicon EDX elemental mapping.....126

Figure 5.17 Typical STEM-EDX spectra for AZ1 (black) and AZ1-2 (red). The inset shows an enlarged region within the dashed area and the increased Na-K content of AZ1.....128

Figure 5.18 STEM-HAADF micrograph showing the area scanned to obtain the EDX spectrum for Si-K, Na-K, O-K and Zr-K elemental maps of (a) AZ1 and (b) AZ1-2.129

Figure 5.19 Particles with highlighted hotspot region rich with sodium: (a) AZ1, (b) AZ1-2.132

Figure 5.20 STEM-EDX line profile across (a) AZ1 and (B) AZ1-2 indicate Na/Si composition is uniform within both samples.....133

Figure 5.21 (a) BF-TEM image of AZ1-2 with highlighted region for STEM-EDX elemental mapping (b) STEM-EDX mapping of selected areas.134

Figure 5.22 Schematic of a profile view of a cubic structure down the (a) $\langle 001 \rangle$ and (b) $\langle 011 \rangle$ zone axis. The contrast gradient in the projected image in (b) (orange ellipses) gives an idea of the thickness, with areas towards the top and bottom edges showing some electron transparency sufficient for lattice imaging.136

Figure 5.23 (a) BF-STEM crossed lattice image of AZ1 taken in 450 kX magnification, (b) enlarged area taken from the highlighted dotted box, (c) SAED pattern from the crystal in (a) initially orientated close to $[312]$ direction, (d)-(e) simulated electron diffraction pattern of crystal orientation along $[312]$ direction and the FFT from (b).138

Figure 5.24 BF-STEM lattice image of AZ1 and corresponding FFTs were taken from areas marked by orange, green, blue and yellow squares indicating the slight displacement of the (021) reflection of 0.57 nm lattice spacing by 1-2 degrees suggesting the presence of strains.....139

Figure 5.25 Experimental BF-STEM, corresponding Wiener filtered images and line profiles of AZ1.....140

- Figure 5.26 (a) BF-STEM crossed lattice image of AZ1-2 taken in 450 kX magnification, (b) enlarged area taken from highlighted dotted box (c) FFT from crystal (A) of which zone axis was indexed of [012] direction, (d)-(e) simulated electron diffraction pattern and crystal orientation along [012] direction. Orange circles correspond to (200) reflection of 0.61 nm lattice spacing, green circles correspond to (021) reflection of 0.57 nm lattice spacing.141
- Figure 5.27 BF-STEM lattice image of AZ1-2 and corresponding FFTs were taken from areas marked by yellow and red squares indicating the slight displacement of the (200) reflection of 0.61 nm lattice spacing by 2 degrees suggesting the presence of strains.142
- Figure 5.28 Experimental BF-STEM and corresponding Wiener-filtered images of AZ1-2. Defects are marked by yellow and red lines/arrows.....143
- Figure 5.29 BF-STEM crossed lattice image and Wiener filtered images of AZ1-2 taken in 450 kX (pixel size of 0.165 nm) and 640 kX magnification (pixel size of 0.116 nm). Enlarged areas taken from highlighted red boxes show defects in lattice planes.144
- Figure 5.30 Geometric phase analysis of AZ1 (a)-(d) and AZ1-2 (e)-(h): BF-STEM image, FFT, GPA strain image ϵ_{xx} component of the strain tensor and GPA strain image ϵ_{yy} component of the strain tensor.....145
- Figure 6.1 Schematic of phase transformation pathways between theophylline form II and monohydrate. Hydration is a one-step process, however, dehydration can be a one or two-step process depending on dehydration conditions (temperature and/or relative humidity).....151
- Figure 6.2 Structures with simulated BFDH morphology of the forms of theophylline: (i) form II and (ii) monohydrate calculated in Mercury 2022.2.0. Small voids of form II can be seen when crystals are orientated in [010] and water channels of monohydrate form can be observed in [100].151
- Figure 6.3 Recrystallisation of theophylline monohydrate: (a) form II powder was dissolved in water/ethanol solution and heated to ~55 °C; (b) the solution was allowed to cool slowly to ~35 °C and precipitation occurs and (c) the solution is cooled to room temperature and then precipitates were filtered out for pXRD measurement.154
- Figure 6.4 BF-TEM images with corresponding indexed SAED patterns (taken from areas marked by red circles) and overlay of corresponding experimental and simulated powder XRD patterns of: (a) 'as-bought' anhydrous theophylline form II (A1) and (b) anhydrous theophylline form II recrystallised from nitromethane solution (A2). The strong, distinct Bragg peaks of theophylline anhydrous form II are labelled with corresponding Miller indices.158

- Figure 6.5 (a) Cryo-BF-TEM, polarised light microscopy image and SAED pattern taken from the area marked by a red circle of theophylline form II plates after contact with water (A3); (b) overlay of experimental A3 and simulated powder XRD patterns (green – theophylline monohydrate, red – form II, burgundy – preferred [131] orientation of form II). Unindexed peak is marked by an asterisk; (c) overlay of experimental patterns of A2 and A3. The red arrows indicate a decrease in the peak intensities and the blue arrow indicates an increase in peak intensity at 12.64° (201) 2θ159
- Figure 6.6 (a)-(b) BF-TEM and SAED pattern of M1 stored in 93% relative humidity for 1 week, identifying both: mainly form II (a) and some monohydrate phases (b), respectively; (c) polarised microscopy image of M1 after 3 weeks showing significant fragmentation of the original triangular form II plates or growth of new monohydrate phases; (d) powder XRD patterns of M1 taken after 1, 3 and 7 weeks of storing A2 in 93% RH condition. Characteristic peaks of theophylline monohydrate are marked by green arrows.160
- Figure 6.7 BF-TEM image with corresponding indexed SAED pattern (taken from areas marked by the green circle) and overlay of corresponding experimental and simulated powder XRD patterns of: (a) theophylline monohydrate recrystallised from water (M2) and (b) theophylline monohydrate crystallised from ethanol:water (M3). The distinct form M peaks are labelled with corresponding Miller indices.....162
- Figure 6.8 BF-TEM image of theophylline form II plate (A2) (a) before increasing fluence (b) after acquiring a series of electron diffraction patterns. (c) Typical diffraction pattern of A2 indexed to [100] zone axis and corresponding decay profiles of (d) (002) plane, (e) (011) and (f) (020). Green shading indicates a suggested 'safe zone' of C_F to acquire lattice imaging.....164
- Figure 6.9 (a) SEM image of theophylline monohydrate (M3) with distinct morphology; (b) FIB-TEM cross-section from the area marked by red in (a). Corresponding diffraction patterns from regions (i)-(ii) confirm that the sample is still crystalline, however, channels are not orientated parallel to the view direction.....166
- Figure 6.10 (a) Low-magnification BF-TEM image of theophylline form II (A2); (b) SAED pattern indexed to [100] zone axis and taken from the area marked by the red circle in (a); (c) cropped phase-contrast lattice image from the area marked by the blue square in (a). Yellow square in (a) indicates a sacrificed area for focusing. The inset shows an inverse FFT of the image. (d) FFT from the area in (c) and 0.35 nm d -spacing indexed to (011) lattice plane can be resolved.....168

- Figure 6.11 (a) Low-magnification BF-TEM image of theophylline form II (A2); (b) SAED pattern indexed to [100] zone axis and taken from the area marked by the red circle in (a); (c) cropped phase-contrast lattice image from the area marked by the blue square in (a) resolving cross-fringes. The inset shows an inverse FFT image. (d) FFT from the area in (c) and 0.35 nm *d*-spacing indexed to (011) and (011) lattice planes and 0.424 nm *d*-spacing indexed to (002) can be resolved.....169**
- Figure 6.12 (a) Low-magnification BF-TEM image of theophylline monohydrate (M1); (b) SAED pattern indexed to [531] zone axis and taken from the area marked by the red circle in (a). The inset represents the orientation of the unit cell and the direction of water channels is marked by a blue arrow; (c) cropped phase-contrast lattice image from the area marked by the blue square in (a) resolving cross-fringes. 0.34 nm lattice spacing is marked by blue lines. (d) FFT from the area in (c) and 0.34 nm *d*-spacing indexed to (121) 0.38 nm *d*-spacing indexed to (112) and 0.415 nm *d*-spacings indexed to (013) lattice planes can be resolved. (e) comparison between simulated diffraction pattern of theophylline form II oriented to the [100] zone axis and monohydrate oriented to the [531] zone axis. The differences in *d*-spacings and the relative angles between the planes allow for the unambiguous identification of the area in (a) as a monohydrate phase.....171**
- Figure 6.13 Comparison between different cameras and modes i.e. direct electron detector DE16 (counting vs integrating mode) and OneView (low dose mode) within the same total electron dose range of $\sim 20 \text{ e}^-/\text{\AA}^2$ on the model sample of gold particles. DE16 in counting mode provides substantial improvement in resolving lattice planes. Data acquired by Dr Thomas Slater, ePSIC, Diamond Light Source, UK.....172**
- Figure 6.14 a) Low-magnification BF-TEM image of theophylline monohydrate (M3) acquired at ePSIC using the direct electron detector DE16; (b) phase contrast lattice imaging of the area marked by the blue square in (a); (c) cropped phase contrast lattice image from (b) and 0.34 nm lattice spacing corresponding to (131) lattice plane are marked by red lines; (d) FFT from the area in (a) that can be used for indexing the crystal orientation to [411] zone axis.....174**
- Figure 6.15 Phase-contrast lattice image of the area presented in Figure 6.14. Corresponding FFTs from the different parts of the image (i)-(iv) indicate the change in the position (a relative angle to a vertical line) of spots corresponding to (131) and (122) planes but the position of a spot corresponding to (113) plane is constant.175**
- Figure 6.16 Cropped (a) the raw phase contrast lattice image and (b) the effect of applying a non-linear filter reported elsewhere (Du, 2015) to the same area from Figure 6.14. Lattice planes are marked by red in the corresponding: (c) - raw and (d) – filtered images; (e) residual image and (f) its auto-correlation.175**

- Figure 6.17 Proposed dissolution – re-precipitation phase transformation model for hydration of theophylline form II (A2). 178**
- Figure 6.18 Water interaction map of (100) lattice plane of theophylline anhydrous form II (A2) generated in Mercury 2022.2.0. Particles oriented to [100] have the (100) projected surface facet. 179**
- Figure 6.19 ADF-STEM image of theophylline anhydrous form II (A3). SED reveals two orientations: (i) original [100] and (ii) dominant [131]. Corresponding ADF-STEM images are formed by plotting the intensity within the red and orange disks marked in SED patterns as a function of probe position. Disordered sites are marked by blue circle and line. 180**
- Figure 6.20 (a) ADF-STEM image of theophylline anhydrous form II (M1) and (b) corresponding SED indexed to [130] zone axis. (c) Virtual ADF-STEM image was formed by plotting the intensity within the orange disks marked in the SED pattern as a function of probe position. 181**
- Figure 6.21 (a) ADF-STEM image of theophylline monohydrate (M1) and (b) corresponding SED indexed to [732] zone axis. (c) Virtual ADF-STEM image was formed by plotting the intensity within the green disks marked in the SED pattern as a function of probe position. 182**
- Figure 6.22 Dehydration routes of theophylline monohydrate. 185**
- Figure 6.23 ADF-STEM image of theophylline monohydrate (M3) after (a) 30 min and (b) 17 hrs in a vacuum. (c) shows the overlay between (a) and (b). Characteristic surface erosion by etching is marked by red arrows in (b) and (c). 186**
- Figure 6.24 ADF-STEM image of theophylline monohydrate (M3) and SED patterns from the selected regions (i) – (v). The blue arrow indicates the direction of the water channels. 188**
- Figure 6.25 (a)-(b) Identification of three different areas within one particle and their relative orientation. (c) the relationship between the orientations of individual areas and the presence of channels on the common surfaces. BFDH morphology and channel propagation were modelled in Mercury 2022.2.0. 190**
- Figure 6.26 (a) ADF-STEM image of theophylline monohydrate (M3) and its (b) SED pattern from the bottom part of the crystal. (c)-(d) Virtual ADF-STEM images formed by plotting the intensity within the disks marked in the SED pattern in (b) as a function of probe position. Defect sites are marked by blue lines (dislocation) and a circle in (d). (e) cropped area in (a) and two diffraction patterns from same-sized regions: red- at the edge of the crystal and yellow – slightly above the edge of the crystal. Red arrows indicate disordered regions. 192**

- Figure 6.27 (a)-(b) Vacuum dehydration of another area from *M3* also reveals the etching on the surface. (c) New crystal growth in the corner of the main particle during dehydration can be indexed to (d) theophylline monohydrate orientated to [310] zone axis (red square in (c)). (e) Initial particle can be indexed to theophylline monohydrate or metastable theophylline form III upon partial dehydration.193**
- Figure 6.28 Dehydration of theophylline monohydrate *M3* using a heating holder: (a) *M3* particle orientated close to [312] zone axis and heated to 60 °C and (b) *M3* particle orientated close to [311] and heated to 100 °C. There is a significant change in morphology at 100 °C and the resulting SAED can be indexed to the anhydrous form II [101] zone axis. Blue arrows indicate the direction of the water channels, and red and yellow arrows indicate smaller and bigger particle sizes within one area, respectively, with different surface etching rates.....195**
- Figure 7.1 (a) Schematic of nanoparticle preparation via the nanoemulsion process. Adapted from Song et al. (2016) and (b) chemical structure of the components: AZD2811, pamoic acid and PLA-PEG co-polymer.....200**
- Figure 7.2 Cryo-TEM micrograph of polymeric nanoparticles: (a) Low magnification cryo-BF-TEM image taken close to focus and (b) higher magnification image with 4 μm under-focus applied, (c) CTF comparison between in-focus (green) and under-focus condition (red), (d) identification of three individual layers in each nanoparticle (as labelled in the image).....204**
- Figure 7.3 Comparison between the high-magnification cryo-BF-TEM images of the same area taken: (a) close to focus and (b) by applying 4 μm under-focus to the same area to increase the particle contrast.....205**
- Figure 7.4 Electron beam damage observation in cryo-BF-TEM based on imaging the same area with a total electron fluence of (a) 20 $\text{e}^-/\text{\AA}^2$, (b) 40 $\text{e}^-/\text{\AA}^2$ and (c) 80 $\text{e}^-/\text{\AA}^2$. Yellow arrows indicate the layer 1 boundary which begins to fade at 40 $\text{e}^-/\text{\AA}^2$ indicating damage to the structure of the nanoparticles. The blue arrows indicate bubble/void formation, especially at the interface between layer 1 and layer 2, related to severe radiation damage. Based on this observation of damage propagation, < 40 $\text{e}^-/\text{\AA}^2$ (marked in red font) is considered as a safe dose for cryo-TEM imaging.....208**
- Figure 7.5 Electron beam damage observation in cryo-ADF-STEM based on imaging the same area after total frames of: 1, 3, 5, 8, 11, and 14 scans and using a 40 pA probe current and 20 μs dwell time. Based on the observation of the damage propagation, < 80 $\text{e}^-/\text{\AA}^2$ (marked in red font) is considered as a safe dose for cryo-STEM imaging.....209**
- Figure 7.6 Measurement procedure to calculate the radius of individual layers.210**

- Figure 7.7 Particle size distribution histograms of the radius of (a) layer 1 and thickness of (b) layer 2 measured on the de-focused images. The inserts represent the cumulative mean radius, suggesting that a minimum of 80 particles is required to accurately measure the particle size distribution (since after that number the cumulative radius does not vary significantly). (c) Table with the mean values for layers 1-3. The average diameter of nanoparticles is 88 ± 9 (\pm SD) nm.210**
- Figure 7.8 Comparison between corresponding cryo-BF-STEM, cryo-ADF-STEM and inversed contrast cryo-ADF-STEM revealing: (i) different contrast within the core (marked by green arrows), (ii) layers 1 and 2 (yellow and orange curves) and (iii) layer 3 (blue curves) components.....212**
- Figure 7.9 (a) Cryo-(S)TEM images of polymeric nanoparticles taken from the same region. A high-pass filter applied to the cryo-ADF-STEM image significantly enhances the contrast of layer 3. (b) The intensity line profile from the region marked by the red rectangle in (a) shows that the particle diameter is the same across all images and high-pass filtering can be used for particle measurement. ..213**
- Figure 7.10 (a) Typical cryo-STEM-EDX and (b) background subtracted EEL spectra identifying C-K, N-K and O-K edges from the area containing nanoparticles in the field of view.214**
- Figure 7.11 (a)-(b) Cryo-ADF-STEM images before and after EDX acquisition, respectively, and corresponding: (c)-(d) C-K EDX elemental maps using 1 and 38 px average filter, respectively and (e) N-K EDX elemental map using 38 px average filter. (f) Radial elemental distribution measured using 'radial plot profile' plug-in in ImageJ from the area in (a).216**
- Figure 7.12 Cryo-STEM EELS carbon and nitrogen mapping. A linear intensity profile taken from the C-N overlay map and ADF image indicates that C occurs also between the nanoparticles and N is located approximately in the centre of individual nanoparticles (yellow boxes). Cryo-STEM-EEL spectrum acquired over the whole area shows the presence of C, N and O elements (below and left).217**
- Figure 7.13 Principal component analysis: (a) scree plot used for identification of (b)-(f) first five significant components that are presented as loading (spectra) and scores (image).218**

- Figure 7.14** PCA treated carbon cryo-STEM-EELS mapping of the area marked in red in the under-focus cryo-BF-TEM image. Below, under-focus cryo-BF-TEM, cryo-ADF-TEM and C EELS mapping of a cropped fragment marked in yellow and showing carbon presence between the particles and confirming the C-content to layer 3. The corresponding diameter of layer 1+2 is identical between cropped under-focus cryo-BF-TEM, cryo-ADF-STEM and C-map images (yellow arrows) and the thickness of layer 3 is consistent with earlier measurements of the spacing between nanoparticles by under-focus cryo-BF-TEM (blue arrow). Red arrows indicate severe electron beam damage in layer 2 visible in a post-EELS acquisition, cryo-ADF-STEM image.219
- Figure 7.15** (a) Cryo-ADF-STEM image of particles and areas where spectra were extracted from – layer 1 (yellow box), layer 2 (orange boxes), layer 3 (blue boxes) and amorphous ice (purple box). (b) Background stripped, as-acquired (faint dots) and smoothed (bold lines) STEM-EELS from layer 1, layer 2 layer 3 and amorphous ice areas in (a). Layer 1 is C rich and also has a clear N peak identifiable. Layers 2 and 3 have progressively less C and relatively more O per layer and less than that of the amorphous ice. (c) Background stripped, as-acquired (faint lines) and smoothed (bold lines) STEM EELS at the C K-edge reveal that layer 2 and layer 3 have slightly different edge structures to that of layer 1 suggesting a different polymer composition.221
- Figure 7.16** Cryo-STEM-EDX and background subtracted cryo-STEM-EEL spectra identifying C-K, N-K and O-K edges from the amorphous ice.222
- Figure 7.17** Under-focus cryo-BF-TEM and cryo-STEM-EELS mapping of non-standard nanoparticles named as: debris (non-spherical particles, marked as orange arrows) and blank (no visible layer 1, marked as red arrows). Cryo-STEM-EELS mapping suggests that debris and blank particles consist of the same material as layer 2 in the standard particle (i.e. have negligible N content and are highly beam sensitive).223
- Figure 7.18** Final multi-modal data-driven model of the polymeric nanoparticles based on phase contrast-TEM, ADF-STEM (*high-pass filtered) and STEM-EELS analysis. The likely content of each layer is HIP and some PLA material in layer 1 with a core enriched in HIP material. Only PEG and PLA are in layer 2 and diffuse PEG packing is in layer 3.225
- Figure A.1** (a) BF-TEM initial image and (b) BF-TEM image after taking diffraction series confirm loss in diffraction contrast and therefore crystallinity. The scale bar represents 2 nm^{-1}235
- Figure A.2** Example of (A) indexed experimental and (B) simulated diffraction pattern of furosemide form I orientated along the [201] zone axis.236
- Figure A.3** Explanation of critical fluence C_F calculation for a specific site of diffraction spot in the furosemide diffraction pattern.238

Abbreviations

(hkl)	Miller indices of a crystal plane
[UVW]	indices of beam direction
Å	Angstrom, a unit of length equal to 10^{-10} m
ADF	annular dark field
API	active pharmaceutical ingredient
AZ1/AZ1-2	sodium zirconium silicate – development batches
BF	bright-field
BFDH	Bravais-Friedel-Donnay-Harker
BFP	back-focal plane
BSC	Biopharmaceutical Classification System
CCD	charged-couple device
C_F	critical fluence
CL	Cliff-Lorimer
cryo-STEM	cryogenic scanning transmission electron microscopy
cryo-TEM	cryogenic transmission electron microscopy
CSD	Cambridge Structural Database
CTEM	conventional transmission electron microscopy
CTF	contrast transfer function
DE	detection efficiency
DF	dark field
d_l	real space lattice of the crystal [nm]
DLS	dynamic light scattering
d_s	size of the electron probe in STEM [nm]
DSC	differential scanning calorimetry

e	elementary charge of an electron (1.6×10^{-19} C)
EDS/EDX	energy dispersive X-ray spectroscopy
EELS	electron energy loss spectroscopy
EM	electron microscopy
F	cumulative electron fluence [$e^{-}/\text{\AA}^2$]
FFT	fast Fourier transform
FIB	focus ion beam
FTIR	Fourier transform infrared spectroscopy
GMS	Gatan Microscopy Suite
GPA	geometric phase analysis
HIP	hydrophobic ion pairing
HR-TEM	high-resolution transmission electron microscopy
J	electron flux (dose) [$e^{-}/\text{\AA}^2\text{s}$]
NP	nanoparticle
PCA	principal component analysis
PEG	polyethylene glycol
PLA	polylactic acid
PLA-PEG	polylactic acid - polyethylene glycol
PSD	particle size distribution
pXRD	powder X-ray diffraction
RH	relative humidity
SAED	selected area electron diffraction
SED	scanning electron diffraction
SEM	scanning electron microscopy
SI	spectrum image
SMF	scanning moiré fringes
SNR	signal-to-noise ratio

STEM	scanning transmission electron microscope
T_e	exposure time
TEM	transmission electron microscope
VDF	virtual dark-field
WAXS	wide-angle X-ray scattering

Chapter 1 Introduction

1.1 Background

There is an increasing drive within the pharmaceutical industry to link structure to performance in order to realise the full potential of a drug in a formulated medicine. The mainstay of the pharmaceutical industry up to now has been small molecule drugs because most can be administered orally and they can generally reach intracellular targets by passing through cell membranes (Békés et al., 2022; Hare et al., 2017; Torchilin, 2006; Wallace et al., 2012). A major proportion of the more recently developed small molecule drugs or active pharmaceutical ingredients (APIs) exhibit poor aqueous solubility and low dissolution rates and hence have poor bioavailability (Goud et al., 2012). One of the key challenges is to improve bioavailability by limiting the degree of crystallinity (and therefore improving solubility) of an API within a medicine (Bhalani et al., 2022). This requires an understanding of the crystalline form and the type and distribution of crystal defects that an API can have, the latter being particularly challenging to assess by techniques that probe molecular periodicity such as X-ray diffraction (Saleki-Gerhardt et al., 1994; Shekunov and York, 2000).

In addition, the rapid advancement of biopharmaceutical research and technology opens up possibilities for other therapeutics. For example: microporous inorganic compounds, especially zeolites and related silicates may replace cation exchange resins for potassium absorption in the small intestine (potentially providing a more effective treatment for hyperkalaemia) (Rafique et al., 2015; Sader et al., 2010; Sekhon and Gandhi, 2006). However, the distribution of the counter cation located within the micropore channels has not been fully identified yet. Some APIs are susceptible to relative humidity during processing or storage and may convert to unwanted or more stable hydrate/anhydrate forms, hindering dissolution and bioavailability (Behme and Brooke, 1991; Censi and Di Martino, 2015; De Smidt et al., 1986; Jurczak et al., 2020). Channel hydrates are of particular interest here because water molecule diffusion in and out of these structures is relatively easy yet transformation pathways are not well understood (Farias and Carneiro, 2014). Finally, there is growing interest over recent years in new drug delivery

modalities such as polymeric nanoparticles due to properties such as size, biological retention time and stability in suspension that promise great potential for controlled release of an API (Nimesh et al., 2006; Torchilin, 2006). However, their structure and API loading are not sufficiently understood to explain and predict the API release kinetics (Mahapatro and Singh, 2011; Mahdavi et al., 2020). Ultimately, a complete molecular and crystallographic description and understanding of drug structure in a formulation will help improve bioavailability and provide control over any inherent instability of a formulated product (Shalgunov et al., 2017).

The degree of crystallinity is commonly measured by powder X-ray diffraction (pXRD) or inferred from techniques such as Fourier-transform infrared spectroscopy (FTIR) or differential calorimetry (DSC) (Smeets et al., 2018). However, these methods for identifying and characterising crystal or phase concentration as well as the amount and type of crystal defects are limited. It has been emphasised that most of these 'bulk' techniques can detect no less than about 10% of disorder, which is insufficient for determining potential performance inhibiting, low levels of defects or amorphous regions in highly crystalline samples (Saleki-Gerhardt et al., 1994).

Transmission electron microscopy (TEM) and its ability for electron diffraction is a promising technique for the analysis of pharmaceutical compounds at a resolution unattainable by most other analytical techniques (Eddleston et al., 2010). Its application is, however, currently very limited. This is mainly associated with (i) difficulties related to sample preparation (the requirement that a specimen must be thin enough to be transparent to an electron beam (Jones, W. and Thomas, 1979) and (ii) that organic compounds are highly sensitive to radiolysis, leading to significant electron beam damage (Egerton, 2013; Egerton, 2019; Egerton et al., 2004). Nonetheless, recent work demonstrates that the identification of crystalline imperfections is obtainable by electron microscopy techniques (S'ari et al., 2018; Smeets et al., 2018; Su and Zhu, 2010). For example, it has been suggested that the identification of crystal disorder in theophylline could not be attained with any other analytical technique, highlighting the potential effectiveness of TEM here (Eddleston et al., 2010).

TEM has the potential to image crystal structures at the molecular level and analyse the elemental content, it can be used to measure crystallite size and orientation, crystal defects as well as surface structures at a single particle level. The issues related to sample preparation can be mitigated to some extent by careful specimen preparation (including keeping samples frozen and hydrated with cryo-techniques, and by cutting thin lamellae from specific sites by focussed ion beam microscopy) while those related to electron beam damage may be limited by implementing low-dose techniques (Bassim et al., 2012; Jasim et al., 2021; Nicholls et al., 2020; Velazco et al., 2022). These developments have opened the door to TEM analysis providing a more complete physical description of pharmaceutical compounds yet the optimum microscope settings and configurations are not yet fully established (Ilett et al., 2020).

This project explores the development of low-dose transmission electron microscopy methods for the study of a range of common pharmaceutical compounds including small molecule drugs (furosemide), inorganic cation exchangers (development batches of sodium zirconium silicate; any conclusions drawn based on these samples cannot be considered directly transferable to the commercially produced product), a channel hydrate (theophylline) and a new drug delivery modality (polymeric nanoparticle). A range of TEM techniques will be explored including electron diffraction and crystal lattice imaging in TEM, Scanning TEM in bright field and annular dark field modes at crystal lattice resolutions, scanning moiré fringe imaging, elemental analysis by energy dispersive spectroscopy and electron energy loss spectroscopy, and scanning electron diffraction. These techniques and where their potential for API analysis lies will be reviewed in the next chapter (Chapter 2) and then, in the light of this review, the project aim and objectives are stated at the end of the chapter. The materials and methods chapter (Chapter 3) will then outline the specific imaging techniques and sample preparation procedures used such as cryo-S/TEM with cryo-transfer, focussed ion beam lamellar preparation etc. The results chapters (Chapter 4-7) will demonstrate an analysis on each of the four model compounds discussed in the literature review (Chapter 2) and final conclusions and future work will be discussed in Chapter 8.

Chapter 2 Literature Review

This chapter will explore the literature on current challenges in pharmaceutical product development and will identify how electron microscopy might address some of these challenges by analysis of specific model compounds introduced in this thesis. The limitations associated with analysing pharmaceutical compounds using bulk methods will be presented, further highlighting the opportunity for the high spatial resolution method of (scanning) transmission electron microscopy to gain structural insight and provide an understanding that can enhance the performance of a pharmaceutical formulation. Finally, the current state of the art of the electron microscopy method for analysis of pharmaceuticals will be outlined.

2.1 Problems of Pharmaceutical Product Development

One challenge currently faced by pharmaceutical product development is the ability to link structure to performance in order to realise the full potential of a drug within a medicine. The effects of crystallisation and processing (e.g. milling, grinding, tableting) have an influence on the structure and defects of a drug within a pharmaceutical formulation. Structural changes of a drug are the subject of a wide range of performance problems, such as a decrease in aqueous solubility and intestinal permeability, as well as inducing chemical and physical instability in the final form of a product (Shekunov and York, 2000) (Figure 2.1).

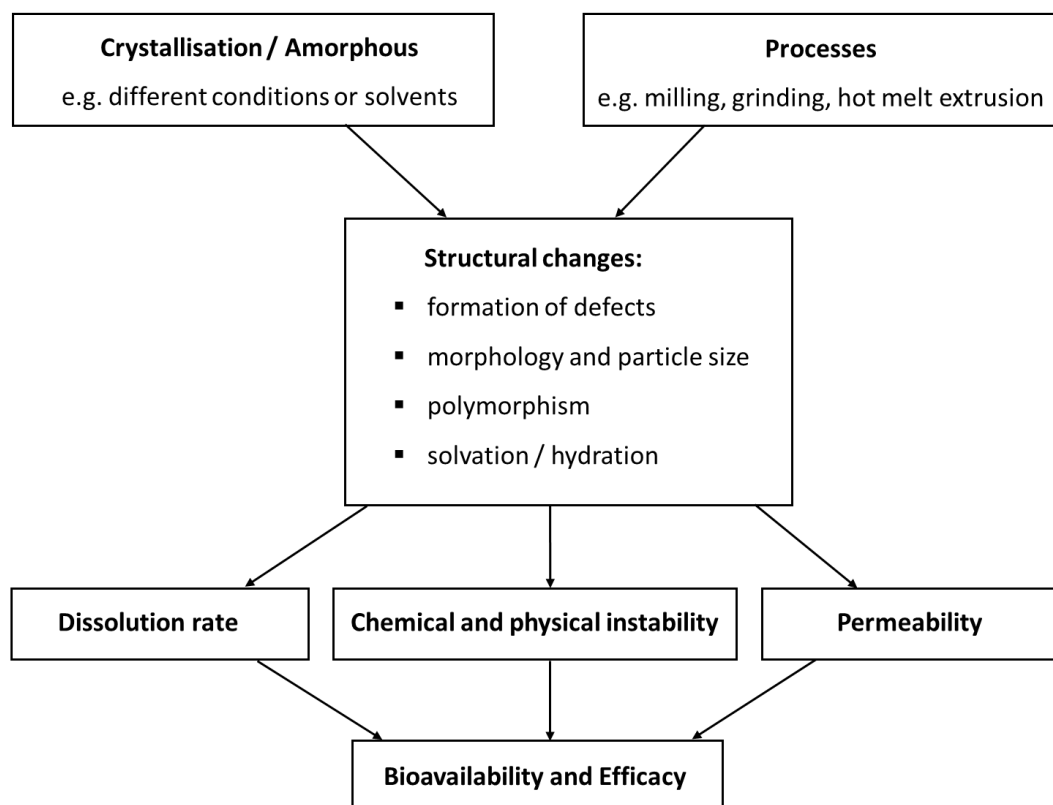


Figure 2.1 Potential causes and effects of structural changes in pharmaceutical compounds.

The biopharmaceutics classification system (BCS) categorizes drug substances based on their aqueous solubility and intestinal permeability into one of four categories: Class I (high solubility/high permeability), Class II (low solubility/high permeability), Class III (high solubility/low permeability), and Class IV (low solubility/low permeability) (Amidon et al., 1995). Oral delivery is the preferred and commonly employed route for drug administration. More

than 80% of marketed drugs are sold as tablets, of which 40% have low solubility and limited oral bioavailability (Goud et al., 2012). Poor solubility is associated with a low dissolution rate and plays a crucial role in drug absorption. The main factors responsible for low aqueous solubility of the drug or active pharmaceutical ingredient (API) are: (i) high lipophilicity and (ii) strong intermolecular interactions (Faller and Ertl, 2007).

Various approaches have been employed to enhance aqueous solubility and/or the dissolution rate of poorly soluble small molecule drugs, in order to influence bioavailability and therapeutic effectiveness (Nielsen et al., 2013). The common routes used to produce drugs with improved solubility properties range from crystal modification (e.g. metastable polymorphs, salts, co-crystals), particle size reduction (e.g. micronization, nanocrystals), amorphisation (amorphous solid dispersions), ion-exchange matrices (e.g. zeolites) to new modalities (polymeric nano-carriers e.g. polymeric nanoparticles encapsulating a drug). However, each of these methods used to increase the solubility of a drug have limitations and requires control at the molecular level (Chan et al., 2014; Kawabata et al., 2011). For example, particle size reduction could lead to the improvement of dissolution properties through an increase in surface area but the extensive mechanical processing can cause significant changes such as polymorphic transformations, disorder to the crystal lattice (i.e. crystal defects) and partial amorphisation. Many manufacturing processes can cause changes to the physical structure of APIs, such as the formation of a hydrate during granulation followed by a conversion to an anhydrous form during drying (Thakral et al., 2019). Amorphous solids are thermodynamically unstable and tend to revert to a more stable crystalline state over time (Adrjanowicz et al., 2011).

Newer therapeutic agents can require further structural understanding before optimisation for performance will be achieved. For example, the use of microporous materials for drug loading or cation exchange requires complete characterisation of particle sizes and pore structures to understand available surface areas and ensure the optimization of drug or ion loading (Farzan et al., 2023). While new modalities such as polymeric nanoparticles have potential because of their size and surface chemistry; they can be long-lived, stable colloids that provide controlled release at only target cellular sites,

thereby enhancing bioavailability and therapeutic index (Zielińska et al., 2020). However, particle structures, drug loading, targeting and release mechanisms are not well understood, contributing to very few of these formulations achieving regulatory approval (Patra et al., 2018) and even raising concerns regarding their nanotoxicology (Doktorovova et al., 2014).

Understanding the effect of crystallisation and processing on the formation of defects and crystal properties can help improve bioavailability and provide control of any inherent instability of an API within a pharmaceutical formulation (Shekunov and York, 2000). In addition, identifying and understanding the hydration and dehydration of small molecule drugs can help develop improved processing, formulation, and storage conditions.

Different bulk characterisation techniques are commonly used for the evaluation of the chemical and physical properties of pharmaceutical formulations, however, (scanning) transmission electron microscopy ((S)TEM) offers exceptional benefits due to its high spatial resolution and has the potential to provide insight into these processes at the molecular and nano-scale. In order to realise the benefits of STEM we need to overcome the main challenges which ensuring the representability of data by controlling specimen preparation, electron beam damage and area sampling. This thesis will address these challenges and demonstrate the potential for using STEM in four different pharmaceuticals: 'traditional' small molecule drugs, microporous inorganics, channel hydrates and new modality polymer nanoparticles.

2.2 Different Types of Drug Products and The Main Challenges That Can Be Addressed by (S)TEM

2.2.1 Small Molecule Drugs - Monitoring Crystal Defects and the Potential Impact on Dissolution

The crystal structure of organic solids is composed of ordered molecules, which are held together by relatively weak intermolecular forces, such as van der Waals interactions and hydrogen bonds. The crystallographic structure of the molecular compound is defined by a specific unit cell, which is the smallest repeating unit of a crystal. Low-symmetry crystals have strongly anisotropic

properties and each crystallographic face can exhibit different properties e.g. a different growth rate or rate of dissolution (Hadjittofis et al., 2018). Recent studies in this field have concentrated on understanding, controlling and predicting the directional properties of these crystals (Taylor et al., 2021).

Crystalline small molecule drugs are of high importance to the pharmaceutical industry as most of these drugs or APIs are formulated in this form. Almost 80% of *new* API candidates exhibit a solubility problem (Goud et al., 2012). Poor solubility is linked with slow dissolution, which is the first step in drug absorption from the solid form (Goud et al., 2012; Qiu et al., 2017). Yet the presence of crystal defects can enhance dissolution rates (Burt and Mitchell, 1981).

Crystals are always likely to contain imperfections and defects they are an integral part of the crystallisation process; however, thermal and mechanical processes can also generate crystal imperfections (Hadjittofis et al., 2018; Newman, A. and Zografi, 2014). Crystal defects are classified into point defects, line defects, planar defects and bulk defects (Swalin and Arents, 1962). Point defects, the smallest of those listed, mostly associate with a few atoms or molecules and do not expand beyond this scale. Line defects, known as dislocations, involve at least a line of atoms or molecules in the crystal lattice out of alignment from the regular order. Planar defects arise during changes in the crystallographic growth direction. Bulk defects are small voids or regions that contain an accumulation of vacancies in a crystal lattice (Chamarthy and Pinal, 2008).

Dissolution is often initiated at crystal defect locations (Vasilchenko et al., 1999), and rates are affected by the number of defects present at a surface (Burt and Mitchell, 1981). Dislocations and voids affect dissolution processes by inducing etch pit formation (Sangwal, 2012). The pitting process generates roughness, thus increasing the specific surface area as well as creating microdomains (pit walls) with higher surface energy leading to faster dissolution (Adobes-Vidal et al., 2016; Perry et al., 2015). Therefore, the characterisation of crystalline defects is crucial in considering the performance and processing of pharmaceutical products.

Understanding the type and distribution of crystal defects at the microscopic level could lead to modifications and control of a drug's solubility, impacting bioavailability. Understanding of the physical properties of metals and semiconductors has been significantly enhanced through defect analysis by electron microscopy (Williams and Carter, 2009). Yet, dislocations in organic crystals have been referred to as *terra incognita*, because of the challenges of characterising them by electron microscopy (Olson et al., 2018). This study will address the fragility of organic crystals under high-energy electron beam irradiation and will investigate, by (scanning) transmission electron microscopy methods (i.e. by phase contrast lattice imaging, scanning moiré fringe imaging and scanning electron diffraction), the structure-property relationships of a small molecule drug, furosemide as a model for poorly soluble organic compounds in general. Results from this study will be presented in Chapter 4 and have been part published in S'ari et al. (2020).

Model Small Molecule Drug - Furosemide

Furosemide (brand name Lasix) is a loop diuretic and antihypertensive drug, used to control cardiovascular and heart failure disease (Aceves et al., 2000). According to BCS, furosemide belongs to the last Class IV category, because of its low permeability and poor solubility (Babu et al., 2010; Tang, N. et al., 2019). Furosemide $C_{12}H_{11}ClN_2O_5S$ is a weak acid that can be present in four known polymorph forms (I-IV), two solvates (IV-DMS and V-dioxane) and one amorphous form (Beloborodova et al., 2017; Goud et al., 2012; Matsuda and Tatsumi, 1990; Nielsen et al., 2013). The thermodynamically stable polymorph form I is the only form present in the commercial drug. It has a triclinic crystal system ($P\bar{1}$) with cell parameters as follows: $a = 9.5150 \text{ \AA}$, $b = 10.4476 \text{ \AA}$ and $c = 15.5826 \text{ \AA}$, as reported in the Cambridge Structural Database (reference FURSEM13) (Babu et al., 2010). Furosemide is a conformational, flexible molecule due to the presence of sulfamoyl and furanylmethylamino fragments and three hydrogen bond donating groups: -NH-, -COOH and, $-\text{SO}_2\text{NH}_2$, which is why it can crystallise to different polymorphs and conformers, salts and solvates (Banik et al., 2016; Beloborodova et al., 2017). Poor solubility of furosemide is linked to strong intra- and intermolecular H-bonding in the crystal structure and the presence of furan rings which cause slower solvation of the drug (Babu et al., 2010).

Furosemide is the subject of many recent scientific studies designed to enhance therapeutic effectiveness by improving dissolution rate. One of the methods is particle size reduction by mechanical treatment (milling or cryomilling). However, furosemide is found to be unstable after extensive cryogenic grinding, not only due to structural changes (amorphisation) but also to unwanted chemical decomposition (Adrjanowicz et al., 2011). Another approach revealed modification in dissolution by making amorphous solid dispersions of furosemide in a polymer matrix (a higher dissolution rate was observed with higher furosemide concentration in the matrix) (Aceves et al., 2000). Nielsen et al. (2013) used a spray-drying method with an amorphous sodium salt of furosemide and found an 8-fold improvement in dissolution rate. In another study, Ambrogi et al. (2012) used mesoporous MCM-41 silica as a carrier to improve furosemide dispersion and dissolution rate. The most recent study has revealed that preparing furosemide nano-suspensions (by an antisolvent precipitation method) enhances its dissolution rate in gastric media (Shariare et al., 2019). It is clear therefore that the physicochemical properties of furosemide can be modified, however, different processes result in significant changes in the crystal structure and different stability likely due to the presence of defects. Therefore, it is crucial to obtain information on the crystal lattice defects present after processing (e.g. number density and type).

Furosemide has been routinely characterised by powder X-ray diffraction (pXRD), Differential Scanning Calorimetry (DSC) and Fourier Transform Infrared Spectroscopy (FTIR). Adobes-Vidal et al. (2016) reported on the investigation of dissolution kinetics of the individual crystal faces of furosemide form I by a versatile in situ multi-microscopy method (optical microscopy, scanning ion-conductance microscopy and atomic force microscopy). They found that increases in surface pitting density (surface area and roughness) increase the dissolution rate of particular crystallographic faces. For example, the (001) surface has been found to have a lower number of pits compared to the (010) face consistent with the calculated surface energy model and dissolution rate i.e. (001) < (010). It is probable that crystal defects e.g. dislocations and voids are sites for the initial formation of pits during dissolution (Sangwal, 2012). Understanding the defect structure of furosemide is therefore of interest.

2.2.2 Microporous Inorganics - Monitoring the Compositional Changes and Ion Distribution Upon Cation Exchange

There have been successful therapeutic applications of metal complexes for the treatment of a wide variety of diseases (Sadler, 1991), and so there is a growing interest in the potential of inorganic crystals (held together by stronger covalent or ionic bonding) for pharmaceutical applications. One of the promising groups of inorganic compounds are zeolites. Zeolites are microporous crystalline hydrated aluminosilicate minerals with well-defined and uniform pore sizes of 0.3 - 1.5 nm (Khaleque et al., 2020). They are widely used generally, because of molecular sieving, ion exchange, and catalytic properties. An inherent porosity can result in the outer surface area of a zeolite particle being only a few percent of the total available surface area (Khaleque et al., 2020), allowing for the incorporation of reactive ionic species inside pores and providing ion exchange selectivity (Khivantsev et al., 2023).

Early work on zeolites and their capabilities for the exchange adsorption of ions from aqueous solutions has been done by Boyd et al. (1947). Over the last three decades, microporous zeolites have been the subject of much research i.e. framework modification by substituting metal ions with different oxidation states to enhance ion-exchange capacities (Ferreira et al., 2001; Jale et al., 1999). This leads to a number of new approaches for the synthesis of materials with enhanced physicochemical properties and targeted exchange mechanism for specific cation removal (Bortun et al., 1996; Bortun et al., 1997; Ferreira et al., 2001; Zhang et al., 2001). The unique microporous structure of zeolites and silicates make them the most important inorganic cation exchanger in the pharmaceutical industry (Kraljević Pavelić et al., 2018), e.g. applications that relate to detoxifying roles by removal of contaminants from the body or to provide control of alkali levels (Kraljević Pavelić et al., 2018; Stavros et al., 2014). For example, cation exchange resins are currently approved for hyperkalemia treatment however microporous inorganics may be more effective because they can provide a more rapid reduction of serum potassium levels (Shrestha et al., 2021).

This study will investigate, by (scanning) transmission electron microscopy methods including elemental analysis, the structure and composition of

development batches of sodium zirconium silicates with different sodium compositions, manufactured in laboratory conditions not consistent with the commercial manufacturing method of AstraZeneca's model potassium cation exchanger Lokelma (however any conclusions drawn based on these samples cannot be considered directly transferable to the commercially produced product). Results from this study will be presented in Chapter 5.

Model Microporous Inorganic – Monitoring Na⁺ Content and Distribution in Laboratory Development Batches of Sodium Zirconium Silicate

Samples of a model microporous inorganic, sodium zirconium silicate were supplied by AstraZeneca for this study and were taken from development batches manufactured in laboratory conditions not consistent with the commercial manufacturing method of this material. Therefore, any conclusions drawn based on these samples cannot be considered directly transferable to the commercially produced product. The background of the commercial product will be presented in Chapter 5 section 5.1. Briefly, sodium zirconium silicate is a new orally administered, non-absorbed, highly selective potassium binder used for the treatment of hyperkalaemia (Rafique et al., 2015). The three-dimensional framework of this silicate is composed of Zr in octahedral and Si in tetrahedral oxygen-coordination (cubic crystal system, $P\bar{6}3$, $a = 12.7024 \text{ \AA}$), which results in a microporous structure containing cation-binding pores (Stavros et al., 2014). The microporous compositions can incorporate alkali metal ions, i.e. Na⁺, Ca²⁺ or protons, H⁺, which act as exchangeable counter ions to K⁺ and provide electrical neutrality to the structure (Linder et al., 2016). An uniform opening pore diameter of $\sim 3 \text{ \AA}$ allows preferential trapping of potassium ions as its unhydrated diameter is $\sim 2.98 \text{ \AA}$ (Stavros et al., 2014). This unique pore structure gives the opportunity for composition modification upon cation exchange. Transmission electron microscopy has the spatial resolution to investigate the microporous structure of these development batches of laboratory material that are (a) full of Na⁺ ions (sample AZ1) and (b) partially protonated, with a fraction of Na⁺ ions exchanged for H⁺ (sample AZ1-2) and to specifically explore the occupancy of pores and the distribution of the Na⁺ cation located within the micropore channels. Many zeolite and silicate structural studies show that electron microscopy is a powerful tool for this type of material characterisation since it

allows direct observation of the pore structure (van Vreeswijk and Weckhuysen, 2022).

2.2.3 Channel Hydrates – Monitoring Hydration and Dehydration of Organic Compounds

Around one-third of active pharmaceutical ingredients can exist in hydrate forms (in 2006, 29% of the 808 solid organic compounds listed in the European Pharmacopoeia were reported to have this capability) (Griesser, 2006). Hydrate formation in pharmaceuticals is primarily attributed to the water-attracting (hydrophilic) and ionically charged properties of many drugs (Griesser, 2006). Water becomes integrated into the crystal structures of hydrates, playing various roles, including reducing electrostatic repulsion between ions, forming hydrogen bonds with functional groups in drug molecules and coordinating with ions (Sanii et al., 2021). The common method used to confirm the existence of hydrates is single-crystal X-ray diffractometry (Jurczak et al., 2020). However, obtaining appropriately sized crystals (> 1 μm) is challenging and alternative techniques such as powder X-ray diffraction, thermal analysis, Karl Fischer titrimetry, polarized light microscopy, infrared spectroscopy, and solid-state nuclear magnetic resonance (NMR) spectroscopy can be employed.

Hydrate formation can occur during drug formulation (e.g. wet granulation, lyophilization, crystallization) or under storage conditions (usually above critical relative humidity (RH)) (Jurczak et al., 2020). Fluctuations in temperature and humidity during manufacturing can lead to partial hydration or dehydration and phase transformation, resulting not only in variations in the water content of the final product but also potentially altering the dissolution profile and bioavailability (Censi and Di Martino, 2015). In addition to environmental and processing conditions (i.e. humidity, temperature, pressure), other factors such as particle size, defects and impurities in the primary crystalline structure can affect this phase transformation. For example, anhydrous theophylline (form II) rapidly transforms to the monohydrated form when placed in contact with water during manufacturing processes (e.g. wet granulation) or on storage in high humidity conditions (De Smidt et al., 1986; Rodríguez-Hornedo et al., 1992; Suzuki et al., 1989). This

has negative consequences on therapeutic applications as it leads to lower dissolution rates and lower bioavailability (De Smidt et al., 1986). Another example of a channel hydrate exhibiting dissolution problems, variability in phase stability and clinical failures is carbamazepine (Flicker et al., 2011). Carbamazepine form III is thermodynamically stable and used as a drug (Behme and Brooke, 1991; Kobayashi et al., 2000). However, form III can transform rapidly into a more stable dihydrate form under storage in high humidity conditions (full conversion occurred in 2 weeks at 98% relative humidity) significantly decreasing the dissolution rate of the commercial product (solubility of form III was found to be 1.5–1.6 times higher than that of the dihydrate) (Kobayashi et al., 2000). Therefore, the polymorphic transitions on hydration and or dehydration that can occur both during drug formulation processes and storage of commercial tablets need to be carefully monitored and appropriate analytical techniques implemented to monitor these changes at the particle size level (Farias and Carneiro, 2014).

Hydrates are categorized into three groups based on the arrangement of water molecules within the crystal lattice: (i) water at isolated lattice sites, (ii) water within lattice channels i.e. channel hydrates (e.g., ampicillin trihydrate, theophylline monohydrate), and (iii) water coordinated with ions (e.g., nedocromil salts) (Vippagunta et al., 2001). Hydrates can also be classified as: (i) stoichiometric and (ii) nonstoichiometric. In stoichiometric hydrates, the number of both water/OH ions and host molecules is preserved (and charge balances), while in nonstoichiometric hydrates, the water content varies and depends on the relative humidity (RH) of the environment. This non-stoichiometry is of particular interest in channel hydrates because it may enhance the metastability of a phase. The formation of hydrates is a process that can be controlled by water activity, with the transition from anhydrate to hydrate occurring when water activity exceeds a critical value. The physical stability of hydrates depends on the arrangement of water molecules and the strength of host-water interactions within a crystal.

Understanding the kinetics of hydration and dehydration processes, especially in the context of different APIs and environmental conditions, remains challenging despite many years of research. The description of a hydration/dehydration phase transformation is still based on both

experimental and theoretical methods (Jurczak et al., 2020). Analyses of these transformations are important for determining if the transformation of APIs under some given conditions would take place spontaneously, and if so, at what rate (Feth et al., 2011). However, solid-state characterisation methods have a limit of sensitivity to the presence of trace amounts of intermediate phases. Therefore, there is an opportunity for transmission electron microscopy to characterise these phase transformations at even smaller length scales and to detect small quantities of intermediate phases. For the pharmaceutical industry, this information can help to develop an understanding of hydration/dehydration processes in order to improve processing, formulation, and storage.

This study will investigate, by (scanning) transmission electron microscopy methods (i.e. phase contrast lattice imaging and scanning electron diffraction) the structure and phase transformation of a model channel hydrate, theophylline. Results from this study will be presented in Chapter 6 (including some dislocation analysis that has contributed to a Nature Materials submission (Pham et al., 2023) and also shown in the Appendix C).

Model Channel Hydrate – Theophylline

Theophylline, also known as 1,3-dimethylxanthine, is a xanthine drug used to treat chronic obstructive pulmonary disease and asthma. Theophylline can exist either as an anhydrate form (form I, II, IV, VI, VII) or a monohydrate form. Theophylline anhydrous form II is a kinetically stable polymorph at room temperature under 'dry' conditions and this form is used as an API. Form II rapidly transforms to the monohydrated form when placed in contact with water at ambient temperature or during storage in high humidity conditions (> 66%) (De Smidt et al., 1986; Rodríguez-Hornedo et al., 1992; Suzuki et al., 1989). Depending on the conditions, dehydration of the monohydrate form can be a one-step process leading to the formation of the anhydrous form II or a two-step process, with the first and second steps leading to the formation of a metastable intermediate form III (similar structure to the monohydrate form, but with the water removed from channels in the crystal structure) and then the anhydrous form II, respectively (Agbada and York, 1994; Nunes et al., 2006; Paiva et al., 2021). The presence of metastable form III or the

monohydrate form in a final product can have serious consequences on performance leading to increased tablet hardness and lower dissolution rate (Phadnis and Suryanarayanan, 1997).

Many studies have reported that theophylline phase transformations occur in the solid state by fitting hydration/dehydration experimental data to solid-state transformation equations and rate-controlling models (Amado et al., 2007; Matsuo and Matsuoka, 2007; Nunes et al., 2006; Paiva et al., 2021; Tantry et al., 2007) unless there is a clear indication of using a solvent as a hydration/dehydration medium (De Smidt et al., 1986; Jørgensen et al., 2004; Rodríguez-Hornedo et al., 1992). Amado et al. (2007) postulated that the hydration of theophylline form II to monohydrate form is a one-step nucleation process, described by the Avrami–Erofeev equation of exponent 0.5 i.e. by heterogeneous nucleation and diffusion-limited growth of monohydrate needles on the existing form II phase. Suzuki et al. (1989) reported that the dehydration under isothermal conditions followed the Avrami-Erofeev equation with the same exponent of 0.5 or with a slightly lower exponent of 0.25 (suggesting more limited growth) (Agbada and York, 1994; Duddu et al., 1995). These studies linearized the experimental data using the best-fit solid-state models i.e. by assuming these processes occur through to completion in the solid state (Duddu et al., 1995). However, if the water released by dehydration remains localised as a solution or more likely a vapour it may be that the phase transformation is solution or vapour-mediated. De Smidt et al. (1986) reported the monohydrate form of theophylline crystallizes on the surface of the anhydrous form on contact with water and that the transformation kinetics depend on a dissolution boundary layer thickness between the form II and monohydrate form. These observations indicate a solvent-mediated phase transformation. Rodríguez-Hornedo et al. (1992) also observed that anhydrous form II crystals in an aqueous suspension act as a substrate for nucleation and epitaxial crystal growth of the monohydrate phase i.e. a solvent-mediated transformation.

Thus, theophylline provides a good model compound for assessing nucleation and early-stage growth of the hydrate phase and dehydration to metastable and stable anhydrate phase transformations by (scanning) transmission electron microscopy at the individual particle length scale. This information

can provide a mechanistic understanding of the initial reaction pathway and nucleation sites for these phase transformations.

2.2.4 New Modalities – Monitoring API Loading in Polymeric Nanoparticles

The field of nanoparticle-mediated drug delivery is increasing rapidly as a promising tool to provide site-specific, target-oriented and efficient drug delivery for anticancer therapeutics, but translation into clinical use remains challenging (Avgoustakis, 2004; Ferrari, 2005; Gavas et al., 2021; Hare et al., 2017; Hu et al., 2013; Labhasetwar et al., 1997; van der Meel et al., 2017). This is mainly related to understanding API release mechanisms from particles even before clinical trials, but also with a requirement of obtaining consistent reproducibility and homogeneity in scale-up manufacturing (Herdiana et al., 2022; Patra et al., 2018). Classical drug delivery via solid formulations such as oral tablets can be limited by poor solubility and low bioavailability of the APIs. Encapsulation of an API within a functionalized polymeric nanostructure, however, has shown potential as an alternative delivery formulation that could improve therapeutic efficacy by increasing the half-life of drug circulation, targeting of specific cellular sites while reducing side effects such as lack of toxicity to non-target organs (Nimesh et al., 2006; Torchilin, 2006). One of the promising groups of nano-carriers are polymeric core-shell nanoparticles (NPs) because they are able to encapsulate APIs by accumulation in a hydrophobic polymer matrix assumed to be at a particle's core (Labhasetwar et al., 1997; Matsumura and Maeda, 1986; Wallace et al., 2012). A hydrophilic shell provides a hydrated steric barrier to increase the dispersion stability of the NPs in aqueous suspension and to protect them from recognition and removal by the reticuloendothelial system (Tang, Y. et al., 2019), prolonging blood circulation time (Xiao et al., 2010). The API delivery then depends on the loading efficiency, the rate of diffusion through the polymeric matrix and any degradation of the polymeric NPs themselves (Lim Soo et al., 2008). An important aspect of understanding the potential of new drug-loaded polymeric NPs is to characterise the particle structure, i.e. identification of the size and morphology of the core-shell nanoparticles and

measure the distribution of the API within the polymer matrix (Mahapatro and Singh, 2011; Mahdavi et al., 2020).

This study will investigate, by cryogenic (scanning) transmission electron microscopy methods and elemental analysis, the structure and composition of development batches of a new modality, polylactic acid - polyethylene glycol (PLA-PEG) polymer NP encapsulating drug system provided by AstraZeneca. Results from this study will be presented in Chapter 7 and have been published in Heliyon (Koniuch et al., 2023).

Polylactic acid - polyethylene glycol (PLA-PEG) polymer NPs encapsulating a drug

Polylactic acid - polyethylene glycol (PLA-PEG) polymer NPs have been extensively investigated as anticancer drug delivery vehicles (Avgoustakis, 2004; De Souza Guimarães et al., 2022; Riley et al., 2003; Xiao et al., 2010). PLA is commonly used as a drug carrier. However, PLA is hydrophobic and therefore does not disperse well in aqueous suspension, requiring surface modification by hydrophilic PEG to increase the dispersion stability and blood circulation time of any NP form (Avgoustakis, 2004). PLA-PEG NPs are commonly synthesized by the emulsion solvent evaporation or emulsion solvent diffusion methods (Wadhawan et al., 2022; Xiao et al., 2010). Multiple studies show high efficiency of encapsulation and conjugation of various APIs (chemotherapy drugs, nucleic acids, peptides) by PLA-PEG based NPs (Afsharzadeh et al., 2019; Andima et al., 2018; Hami et al., 2014a; Hami et al., 2014b; Kumar et al., 2014; Song et al., 2016; Wadhawan et al., 2022).

In order to tune nanoparticles to meet a therapeutic profile, analytical techniques provide insight into the physical and chemical structure of the particles and enable the link between nanoparticle structure and product performance to be established (Kamaly et al., 2016). This should ensure that product quality and performance are maintained for the life-time of the drug, yet characterising the complete structure of drug-loaded PLA-PEG polymeric NPs is challenging to do directly at the individual particle level due to a lack of appropriate analytical methods of necessary spatial resolution. Particle size distributions are commonly measured by dynamic light scattering (DLS) and can include surface charge assessment with a zeta potential analyser

(Wadhawan et al., 2022). The sensitivity of laser scattering of polydispersed particles of significantly different diameters makes interpretation complex and can lead to highly variable results (Bootz et al., 2004; Mahl et al., 2011). Other analytical techniques such as optical nanoparticle tracking algorithms, X-ray scattering or standard electron microscopy (EM) might only measure the diameters of a dense particle core because the hydrated shell is significantly less dense and/or collapsed in a high vacuum. The components of PLA-PEG NPs can be distinguished using proton nuclear magnetic resonance (^1H NMR) by identifying distinct spectral peaks for each synthesized co-polymer but their co-localization can only be assumed from this method (Wadhawan et al., 2022). Small-angle neutron scattering (SANS) has shown that the thickness and structure of the PEG layer depend on the molecular weight of the PLA in PLA-PEG NPs (Riley et al., 2003). The analysis however involves a model that assumes the core to be homogeneous, and have a uniform scattering profile and the shell to be less dense and have a diffuse scattering profile. Pustulka et al. (2013) have used multiple characterisation techniques (^1H NMR, dynamic light scattering, X-ray Diffraction and cryogenic TEM) to suggest a three-layer core-shell-corona particle structure to polymeric nanoparticles containing an insoluble low molecular weight compound encapsulated within a particle structure stabilized by amphiphilic diblock copolymers. Moreover, Han et al. (2015) reported that cryo-TEM can reveal a three-layer core-shell-corona nanoparticle structure of PEG-*b*-PLGA based nanoparticles, but the PEG layer halos around each nanoparticle were difficult to image due to it having a very low scattering density and its presence was identified in only a minority of images. A polyethylene glycol-*b*-polylactic co-glycolic acid (PEG-*b*-PLGA) block copolymer was shown to be most suitable for potential drug delivery systems based on colloid stability measures and good coprecipitation with the API (within the hydrophobic block), however, a PEG corona was generally assumed to be present rather than being directly identified. STEM techniques have the potential to enhance the image contrast of each of these layers over TEM (see section 2.7 for details). Furthermore, the distribution of APIs in these systems is often based on an assumption related to the preparation or polymerization method. For example, Song et al. (2016) reported the potential for the use of hydrophobic ion pairing (HIP) of an

API (AZD2811) with pamoic acid for controlled release of the API from PLA-PEG NPs, however, the structure and distribution of the HIP material in the final NPs was only assumed from the preparation method and release kinetics (Song et al., 2016; Wren et al., 2021). A complete analysis of the structure, chemistry and API loading of these particular PLA-PEG NPs could confirm whether these assumptions are appropriate and provide accurate parameters for predictive modelling of the release kinetics.

Scanning transmission electron microscopy ((S)TEM) equipped with an electron energy loss spectrometer and energy-dispersive X-ray detectors can address the challenge of a full characterisation of PLA-PEG NPs because it can determine all of the morphology, structure and chemistry at the single particle level.

2.3 Common Bulk Characterisation Techniques

Characterisation of bulk materials (e.g. the degree of crystallinity, polymorph type etc.) is commonly distinguished by powder X-ray diffraction (pXRD), Fourier transform infrared spectroscopy (FTIR) or differential scanning calorimetry (DSC) (Newman, A.W. and Byrn, 2003; Smeets et al., 2018). These methods are used during the various steps of processing and drug development but have some limitations. This is particularly problematic during the characterisation of amorphous materials e.g. amorphous solid dispersions or multicomponent phases. It has been emphasised that most techniques can detect no less than about 10% of disorder, which is insufficient for determining low levels of defects or amorphous regions in highly crystalline samples (Saleki-Gerhardt et al., 1994).

Powder X-ray diffraction, considered a “gold standard” technique, has been widely used to characterise crystalline pharmaceutical solids (Chieng et al., 2011). In this technique, a diffractometer generates X-rays of wavelength similar to the spacing of planes in a crystal. The interaction between the X-ray and the powder sample is recorded by detecting scattered X-rays which fulfil the Bragg diffraction conditions for coherent scattering. This produces a pXRD pattern characteristic of the crystal structure of the analysed material and therefore contains information about the atomic or molecular arrangement in a crystal. This is useful for determining the crystal phase of samples by pattern

comparison against known references or by full pattern fitting or refinement. A sufficient amount of sample powder is needed to perform pXRD analysis (at least 10 mg) (Kabova et al., 2022). The method is often limited due to the fact that the characterisation of complex structures is complicated by patterns that contain many overlapping peaks, making the unit cell parameters of the crystal difficult to determine (Holder and Schaak, 2019). The pharmaceutical industry commonly focuses on the reduction of the API particle size to increase its bioavailability, and diffraction from nano-crystals will have peak broadening which will reduce the diffracted peak intensity relative to a well-crystallized material, potentially causing misinterpretation of the data (Holder and Schaak, 2019). If the number of defects in a particular plane is small, this information is likely not to be detected by pXRD due to the overlap of the scattering peaks. Moreover, In commercial formulations (tablets) the API is mixed with excipients and compressed and the excipients themselves have varying crystal habits and particle sizes, resulting in a complex diffraction pattern with many peaks (Farias and Carneiro, 2014). This complexity reduces the sensitivity of pXRD to detect and characterise changes of an API in tablet formulation.

Fourier Transform Infrared spectroscopy (FTIR) has been used to study crystals, co-crystals and the polymorph, hydrate/solvate forms of pharmaceutical samples (Healy et al., 2017). The FTIR method measures or absorption of light by a molecular material, in particular showing changes in the vibrational frequency (or absorption) of specific molecular bonds. This spectroscopic technique is considered to be a complementary method to pXRD and provides information about characteristic absorption bands of some functional groups in a formulated product as well as band shifts in frequency which might indicate structural changes (but the technique does not measure crystalline structure directly) (Bugay, 2001). This method has some limitations related to sample preparation, the complexity of absorption bands within spectra and a reduced sensitivity for impurities in a sample compared to pXRD. Moreover, analysing tablet formulations is complex due to the high absorption behaviour of excipients in comparison to the API (Bugay, 2001; Farias and Carneiro, 2014).

Another method, differential scanning calorimetry (DSC) is a commonly used thermal technique. It can be used to measure the difference in the amount of heat required to increase the temperature of a sample (parallel to an inert reference standard) as a function of temperature. DSC is used to study phase transitions (i.e. melting and exothermic decompositions) and sample purity of a drug formulation. The limitations are related to the low sensitivity of thermal transitions involving small energy changes, and difficulty with the interpretation of overlapping peaks (Hadjitofis et al., 2018). Moreover, heating can induce phase transformation and an API can convert to another polymorphic form with very little energy change. It is problematic for samples with mixed phases that readily convert to another form because phase quantification becomes difficult.

Dynamic light scattering (DLS) is commonly used to measure particle size distribution profiles suspensions in the sub-micron range and to evaluate the colloidal stability of the nanoparticle suspensions but can include surface charge assessment with a zeta potential analyser (Wadhawan et al., 2022). However, the limitation of the sensitivity of laser scattering by polydispersed particles of significantly different diameters restricts the use of this technique (Bootz et al., 2004; Mahl et al., 2011).

2.4 Transmission Electron Microscopy (TEM)

Within the development of electron microscopy techniques, transmission electron microscopy (TEM) and its ability for electron diffraction holds great promise for the analysis of pharmaceutical compounds at a ground-breaking single particle or crystal scale (Eddleston et al., 2010). In TEM, a high-energy beam of electrons is used for imaging objects. Based on theoretical work by Louis de Broglie, it can be shown that an electron's wavelength is inversely proportional to a voltage it is accelerated through; the resolving power for typical electron voltages in the TEM (80 – 300 kV) is of the order of 0.001 nm although this is usually practically limited by lens aberrations and stability to ~0.1 nm. The latter is mainly related to lens imperfections which are a source of spherical and chromatic aberrations (Williams and Carter, 2009). The electrons are emitted by an electron gun and are transmitted through a thin specimen (< 500 nm) where a number of interactions can occur. The scattered

electrons can be collected, focused and magnified by a set of lenses in order to produce a projected image of the internal structure of a specimen. Moreover, other interaction products e.g. X-rays can be collected by a corresponding detector or spectrometer that allows for elemental analysis of a specimen. The contrast formation in TEM images is generally produced by mass difference, thickness difference, diffraction scattering and even phase difference in ultrathin specimens (< 50 nm) (Egerton, 2005). TEMs can operate in diffraction mode, thus an electron diffraction (ED) pattern can be collected to study the crystal structure, offering some advantages over powder X-ray diffraction as ED can be implemented on very small crystals (sub-micron sized) and small quantities of material (even pictogram). The ED technique is however not as accurate as XRD unless internal standards are used for calibration (Eddleston et al., 2013).

As pharmaceutical research increasingly focuses on nano-scale product development, TEM is becoming an important complementary method to measure crystallite size and orientation, crystal defects as well as surface structures down to a single particle level (Eddleston et al., 2010). Moreover, a TEM can operate at different magnifications, thus allowing quick characterisation of both micro and macro scale features of a material.

TEM is a powerful analytical technique allowing, potentially, direct imaging of crystal structures however, the application to pharmaceuticals is often limited. This is mainly associated with difficulties related to sample preparation (it is required that a specimen must be thin enough to be transparent to an electron beam, typically < 500 nm) (Jones, W. and Thomas, 1979) plus the fact that organic samples are highly sensitive to electron beam damage by the irradiating high energy electrons (Egerton, 2005).

2.5 Electron Beam Damage in TEM

Radiation damage is the main limiting factor for the high-resolution imaging of materials such as: organic compounds, soft materials, biological samples as well as hydrated inorganics such as some zeolites and silicates. Electron beam damage can be categorised by two mechanisms: elastic or inelastic scattering or a combination of both (Egerton et al., 2004) (Figure 2.2).

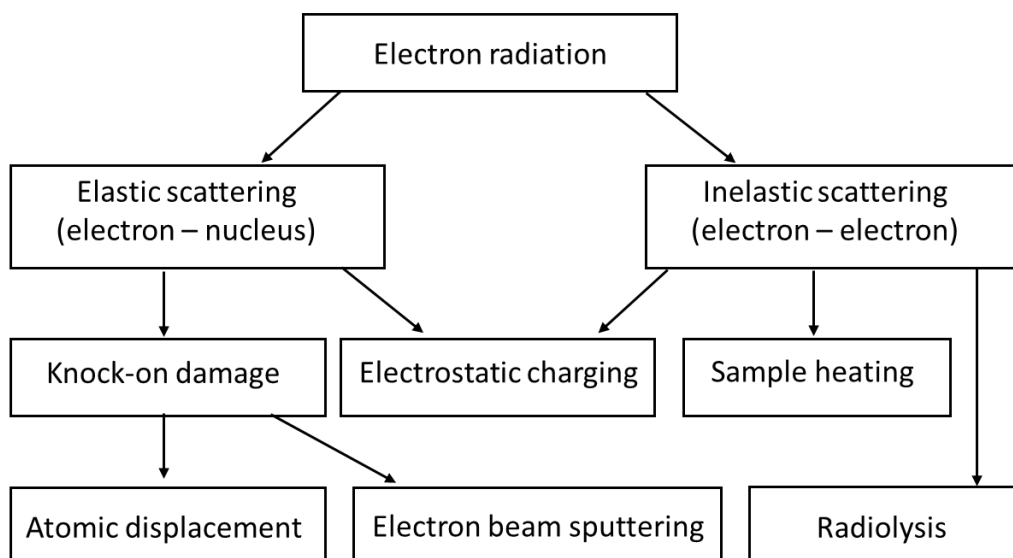


Figure 2.2 Electron beam damage mechanism (adapted from Egerton (2005)).

The elastic interaction of incident electrons with the nucleus of an atom causes knock-on damage such as direct atomic displacement or electron beam sputtering. This is the main damage mechanism for electrically conducting specimens (e.g. conducting inorganic compounds) because good conductors contain a high density of mobile electrons, which inhibit radiolysis (Egerton, 2005).

In the case of non-conducting organic materials, electron–specimen interactions generate various types of radiation damage such as atomic displacement, electrostatic charging and sputtering (Egerton et al., 2004; Leijten et al., 2017), however, radiolysis resulting from inelastic electron scattering is the main mechanism for damage (Egerton et al., 2004). Radiolysis is associated with the indirect degradation of chemical bonds as a consequence of the excitation of electron states within a molecule or atom in the specimen by the electron beam. Due to the fact that crystalline organic compounds have poor conductive properties, de-excitation is not always possible and this leads to a number of effects such as bond breakage, changes in molecule position, and potentially a loss of crystallinity. It is reported that for organics, aromatic compounds are generally more stable

than aliphatic ones, as they contain relatively stable ring structures. Recent work has shown that the number of conjugated carbons and the ratio of conjugated carbons to non-conjugated carbons affects the stability of organic compounds in TEM (S'ari et al., 2018).

The effect of electron beam-induced radiolysis on griseofulvin crystals is shown in Figure 2.3. In this diffraction pattern series, the Bragg reflections of the crystal gradually reduce in intensity and disappear as the electron intensity (fluence) accumulates due to a progressive loss of crystallinity. This is typical for the radiolysis decay of an organic material, where the loss of short-range order (intramolecular positions) occurs before the loss of long-range order (molecular positions). Inelastic scattering can also cause sample heating and electrostatic charging however, radiolysis is the most common mechanism of damage in organic materials (Egerton, 2005).

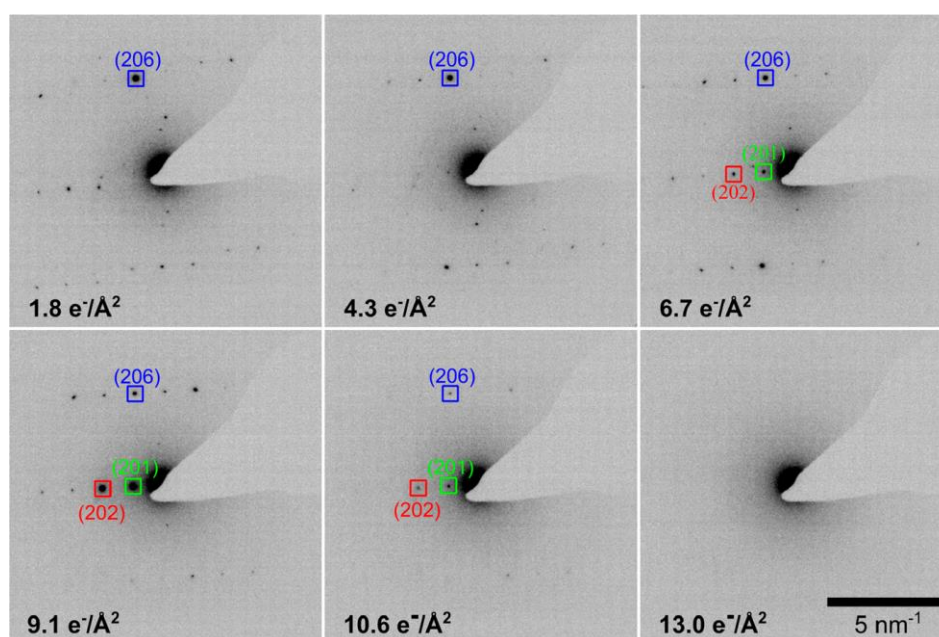


Figure 2.3 Example of an electron diffraction pattern time series of griseofulvin, acquired using an electron flux of $0.02 \text{ e}^-/\text{\AA}^2\text{s}$. Taken from S'ari et al. (2018).

2.6 Mitigating of Radiolytic Damage of Organic and Inorganic Crystals under TEM Analysis

Radiation damage in the TEM cannot be eliminated but may be minimised through various procedures that minimise dose. The radiation dose, G , is quantified in units of Grays (Gy) and 1 Gy represents the absorption of one

joule of ionizing radiation by a kilogram of substance. The radiation dose depends on the acceleration voltage and thickness of the specimen and the radiation damage is directly proportional to the energy deposited into the specimen (Egerton, 2019; Egerton et al., 2004). Electron fluence, F , represents the number of incident electrons per square meter and it is more practical to express the degree of irradiation a sample has undergone using the number of incident electrons per unit area during an exposure (e.g. e^-/A^2) and then to assume this is related to the electron dose received. Electron fluence is defined as the electron flux (current density, e^-/A^2s) over the duration of illumination (s). The terms 'dose' and 'fluence' are commonly used interchangeably in the TEM literature, but if the measured value is expressed in units of e^-/A^2 it is strictly the 'fluence' (not 'dose') and this term will be used in this thesis. Radiolytic damage of a crystal of fixed thickness irradiated at a fixed kV is dependent on the cumulative exposed electron fluence (as shown in Figure 2.3), thus under such conditions the first damage mitigation strategy is to minimize the fluence.

Radiolysis damage will decrease with increasing accelerating voltage but there is no clear evidence that this will improve the image quality (Egerton, 2013; Egerton, 2019). Higher accelerating voltages (for typical ranges of 80 – 300 kV) decrease both the elastic and inelastic cross-sections of the electron beam (the number of interactions between the electrons and the specimen), due to the shortening of the electron wavelength and this results in lower image contrast, hence lower SNR as well as less radiolytic damage. Egerton (2019) suggested that there is no useful kV threshold for radiolysis and that the signal/damage ratio is independent of accelerating voltage. The damage is however proportional to the deposited energy so higher accelerating voltage can be beneficial for thicker specimens as thickness improves the image contrast while the damage per unit volume remains the same, i.e. the signal-to-damage ratio improves (Egerton, 2005). This is captured in the concept of dose-limited resolution reported by Egerton (2013). Clearly, the most important point is the optimal balance between decreasing damage and having sufficient signal generation (Williams and Carter, 2009) and we have found 300 kV to be acceptable for the work reported in this thesis.

For a fixed kV the objective then becomes to reduce the number of electrons illuminating an area and one requirement is to prevent too much pre-irradiation of an area of interest. All TEM beam alignment as well as coarse focusing of the TEM image should be done at a sacrificial area before shifting the electron beam to the region of interest in the specimen (Egerton, 2013). Then one can reduce the current and current density in the electron beam (fluence and fluence rate respectively): in standard TEM - by using smaller spot sizes and spreading the beam; in scanning TEM (STEM) by reducing the beam current (with a monochromator this can be done using a lens in front of the imaging optics thereby taking intensity out of the beam without compromising spot sizes, see Materials and Methods Chapter 3). This low fluence approach can limit cumulative damage mechanisms (i.e. radiolysis plus heating and charging), however, this can only slow down radiolysis rather than eliminate it. It should be noted, that this approach also reduces the signal-to-noise (SNR) ratio in the image such that the SNR can become the limiting factor rather than damage (Egerton, 2013).

In addition to the low-intensity approach, temperature can affect the degree of radiolysis. Lowering the specimen temperature decreases inelastic cross sections to some extent (thermal effect) and can reduce the removal or loss of volatile elements, because of slow diffusion rates at low temperatures (Egerton et al., 2004). Less stable compounds have a greater dependence on lowering temperature than more stable ones (Egerton, 2013). The use of cryo-cooled EM is common for biological samples, as it prevents the motion of organic molecules, limits the radiation damage, and allows analysis without prior staining or fixation of the sample (the additional benefits of cryo-transfer of rapidly frozen aqueous suspensions will be discussed in the Materials and Methods Chapter 3 section 3.2.5).

Radiolysis damage in non-conductive samples can be also reduced by a thin, continuous coating of conductive metals (e.g. gold, graphene). Such a coating provides a barrier to out diffusion of damage products, slowing degradation. However, it may not be an advantage for thicker specimens as it is believed thickness itself can protect by reducing the out-diffusion of mobile species (Fryer, 1987). Adding a conductive surface coating to a specimen is often not done in a TEM because it can reduce image resolution by increasing thickness

while electrostatic charging effects are only limited in thin samples (Egerton, 2013).

Radiation damage can be quantitatively measured in the TEM. A common method is to measure loss in structural integrity with cumulative fluence and by assuming an exponential decay, a characteristic or critical fluence for the decay can be calculated. This is frequently done by electron diffraction by acquiring an electron diffraction pattern series over a range of increasing electron fluence. The resulting changes in the intensity of diffraction spots as a function of the accumulated electron fluence can be measured, fitted by an exponential function and then the value at which the intensity falls to $1/e$ of its highest value is identified (Leijten et al., 2017). The measured critical fluence (C_F) indicates the number of primary electrons (per unit area of the specimen) required for damage (commonly expressed in $e^-/\text{\AA}^2$). This method is described in detail in Appendix A. Consideration of electron beam damage and measurement of critical fluence of a specimen defines the fluence budget for the acquisition of appropriate information by TEM analysis.

2.7 Scanning Transmission Electron Microscopy (STEM)

Another approach to achieving similar image resolution is scanning transmission electron microscopy (STEM). Many conventional TEMs can operate in STEM imaging mode, wherein instead of the parallel illumination used by TEM, a converged electron probe is scanned across the specimen. The scattered electrons are collected by a post-specimen detector. Chromatic aberration, which is one of the factors limiting resolution, is eliminated since in STEM mode because post-specimen imaging lenses are not used. However, the more dominant distortion of spherical aberration is still present in the probe-forming lens although it can be significantly reduced in modern aberration-corrected STEMs to enable sub-angstrom electron probes (without C_s correction STEMs can achieve $\sim 1.5 \text{ \AA}$ probes). This allows imaging at ultra-high magnification with sub-angstrom resolution (Brydson et al., 2014). Figure 2.4 shows a comparison of beam propagation in STEM and TEM modes.

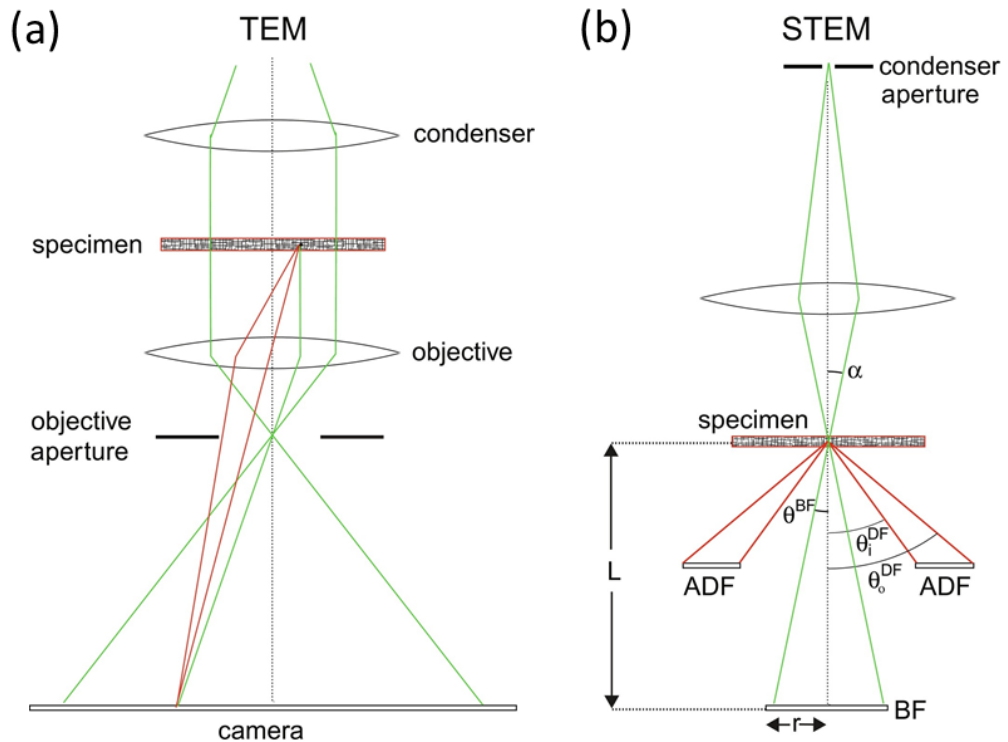


Figure 2.4 Beam propagation in (a) TEM and (b) STEM mode. Taken from Wolf and Elbaum (2019).

The degree of radiation damage in STEM is more complicated than in TEM. In TEM, this depends only on the electron flux and the exposed time, whereas in STEM damage can be produced in the probe illumination area and may extend to a few nm outside the probe (due to delocalisation of the inelastic scattering) (Eddleston et al., 2013). In addition, the dose rate is orders of magnitude higher than in TEM, due to the nature of the highly focused electron probe, and the damage rate may become saturated enabling more signal to be obtained for the same amount of damage (Egerton, 2019). Also, it has been suggested, that repeatedly re-scanning the specimen at short probe dwells to build up SNR in images rather than doing single scans with long dwells gives time for the ‘healing’ of a sample due to the diffusive recovery of damage products between probe dwells (Jones, L. et al., 2018). However, it is still unclear which of TEM or STEM decreases radiation damage more (if they are different at all) (Ilett et al., 2019) and in this thesis, STEM is mainly used for the additional signals it can bring, as outlined below. Low-dose conditions can be implemented in STEM by reducing the probe current and dwell time, and also by lowering magnification, but sufficient or required SNR to resolve features of interest in the image should still be considered.

In conventional transmission electron microscopy (CTEM), phase contrast imaging enables the projected atomic lattice to be viewed but is extremely sensitive to a range of conditions in any sample (primarily objective lens defocus and thickness of the specimen), and mostly to radiation damage for organic specimens. The latter leads to a decrease in resolution during imaging (Haruta and Kurata, 2012). Similarly, phase contrast can be achieved in STEM at a slightly lower resolution to TEM due to the convergent probe (and a lack of complete reciprocity to the equivalent TEM image condition because the BF-STEM detector collects only a smaller fraction of the low-angle transmitted electrons compared to the parallel illumination of TEM). However, in STEM, the focussing of the probe can be done using a static probe and the far field diffraction pattern within the image of the probe (called the Ronchigram) and this is instead of exposing whole areas to the beam irradiation for focussing in conventional TEM. Therefore, only a very small (nm-sized) area is sacrificed for focusing the probe and this method significantly reduces pre-exposure (fluence) when finding and focussing areas of interest.

Alongside BF-STEM imaging, other STEM detectors can be used to image electrons that have been scattered to higher angles. An annular dark field detector (ADF) can collect electrons scattered < 50 mrad, and as per the BF-STEM image, both mass thickness and diffraction contrast can contribute to the ADF image making the interpretation of images more complex although for a poorly diffracting or amorphous specimen the ADF image becomes sensitive to mass-thickness and has been used to measure relative masses of polymers and proteins (Isaacson et al., 1976). Furthermore, a change in diffraction pattern collection can move the annular detector to high-angle annular dark field (HAADF) imaging as under these conditions it can collect incoherent Rutherford scattered incident electrons (scattered by atomic columns of the specimen), scattered to high angles < 50 mrad where Bragg or diffraction contrast is minimised and so mass or Z-contrast dominates the images. It is even possible to resolve individual atoms or aligned atomic columns and interpret their positions directly in the STEM-HAADF images (Crewe, 1966; Pennycook and Nellist, 2011). However, HAADF STEM collects a much lower fraction of the incident electrons than BF-STEM due to

the relatively low number of electrons scattered to high angles and so is less than ideal for low-dose STEM imaging of very beam-sensitive materials. In fact, reports of direct crystal lattice images of organic crystals and defects within them by BF or ADF STEM imaging are rare and will be discussed in Section 2.8.

One of the alternative low-dose methods to analyse and quantify crystals by STEM is scanning moiré fringes (SMFs) (Haruta and Kurata, 2012; Murakami et al., 2015; Su and Zhu, 2010). SMF imaging provides magnification of the crystal lattice through the interference pattern created between closely aligned and similarly sized crystal and scanning lattices (Figure 2.5) (S'ari et al., 2019; S'ari et al., 2020; Su and Zhu, 2010). This technique can enable a lattice and defect image of pharmaceutical compounds to be achieved (S'ari et al., 2019; S'ari et al., 2020). The interference pattern efficiently magnifies the crystal lattice and allows it to be viewed indirectly at lower microscope/scanning magnifications and therefore lower electron fluence than would normally be required in phase contrast imaging (S'ari et al., 2019; S'ari et al., 2020; Su and Zhu, 2010). A recent study reports the effects of pixel size and relative angle between the two lattices on the size of the measured SMFs in bright field (BF) STEM (S'ari et al., 2019). The scanning moiré fringe method has been successfully used to indirectly examine the crystal lattice of organic compounds as well as identify the presence of defects; however, further work is needed to investigate the relationship between the various defects and their appearance in SMF images (S'ari et al., 2019; S'ari et al., 2020).

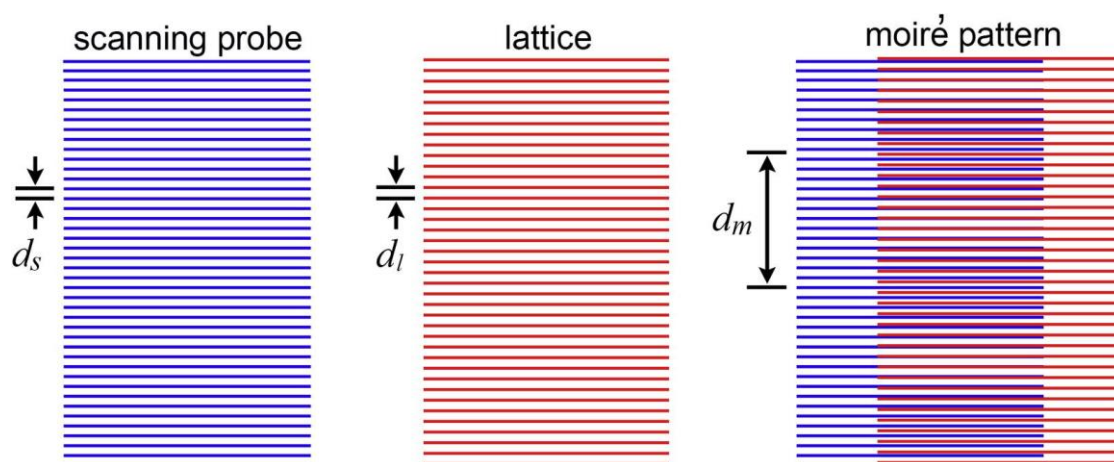


Figure 2.5 Schematic representation of the formation of artificial moiré fringes. Taken from Murakami et al. (2015).

A recent development in low-dose STEM is the scanning electron diffraction (SED) technique. Here a focused probe is scanned over the sample in a two-dimensional array and at each x,y probe position, a 2D diffraction pattern is recorded on a fast read-out, pixelated detector or camera (Figure 2.6). The convergence semi-angle of the focussed probe needs to be relatively low (around 1 mrad at 1-300 kV) to avoid diffraction disk overlap so that each diffraction disk can be measured and analysed independently, and this low convergence compromises the spatial resolution of the probe to a nm or so (given by the diffraction limit of a low convergence probe). The resulting diffraction patterns contain information about the crystallographic orientation, phase and defects across scanned materials. By carefully controlling the electron beam current and dwell time, low-dose SED can reduce radiation damage to the sample and enable the examination of beam-sensitive materials.

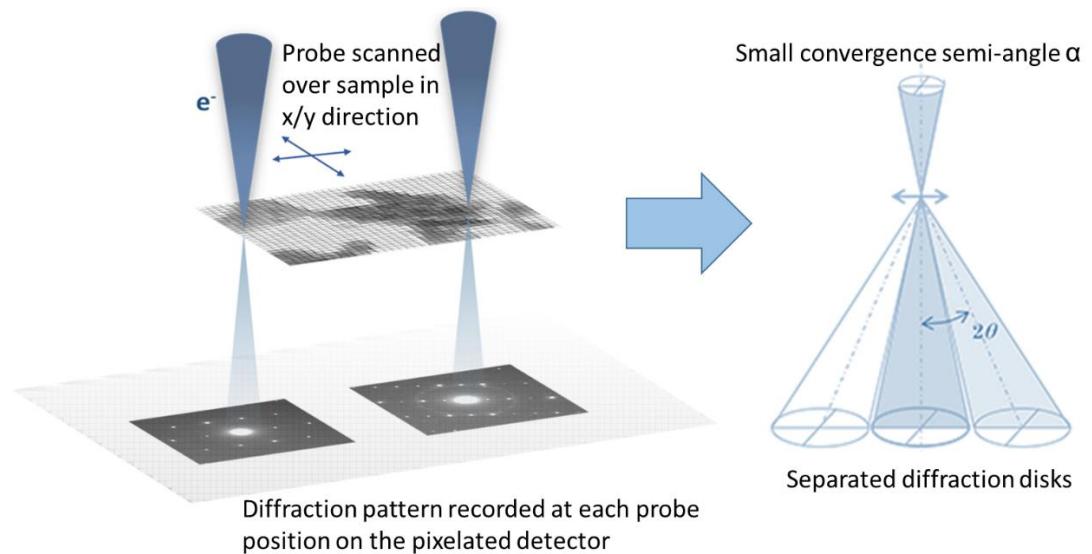


Figure 2.6 Schematic representation of STEM for scanning electron diffraction (SED; LHS) and the need for a low convergence angle to keep the diffraction disks from overlapping (RHS).

Finally, cryo-annular dark-field STEM (cryo-ADF-STEM) imaging has been shown to be a complementary method to BF-TEM or STEM phase contrast imaging by identifying changes in material density and potential composition within particles (Elbaum et al., 2021). Moreover, modern ADF-STEM imaging can be coupled with an electron energy loss (EEL) spectrometer and energy-

dispersive X-ray (EDX/EDS) detector (Figure 2.7). The EELS spectrometer detects the forward scattered energy loss events while EDX detectors collect X-rays over a small solid angle to the sides of the specimen. Both techniques can provide good spatial resolution (down to sub-nm), however, the spatial resolution and detection efficiency (DE) of EELS is higher than for EDX/EDS (<1 eV resolution and < 80% DE for EELS vs. ~ tens of eV and <1 % DE for EDX/EDS) (von Harrach et al., 2010). EELS is more sensitive to light elements and also can provide a chemical fingerprint by identifying the oxidation state of atoms from shape analysis of the characteristic ionization edges. However, sample thicknesses of > 30 nm can limit EELS analysis. On the other hand, EDX is particularly sensitive to heavier elements (metals and heavier) and is useful for analysing thicker samples. The relative comparison between cryogenic EELS and EDX spectra acquired from polymeric nanoparticles analysed in this thesis (Chapter 7) is presented in Figure 2.8. This shows that the thickness of the specimen and amorphous ice in the cryo-preparation reduce the peak-to-background ratio for EELS spectra (marked by red arrows) and data analysis requires careful interpretation.

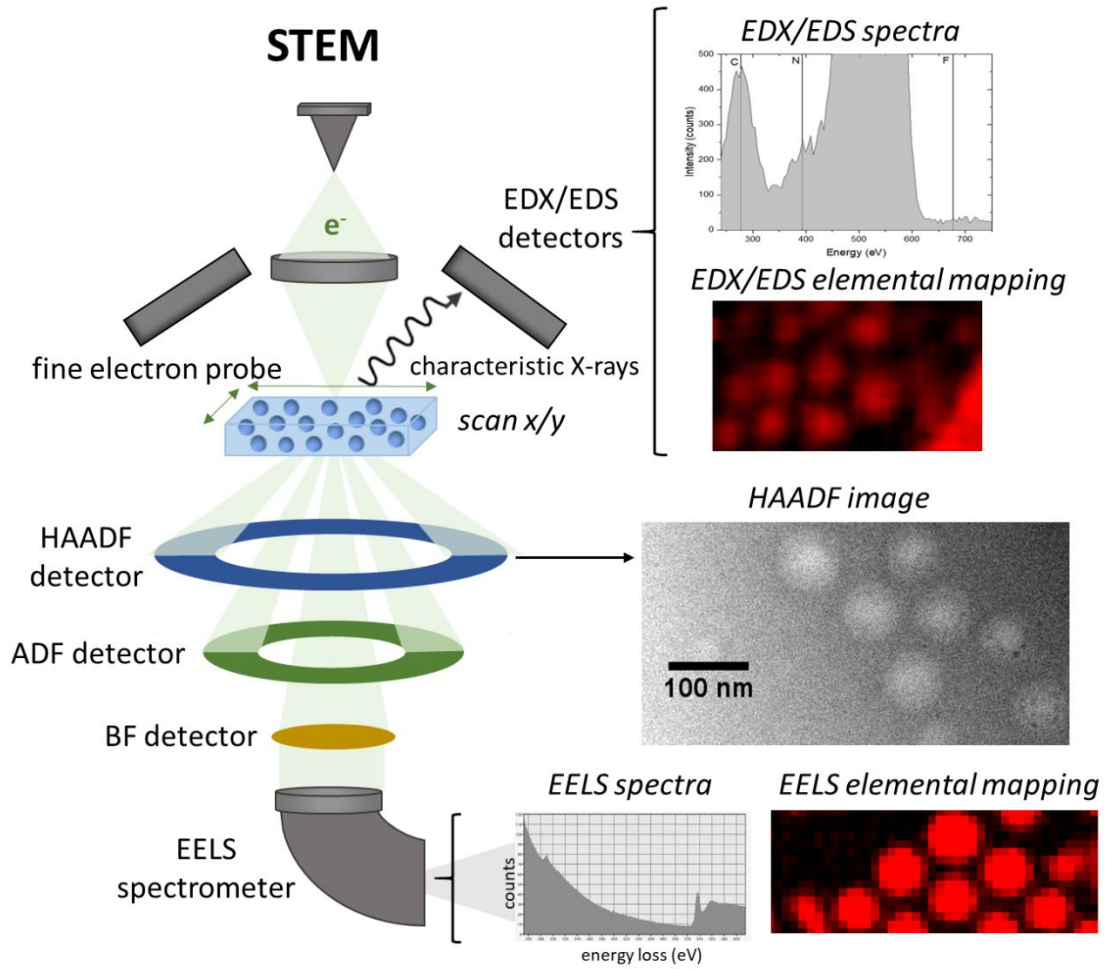


Figure 2.7 Schematic of analytical scanning transmission electron microscopy showing image detector configurations and a typical HAADF image of polymer nanoparticles in vitreous ice. STEM can be coupled with an electron energy loss (EEL) spectrometer and an energy-dispersive X-ray (EDX/EDS) detector.

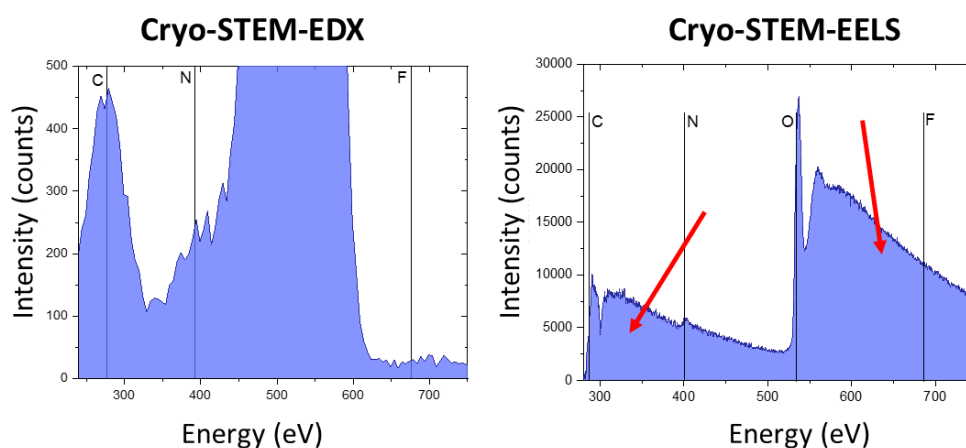


Figure 2.8 Cryo-STEM-EDX and cryo-STEM-EELS spectra of polymeric nanoparticles in vitreous ice (see Chapter 7). The improved spectral resolution of EELS is evident however the red arrows in the cryo-STEM-EELS spectrum show the multiple scattering regions due to the thickness of the ice in the cryo-sample and indicate the reduced sensitivity (peak-to-background ratio) for elements such as N and F.

Ultimately, in STEM elemental mapping can be performed simultaneously with annular dark field imaging for nanoscale physicochemical analysis and so, EDX and EELS have the potential to characterise and identify the elemental content of a number of pharmaceutical compounds with high spatial resolution unobtainable by other analytical techniques (Das et al., 2020).

2.8 Recent Development Electron Microscopy of Pharmaceutical Compounds

As discussed earlier, (S)TEM is a promising technique for the analysis of pharmaceutical compounds at a nano-scale unattainable by other analytical techniques. Moreover, it can provide chemical characterisation by EDX and EELS. Since pharmaceutical product development is concentrated on understanding, controlling and predicting the directional, physical properties of crystals, this method has major potential for drug characterisation particularly for new modalities such as polymeric nanoparticles. The application of electron microscopy (EM) methods in the pharmaceutical industry is briefly reviewed here in the context of the characterisation of small molecule drugs, microporous inorganics, nanoparticles and microparticles,

nanocarriers, liquid crystals and other drug delivery systems (Klang et al., 2013).

(S)TEM analysis has barely been performed on poorly water-soluble small molecule drugs such as furosemide, or on hydration and dehydration of channel hydrates such as theophylline, and not at all on the development batches of sodium zirconium silicate manufactured in laboratory conditions. The reason may be the combination of electron beam sensitivity and a lack of commercial interest, as well as difficulties during analysis. However, there is a growing interest in using cryogenic-(S)TEM for nanoparticle characterisation. In cryo-EM, it is important to prepare nanoparticle specimen grids with a thin, well-dispersed distribution of particles of interest within an aqueous suspension by a rapid vitrification process (to prevent crystalline ice formation and redistribution of particles), to provide structural and chemical information of hydrated samples (De Yoreo and Sommerdijk, 2016).

For imaging of any of these compounds, first, the 'electron budget' must be identified and S'ari et al. (2018) outlined a model to predict electron beam stability of small molecule APIs. The critical fluence for furosemide was measured at $7.1 \pm 4.0 \text{ e}^-/\text{\AA}^2$ using a microscope operated at 200 kV at room temperature (S'ari et al., 2018). A more recent study by S'ari et al. (2019) presents low electron fluence TEM imaging and scanning moiré fringe method in STEM to image lattice defects in theophylline and furosemide, respectively. This work demonstrates the new opportunity for indirect characterisation of crystal defects in small molecule compounds. S'ari et al. (2019) indirectly image and identified defects in the (001) crystal lattice planes of furosemide (Figure 2.9). The fast Fourier-filtered image from within the red box highlights a defect seen within the crystal (Figure 2.9b, SMF lattice image with red lines). It should be noted that the image was taken at 300 kV with a cumulative electron fluence of $17.3 \text{ e}^-/\text{\AA}^2$, ~ two/three times higher than the C_F measured for furosemide at 200 kV in CTEM (S'ari et al., 2018). Regardless, the results suggest the STEM method could be beneficial for furosemide analysis, but further work is needed to improve image analysis of the defects as well as to identify the type of defects (point, edge and screw dislocations) and to allow quantification of the number of defects on specific planes within a crystal structure. The interesting and promising SMF method gives rise to an

opportunity for further investigation of defects in furosemide crystals (Chapter 4).

Generally, the moiré fringe method has been used to measure and understand the deformation of materials (Kishimoto, 2012). SMFs have been used for strain measurement in semiconductors and functional oxides (Murakami et al., 2015; Su and Zhu, 2010). Moreover, the STEM moiré method was successfully applied to atomic column elemental mapping by X-ray and core energy loss elemental images (Kondo et al., 2017; Kondo and Okunishi, 2014; Okunishi et al., 2014).

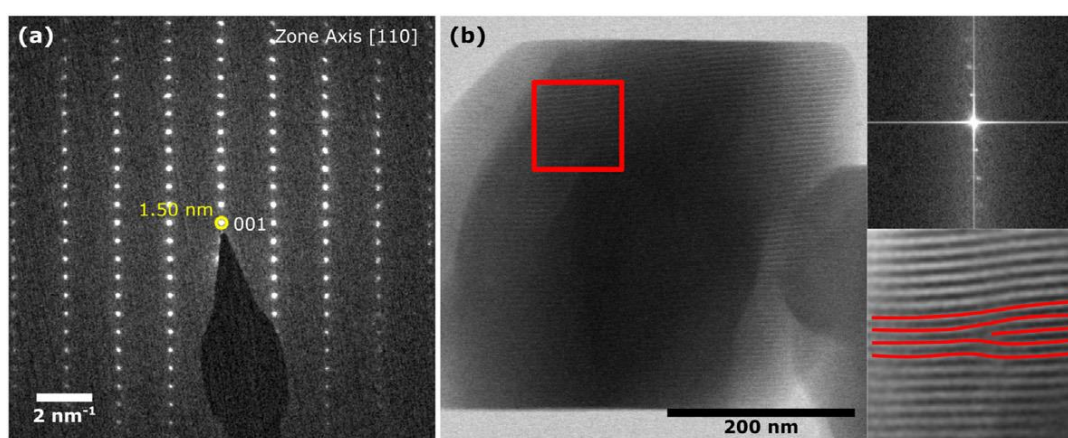


Figure 2.9 Scanning moiré fringes of furosemide form I (a) SAED of [110] zone axis, (b) BFSTEM image of SMFs produced by using a pixel size of 1.32 nm and 1.50 ± 0.10 nm d -spacing. The Fourier-filtered image from within the red box highlights a defect seen within (100) planes of the crystal (red lines). Taken from S'ari et al. (2019).

In the case of other pharmaceutical compounds, there are several reports that suggest the identification of crystalline imperfections might be obtainable by electron microscopy techniques (Eddleston et al., 2010; S'ari et al., 2019; Smeets et al., 2018; Su and Zhu, 2010). It has been argued that the identification of crystal disorder in theophylline could not be attained with any other analytical technique (Eddleston et al., 2010). Moseson and Taylor (2018) demonstrated that by fast Fourier transform analysis of bright-field TEM images it might be possible to detect nanocrystalline domains and crystal defects within indomethacin/polyvinylpyrrolidone/vinyl acetate copolymer (PVPVA) amorphous solid dispersions produced by hot melt extrusion. Moreover, work done by Ricarte et al. (2015) shows that electron diffraction

and dark-field TEM imaging can detect crystallinity in griseofulvin/hydroxypropyl methylcellulose acetate succinate (HPMCAS) solid dispersions at levels below the sensitivity limits of laboratory-scale wide-angle X-ray scattering (WAXS) and modulated DSC. S'ari et al. (2021) used conical dark field microscopy to detect crystallinity in hot melt extruded ASDs of felodipine and polyvinylpyrrolidone/vinyl acetate copolymer (PVP/VA).

Therefore, there is a growing body of evidence that the issues related to sample preparation and electron beam damage, which may restrict pharmaceutical compound characterisation can be sufficiently mitigated by careful sample preparation and implementing low electron fluence techniques.

As zeolites and other silicate minerals are beam-sensitive compounds that exhibit a large range of critical fluence (from hundreds to thousands $e^-/\text{\AA}^2$) (S'ari et al., 2018; Wang et al., 2000), different techniques have been used to study their structure. Zeolites and silicates with larger pores (> 1 nm) are generally more beam stable (Wang et al., 2000), and this suggests that sodium zirconium silicate (AZ-1, AZ1-2), with a pore opening of 0.3 nm, might be more susceptible to beam damage.

STEM has become a promising method for studying beam-sensitive materials. Sader et al. (2010) analysed the image performance on samples of vermiculite (relatively beam-sensitive silicate minerals) in two modes: low fluence TEM and STEM and found that STEM images have better contrast but less SNR (as scintillator-based TEM detectors were more efficient). Moreover, Buban et al. (2010) described protocols for low-dose STEM image recording and found that it is possible to resolve a 2.8 \AA spot with the electron fluence reduced to $\sim 15 e^-/\text{\AA}^2$, but only by image processing (Fast Fourier Transform, FFT). Mayoral et al. (2015) acquired images of a $\text{TiO}_6 - \text{SiO}_4$ zeolite and other microporous solids at atomic resolution using low fluence STEM at 300 kV (Figure 2.10). They also analysed structural defects.

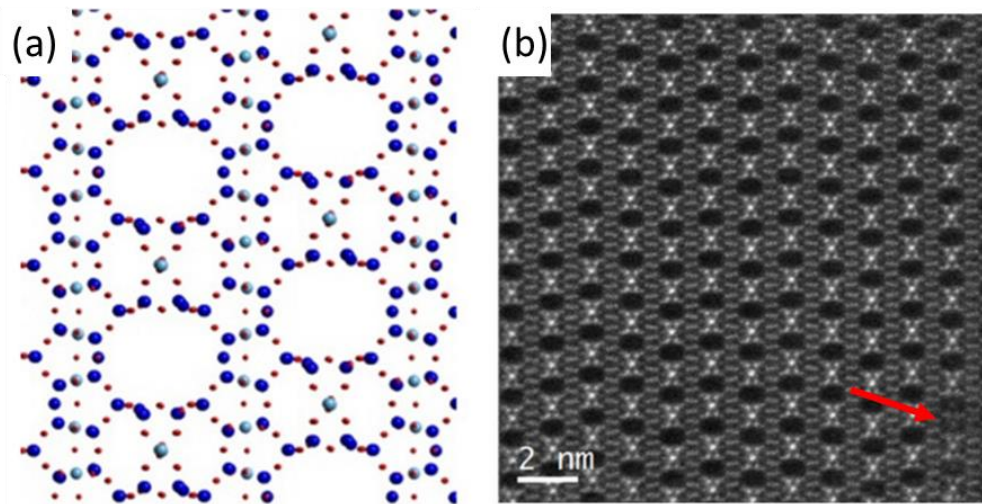


Figure 2.10 (a) Simulated atomic packing structure of the TiO_6 - SiO_4 zeolite, (b) HAADF-STEM image of the corresponding structure. Some stacking faults are visible in the bottom right of the image (red arrow). Images taken with electron fluence of $\sim 1000 \text{ e}^-/\text{\AA}^2$. Taken from Mayoral et al. (2015).

Low-dose SED using electron fluence of $\sim 5 \text{ e}^-/\text{\AA}^2$ was successfully used to explore the structure of a rod-like morphology paracetamol-theophylline co-crystal produced by mechanochemically transformed powders (Johnstone et al., 2019) (Figure 2.11). The SED observations showed that the rod has a twisted structure, and the axes of the rod and twist are aligned. Moreover, by rotating this crystal structure around an axis that is perpendicular to the rod and twist axis, SED data suggest that the twist axis might be perpendicular to the hydrogen-bonded planes in the crystal structure. This example confirms low-dose SED as a potential method for investigating the nanostructure of beam-sensitive pharmaceutical materials.

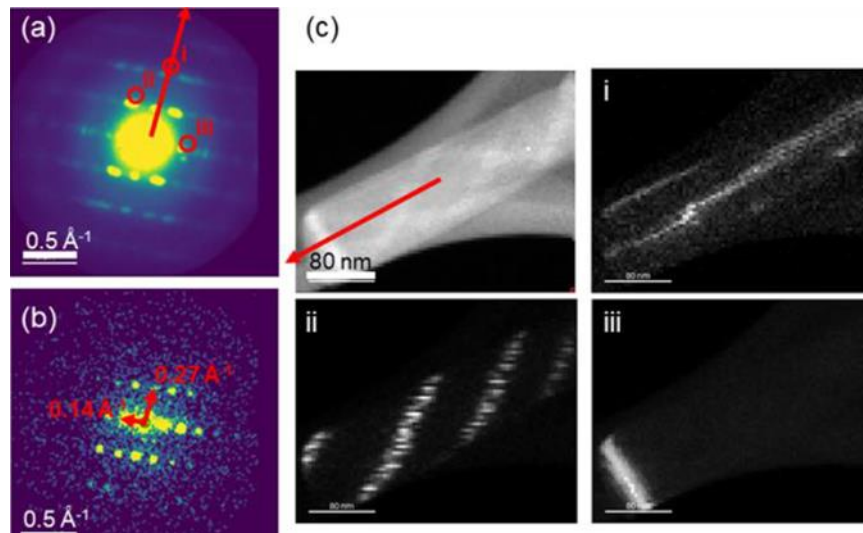


Figure 2.11 Scanning electron diffraction of a paracetamol-theophylline co-crystal. (a) Spatially averaged diffraction pattern, (b) individual diffraction pattern from near the tip of the rod, (c) Dark-field images formed by plotting the intensity within the disks marked in (a) as a function of probe position. Taken from Johnstone et al. (2019).

Complete native state analysis of polymeric nanoparticles is possible by capturing aqueous suspensions in rapidly frozen, vitreous ice followed by transfer into a microscope for cryogenic (S)TEM imaging with electron energy loss spectroscopy (cryo-STEM-EELS) (Ilett et al., 2017; Ilett et al., 2019; Pal et al., 2021; Weiss et al., 2019; Yakovlev and Libera, 2008). Cryo-phase contrast TEM imaging has been used to analyse the particle size distribution, shape and internal packing of polymeric nanoparticles (Rabanel et al., 2015; Weiss et al., 2019) (Figure 2.12). Moreover, analytical STEM, in particular cryo-STEM-EELS was used to reveal changes in elemental distribution and chemistry within polymer particles (Kim et al., 2006). Therefore, morphology, size and size distribution, structure and chemical composition of a polymeric nanoparticle system can be obtained in one multi-modal analysis at sub-particle spatial resolution. The intrinsic sensitivity of polymers and vitreous ice to high-energy electron irradiation does, however, present an additional challenge (Egerton et al., 2004; Friedrich, 2021; Yakovlev and Libera, 2008). This can be managed by limiting electron fluxes to preserve both the structure and composition of a nanoparticle encapsulated in vitreous ice (Ilett et al.,

2019). To date however, there are no examples of multi-modal STEM characterisation of polymeric nanoparticles at the single particle level despite reports that cryo-TEM can reveal a three-layer core-shell-corona nanoparticle structure of PEG-*b*-PLGA based nanoparticles (Han et al., 2015) (Figure 2.12) and, as outlined above, that STEM techniques have the potential to enhance the image contrast of each of these layers.

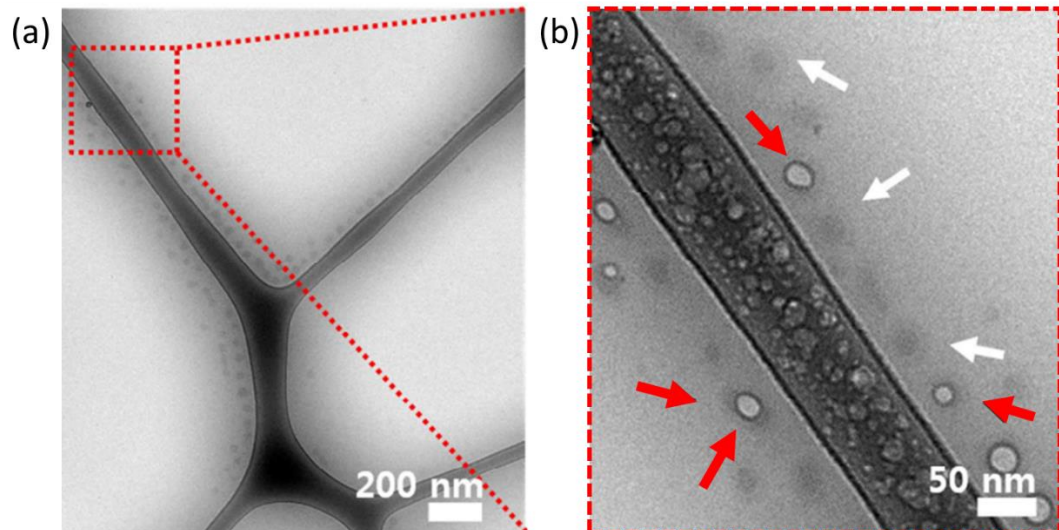


Figure 2.12 Cryo-TEM images of PEG-*b*-PLGA block copolymer nanoparticles taken in (a) low and (b) high magnification of the area marked in red square in (a). White arrows show the ‘halo’ around some nanoparticles indicating the PEG layer. Red arrows indicate the bubble formation due to extensive beam damage of some nanoparticles. This allows the differentiation of particles without API (more beam-sensitive due to the presence of polymer blocks only) and with API. Reproduced from Han et al. (2015).

2.9 Summary

The literature review presented here shows the potential for the use of multi-modal (S)TEM to characterise pharmaceutical compounds, in particular in identifying crystal defects, characterising structure and composition as well as monitoring phase transformation at a single particle level. The challenge is to do so while managing the sensitivity of those compounds to high-energy electrons. Recent developments suggest it is possible to further explore what (S)TEM can achieve and so this thesis will address these challenges by developing methods to characterise the structure and composition of four

model pharmaceutical compounds: small organic molecules, porous inorganics, channel hydrates and polymer nanoparticles.

2.10 Project Aim

The aim of the project is to demonstrate that molecular scale analysis of pharmaceutical compounds by STEM is possible. Such analysis will enable structure-property relationships to be developed for performance control of a drug within a medicine.

2.11 Objectives

The specific research objectives for this research with a link to the results chapters in which they are addressed are presented below:

- To measure the critical fluence of the model small molecule drug, furosemide, at 200 and 300 kV and investigate phase contrast lattice images, scanning moiré fringes and scanning electron diffraction in order to identify and characterise defects in the crystal structure. The results will be presented in Chapter 4 and are part published in S'ari et al. (2020).
- To identify compositional and structural changes in laboratory development batches of a model inorganic cation exchanger, sodium zirconium silicate on protonation and removal of Na from the materials micropores using (S)TEM and elemental analysis (EDX). The results will be presented in Chapter 5.
- To develop sample preparation and (S)TEM methods (TEM imaging and diffraction, phase contrast lattice imaging and scanning electron diffraction) to investigate the phase transformation of a model channel hydrate, theophylline, during hydration and dehydration. The results will be presented in Chapter 6 and will be part published in Pham et al. (2023).
- To identify and characterise the structure and composition of a model polymeric nanoparticle system of PLA-PEG encapsulating a drug by multi-modal cryogenic (S)TEM. The results will be presented in Chapter 7 and are published in Koniuch et al. (2023).

Chapter 3 Materials and Methods

The aim of this chapter is to provide an overview of the materials and methodology used for the characterisation of a range of pharmaceutical compounds. Sample preparation methods and an outline of the methods used will be provided along with a detailed methodology for data acquisition and interpretation of the data used in this thesis. The method of sample preparation and the general method of analysis will be also included in the relevant experimental chapters to provide the reader with an easier overview of the sample and methods used.

3.1 Materials

Furosemide

Furosemide form I was provided by AstraZeneca. Two methods were used to prepare the samples for TEM analysis – grinding and recrystallisation from ethanol. In the first method, furosemide crystals were lightly crushed between two glass slides and approximately 1 mg was transferred to a 100 mL container and filled with deionised water. Two drops of the solution were pipetted onto TEM grids (holey-carbon support film on 400 mesh copper and continuous carbon film) and allowed to evaporate. In the second method, furosemide crystals were prepared by mixing 0.5 mL of a 10 mM solution of furosemide in ethanol with 3.5 mL of deionized (DI) water in order to create a supersaturated solution (as described in Adobes-Vidal et al. (2016)). After 5 min incubation crystals or precipitates were visible by eye, two drops of the mixture were pipetted onto continuous carbon TEM grids and allowed to evaporate.

Crocidolite

Crocidolite on carbon film was acquired from Agar Scientific Ltd and used as a standard sample for low-dose STEM and Scanning Moiré Fringe (SMF) analysis.

Sodium Zirconium Silicate (AZ-1/AZ1-2)

The samples supplied by AstraZeneca as part of this study were taken from development batches manufactured in laboratory conditions not consistent with the commercial manufacturing method. Therefore, any conclusions drawn based on these samples cannot be considered directly transferable to the commercially produced product. AZ1 (pre-protonated sodium zirconium silicate, full of Na⁺ ions) and AZ1-2 (partially protonated sodium zirconium silicate, with part of the Na⁺ ions exchanged to H⁺) were used as received. A grinding method was used to prepare the samples for TEM analysis. AZ1/AZ1-2 crystals were lightly crushed in a pestle and mortar with the addition of a few drops of ethanol. Two drops of the ground solution containing suspended particles were pipetted onto TEM grids (holey-carbon films on 400 mesh copper and continuous carbon film) and allowed to evaporate.

Theophylline

Theophylline anhydrous form II was purchased from Sigma-Aldrich and the samples of form II were prepared for TEM by two different methods. In the first method, as-bought powder of anhydrous form II was slightly crushed using a mortar/pestle to reduce the size of crystallites for TEM analysis. In the second method, as-bought powder of anhydrous form II was dissolved in nitromethane followed by heating to ~60 °C to obtain a saturated solution. Then, a drop of the solution was drop-cast onto a TEM holey or continuous carbon grid and left to evaporate.

Partially hydrated form II plates were produced after contacting recrystallized form II plates on a TEM grid (i.e. from sample recrystallized from nitromethane) with water for 10 minutes and then rapidly plunge frozen into liquid ethane or liquid nitrogen, thereby retaining any absorbed water.

Theophylline monohydrate was prepared by three methods. In the first method, TEM grids and a silicon substrate with recrystallized anhydrous form II from nitromethane were stored in high humidity conditions in a desiccator maintained at 93% relative humidity over a saturated potassium nitrate solution (KNO₃) and monitored for 7 weeks. In the second method, a TEM sample was prepared by evaporative recrystallisation from water by dissolving anhydrous form II powder in ultrapure water at ~70 °C under continuous stirring. When fully dissolved, the system was allowed to cool slowly to room temperature (~20 °C) under continuous stirring for a period of 24 h. The precipitate was filtered and allowed to dry at room temperature for 2 days. In the third method, a TEM sample was prepared by evaporative recrystallization from ethanol:water by dissolving anhydrous form II powder in ethanol:water solution at a 3:2 molar ratio and heated to ~55 °C. The solution was allowed to cool slowly to ~35 °C under continuous stirring for a period of 3 h. When the first precipitation occurred, a drop of the solution was pipetted onto a holey carbon or continuous carbon film TEM grid and left to evaporate. The precipitate was filtered and analysed by pXRD. Moreover, the dehydration of this theophylline monohydrate was studied *in situ* by thermally accelerated dehydration using a Gatan heating holder (up to 100 °C) and by vacuum dehydration in the TEM column at room temperature (~20 °C).

Polymeric Nanoparticles

Polymeric nanoparticles were obtained from AstraZeneca Ltd. Polymeric nanoparticles containing polylactic acid - polyethylene glycol (PLA-PEG) block copolymer (a number average molecular weight of approximately 16 kDa for PLA and approximately 5 kDa for PEG, determined via nuclear magnetic resonance, NMR), an active pharmaceutical ingredient (API) (AZD2811, ~20% nanoparticle) and pamoic acid (the functional excipient that forms a hydrophobic ion pair with the API, AZD2811:Pamoic 1:0.5) were prepared following the method of Song et al. (2016) via a nanoemulsion process at an estimated concentration of 137 mg/ml. The small molecule API contains 19% nitrogen in its molar mass. As produced suspensions potentially containing excess API and residual Tween (detergents for protein solubilisation) were further diluted with ultrapure water (Synergy® purification systems, Type 1, 18.2 MΩ·cm at 25 °C) to a final concentration of ~1.5 mg/mL and stored at 4°C.

3.2 Electron Microscopy

3.2.1 Basics

3.2.1.1 Electron

In 1897, English physicist Sir Joseph John Thomson discovered the electron. In 1924, Louis de Broglie introduced a revolutionary idea of electrons and proposed that all matter, including electrons, could exhibit both wave-like and particle-like characteristics (Weinberger, 2006). De Broglie's hypothesis stemmed from the notion that if light, traditionally seen as waves, could exhibit particle-like behaviour (photons), then particles like electrons should also display wave-like attributes. To experimentally confirm the wave-like nature of electrons, ground breaking work was carried out by Clinton Davisson and Lester Germer in 1927 (Weinert, 2009). They observed that when electrons were directed at a crystalline substance, they exhibited diffraction patterns, much like X-rays interacting with a crystal lattice. This diffraction phenomenon conclusively demonstrated that electrons could behave as waves. The famous double slit experiment performed by Claus Jönsson in 1961 also confirmed the wave-particle duality of electrons (Jönsson, 1961). When electrons are

sent through two closely spaced slits, they produce an interference pattern on the screen behind them (similar to light waves).

The electron's dual nature has profound implications in various scientific disciplines. It underlies the principles of quantum mechanics, shaping our understanding of the atomic and subatomic world. In fields of electron microscopy, electron diffraction, and quantum computing, wave-particle duality of electrons is used to explore matter at the atomic scales.

In 1931, two German scientists, Ernst Ruska and Max Knoll, found a way to achieve a resolution better than that of light using electrons (Freundlich, 1963). This discovery led to the first transmission electron microscope (TEM). In 1939, Ruska created the first commercially produced electron microscope.

3.2.1.2 Resolution Limits and Lens Aberration

The main goal of a microscope is to create a magnified image i.e. map of the points in an object and match them to equivalent points in an image. Microscopes use lenses to form the image and a schematic ray diagram of image formation using the thin lens approximation is presented in Figure 3.1. The object distance to the lens (u) and the image distance to the lens (v) are related to the focal length of the lens (f) by the Equation 3.1:

$$\frac{1}{u} + \frac{1}{v} = \frac{1}{f} \quad 3.1$$

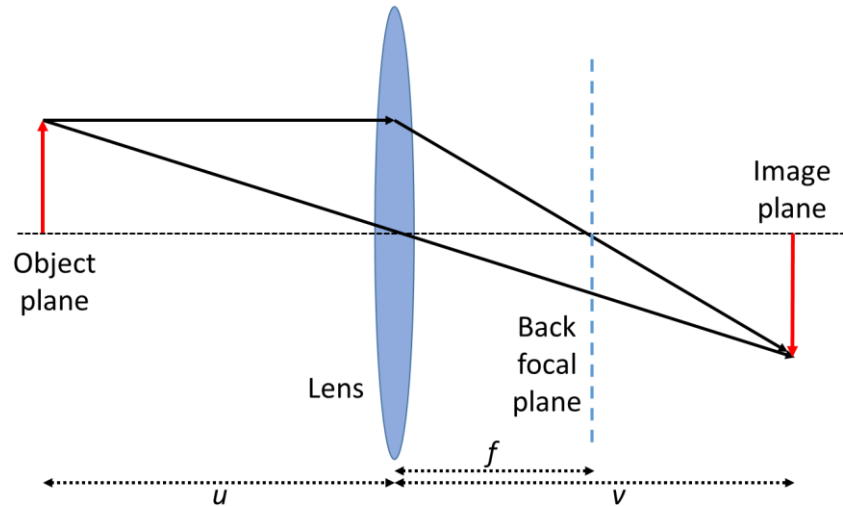


Figure 3.1 Schematic of the ray diagram representing image formation using thin lens approximation.

If the object is situated closer to the focal length of the lenses, then the magnified image is greater. However, the limit of resolution in the microscope can be defined by the Rayleigh criterion. A single point source is imaged as a series of concentric rings rather than the single point due to diffraction and interference constructively or interferences both constructively and destructively between disks (similar to that produced by a single slit) when the illuminating rays pass through a circular aperture. These Airy disks can overlap so closely that it is not possible to resolve two objects. The Rayleigh criterion defines the minimum resolution limit to resolve any two points by the Equation 3.2:

$$r_d = \frac{0.61 \lambda}{n_r \sin \alpha} \quad 3.2$$

where λ is the wavelength, n_r is the refractive index of the medium and α is the collection semi-angle of the lens or aperture. Three scenarios when two objects can be (a) distinguishable, (b) on the resolution limit defined by the Rayleigh criterion and (c) not resolvable are presented in Figure 3.2.

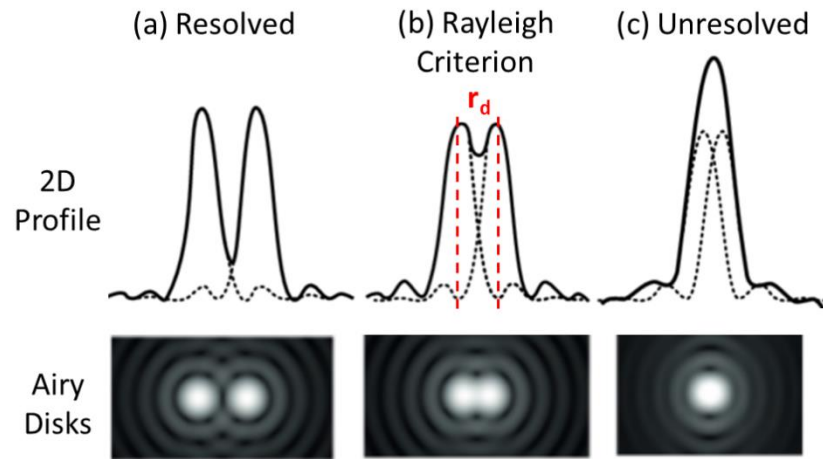


Figure 3.2 2D profile and representation of Airy disks when two objects (a) can be resolved, (b) are on the resolution limit defined by the Rayleigh criterion and (c) cannot be resolved due to overlapping discs.

However, lens imperfections also limit the resolution particularly in EM due to aberrations that occur in electromagnetic lenses. The main aberrations in TEM are astigmatism, spherical (C_s) and chromatic (C_c) lens aberration (Figure 3.3). Astigmatism is a common aberration in TEM and arises from the variation in the focal positions between the electron beams passing through the electromagnetic lenses. Astigmatism can be easily corrected using stigmators that are available in most TEMs. Spherical aberration relates to the imperfection of the lens and electron rays arriving to the lens further from the optical axis being focussed more strongly than the electron rays close to the optic axis. Therefore, with C_s , each image point becomes a disc (plane) of least confusion and the image is blurred. Spherical aberration can be corrected in modern aberration-corrected microscopes by additional lenses offering better (atomic) resolution. Chromatic aberration affects electrons of different energy emitted from the electron source differently. Lower energy electrons are focussed more strongly than higher energy electrons. The variation in energy spread and difference in focussing electron rays results in another disk of least confusion and again affects the resolution of EM. In modern EMs C_c is reduced by controlling the energy spread of the electron source (e.g. with a field emission gun source or monochromator to limit the energy spread) such that C_s tends to be the dominant aberration. However, thick samples are also a source of chromatic aberration as this produces a

large number of inelastically scattered electrons with a range of energies and this can be reduced by preparing thin samples ($\sim < 100$ nm).

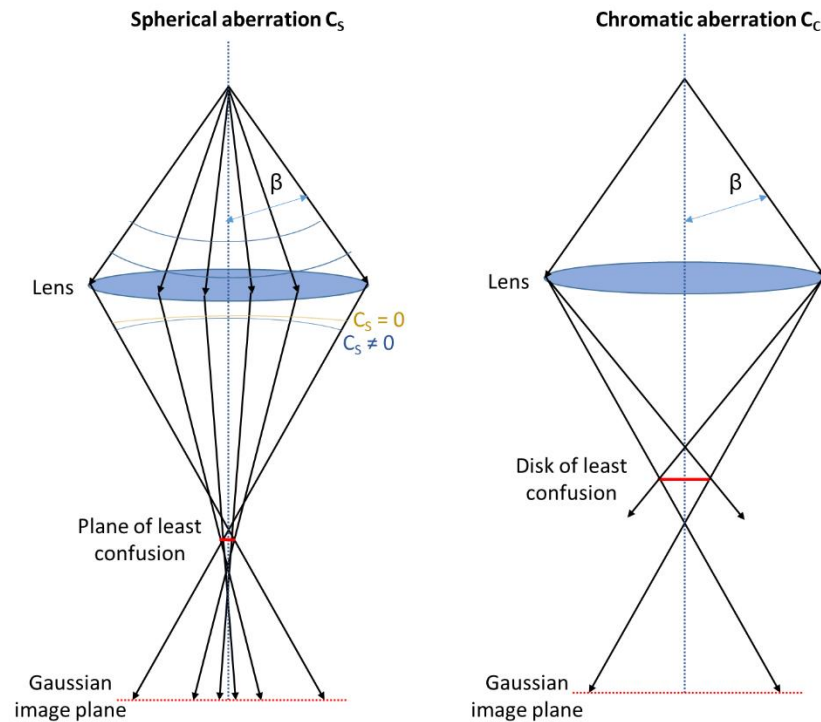


Figure 3.3 Schematic representation of spherical and chromatic aberration in electromagnetic lens.

3.2.1.3 Electron Source

In the electron microscope (EM), high-energy electrons are emitted by an electron gun. These electrons are sourced from a cathode, a material that releases electrons when subjected to heat or other forms of excitation. Within the electron gun, the cathode is often a filament, typically made of tungsten or lanthanum hexaboride (LaB_6). By applying a high voltage, the filament is heated to extreme temperatures (~ 2000 K), causing it to emit electrons into the surrounding vacuum (thermionic emission). The emitted electrons are then focused into a coherent beam. While thermionic emission is the standard method for generating electrons in TEM, field emission sources represent a significant technological advancement. Field emission electron guns utilize nanoscale tips made of materials like tungsten or single-walled carbon nanotubes. By applying a strong electric field to these tips (and sometimes heat too), electrons are emitted with extremely narrow energy spread and high

brightness. This technology has enabled TEMs to achieve more coherent illumination and therefore higher resolution.

In this project, most of the experiments will be performed using Titan Themis³ in LEMAS, Leeds equipped with a thermally assisted field emission electron gun and monochromator offering a high coherence and high brightness of electron beam. Scanning electron diffraction will be performed on JEOL ARM300CF, in ePSIC, Diamond Light Source equipped with a cold field emission electron gun with lower stability of emission and probe currents than a thermally assisted field emission electron gun. A high vacuum is needed in the electron column to prevent shorting with the use of high electric fields (i.e. to prevent ionization of air molecules) and to provide electron mean free paths of a few m (i.e. to avoid collisions with air molecules).

3.2.1.4 Optics and Apertures

To converge the electron beam, magnetic lenses (magnetic equivalent to glass lenses in an optical microscope) are used in EM. There are different sets of lenses in TEM: condenser, objective and projection lenses. The condenser lenses gather the electrons of the first crossover image and focus them onto the specimen. To reduce the spherical aberration of these lenses, a condenser aperture is used. Below, the objective lens is used to produce focus and magnify the image. The specimen stage is situated between the objective lens pole pieces. An objective aperture is used to limit the beam that contributes to the final image, improving contrast and reducing image aberrations, but also limiting resolution. Then, the intermediate lenses are used to magnify the image from the objective lens. The last set of lenses are projector lenses. The image from the intermediate lens is further magnified and projected onto the phosphorescent screen or camera.

3.2.2 Scanning Electron Microscopy (SEM)

In scanning electron microscopy (SEM), an electron beam is generated by an electron gun at the top of an evacuated column, is accelerated (to < 50 keV) and focused into a small probe at the sample surface by a set of condenser and objective electromagnetic lens systems. The focused electron beam is then scanned point by point in a rectangular raster across the specimen using

a set of scanning coils. A variety of interactions between the incident electrons and sample can occur, however, secondary electrons (SE) and backscattered (BSE) are the most frequently used signals for imaging samples. Lower energy secondary electrons (below 50 eV) are emitted as a result of inelastic scattering from a thin surface layer in the irradiated specimen and produce topographical contrast which is important for the analysis of morphology and topography of a sample. Higher energy backscattered, incident electrons (scattering angle $> 90^\circ$) are an example of elastic scattering and can provide elemental contrast in the image of a flat specimen if it contains elements or compounds of different atomic number or mass. Some modern SEMs are equipped with a separate 'optical' column for a focused gallium ion beam which can sequentially sputter or mill away the sample surface and as a result, the freshly milled surface can be imaged using the corresponding electron column and detectors. This method is called dual beam, focused ion beam and scanning electron microscopy (FIB/SEM) and can investigate site-specific internal structural information as well as surfaces.

In this project, SE topography image will be applied to characterise the difference in laboratory development batches of model inorganic cation exchanger samples, sodium zirconium silicate (Chapter 5). Moreover, the FIB/SEM method will be used to investigate the internal structure of these sodium zirconium silicate samples and to attempt to obtain a cross-section of theophylline anhydrous form II crystal oriented to [100] (Chapter 6).

3.2.3 Transmission Electron Microscopy (TEM)

3.2.3.1 Basics of Transmission Electron Microscopy

In TEM, similar to SEM, an electron beam is generated by an electron gun at the top of the column, however, TEM uses much higher energy acceleration typically 80 – 300 kV and high vacuum (10^{-4} to 10^{-7} Pa or higher), enabling electron transmission through a thin specimen and providing very high-resolution images (Table 3.1).

Table 3.1 Electron wavelength as a function of accelerating voltage.

	Voltage (kV)	Wavelength λ [nm]
SEM	10	0.0122
	20	0.0086
TEM	80	0.0042
	200	0.0025
	300	0.0019

In TEM, a parallel electron beam is focused by a set of electromagnetic condenser lenses, and then transmitted through a thin specimen (<500 nm thick, however for high-resolution imaging a specimen must be as thin as possible and certainly <100 nm). A number of interactions between the incident high-energy electron beam and the specimen can occur, which results in a range of signals that can be emitted (Figure 3.4). Forward scattered (both elastically and inelastically) electrons can be collected, focused and magnified by the set of lenses in the TEM column (principally the objective lens) in order to produce a projected image onto a phosphorescent screen or a camera (charged-couple device (CCD), CMOS or direct electron detector). Furthermore, other interaction products e.g. X-rays can be collected by an appropriate detector that allows for chemical analysis of the sample. In order to maximise the mean free path of travel for the electrons, the column is kept under an ultra-high vacuum ($\sim 10^{-7}$ Pa or better).

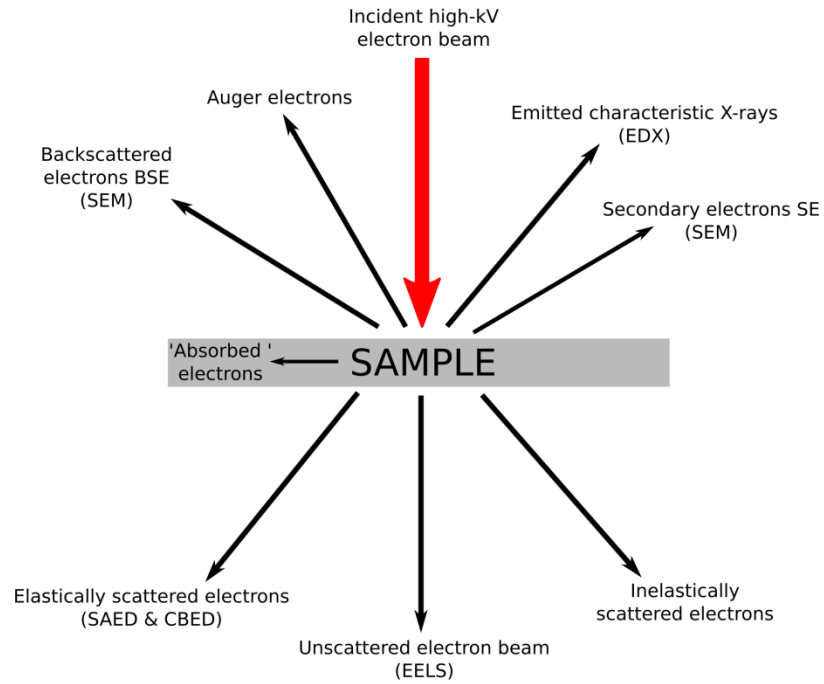


Figure 3.4 Illustration showing various interactions of an incident high-energy electron beam with a thin specimen in TEM, which results in a range of signals that can be emitted and collected.

TEM can operate in two modes: imaging and diffraction, and the scheme of each is shown in Figure 3.5. In the imaging mode, an objective aperture is inserted at the back-focal plane (BFP), in which the diffraction pattern of the sample is first produced. When the aperture is centred, highly scattered electrons are blocked and do not contribute to the final image. Darker areas in the image then correspond to regions of the specimen that scatter electrons strongly, and bright regions to areas in that electrons are relatively unscattered. This bright field (BF-TEM) imaging is the most efficient imaging mode due to the number of transmitted electrons that are collected. Moreover, the objective aperture can be inserted in such a way that the central or zero order diffraction beam is blocked (areas of unscattered electrons then appear dark in the image) and the image formed by the diffracted beam, thus a dark field (DF-TEM) image is obtained. In diffraction mode, a selected area aperture is inserted in the image plane of the objective lens (where the first image is formed). This aperture limits the number of transmitted electrons to the apertured region of the specimen which is to be analysed and so provides diffraction information of the crystal structure of just this region.

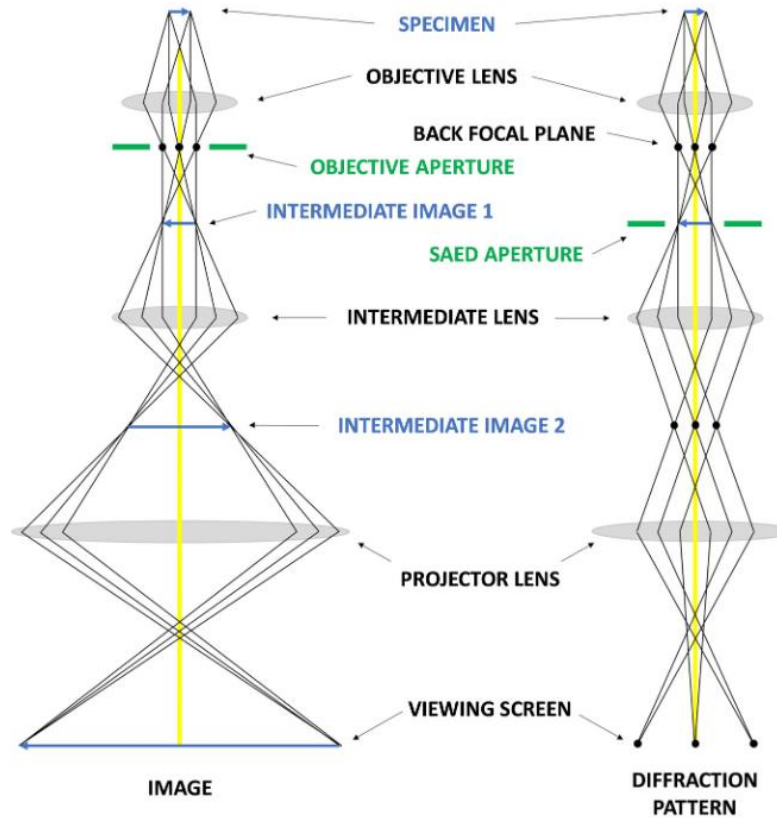


Figure 3.5 Schematic diagram of a TEM operating in two modes: imaging and diffraction. Taken from Braidy et al. (2020).

3.2.3.2 Contrast Mechanism

The image contrast mechanism in TEM is based on changes of both the electron wave amplitude and phase as the electrons travel through the specimen and these contribute to the differences in intensity between the image of the object and the background. In TEM, there are three image contrast mechanisms (Figure 3.6):

- ***Mass thickness contrast***

This relates to the fact that some electrons are absorbed or incoherently, elastically scattered to high angles by thicker specimens or by specimens containing the higher atomic number (Z) atoms. In a bright field (BF) image, an area producing highly scattered electrons appears darker than an area with a smaller number of scattered electrons, which becomes brighter.

- ***Diffraction contrast***

This arises either from the crystalline nature of a specimen or the presence of defects within a crystal. Electrons can be scattered more strongly by crystalline oriented to the beam so that the Bragg condition is satisfied, and these areas appear darker in BF-TEM. Disruption to diffraction contrast features such as bend contours (specific regions of a non-flat crystal lying in the Bragg condition) are often the first evidence of the presence of defects in a crystal structure.

- ***Phase contrast***

Phase contrast arises from electrons that are scattered by lattice planes in the specimen to be either in phase or out of phase with the direct, unscattered beam ($\pi/2$ phase change in the case of Bragg diffraction). The process results in constructive interference between the two types of electrons and a pattern of dark and bright lines are formed in the image, corresponding to a projection of the atomic lattice. The precise position and contrast of these lattice images can be controlled by defocusing the objective lens and with careful interpretation can provide structural information of the analysed specimen.

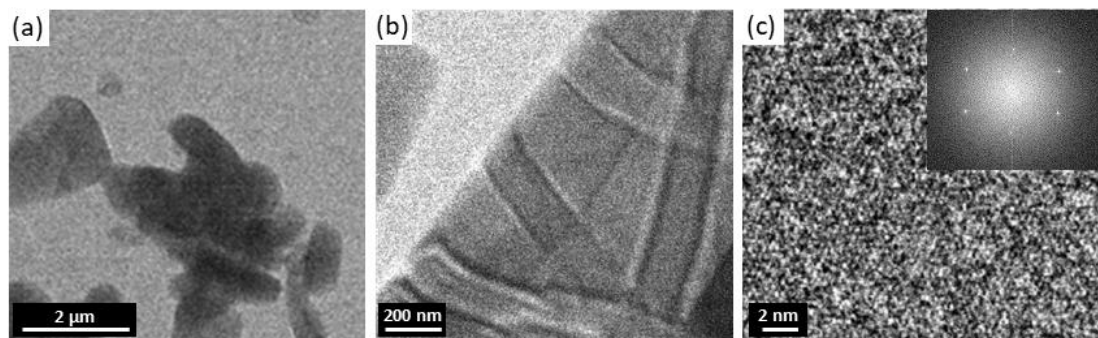


Figure 3.6 Different contrast mechanisms in TEM: (A) mass/thickness (example of theophylline form II, results Chapter 6), (B) diffraction (example of furosemide form I, results Chapter 4) and (C) phase (example of theophylline, results Chapter 6).

In this project, BF-TEM methods will be used to search for a sufficiently thin area (mass thickness contrast) exhibiting strong diffraction contrast in order to identify crystalline regions of interest.

3.2.3.3 Selected Area Diffraction Pattern (SAED)

Diffraction occurs as a result of the elastic scattering of the illumination by the atomic planes in a crystalline specimen and produces an interference pattern in the form of sharp peaks or spots in the back focal plane of the objective lens (Figure 3.5 and 3.7). These peaks correspond to a specific scattering angle that satisfies the Bragg condition and the scattering angles relative to the incident beam are twice the Bragg angle (θ_B) (Egerton, 2005). The geometry of the incident and diffracted beam satisfying the Bragg condition is presented in Figure 3.7a. However, in TEM the wavelength of electrons is much smaller (e.g. ~ 2 pm at 300 keV) than a typical d -spacing in the crystalline specimen (~ 0.3 nm), therefore the Bragg angle θ_B is small and the diameter of the Ewald sphere, that represents all the possible reciprocal lattice points satisfying Bragg condition, is large compared to X-ray diffraction (Figure 3.7b). Therefore, the Ewald sphere in electron diffraction is flat and can intersect with higher-order reflections (satisfying the Laue condition) thus positive and negative higher-order reflections can be detected. The distribution of peaks refers to the arrangement of atoms in a unit cell projected in the direction of electron transmission and can therefore provide information on the crystal structure of a specimen. Depending on the type of sample, the diffraction pattern may appear as a lattice of dots around a central bright spot for a single crystal; as bright spotty rings around a central spot for polycrystalline materials; or as diffuse rings in an amorphous sample.

A selected area aperture of the appropriate size can be positioned in the image plane allowing it to pass electrons from the specific area of interest and contribute to the selected area diffraction pattern (SAED). SAED patterns represent reciprocal spaces, thus low order diffraction spots (exhibiting large d -spacings in the crystal structure) lie closest to the central or zero-order spot of the beam. Electron diffraction patterns can be compared to known crystal structures and indexed to Miller indices. Moreover, a specimen can be orientated to a recognisable orientation or zone axis using a double-tilt specimen holder. Electron diffraction has a limited accuracy of 1% to measure d -spacings due to e.g. differences in sample thickness, while for pXRD this accuracy is much better, being down to a few parts per million (Egerton, 2005). However, SAED can be performed on a specimen of a microscopic volume

(depending on the size of the aperture used but it can be as low as ~ 100 nm in diameter before the aperture itself becomes the limiting feature), while pXRD requires a macroscopic volume of 1 mm^3 .

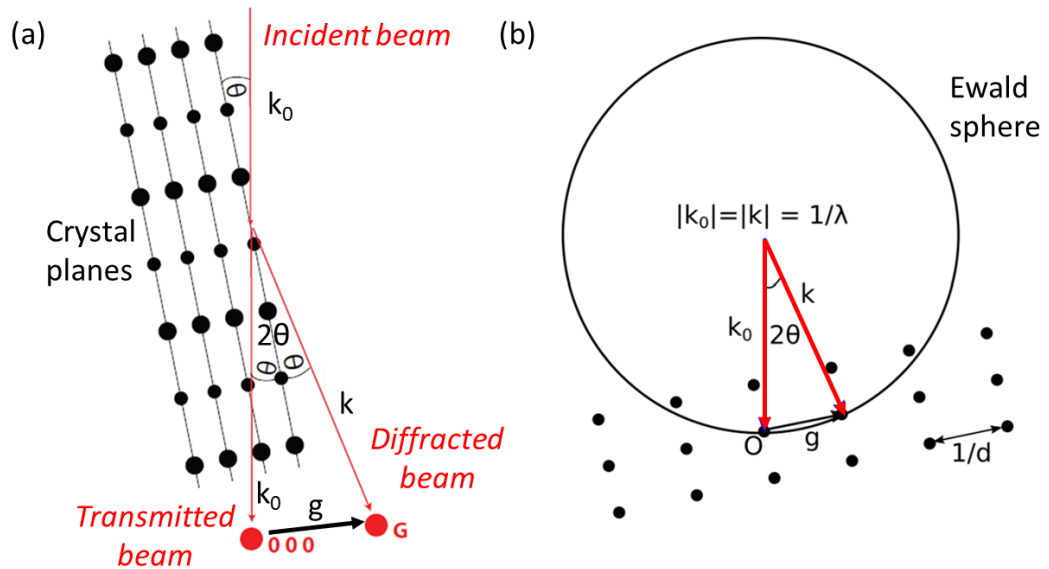


Figure 3.7 (a) Geometry representation of incident, transmitted and diffracted electron beams in a crystalline specimen that satisfies the Bragg condition. (b) Geometry representation of the Ewald sphere showing the equivalence of the Laue condition and satisfying Bragg's law.

In this project, SAED patterns will initially be used to distinguish between crystalline and amorphous areas or particles. The method will then be applied to identify crystal orientation (and tilting a specimen to a recognisable direction or zone if required) for further analysis. Moreover, the SAED pattern series will be acquired to determine critical fluence for the loss of crystallinity of irradiated samples.

3.2.3.4 Energy Dispersive X-Ray Spectroscopy (EDX / EDS)

Energy Dispersive X-ray (EDX or EDS) spectroscopy enables elemental analysis of the sample in an electron microscope. EDX analysis can provide information on the position of certain elements in the sample by SEM, TEM or STEM. The principle of EDX is that when the incident beam interacts with the sample, its energy can excite inner shell electrons (e.g. K or L) causing the

transition of these electrons to a higher energy shell or even removing these electrons from the atom leaving behind a positively charged electron hole. This electron hole can be filled with electrons from an outer shell producing characteristic X-rays whose energy is equal to the difference in energies of the orbitals of the atomic electron transitions in the specimen (between the higher energy shell and the inner shell). The X-ray energies are unique to specific atom type therefore, it is possible to determine the elemental composition of the specimen. The EDX energy resolution limit is ~ 140 eV and EDX can only detect elements above $\sim Z=4$ (due to a Be-window protecting the detector). The principle of EDX spectroscopy and an example of EDX spectra are shown in Figure 3.8.

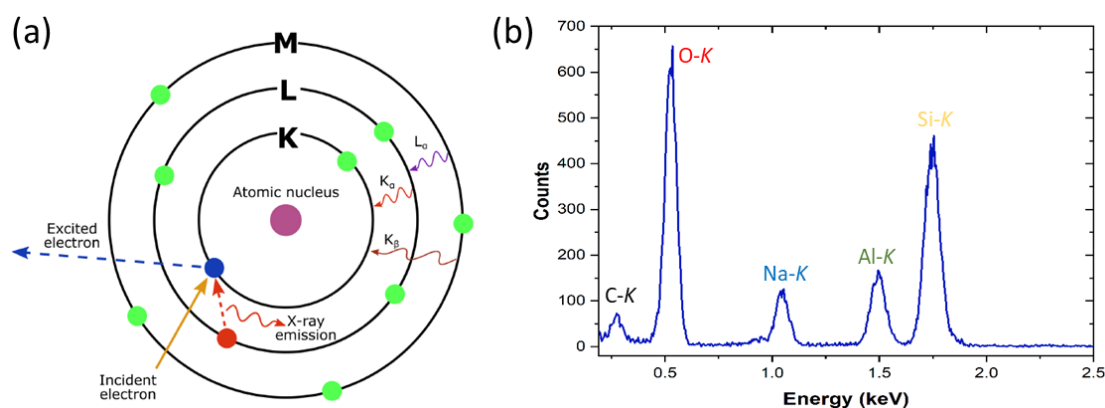


Figure 3.8 (a) Principle of Energy Dispersive X-Ray Spectroscopy (EDX). (b) example of EDX spectrum of silica mineral, albite (see Chapter 5).

In this project, the EDX method will be used to identify compositional changes in laboratory development batches of a model inorganic cation exchanger, sodium zirconium silicate on protonation and removal of Na from the materials micropores (Chapter 5) and to identify the composition of the model polymeric nanoparticle system of PLA-PEG encapsulating a drug (Chapter 7).

3.2.3.5 Electron Energy Loss Spectroscopy (EELS)

Electron Energy Loss Spectroscopy (EELS) is another method used for elemental analysis of the sample in an electron microscope (Figure 3.9). EELS is also based on inelastic scattering, which occurs when high-energy electrons interact with a sample. Energy loss results from the transfer of kinetic energy from the incident electrons to the sample's atoms during inelastic scattering

events. These interactions can include electron-electron interactions, electron-plasmon interactions, and electron-phonon interactions. The best EELS resolution is available for microscopes with cold field emission gun energy source or equipped with a monochromator providing energy resolutions of < 0.1 eV (von Harrach et al., 2010). EELS offers better sensitivity for lighter elements and provides better signal-to-noise and improved spatial resolution than EDX. Different energy loss mechanisms lead to distinct features in the EELS spectrum, providing information about e.g. band structure and specimen thickness (zero-loss and plasmon peak), elemental composition (core-loss edges) or bonding and oxidation states (electron energy loss near edge fine structure of core loss edges).

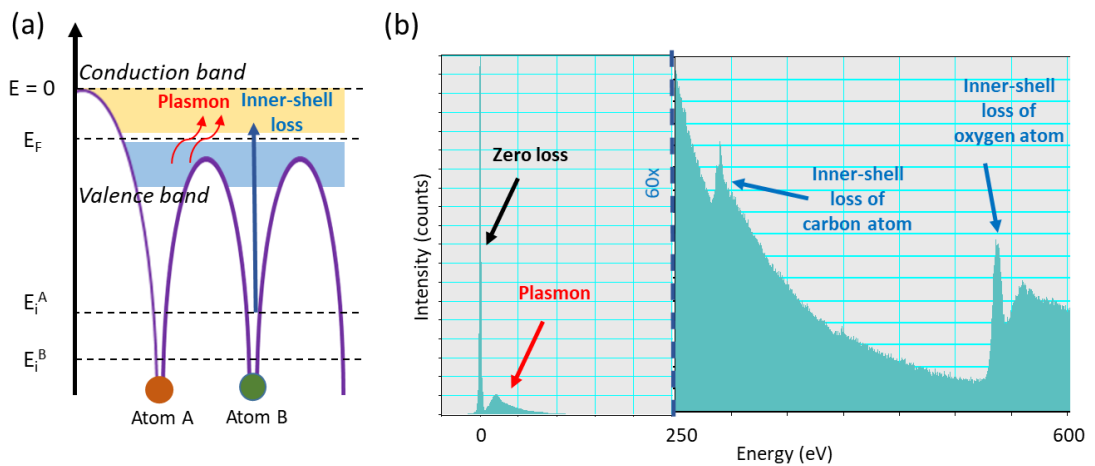


Figure 3.9 (a) Excitation mechanism in the specimen. (b) Example EEL spectrum with features from various loss mechanisms. The vertical scale is enlarged for the higher energy loss peak (above 250 eV) due to their intensity being much lower than the zero-loss and plasmon peaks.

In this project, the EELS method will be used to identify the composition of the model polymeric nanoparticle system of PLA-PEG encapsulating a drug (Chapter 7).

3.2.4 Scanning Transmission Electron Microscopy (STEM)

3.2.4.1 Basics of Scanning Transmission Electron Microscopy

STEM combines the principles of TEM and SEM such that a converged electron probe is scanned across a thin specimen by the scanning coils and a fraction of the transmitted electrons are used to generate an image. The

electron beam is de-magnified and focused by the condenser and upper objective lenses to form a focussed probe (Pennycook and Nellist, 2011). There are then no significant post-specimen lenses and an image is collected in a serial fashion. Chromatic aberration due to the thickness of a specimen is limited, and so slightly higher spatial resolution can be achieved than in TEM. Modern dedicated STEMs can also be fitted with probe correctors to reduce the spherical aberration of the probe-forming lens, improving probe size and resolution further.

Transmitted scattered electrons can be collected simultaneously using different post-specimen detectors. A bright field (BF) detector collects electrons scattered to small angles, thus mass thickness, diffraction and phase contrast can contribute to the image formed. A BF-STEM detector collects a smaller fraction of the low-angle transmitted electrons compared to TEM and is therefore not as efficient. Conversely, a high-angle annular dark field (HAADF) detector that collects incoherent Rutherford electrons scattered to high angles (>50 mrad) to reveal mass Z-contrast images, is more efficient than high-angle DF-TEM because STEM collects over an annulus. However, HAADF STEM collects a much lower fraction of the incident electrons than BF-STEM due to the relatively low number of electrons scattered to high angles. One of the advantages of STEM over TEM is that it enables the collection of signals from various electron-sample interactions simultaneously, and which cannot be spatially correlated by TEM as easily, i.e. characteristic X-rays (EDX) and electron energy loss (EEL) spectroscopy can be used to collect elemental or chemical maps at each probe (pixel) position (X, Y), and thus a spectrum image (STEM SI) can be collected and used for elemental mapping. Although the generation of such maps requires many orders of magnitude more incident electrons than diffraction pattern formation or BF imaging because of the low cross-section for the inelastic electron scattering required to generate these spectroscopic signals.

In this project, BF-STEM will be used for the lattice image of laboratory development batches of a model inorganic cation exchanger, sodium zirconium silicate (Chapter 5) and STEM SI for elemental analysis of sodium zirconium silicate samples (Chapter 5) and polymeric nanoparticles (Chapter 7).

3.2.4.2 Scanning Moiré Fringes (SMFs)

Moiré patterns occur due to interference between two similar-in-size periodic lattices that overlap each other. In STEM, scanning moiré fringes (SMFs) provide magnification of the crystal lattice through the interference between a closely aligned and similarly sized scanning lattice produced by the electron probe in STEM (d_s) and a crystal lattice (d_l) (S'ari et al., 2019; Su and Zhu, 2010). The STEM magnification determines the scanning lattice spacing or pixel size which can only take discrete values. To obtain a large spacing in the interference or moiré lattice a STEM magnification is chosen that gives a scanning lattice (d_s) closest to that of the crystal lattice spacing (d_l). There are two types of moiré fringes that this form: translational and general, and the difference in their formation is shown in Figure 3.10.

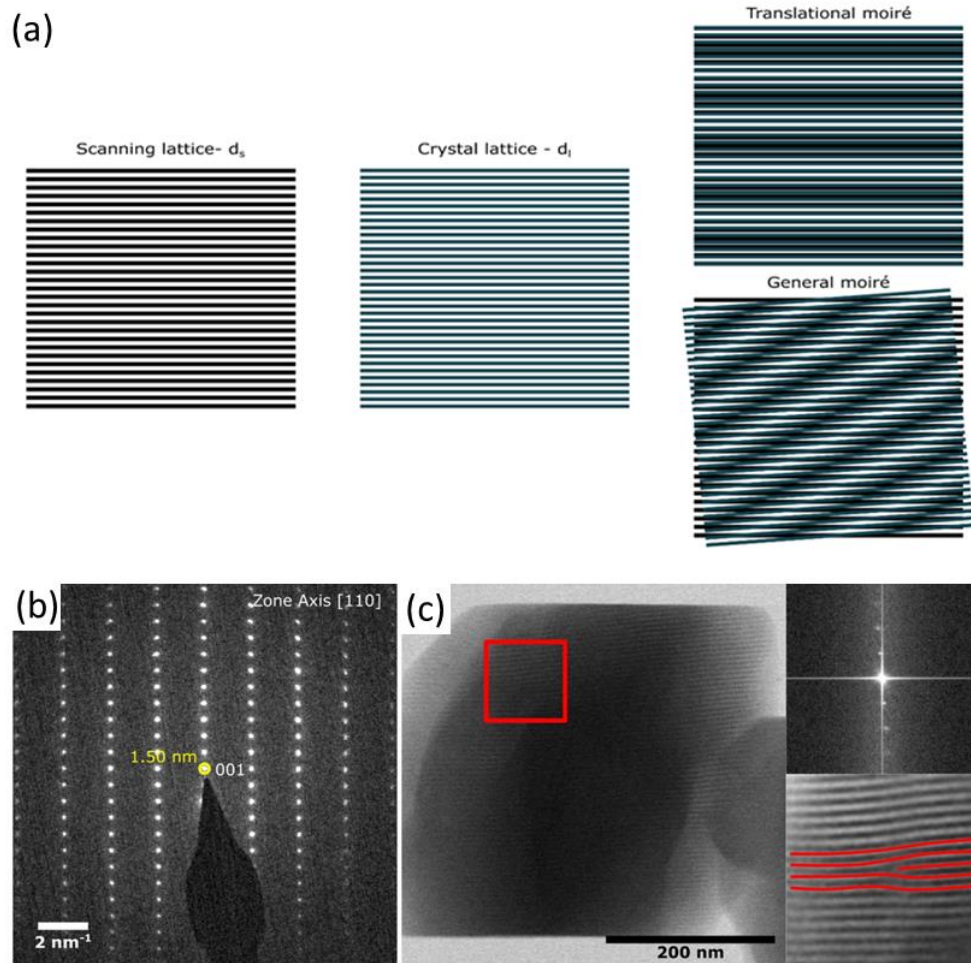


Figure 3.10 (a) Schematic of translational and general moiré fringes created by a scanning lattice (d_s) and crystal lattice (d_l) of similar sizes. (b) SAED of furosemide form I oriented to [110]. (c) BF-STEM image of SMFs produced by using a pixel size of 1.32 nm and $1.50 \pm 0.10 \text{ nm}$ d -spacing. Fourier Fourier-filtered image from within the red box highlights a defect seen within the crystal. Taken from S'ari et al. (2019).

Various factors affect the size of the observed SMFs: STEM magnification gives d_s (size of scanning lattice), the crystal gives d_l (size of crystal lattice) and the relative angle β between fringes d_s and d_l (S'ari et al., 2019; Su and Zhu, 2010; Williams and Carter, 2009). If β is equal to zero, translational moiré fringes (d_{TM}) will form and the spacing can be calculated from Equation 3.3 (Williams and Carter, 2009).

$$d_{TM} = \frac{d_s d_l}{|d_s - d_l|} \quad 3.3$$

It should be noted that if the relative distance between d_s and d_l is close to zero, then the size of SMF tends to infinity. Conversely, if the relative distance

between d_s and d_l increases, the size of SMFs decreases and they become unobservable beyond a certain value. If β is different from zero then general moiré fringes form (with rotational and translational components) and the size of the fringes (d_{GM}) can be calculated by Equation 3.4 (Williams and Carter, 2009).

$$d_{GM} = \frac{d_s d_l}{\sqrt{(d_s - d_l)^2 + d_s d_l \beta^2}} \quad 3.4$$

In this project, the SMF method will be used to magnify the furosemide crystal lattice and allow it to be viewed indirectly at lower magnifications and therefore lower electron fluence than would normally be required in phase contrast imaging by conventional TEM i.e. it becomes possible to image the lattice at sufficiently low electron fluence to avoid damage destroying the lattice structure as the image is formed. The general workflow and detailed description of scanning moiré fringe acquisition are described in Appendix A.3.

3.2.4.3 Scanning Electron Diffraction (SED)

Scanning electron diffraction (SED) is an advanced electron microscopy technique that allows simultaneous acquisition of diffraction patterns at each pixel of the scanned probe position (Figure 3.11). For SED, a low convergence semi-angle is required and is often set to be 1 mrad or lower at 300 keV (for organic samples with larger unit cell) to prevent diffraction disk overlapping such that each diffraction disk can be measured and analysed independently (Figure 3.11). These diffraction patterns are collected using a sensitive electron detector, such as a pixelated direct electron detector. SED offers nanoscale spatial resolution to resolve structural details and crystallographic information at the atomic level. The collected SED dataset consists of a vast amount of diffraction data, which requires advanced data analysis and reconstruction techniques e.g. using HyperSpy software (Python-based library). SED is an emerging technique that has a wide range of potential applications in materials science, nanotechnology, and semiconductor research. It can be used to investigate the structural properties of nanomaterials, characterize defects, study strain and deformation, and analyse crystallographic textures.

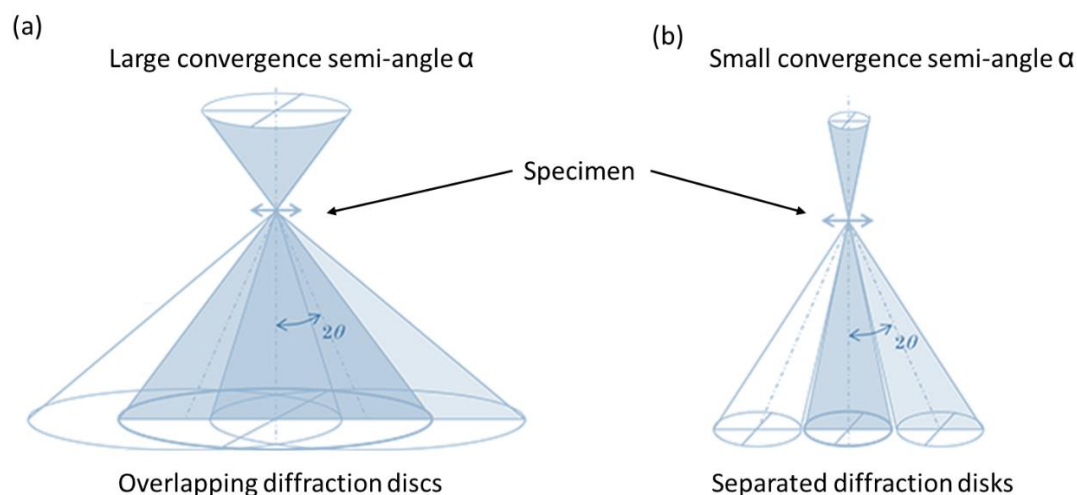


Figure 3.11 Schematic representation of the impact of (a) large and (b) small convergence semi-angle α on the size of the diffraction discs.

In this project, SED will be used to characterise probe structural information at the unit cell level of furosemide (Chapter 4) and theophylline (Chapter 6). Moreover, SED will be used to investigate the structural changes during the hydration and dehydration of theophylline.

3.2.5 Cryogenic - (Scanning) Transmission Electron Microscopy (Cryo-(S)TEM)

Cryogenic - (scanning) electron microscopy (cryo-(S)TEM) observes a specimen at very low temperatures and also refers to the observation of rapidly frozen thin specimens transferred into the microscope at cryogenic temperature. Cryo-(S)TEM offers the analysis of frozen but still hydrated soft matter and biological samples at the near-native state. In cryo-EM, it is important to prepare grids with a thin, well-dispersed distribution of particles of interest within an aqueous suspension by a rapid vitrification process (to prevent crystalline ice formation redistributing the particles) and can provide structural and chemical information of hydrated samples (De Yoreo and Sommerdijk, 2016). A schematic representation of cryo-EM sample preparation is presented in Figure 3.12. A drop of suspension (3 – 5 μL) is loaded onto a plasma treated, thin carbon film EM grid (plasma treated to make the surface of the film hydrophilic) and blotted to form a thin layer of the aqueous suspension and sample (Figure 3.12a, 'A'). Then, the EM grid is

rapidly plunge frozen into liquefied ethane (Figure 3.12a, 'B'), transferred into a cryo-transfer holder under liquid nitrogen (Figure 3.12b) and loaded, cold into the microscope. This vitrified thin film containing a dispersion of the particles of interest can be then analysed via cryo-(S)TEM techniques, preferentially of a suspension over a hole in the carbon film in the EM grid (Figure 3.12c, d).

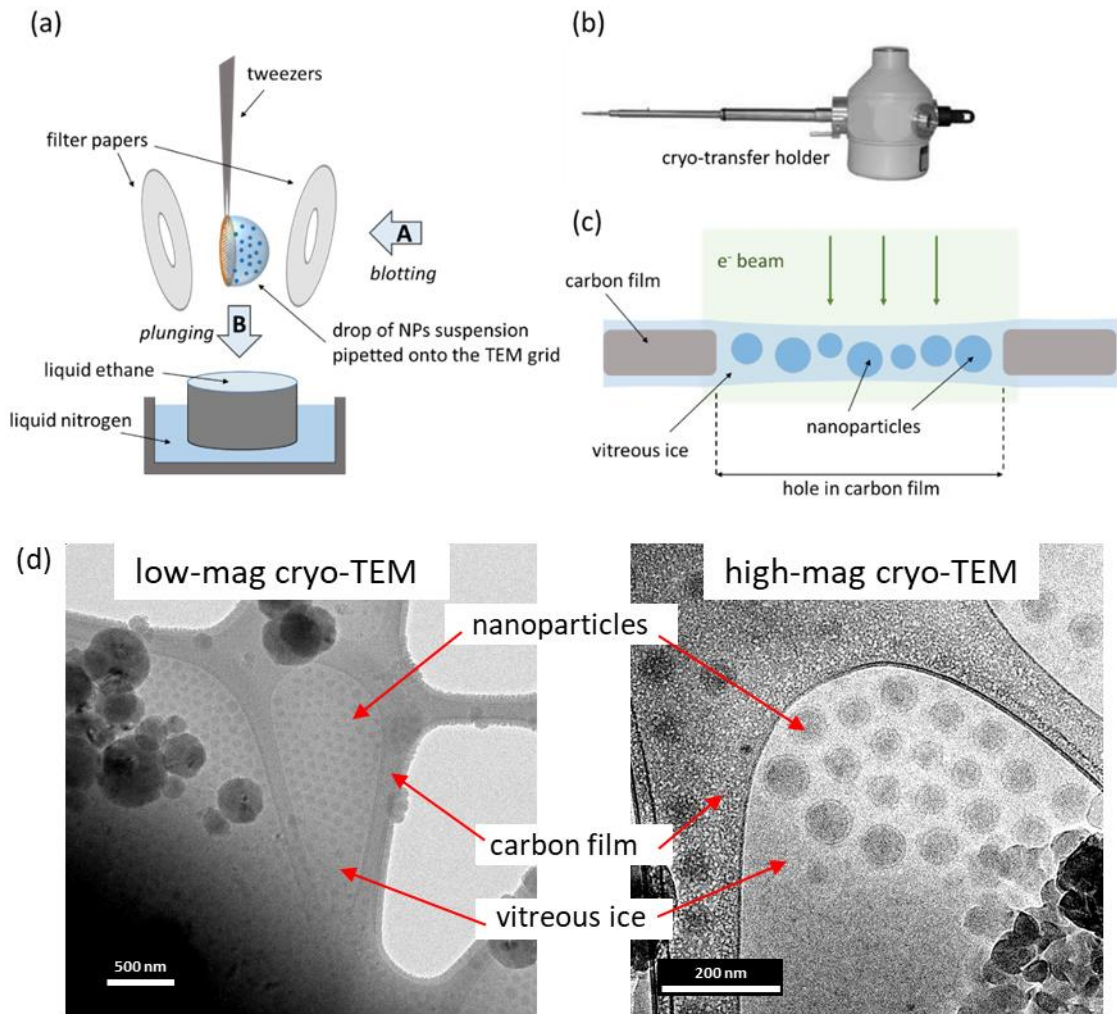


Figure 3.12 Schematic representation of cryo-EM sample preparation: (a) the drop of suspension is loaded onto the EM grid and blotted (A) and then the grid is rapidly plunge frozen into liquefied ethane (B) and (b) transferred into a cryo-transfer holder under liquid nitrogen. (c) Cryo-EM thin film of dispersion can be then analysed via cryo-(S)TEM techniques. (d) examples of cryo-TEM images of polymeric nanoparticles taken in low and higher magnification (see results Chapter 7).

In this project, the cryo-(S)TEM will be used to reduce electron beam damage during STEM-EDX acquisition of laboratory development batches of a model

inorganic cation exchanger, sodium zirconium silicate (Chapter 5) and to analyse the structure of polymeric nanoparticles suspended in water (Chapter 7).

3.3 Powder X-Ray Diffraction (pXRD)

Powder X-ray Diffraction (pXRD) is a 'gold standard' analytical technique used in the characterization of crystalline materials e.g. to identify phases, to determine crystal structures and to quantify sample composition. The fundamental principles of pXRD rely on Bragg's Law. The diffraction angle (θ) is related to the wavelength (λ) of X-rays and the interplanar spacing (d) within the crystal lattice by Bragg's Law presented in Equation 3.5:

$$n\lambda = 2d \sin(\theta_b) \quad 3.5$$

where n is an integer, λ is the wavelength of the X-ray, d is the inter-planar spacing and θ_b is the incident angle. X-rays interacting with (or 'reflecting' off) the periodic crystal lattice constructively interfere at specific angles at which the path difference of rays from successive crystal planes is an integer number of whole wavelengths, producing characteristic diffraction peaks on a detector.

For pXRD, the sample is prepared as a finely ground powder to ensure the random orientation of crystalline grains and loaded onto a flat holder. A detector records the intensity of diffracted X-rays as a function of the diffraction angle (2θ). The obtained pXRD pattern can be analysed to identify and quantify the diffraction peaks, measure their positions and intensities, and match the pXRD pattern to known crystal structures.

In this project, pXRD will be used for phase identification of laboratory development batches of a model inorganic cation exchanger, sodium zirconium silicate (Chapter 5) and theophylline (Chapter 6) samples.

Chapter 4 Moving from TEM to STEM: Low-dose Techniques to Acquire Structural Information of Furosemide Form I

This chapter demonstrates the possibility of using low-dose transmission electron microscopy as a method to identify the presence of defects and disordered sites in a beam-sensitive active pharmaceutical ingredient, furosemide form I. The results suggest scanning transmission electron microscopy may have benefits over conventional transmission electron microscopy in terms of improved signal-to-noise ratio (SNR) in images of defects in these materials.

The critical fluence of furosemide form I was shown to be $21 \pm 8 \text{ e}^-/\text{\AA}^2$ at 300kV and using continuous carbon film more than twice that at 200kV and using holey carbon film ($9 \pm 3 \text{ e}^-/\text{\AA}^2$). Phase-contrast lattice imaging by TEM has been acquired using a total electron fluence of $\sim 16 \pm 8 \text{ e}^-/\text{\AA}^2$, however, the small sampling area and low SNR make the lattice image low quality and unsuitable for robust defect analysis. This gives the opportunity to use alternative STEM techniques that can achieve better SNR at low total electron fluences below $<10 \text{ e}^-/\text{\AA}^2$, making the technique applicable to a larger number of beam-sensitive samples.

The scanning electron diffraction (SED) method was successfully applied to identify defects in a furosemide crystal using disruption to bend contours in the bright field image and also to identify a potential twin boundary. Scanning moiré fringes generated in bright field STEM were used as an alternative method to acquire an indirect lattice image of furosemide form I and inspect two families of lattice planes that exhibit different dissolution rates, the {001} and {010}, (Adobes-Vidal et al., 2016). The difference in disruption to the moiré fringes in each set of images is consistent with the difference in dissolution rates of these planes as well as with a hydrogen bonding model of the crystal structure. The STEM images show that the (001) lattice images have fewer disordered sites and less strain than the equivalent (010) images. The low-dose STEM techniques can be used as a complementary method to bulk techniques to ultimately correlate with computational modelling to help understand dissolution kinetics and predict performance.

4.1 Background

Furosemide (brand name Lasix) is a loop diuretic and antihypertensive drug, used to control cardiovascular and heart failure disease (Aceves et al., 2000). Furosemide $C_{12}H_{11}ClN_2O_5S$ is a weak acid when dispersed in a solution that can be present in four known polymorph forms (I-IV), two solvates (IV-DMS and V-dioxane) and one amorphous form (Beloborodova et al., 2017; Goud et al., 2012; Matsuo and Matsuoka, 2007; Nielsen et al., 2013). The thermodynamically stable polymorph form I is the only one present in the commercial drug. It has a triclinic crystal system ($P\bar{1}$) with cell parameters as follows: $a = 9.5150 \text{ \AA}$, $b = 10.4476 \text{ \AA}$ and $c = 15.5826 \text{ \AA}$, as reported in the Cambridge Structural Database (reference FURSEM13) (Babu et al., 2010) (Figure 4.1). According to the Biopharmaceutics Classification System (BSC), furosemide belongs to the Class IV category, because of its low permeability and poor solubility (Babu et al., 2010; Tang, N. et al., 2019). Poor solubility of furosemide is linked to strong intra- and intermolecular H-bonding in the crystal structure and the presence of furan rings which cause slower solvation of the drug (Babu et al., 2010). It has been shown that the physiochemical properties of furosemide can be modified by laboratory processing, however, this can result in significant changes in the crystal structure and stability i.e. presence of defects. Adobes-Vidal et al. (2016) reported on the dissolution kinetics of individual crystal faces of furosemide form I by a versatile in situ multi-microscopy method (optical and scanning probe microscopes). They found that increases in pitting density (surface area and roughness) increase the dissolution rate of particular crystallographic faces and that the (010) face dissolved more rapidly than the (001) – $12.6 \text{ vs } 2.8 \text{ mol m}^{-2} \text{ s}^{-1}$ respectively. It is probable that crystal defects e.g. dislocations and voids are sites for the initial formation of pits during dissolution (Sangwal, 2012). Therefore, it is of interest to obtain information on the crystal lattice defects present in furosemide particles after processing into medicine in order to understand and implement strategies for ensuring bioavailability. Low-dose (S)TEM can provide insight into the identification of these defects and potentially correlate results with the reported dissolution rate of different crystal faces.

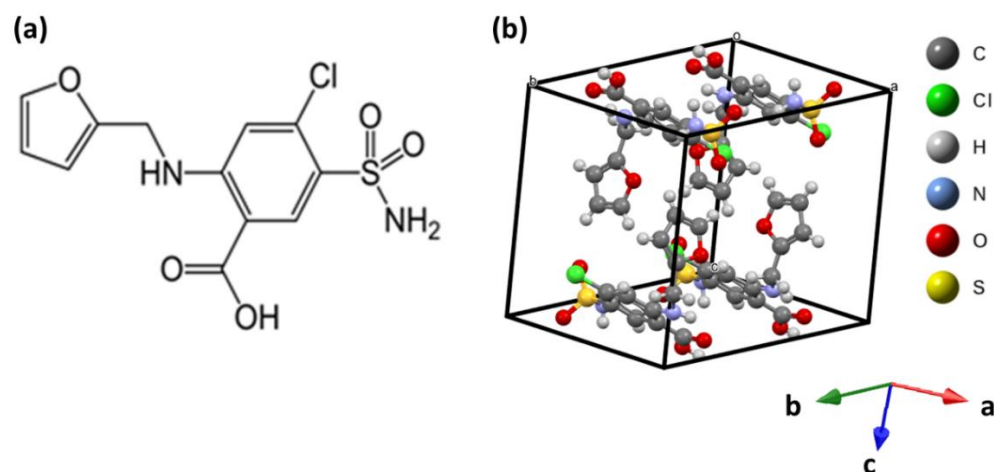


Figure 4.1 (A) Molecular and (B) crystal structure of furosemide form I.

4.2 Materials and Methods

4.2.1 Sample Preparation

Furosemide form I was provided by AstraZeneca. Two methods were used to prepare the samples for TEM analysis: (i) grinding and (ii) recrystallisation from ethanol. In the first method, furosemide crystals were lightly crushed between two glass slides and approximately 1 mg was transferred to a 100 mL container and filled with deionised (DI) water. Two drops of the solution were pipetted onto TEM grids (holey-carbon support film on 400 mesh copper and continuous carbon film) and allowed to evaporate. In the second method, furosemide crystals were prepared by mixing 0.5 mL of a 10 mM solution of furosemide in ethanol with 3.5 mL of DI water in order to create a supersaturated solution (as described in Adobes-Vidal et al. (2016)). After 5 min incubation crystals or precipitates were visible by eye, two drops of the mixture were pipetted onto continuous carbon TEM grids and allowed to evaporate.

Crocidolite (an aluminosilicate mineral with needle habit) mounted on a TEM grid was acquired from Agar Scientific Ltd and used as-received as a standard sample for optimising low-dose bright-field STEM (BF-STEM) and Scanning Moiré Fringe (SMF) analysis.

4.2.2 (S)TEM Operating Condition

TEM analysis was performed at room temperature on the FEI Tecnai TF20 and Titan Themis³ operated at 200 and 300 keV acceleration voltages, respectively. For initial diffraction pattern collection, all TEM analysis was carried out using bright-field (BF) mode with a 40 μm objective aperture and a 1-second exposure time for the camera. A combination of the following parameters: spot size (a monochromator was used to control beam intensity in the Titan³ Themis instead of changing spot size as is done in the Tecnai), magnification, and condenser lens focus, were changed in order to achieve the desired pattern signal at a low value of an electron flux of 0.04 - 0.06 $\text{e}^-/\text{\AA}^2\text{s}$. Phase contrast lattice imaging was acquired at a total electron fluence of $\sim 16\text{-}18 \text{ e}^-/\text{\AA}^2$ (sum of fluence during searching particles, initial BF-TEM and SAED pattern acquisition and phase-contrast lattice image acquisition) and an image pixel size of 0.076 nm. Focusing was performed on a sacrificed part of the particle and this fluence is not counted in the total electron fluence.

Bright-field scanning transmission electron microscopy characterisation was carried out in the FEI Titan³ Themis 300 microscope, with a 50 μm condenser aperture, 10 mrad convergence semi-angle for the probe and a 5.5 mrad collection angle for the bright field detector. The probe current was reduced to 5 pA by using the monochromator focusing. The pixel dwell time (t) was set to 10 / 20 μs .

Low-dose scanning electron diffraction (SED) was performed within a total electron fluence of $\sim 8 \text{ e}^-/\text{\AA}^2$ using a Merlin/Medipix pixelated electron counting detector on a JEOL ARM300CF at ePSIC.

Double-tilt holders (Gatan and JEOL) were used for (S)TEM acquisition.

4.2.3 Data Analysis

BF-TEM micrographs and SAED patterns were acquired and further processed using Digital Micrograph (Gatan Microscopy Suite) and ImageJ. SED data were processed using HyperSpy and pyXem. The structural .cif file of furosemide (reference FURSEM13, (Babu et al., 2010)) was downloaded from the Cambridge Structural Database and the structure file of crocidolite was acquired from the Supporting Information in Whittaker (1949). Further

analysis was performed using CCDC Mercury 2022.2.0 (Macrae et al., 2020) and the CrystalMaker crystal visualisation packages.

4.3 Critical Fluence Measurement

The critical fluence (C_F) of furosemide has been measured recently to be $7.1 \pm 4.0 \text{ e}^-/\text{\AA}^2$ using a microscope operated at 200 kV accelerating voltage at room temperature (S'ari et al., 2018). To optimise any lattice imaging of furosemide and to conduct further scanning transmission electron microscopy data acquisition, C_F was re-examined at different kVs and on different support films. Cattle et al. (2016) examined the effect of sample preparation and experimental conditions on the C_F of another organic beam-sensitive sample, theophylline. They reported that the C_F of theophylline benefits most significantly by increasing acceleration voltage from 200 to 300 kV improving the C_F from $23 \text{ e}^-/\text{\AA}^2$ to $36 \text{ e}^-/\text{\AA}^2$, respectively. This is related to a lower inelastic scattering cross-section at 300 kV than at 200 kV. Here C_F values were validated at 200 keV and then investigated at 300 keV. C_F was evaluated by analysis of the fading spots of an electron diffraction pattern under continuous electron irradiation and this method is described in detail in the Appendix A.2. Briefly, the C_F for furosemide, defined by the accumulated electron fluence at which the relative intensity of a particular electron diffraction spot decreases to $1/e$ of its original value (i.e. a decrease to $\sim 37\%$ of its initially irradiated intensity values). This method assumes an exponential decay of diffraction spot intensity under continuous electron irradiation. The overall C_F was calculated by averaging all the diffraction spot measurements in a pattern.

Critical fluence at 200 keV

Most of the 16 diffraction patterns used to determine C_F showed different interplanar spacings indicating furosemide crystals in different orientations on the TEM grid. Tilting the particular area of interest into a preferred zone axis was not possible, as furosemide is very sensitive to electron beam irradiation. Therefore, assessing a characteristic C_F for a specific interplanar spacing was difficult. Figure 4.2 shows a series of electron diffraction patterns obtained from a typical furosemide form I crystal, after 120, 167, 182, 208, 226, and 256 s exposure time to electron irradiation at room temperature at 200 keV, acquired using an electron flux of $0.047 \text{ e}^-/\text{\AA}^2\text{s}$ and so giving corresponding

electron fluences of 5.6, 7.9, 8.6, 9.8, 10.6 and 12.0 $e^-/\text{\AA}^2$, respectively. The crystal was initially orientated close to the [100] zone axis. The outer spots, corresponding to smaller d -spacing values decrease in intensity faster than the inner spots that representing larger d -spacing values.

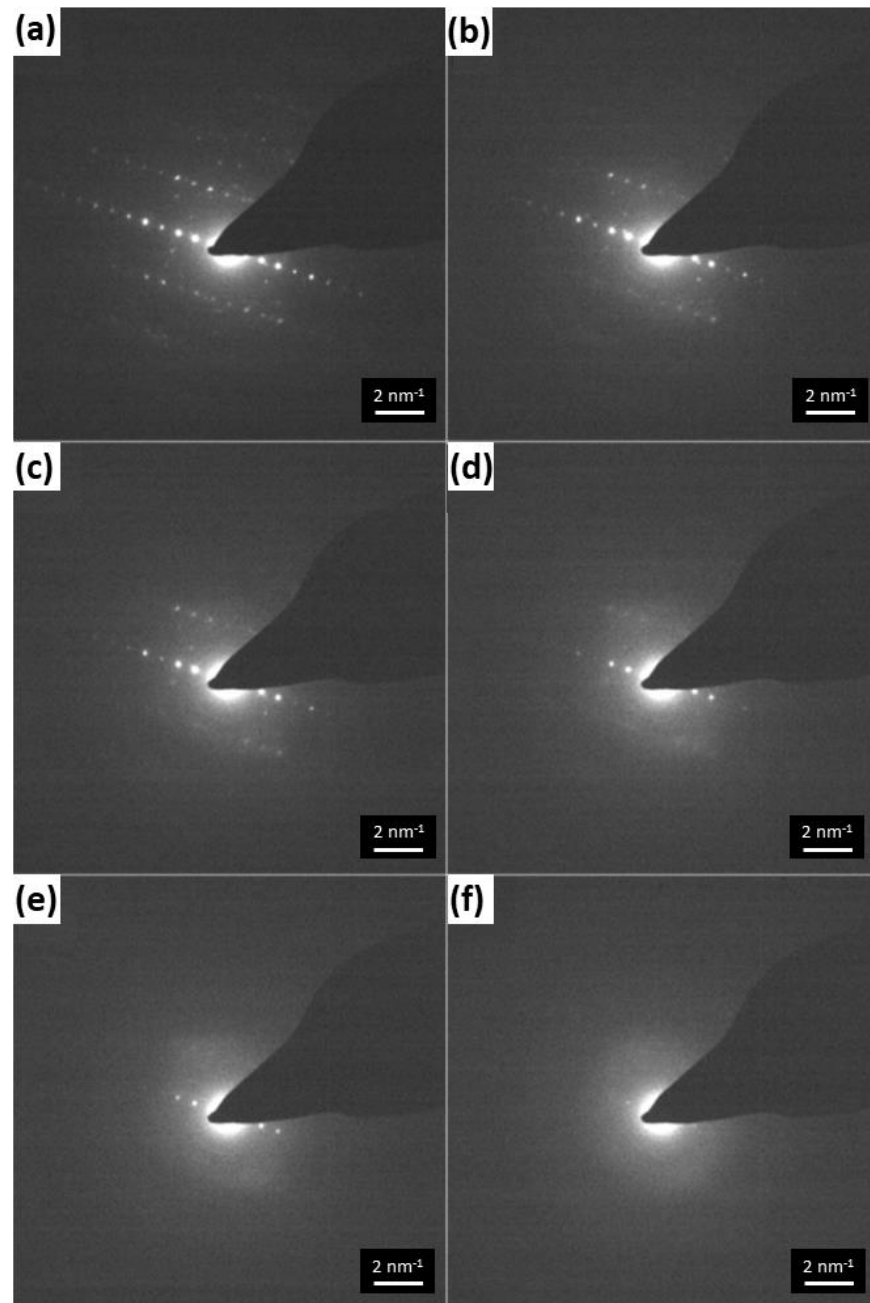


Figure 4.2 Example of an electron diffraction pattern time series of furosemide form I, initially orientated close to [100] zone axis, acquired at 200kV using an electron flux of 0.047 $e^-/\text{\AA}^2$ s and obtained after (a) 120, (b) 167, (c) 182, (d) 208, (e) 226, and (f) 256 s exposure time to electron irradiation.

Some diffraction pattern series exhibit different trends in the normalised intensity of diffraction spots versus cumulative electron fluence, as shown in Figure 4.3 (Figure 4.3d-f). This pattern is from a crystal initially orientated close to the [001] zone axis that then rotates and the pattern changes to a systematic row further off the zone axis, then the reflections gradually reduce in intensity as the electron fluence accumulates until it completely disappears, indicating loss of crystallinity (Figure 4.3a-c). The spot marked as (i) and indexed as a $(\bar{1}10)$ lattice plane, continues to decrease in intensity until around $12 \text{ e}^-/\text{\AA}^2$, where the intensity plateaus and then is no longer visible in the electron diffraction pattern above $25 \text{ e}^-/\text{\AA}^2$. However, the spot marked as (ii) and indexed as a (010) lattice plane, increases in intensity until around $10 \text{ e}^-/\text{\AA}^2$, then plateaus until $16 \text{ e}^-/\text{\AA}^2$ and finally rapidly decreases in intensity until it also fades completely around $25 \text{ e}^-/\text{\AA}^2$. The spot marked as (iii) and indexed as a $(0\bar{2}0)$ lattice plane also exhibits an enhanced intensity effect. At approximately $15 \text{ e}^-/\text{\AA}^2$ the spot is at its maximum intensity and then exhibits a rapid decrease in intensity until it fades around $23 \text{ e}^-/\text{\AA}^2$. These variations might be related to crystal movement, particle morphology changes (not planar surface) or mass loss upon irradiation (as discussed in S'ari et al. (2018)).

The average C_F of furosemide, measured at 200 kV and using a holey-carbon film for support, was calculated here to be $9 \pm 3 \text{ e}^-/\text{\AA}^2$ giving good reproducibility with the earlier work (S'ari et al. (2018) reported $7 \pm 4 \text{ e}^-/\text{\AA}^2$).

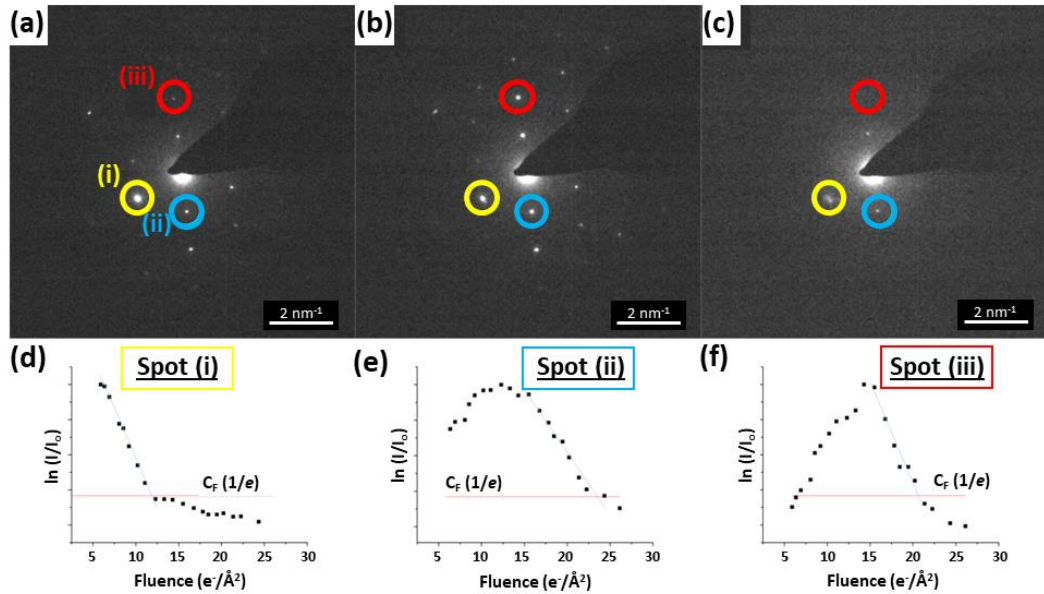


Figure 4.3 Diffraction pattern series of a furosemide crystal orientated close to [001] zone axis. (a)-(c) The diffraction pattern changes to a systematic row, and then reflections gradually reduce in intensity as the electron fluence accumulates until it completely disappears, indicating loss of crystallinity. (d)-(f) Difference in the intensity profiles of marked spots (i)-(iii).

Critical fluence at 300 keV

Subsequently, the analysis was carried out at 300 kV accelerating voltage because the higher accelerating voltage decreases the damage rate to a sample due to an inverse relationship between the inelastic scattering cross-section and accelerating voltage. C_F was initially measured to be $10 \pm 7 e^{-}/\text{\AA}^2$ at 300 kV using a holey-carbon support film. Most diffraction pattern series exhibited a similar trend to that presented in Figure 4.4 which suggests rotation or reorientation of the crystal off the original. This could be due to the fact that this holey-carbon support film had holes sufficiently large to result in most crystals being deposited on a narrow part of the carbon film and therefore being inherently unstable (mechanically).

Additional diffraction pattern series were acquired using continuous carbon films, as it was believed this might mechanically stabilise the crystals. The average critical fluence of these was $21 \pm 8 e^{-}/\text{\AA}^2$ and is \sim two times higher than the C_F of the furosemide sample prepared on holey-carbon films at 200 or 300 kV (C_F is expected to improve by a factor of 1.5 on moving from 200 to

300 kV, as discussed by Cattle et al. (2016)). Therefore, the higher accelerating voltage and the relevant type of the TEM support film are both important factors affecting furosemide crystal stability. Crystal reorientation, however, has been observed in all the diffraction series studies presented here to a greater or lesser extent.

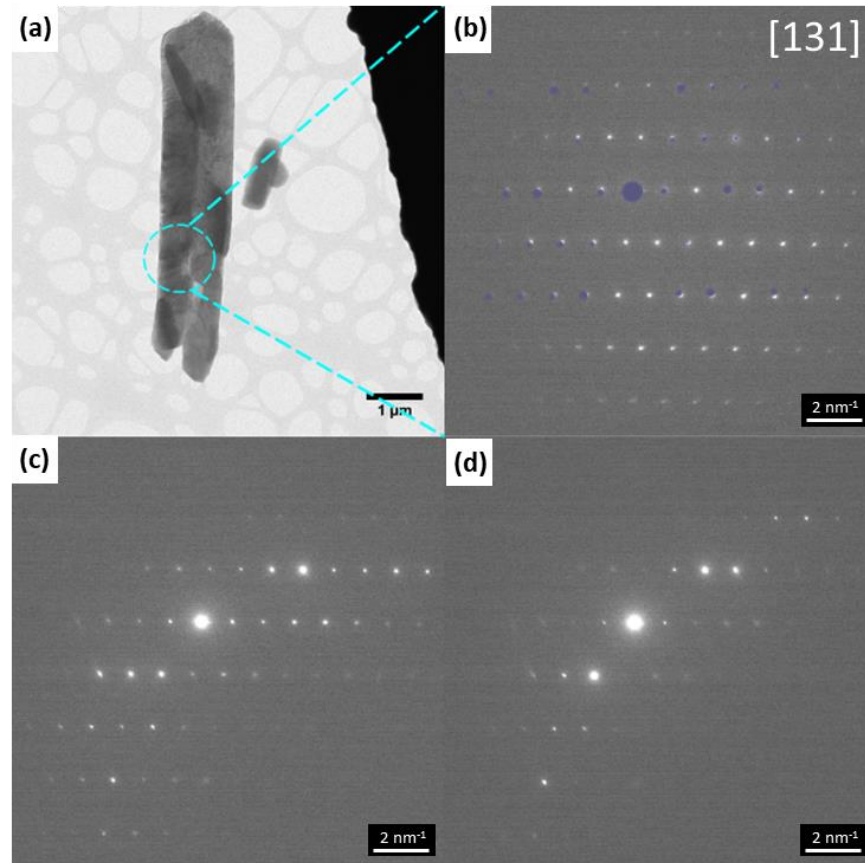


Figure 4.4 Example of an electron diffraction pattern time series of furosemide form I, initially orientated close to [131] zone axis, acquired at 300 kV and using an electron flux of $0.059 \text{ e}^-/\text{\AA}^2\text{s}$, after 55, 171 and 252 s after initial exposure.

Overall C_F results are shown in Table 4.1, where measured diffraction spots for patterns at 2 and 300 kV have been grouped into d -spacing ranges (<2 , 2–4, 4–6, and $>6 \text{ \AA}$). For the sample analysed at 200 keV, larger d -spacings correspond to larger values of C_F ; d - spacings $>6 \text{ \AA}$ have a double average C_F compared to the spacings within the range of $<2 \text{ \AA}$. However, for the samples analysed at 300 keV, this trend is no longer as clear. Sample

thickness influences the critical fluence, thicker samples generate larger C_F values as a result of less scattering-induced heating (S'ari et al., 2018).

Conclusions

Overall C_F results show that the relevant type of TEM support film, i.e. continuous carbon TEM grid, and increased accelerated voltage from 200 kV to 300 kV, proved to be the important factors affecting furosemide crystal stability by increasing the average C_F value ~2 times from 10-20 $e^-/\text{Å}^2\text{s}$.

Table 4.1 Mean C_F and standard deviation (\pm SD) of each measurement calculated from diffraction pattern data.

Accelerating voltage and type of support film	$d < 2\text{Å}$	$2 - 4\text{ Å}$	$4 - 6\text{ Å}$	$d > 6\text{ Å}$	Average critical fluence (C_F)
200 keV (holey-carbon film)	7 ± 2	9 ± 2	10 ± 4	15	9 ± 3
300 keV (holey-carbon film)	12 ± 4	14 ± 9	9 ± 3	10	10 ± 7
300 keV (continuous carbon film)	23 ± 4	21 ± 7	21 ± 10	23 ± 8	21 ± 8

4.4 Phase-Contrast Lattice Imaging

To achieve phase contrast lattice imaging of furosemide, it was important to control the cumulative electron fluence to be below the calculated C_F at 300 kV. Damage still occurs even below C_F and partial amorphisation can reduce the quality of the phase contrast image while low-dose/fluence conditions also affect the SNR in the image reducing the electron flux reduces the SNR in the image. Based on S'ari et al. (2020) initial lattice images of furosemide, the starting dose 'budget' for lattice imaging of furosemide form I was $<16-18 e^-/\text{Å}^2$. The key aspects to minimise pre-exposure of the area of interest to the electron beam irradiation were: (i) use ultra-low electron flux for searching the area of interest ($0.04 e^-/\text{Å}^2\text{s}$), (ii) acquire SAED and quickly adjust α/β tilt to tilt the sample close to a low index zone axis, (iii) focus the beam on a sacrificial

part of the crystal to be close to Scherzer defocus and (iv) keep beam blanked between each step.

One of the indicators of the presence of defects in a crystal structure is the presence of the disruption of Bragg contrast in a bright field image such as seen in the bend contour in the low magnification BF-TEM image of the furosemide crystal in Figure 4.5. Here, the particle is oriented to the $[\bar{2}31]$, and there is an interruption in the continuity and direction of the bend contour in the BF-TEM image (marked by red arrows in Figure 4.5a). This is a clear indication of the presence of defects e.g. dislocations (edge, screw or a mixture of both) (Pham et al., 2023).

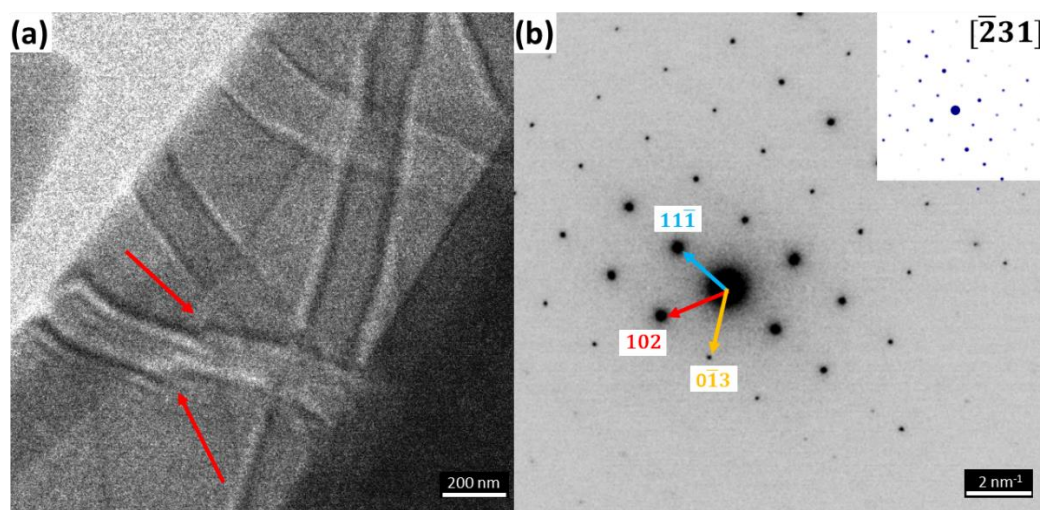


Figure 4.5 (a) BF-TEM image of furosemide form I particle and (b) SAED pattern of the region imaged in (a) indexed to $[\bar{2}31]$. Disruptions in the bend contour are marked by red arrows in (a).

One of the successful attempts for lattice imaging of furosemide form I is presented in Figure 4.6 (oriented to the $[\bar{4}32]$). Focussing of the beam was done in an area nearby but separate from the area to be imaged (Figure 4.6a, blue square). The FFT of the phase contrast lattice image shows visible spots resolving 0.46 nm d -spacing corresponding to the (102) lattice plane (Figure 4.6d). The total electron fluence used was $\sim 16 \text{ e}^-/\text{\AA}^2$.

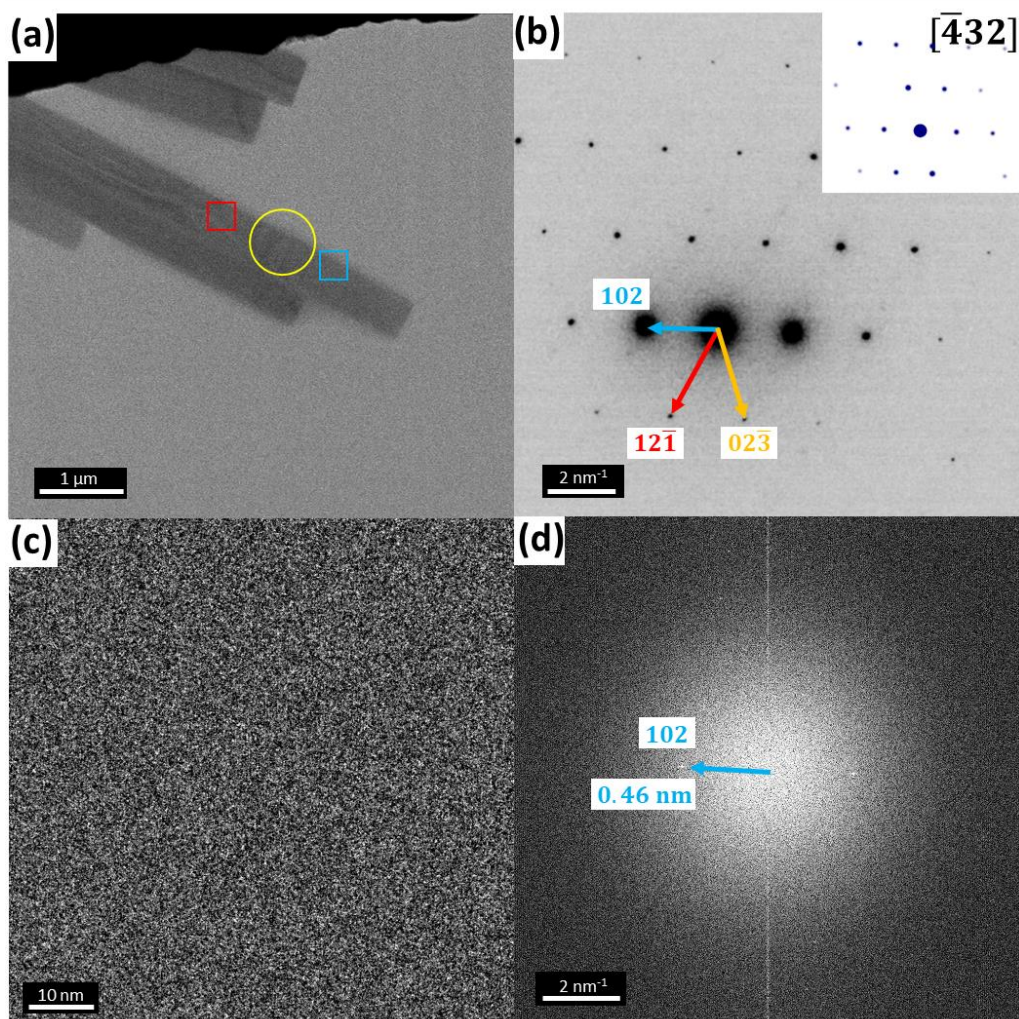


Figure 4.6 (a) BF-TEM image of furosemide form I crystals and (b) SAED indexed to $[\bar{4}32]$ and taken from the area marked by the yellow circle in (a). (c) cropped phase-contrast lattice image of the area marked by the red square in (a). The blue square in (a) indicates a sacrificed area for focusing. (d) FFT from the area in (c) showing 0.46 nm d -spacing indexed to (102) lattice plane.

The cropped phase contrast lattice fringes of furosemide form I from Figure 4.6c are further investigated in Figure 4.7. The lattice spacing of 0.46 nm can be seen in the raw image (just) and is marked by blue lines in Figure 4.7b. FFT from the cropped area shows the 0.46 nm lattice spacing more clearly, corresponding to the (102) lattice plane. The line profile from the yellow box in Figure 4.7b also confirms that the 0.46 nm d -spacings are present in the image.

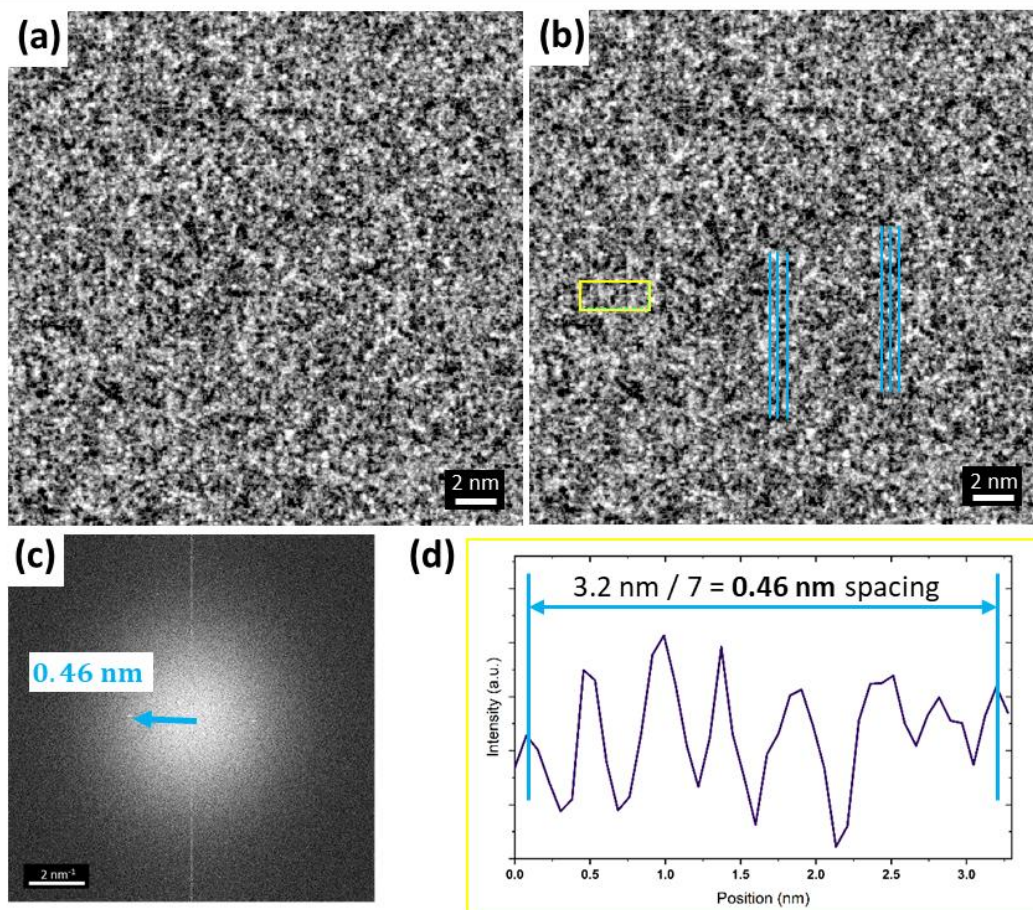


Figure 4.7 (a)-(b) Cropped raw phase-contrast lattice image from the area in Figure 4.6c. The lattice spacing of 0.46 nm is marked by blue lines in (b). (c) FFT from (a) show clearly 0.46 lattice spacing corresponding to (102) lattice plane. (d) line profile from the yellow box in (b) showing that the 0.46 nm *d*-spacings are present in the image.

Thus, it was possible to acquire a phase contrast lattice image of furosemide form I with a total electron fluence $\sim 16 \text{ e}^-/\text{\AA}^2$. However, the image is very noisy with poor contrast of the fringes because of the low fluence required to retain the structure i.e. low-dose phase contrast lattice imaging is not an efficient method for identifying defects due to low SNR and small sampling area. Therefore, further analysis will be performed using alternative methods of low-dose scanning transmission electron microscopy (STEM) techniques.

4.5 Scanning Electron Diffraction – General Defect Identification

The first low-dose STEM technique used to investigate furosemide form I crystals was scanning electron diffraction (SED), which can provide electron

diffraction and so crystallographic data from every image pixel and this allows the identification of potential defect sites. This result has been achieved using an electron fluence of $< 8 \text{ e}^-/\text{\AA}^2$ per SED scan compared to $\sim 16 \text{ e}^-/\text{\AA}^2$ used for lattice imaging.

Figure 4.8a shows an ADF-STEM image of a furosemide form I particle and the contrast (differences in the grey scale that may be related to thickness contrast) suggests that this particle may consist of more than one crystal. SED does indeed reveal two orientations from selected regions: (i) $\sim [\bar{2}01]$ – thicker part, with additional spots (marked by a red arrow) that suggest an underlying particle (Figure 4.8b) and (ii) $[301]$ – thinner part, that is a single crystal (Figure 4.8c). The 0.91 nm d -spacings corresponding to the (010) lattice plane are common for both orientations suggesting that the (010) is a common plane. Virtual dark-field (VDF) images were produced from disks marked by red circles in the average diffraction pattern for orientation (i) (inset in Figure 4.8d). The same procedure was used for yellow circles in the average diffraction pattern for orientation (ii) (inset in Figure 4.8e and f), except that VDFs were obtained in two ways: (a) by selecting the largest d -spacings (Figure 4.8e) and (b) by the exclusion of spots in the systematic row common to (i) and (ii) i.e. (010)/ $(0\bar{1}0)$ lattice planes to minimize the dominance of these planes in the VDF image (Figure 4.8f). The lower edge of the diffracting crystal from the region (i) can be indexed as (010) and corresponds to the upper edge of the diffracting crystal in orientation (ii), which can also be indexed as the (010) plane (Figure 4.8e vs Figure 4.8f respectively). For further inspection, the molecular arrangement and BFDH morphology prediction between these orientations was visualized in Figure 4.8g for orientations (i) and (ii). Figure 4.8h shows that the observed phenomenon may suggest the presence of a twin boundary, as there is a mirror symmetry between the two (i) and (ii) orientations. Twin boundaries are types of planar surface defects and were detected here across the (010) lattice plane. There are also line defects in the upper crystal, (i) orientation, as seen by the disruption to the bend contours in VDF Figure 4.8d and Figure 4.8e.

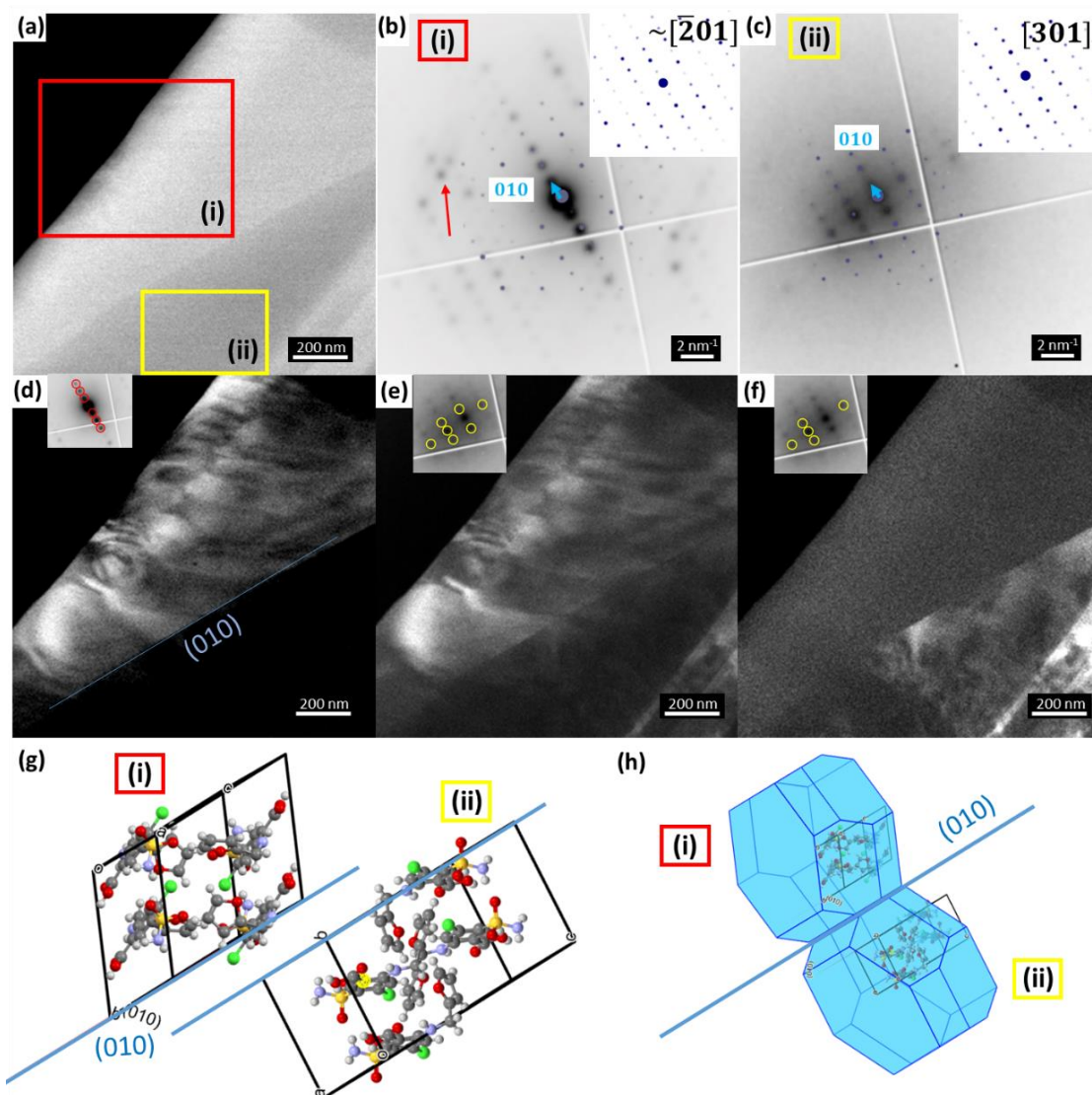


Figure 4.8 (a)-(c) ADF-STEM image of furosemide form I particle and SED reveals two orientations: (i) $[\bar{2}01]$ and (ii) $[301]$ from areas marked by red and yellow boxes in (a). (d) Virtual ADF-STEM images formed by plotting the intensity within the red disks from orientation (i). (e)-(f) Virtual ADF-STEM images formed by plotting the intensity within the yellow disks from orientation (ii), (f) Virtual ADF-STEM images formed by plotting the intensity within the yellow disks from orientation without (010) and $(0\bar{1}0)$ lattice planes. (g) molecular orientation between area (i) and (ii) revealing (010) common plane. (h) BFDH morphology orientation between area (i) and (ii) suggesting the presence of twin boundary (mirror symmetry).

A number of defects can be identified in the (i) orientation crystal in Figure 4.8 by generating additional VDF images formed by plotting the intensity within specific diffraction disks corresponding to particular lattice planes (Figure 4.9). There are clear displacements in bend contours across all VDFs. Moreover, a small circular distortion in bend contour can be observed particularly for VDFs

formed within disks corresponding to $(0\bar{1}0)$ and $(0\bar{2}0)$ lattice planes. Disruptions in the bend contour are marked by red lines and arrows, and the slip plane is marked by a blue line in the summed VDFs in Figure 4.9i. This finding suggests the presence of in-plane line defects running through the crystal as well as a twin boundary.

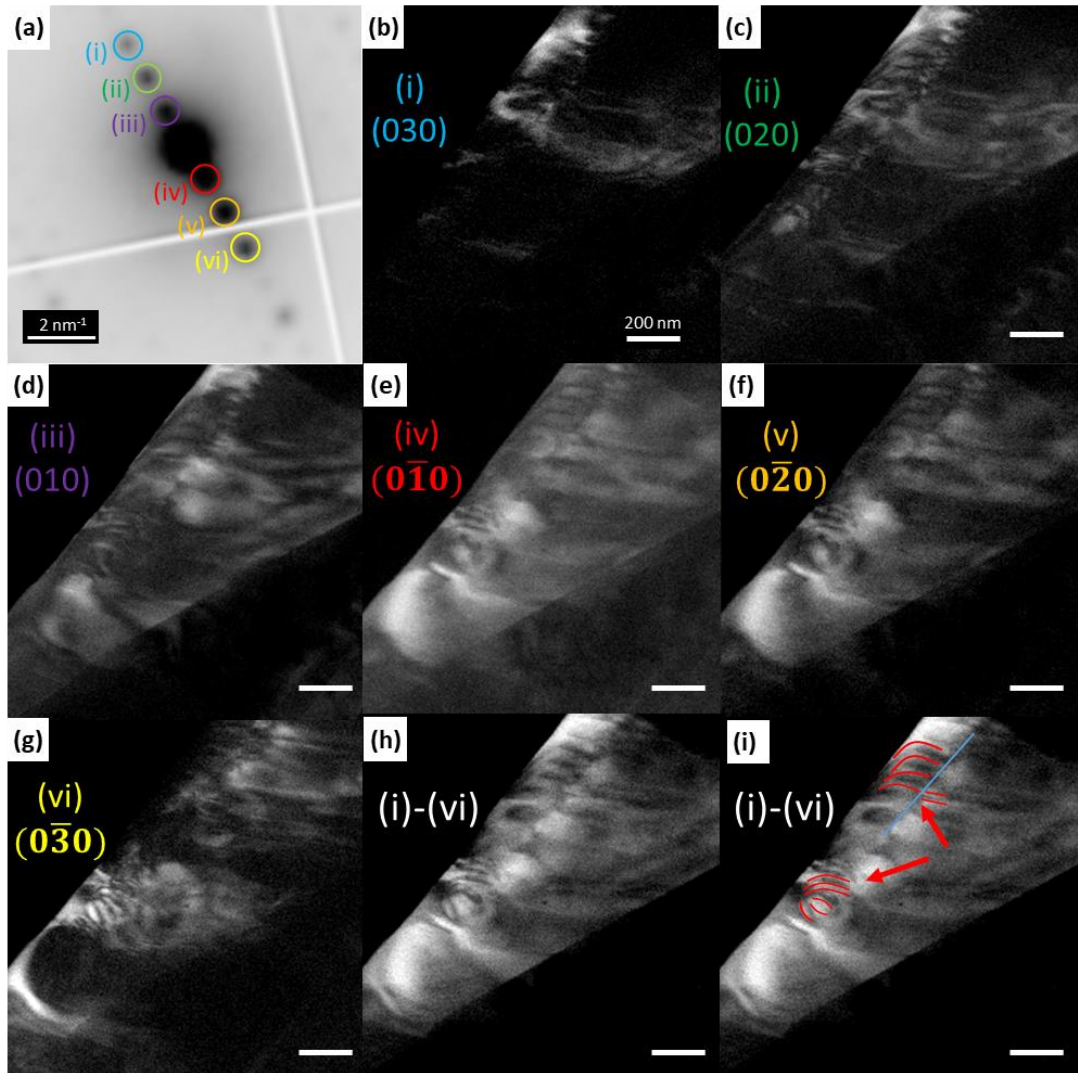


Figure 4.9 (a) SED pattern from the crystal area (i) in Figure 4.8a with marked diffraction disks and (b)-(f) Virtual DF-STEM images formed by plotting the intensity within the specific disks (i)-(vi) marked in the SED pattern as a function of probe position. Disruptions in the bend contour are marked by red lines and arrows. The slip plane is marked by a blue line.

4.6 Scanning Moiré Fringes and Attempts to Correlate Strain to Dissolution Rate

4.6.1 Standard Sample - Crocidolite

Crocidolite, one of six mineral forms of asbestos, has been selected as a standard sample for low-dose STEM and Scanning Moiré Fringe (SMF) tests as it is considered to be a beam-stable compound with similar d -spacing to furosemide ($a = 9.811 \text{ \AA}$ for crocidolite vs $a = 9.515 \text{ \AA}$ for furosemide form I).

Preliminary experiments using a phase contrast TEM method, at the University of Leeds, on crocidolite were performed in order to optimise the minimum conditions to directly observe a crystal lattice by TEM (S'ari et al., 2020). The set of images in Figure 4.10 highlights phase contrast images of crocidolite taken over a range of electron fluxes and fluences to resolve crystal lattice. The best results are obtained at $100 \text{ e}^-/\text{\AA}^2$ of electron fluence and $100 \text{ e}^-/\text{\AA}^2\text{s}$ of electron flux (Figure 4.10). It was possible to clearly resolve 8.9 \AA lattice spacing in the HR-TEM image which is confirmed in the inset FFT. However, this dose is too high to analyse furosemide and other beam-sensitive pharmaceutical as it would cause complete loss of the crystalline structure. One magnitude lower fluence value of $10 \text{ e}^-/\text{\AA}^2$ also shows 8.9 \AA lattice spacing in the FFT, nonetheless, this might not be sufficient signal-to-noise to resolve the crystal lattice clearly in the HRTEM image. At $1 \text{ e}^-/\text{\AA}^2\text{s}$ of electron flux, the lattice spacings are almost not possible to observe in the image. An electron fluence of ca. $10 \text{ e}^-/\text{\AA}^2$ and an electron flux of ca. $10 \text{ e}^-/\text{\AA}^2\text{s}$ are needed to detect 8.9 \AA lattice spacing. Initial direct imaging of the furosemide crystal lattice by phase contrast TEM has so far been achieved only once despite this analysis on crocidolite suggesting it may be possible (S'ari et al., 2020).

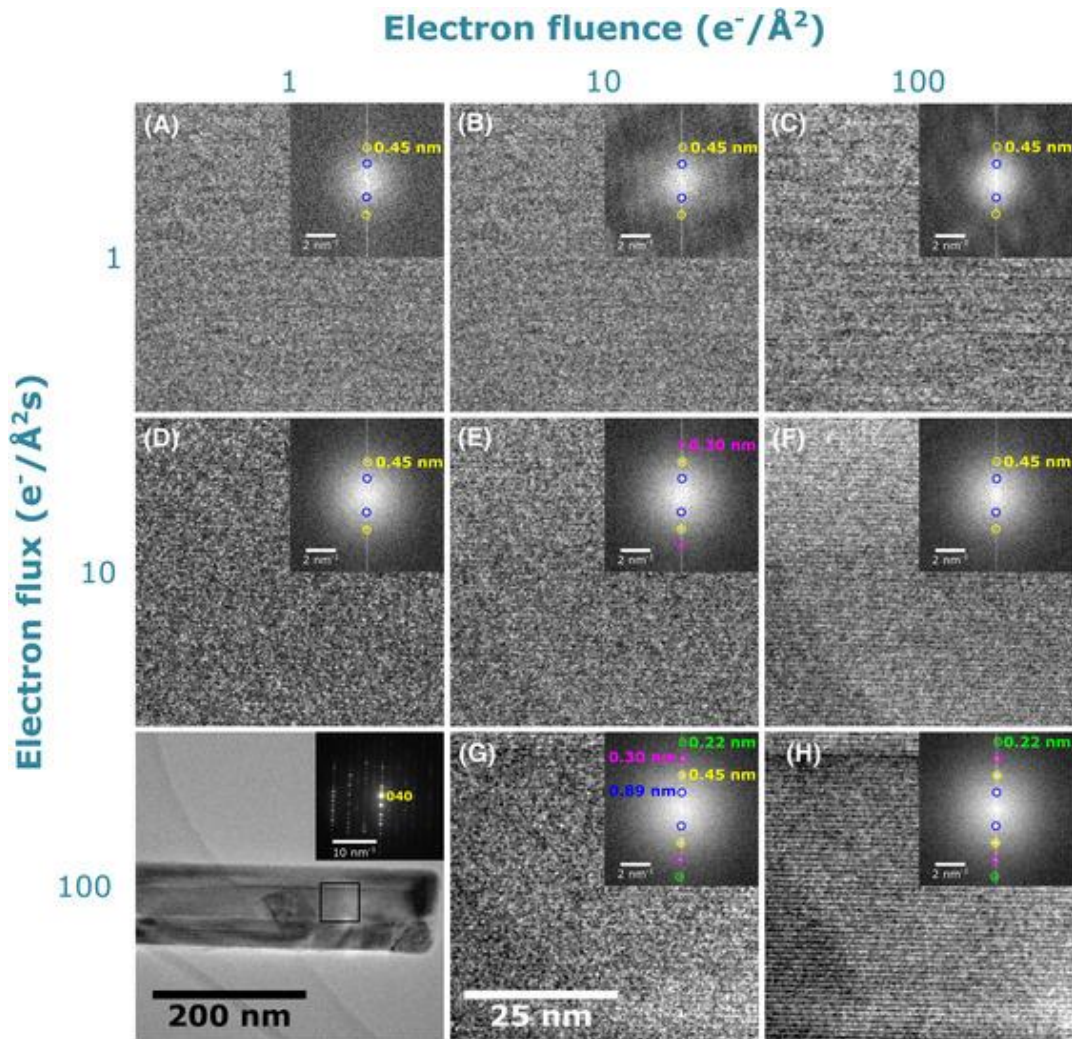


Figure 4.10 Table of phase contrast TEM images with inset FFTs taken over a range of electron fluxes and fluences. It was possible to resolve 8.9 Å spacing at an electron fluence of 10 e⁻/Å² with an electron flux of 10 e⁻/Å²s. Taken from S'ari et al. (2019).

Initial high magnification BF-STEM and BF-STEM SMF experiments were undertaken on crocidolite, which exhibits high electron beam stability in order to gain information on observed defects in the crystal lattice structure and the relationship between the corresponding BF-STEM direct lattice images at high magnification and BF-STEM SMF images at lower magnification from the same area. The SMF method is outlined in detail in the Materials and Methods section 3.5.2, and specifically, the angle β has to be close or equal to zero to observe translational SMFs (which are easy to interpret than SMFs with a rotational component), therefore the scan direction is rotated to align d_s (scanning lattice) to d_i (crystal lattice).

Figure 4.11 shows a high-magnification BF-STEM lattice image of the tip of an elongated crystal of crocidolite. The 0.86 nm d -spacings corresponding to the (020) lattice plane can be clearly resolved from the image and the FFT. The cropped image of the area marked by a red square in Figure 4.11a is presented in Figure 4.11c. Lattice defects i.e. line defects can be resolved in the raw image and these types of defects can have an impact on the size and direction of BF-STEM SMF.

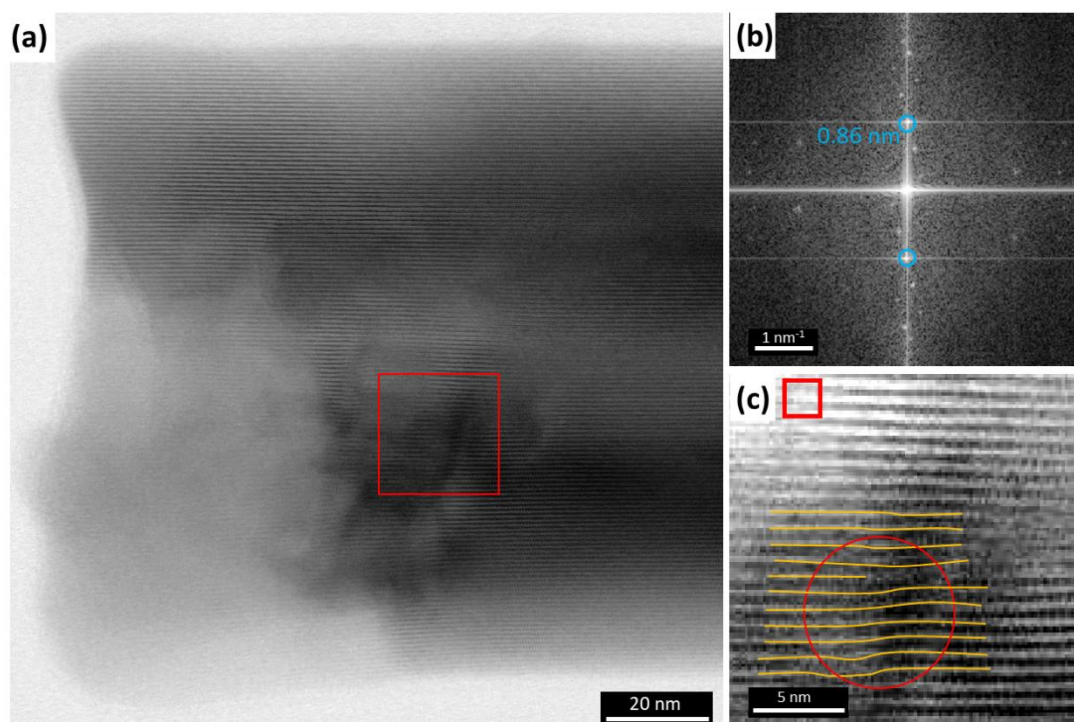


Figure 4.11 (a) High magnification BF-STEM lattice image of crocidolite and (b) corresponding FFT from the area (a) resolving 0.86 nm d -spacing and indexed as (020) lattice plane. (c) the cropped area marked by a red square in (a). The crystal lattice is marked by orange lines and a line defect is highlighted by a red circle.

Figure 4.12a shows the BF-STEM SMF image of crocidolite where magnification was chosen based on the criterion of a similar value of pixel size and atomic d -spacing (80 kX – pixel size 0.933 nm, closest value to the resolved d -spacing in Figure 4.11 of 0.86 nm). The theoretical size of translational moiré fringes as a function of STEM pixel size (d_s) was calculated using Equation 3.1 (see Chapter 3 Materials and Methods) to be 10.99 nm. This image shows SMFs that run slightly diagonal along the elongated particle and finally, the SMF changes direction and size. Two areas were selected for

further analysis: (i) the middle part of the particle (blue box) and (ii) the end part of the particle (red box). Figure 4.12b shows the FFT from the area (i). The average SMFs size measured from the FFT is 10.26 nm and shows good agreement with the predicted value of 10.99 nm. It should be added that the precise measurement of d -spacing from FFT or the correct probe size calibration is crucial e.g. the difference in measured spots from FFT that deviate by a small value of 0.05 nm (still within the error range of measurement) can change the size of SMFs by as much as 0.9 nm. Moreover, the angle between SMFs and scanning lattice deviates by $\phi = -4^\circ$ indicating that the relative angle β can be nonzero and/or small variations in the size or orientation of the (020) lattice plane can occur. In the next area (ii), the size of the SMFs varies in the range of 8.5 – 13.5 nm (Figure 4.12c). Moreover, there is a significant change in SMF direction from $\phi = -18^\circ$ to $\phi = +11^\circ$. This might be the indication of strains in the crystal, as line defects were previously detected in the high magnification BF-STEM from the tip area in Figure 4.11c. Defects can affect the average size and change the direction of the SM fringes. It should be noted that the BF-STEM SMF image was taken at an electron fluence of $7.2 \text{ e}^-/\text{\AA}^2$, while the high magnification BF-STEM image was at a 30 times higher value of $230.1 \text{ e}^-/\text{\AA}^2$. This means the SMF method could be a promising alternative to analysing lattice defects in beam-sensitive materials.

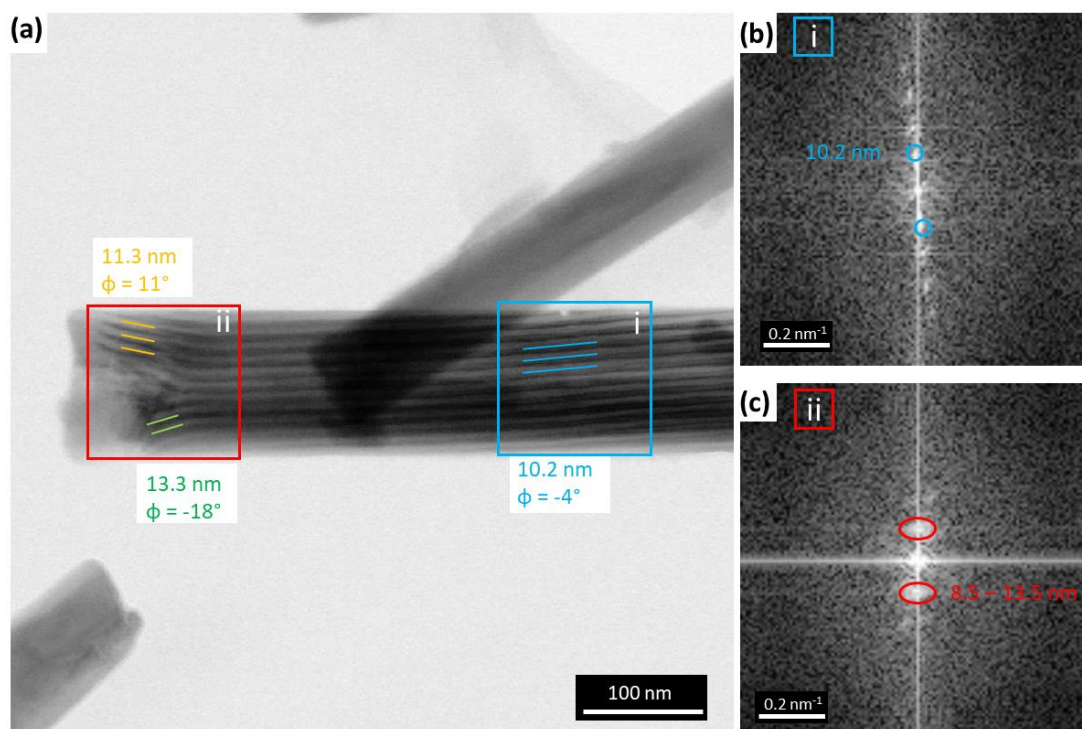


Figure 4.12 (a) Experimental BF-STEM SMFs of crocidolite with corresponding (b)-(c) FFTs from area (i) – blue square and area (ii) – red square. Variations in the size and ϕ of the SMF are labelled.

4.6.2 SMF of (001) Plane of Furosemide

A recent study reported that different faces of furosemide form I exhibit different dissolution rates and this can be related to the presence of surface pits and defects that enhance dissolution (Adobes-Vidal et al., 2016). One of the inspected lattice planes is (001) that have furanyl rings present at the surface and was found to have low surface energy and low dissolution rate (Adobes-Vidal et al., 2016). BF-STEM SMF images of furosemide form I crystals were acquired from selected areas exhibiting diffraction contrast confirmed by the corresponding SAED pattern (Figure 4.13). It was noticed that longitudinal crystals with smooth edges, even without strong diffraction contrast, present large atomic spacing i.e. (001) lattice planes terminate at these surfaces (Figure 4.13). The imaged area consists of two almost parallel and partially overlapping particles (Figure 4.13a). The lower edge of the bottom particle can be indexed to the (001) lattice plane. The upper edge of the top particle can also be indexed to the (001) or (00 $\bar{1}$), however, this edge lies at a slightly different angle compared to the bottom edge, which may result

in variation in the size and relative angle of any SMF acquired from this particle. The angle from the vertical of a selected (001) spacing was measured, which allows the calculation of the change in rotation needed to acquire translational moiré fringes.

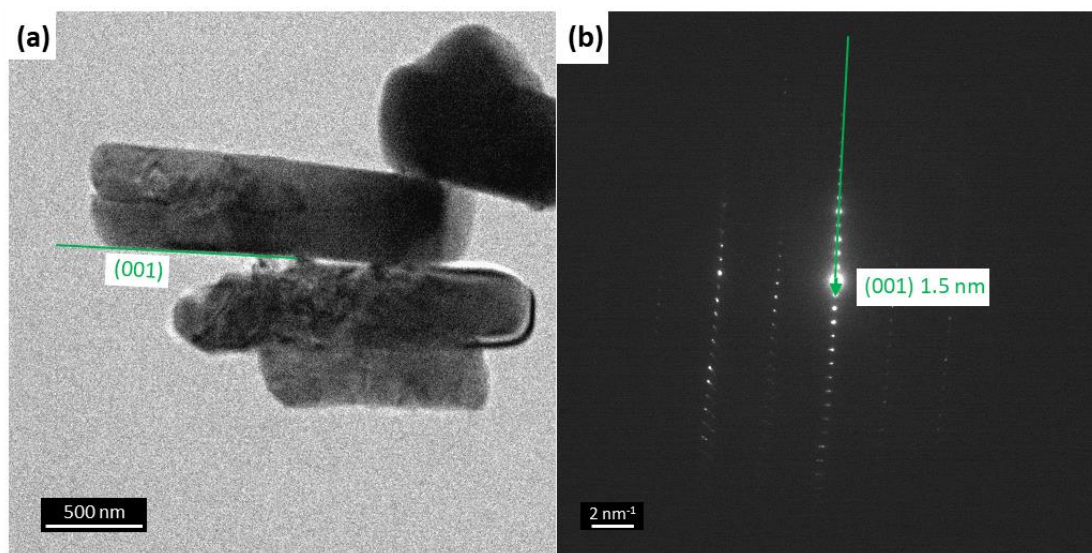


Figure 4.13 (a) BF-TEM image of longitudinal crystals of furosemide form I and (b) SAED pattern initially oriented close to [110] and exhibiting largest atomic spacing of 1.5 nm corresponding to (001) lattice plane.

Figure 4.14 shows a BF-STEM SMF lattice image of the middle crystal of furosemide form I in Figure 4.13a, this time collected at a STEM magnification of 57 kX providing a pixel size (d_s) of 1.32 nm which was closest in size to the first-order (001) diffraction spot of 1.5 nm in the furosemide oriented close to [110]. The total electron fluence used to acquire this image was $3.5 \text{ e}^-/\text{\AA}^2$, which is below the calculated critical fluence of furosemide at 300 kV, however, this does not include the time that the sample was exposed during analysis under TEM i.e. searching area exhibiting diffraction contrast, acquiring BF-TEM image and SAED pattern (estimated to be an additional $\sim 3 - 4 \text{ e}^-/\text{\AA}^2$, such that the total electron fluence remained well below C_F). The predicted value of the scanning moiré fringe spacing was calculated using Equation 3.1 for translational moirés (valid for the bottom particle) and was found to be 10.93 nm.

Three areas from Figure 4.14 were selected for further investigation: (i) the left side of the top particle (blue square), (ii) the area of partial overlapping of both particles (purple square) and (iii) the right side of the bottom particle (red square). The size of SMFs between areas does not vary significantly (range

of 9.5 – 10.5 Å) and is in good agreement with the predicted SMF value, especially the size of the SMFs in the area (iii), which is well aligned with the scan direction. However, the relative angle varies between areas (range $\phi = -22^\circ$ to $\phi = 4^\circ$). Variation in the direction of SMF in the area (i) may be due to this crystal not being well aligned with the scan rotation and the relative angle β being nonzero, however, there is no variation in the size of SMF within this area. Area (ii) contains the greatest variations in the direction of the SMF ($\phi = -18^\circ \div 0^\circ$) and this could be affected by the partial overlapping of two, non-parallel particles. In the cropped BF-STEM SMF image of the area (ii), a missing plane can be identified (example of a line defect). This may be related to, for example, the presence of strains due to an edge dislocation in the structure, or the presence of a grain boundary (although based on Figure 4.13a, the lower edge of the upper particle runs below the region of the line defect). In area (iii), which represents the bottom particle aligned with the scan direction, the size of the SMF remains constant, but the direction of SMFs shows a slight variation ($\phi = -4^\circ \div 4^\circ$), suggesting the presence of strains in the crystal.

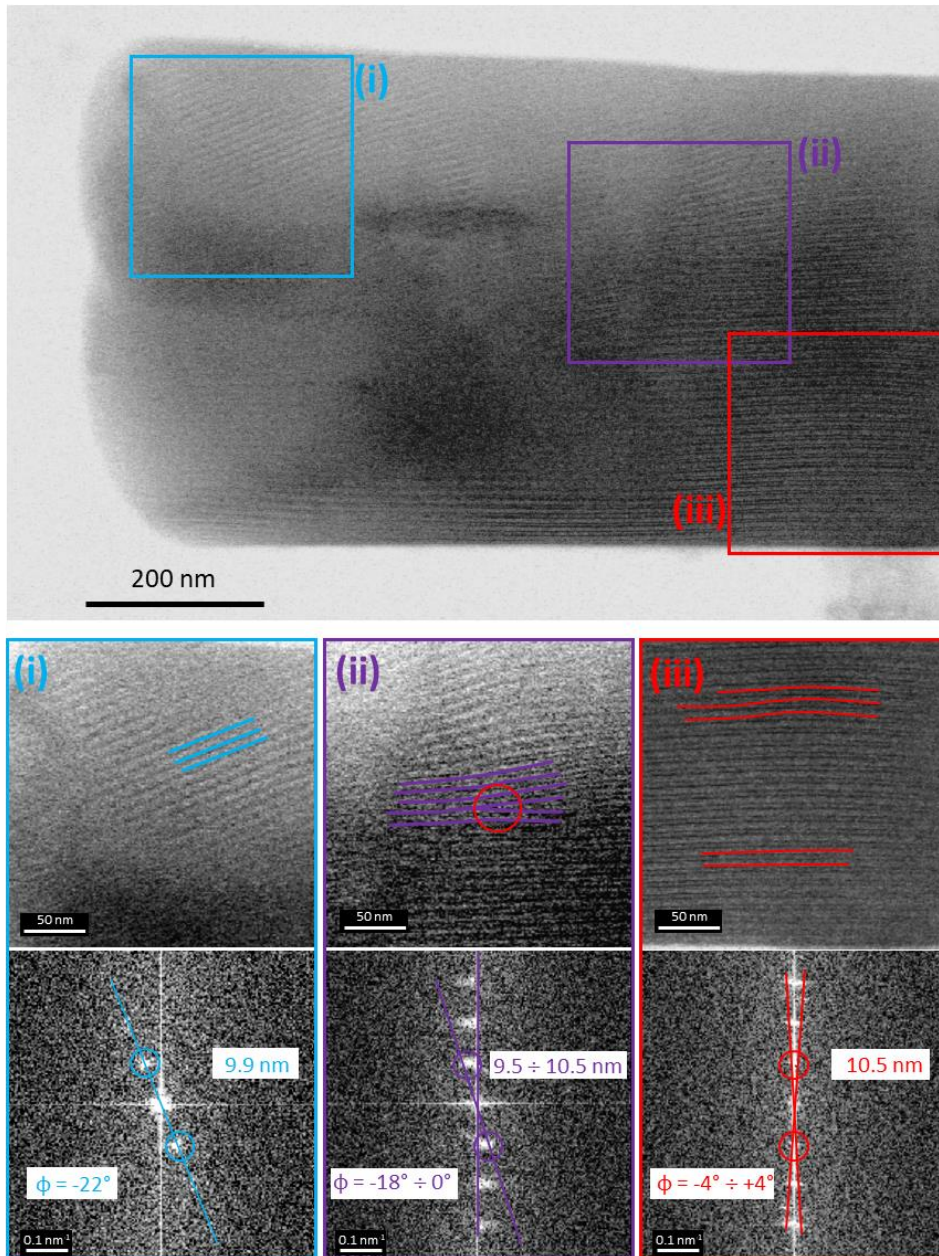


Figure 4.14 BF-STEM SMF image of the particle presented in Figure 4.13 with selected (i)-(iii) regions and corresponding FFTs. Variations in the size and ϕ of the SMF are labelled.

In general, in all analysed crystals oriented close to [110] and representing the largest (001) lattice spacing of furoseme form I, there were small variations in the size and direction of the SMFs. This may indicate that there is some degree of crystal defects in the (001) plane and/or it is related to the accuracy of the d -spacing measurement and scan alignment.

4.6.3 SMF of (010) Plane of Furosemide

In order to analyse another crystal plane i.e. (010) lattice plane, the sample was prepared by making a supersaturated solution with ethanol, which causes the furosemide form I crystals to grow in the [001] direction (Adobes-Vidal et al., 2016). Thus, the (010) lattice plane was more likely to be identified and analysed from the particles lying on a support film, however, it was also possible to find particles oriented to a specific zone axis that (010) can be identified by using the standard method without recrystallization from ethanol (crushed powder). The (010) lattice plane has aminosulfonyl and carboxyl groups present at the surface and was found to have higher attachment energy and higher dissolution rate than the (001) face (Adobes-Vidal et al., 2016).

Figure 4.15 shows a BF-TEM image of furosemide form I recrystallized from ethanol oriented close to [001] and exhibits atomic spacing of 0.96 nm that can be indexed to the closest d -spacing in furosemide form I of (010) lattice plane. The bottom part of the particle can be indexed to the (010) lattice plane. The imaged particle is considered to be a single crystal and no additional overlapping crystals are observed.

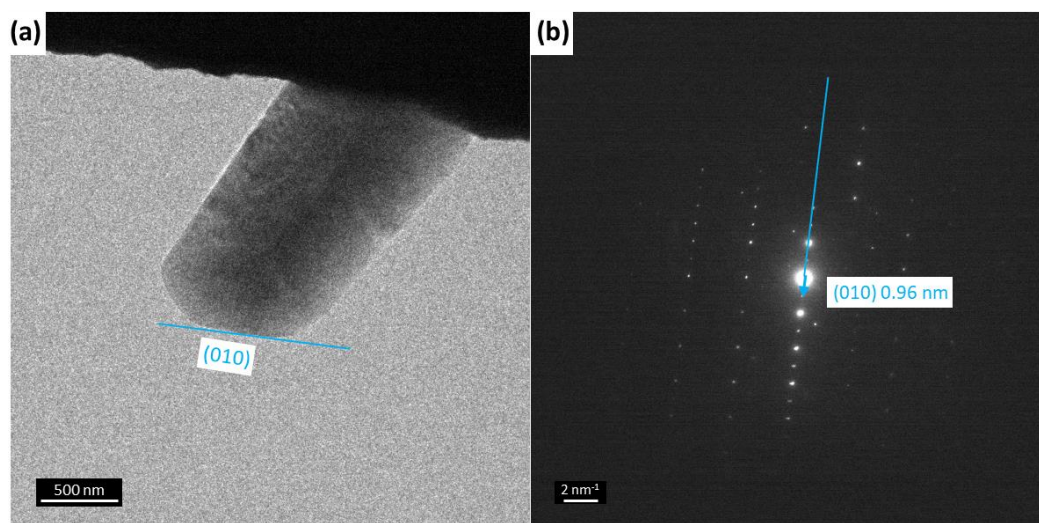


Figure 4.15 (a) BF-TEM image of furosemide form I recrystallized from ethanol and (b) SAED pattern initially oriented close to [001] and exhibiting different atomic spacing of 0.96 nm corresponding to (010) lattice plane.

The BF-STEM SMF lattice image of the same furosemide form I particle oriented close to [001] was collected at a STEM magnification of 80 kX providing a pixel size (d_s) of 0.933 nm and this was closest in size to the first-order diffraction spot at this orientation of 0.96 nm (Figure 4.16). The total electron fluence used to acquire this image was $7.2 \text{ e}^-/\text{\AA}^2$, which is also below the calculated critical fluence of furosemide at 300 kV (total electron fluence of $\sim 10 \text{ e}^-/\text{\AA}^2$ including BF-TEM mode acquisition). The predicted value of the scanning moiré fringe was calculated to be 33.2 nm whereas the measured value ranged from 11.8 to 21.1 nm. This difference may be due to the sensitivity of the predicted SMF value to the precision of the d_l measurement. A difference in measurement of d_l by e.g. 0.02 nm gives a predicted SMF of ~ 20 nm. Alternatively, a difference in rotation angle of 0.07° can reduce the resulting predicted SMF by ~ 18 nm.

The acquired BF-STEM SMF image presented in Figure 4.16 shows that there is a clear variation across the particle in the size and angle between the generated SMFs and so between the crystal and scanning lattice. Therefore, three areas from Figure 4.16 were selected for further investigation: (i) the inner part of the particle (blue square), (ii) the bottom edge of the particle (purple square) and (iii) the right side of the particle (red square). The range of the measured SMF values within these areas fluctuates between 11.8 and 21.1 nm. None of these values are close to the predicted SMF value of 33.2 nm. As mentioned earlier, small differences in d_l or rotational angle measurements have a significant impact on the size of the measured SMF. If measurement accuracy were the main factor in the discrepancy between the size of the experimental and predicted SMF, then the SMF size would be roughly uniform throughout the imaged area. That the SMFs are not uniform suggests the influence of additional factors i.e. that this area is highly strained and contains a number of defects. Areas (ii) and (iii), representing the part of the particle close to the (010) edge, have the greatest discrepancies in the direction and the size of the SMF.

Moreover, the relative angle varies between areas in the range of $\phi = 15^\circ \div 64^\circ$. Area (i), which represents the inner part of the particle, has the smallest fluctuation in relative angle ($\phi = 41^\circ \div 64^\circ$) compared to the other selected

areas, and at the same time has the largest value of the SMF size (closest to the predicted SMF).

Variation in the direction of SMF in the area (i) may be due to this crystal not being well aligned with the scan rotation and the relative angle β being nonzero, however, there is no variation in the size of SMF within this area. In addition, defect sites can be identified within these areas (blue, purple and red lines in panel b of Figure 4.16. These results suggest that (010) planes of the particle are highly strained and that the number of defects is increasing closer to the (010) edge of the particle.

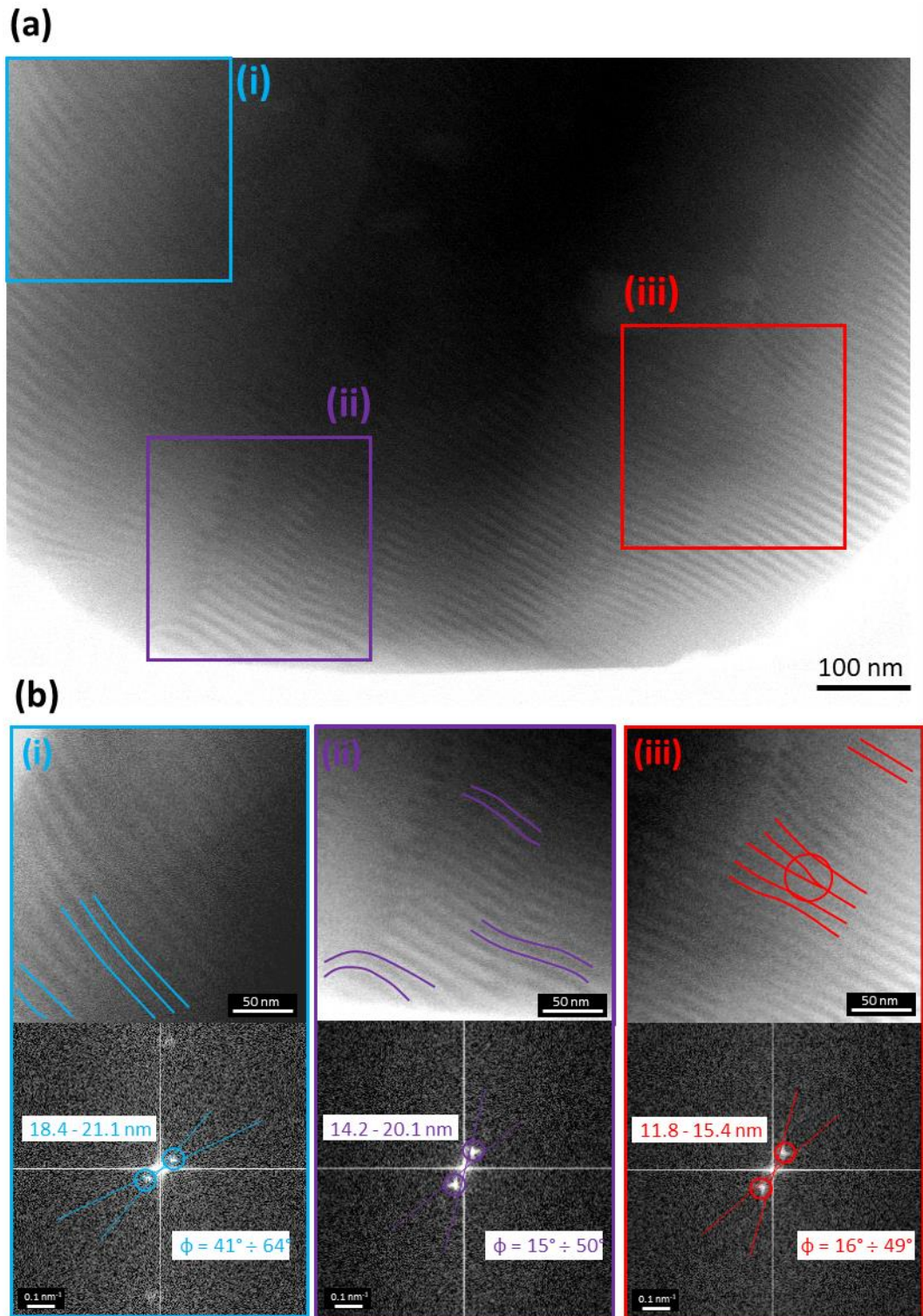


Figure 4.16 (a) BF-STEM SMF image of the particle presented in Figure 4.15 with (b) selected (i)-(iii) regions and corresponding FFTs. Variations in the size and ϕ of the SMF are labelled.

Subsequent attempts to analyse the (010) lattice plane from other particles showed a similar trend. In each case, variations in the size and direction of the SMFs were observed, with simultaneous identification of distorted sites.

4.6.4 Summary

All results from the measurement of the observed (measured) SMF of the (001) and (010) lattice planes of furosemide are summarized in Figure 4.17. The green circles represent the average/most frequent value of the measured SMF of the (001) lattice plane, while the blue triangles represent the average/most frequent value of the measured SMF of the (010) lattice plane. The spread in the measured SMF values (range of min and max values) within one dataset is represented by vertical lines. The Pearson correlation coefficient (r) between the predicted SMF value and the observed SMF value was measured for each group: (001) and (010) lattice plane in order to explore the potential linear relationship between two variables. The Pearson's r value for (001) was calculated to be -0.93 suggesting a strong correlation between the predicted SMF and the observed SMF value. Moreover, a negative value of r indicates that as the predicted SMF value increases, the measured SMF decreases. However, the predicted values of SMF are clustered and there is a marginal spread in the measured SMF values.

A different trend is observed for the (010) lattice plane. The measured Pearson's correlation coefficient for the (010) of -0.24 is considered to be a negligible or weak correlation. Moreover, there is a significant spread between the maximum and minimum values of measured SMF for the individual datasets. As mentioned earlier, the size of SMF is very sensitive to the accuracy of d -spacing measurement and precise rotation angle calculation (particularly for small differences between d_s and d_l). Taking into account the same methodology used to obtain BF-STEM SMF images for the (001) and (010) lattice plane, the lack of correlation and a large spread of the measured SMF values for the (010) lattice plane indicates the disruption or strain to the crystal lattice due to the presence of a number of defects.

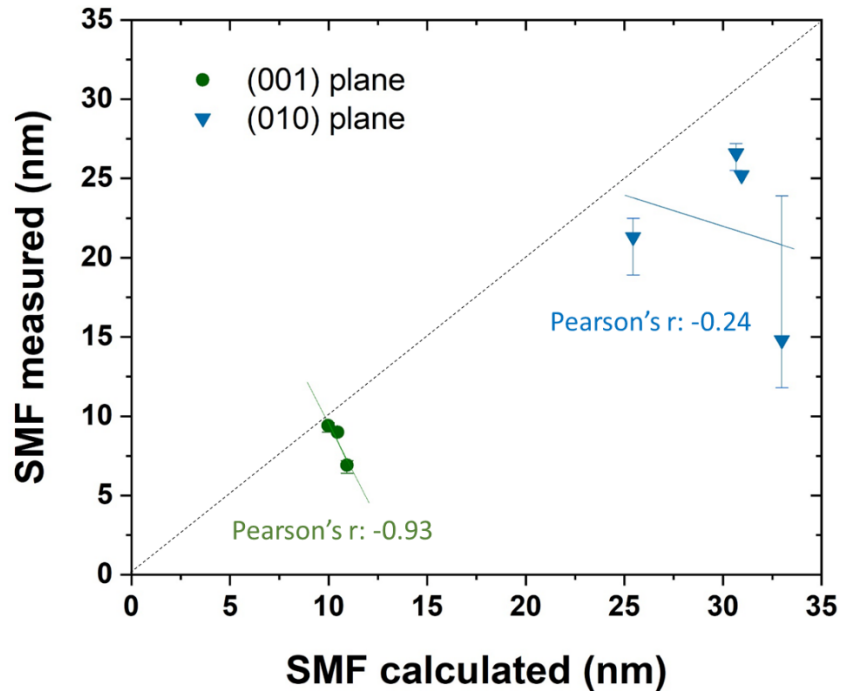


Figure 4.17 Correlation between predicted (calculated) and measured value of SMFs.

The overall results were compared to the corresponding crystal face profile and the rate of crystal face dissolution for furosemide recently reported by Adobes-Vidal et al. (2016) (Figure 4.18). Each crystal face has different surface energetics which affects the dissolution rate. The (001) crystal face has the lowest energetics associated with the presence of furanyl rings and the absence of hydrogen bonds, therefore strong interplanar interactions. It has a low-value dissolution rate compared to other furosemide planes. Some strains are observed within the (001) lattice by SMF, which indicates the presence of a few defects in this orientation. In contrast, the (010) crystal face has higher energetics related to the amino sulfonyl groups forming a hydrogen bonding network, therefore it has a higher dissolution rate than (001). The corresponding SMF shows that (010) crystal face is highly strained and might indicate a higher number of defects in the crystal structure that would enhance the dissolution rate. Moreover, the SED findings from the (010) plane also suggest the presence of a number of defects (Figure 4.9). The order of observed strains in SMF images is consistent with the dissolution rate differences as well as with the hydrogen bonding model, which is (001) < (010).

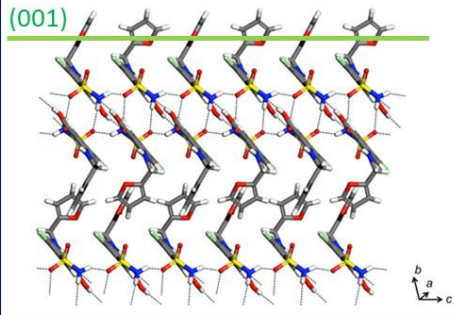
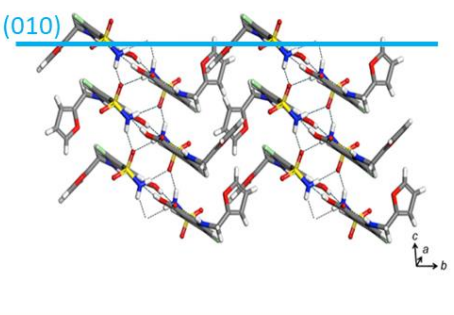
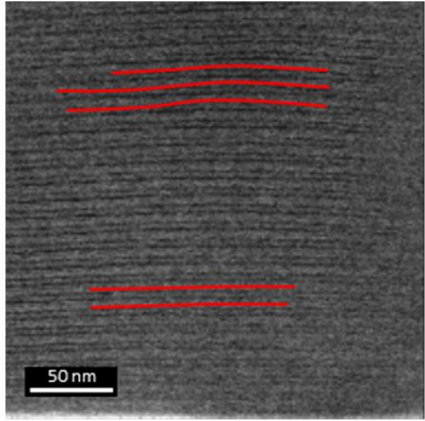
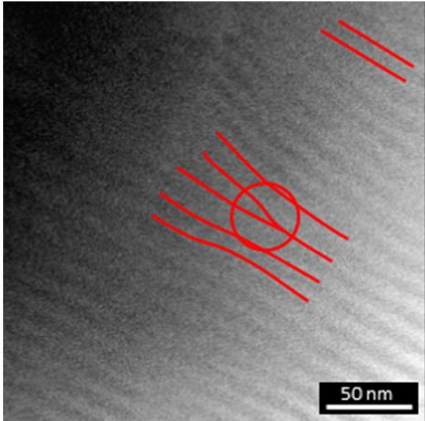
	(001) plane	(010) plane
Lattice profile		
Rate of dissolution	$(2.8 \pm 1.4) \times 10^{-6}$ (mol m ⁻¹ s ⁻¹)	$(12.6 \pm 6.9) \times 10^{-6}$ (mol m ⁻¹ s ⁻¹)
Scanning Moiré Fringes	 <p> Δ SMF: ~ 2 nm Δ ϕ: 26° </p>	 <p> Δ SMF: ~ 10 nm Δ ϕ: 49° </p>

Figure 4.18 Comparison of the corresponding crystal faces to the values of the dissolution rate from Adobes-Vidal et al. (2016) and the observed variations. Δ of SMF spacing and orientation in images of the (001) and (010) furosemide form 1 lattice planes.

Overall, BF-STEM SMF images can be acquired at a very low total electron fluence of $\sim 4\text{-}7 \text{ e}^-/\text{\AA}^2$, while high-resolution BF-STEM image require at least 30 times higher electron dose value of $\sim 230 \text{ e}^-/\text{\AA}^2$. This means the SMF method could be a promising alternative to conventional TEM and STEM for analysing lattice defects in beam-sensitive materials. Further work is needed to ultimately quantify the obtained data.

4.7 Chapter Summary

The study presented in this chapter aimed to demonstrate the possibilities to use low-dose scanning transmission electron microscopy techniques to acquire indirect lattice images and to inspect defects in the crystal structure of furosemide form I.

The calculated critical fluence of furosemide form I at 300 kV and using continuous carbon film was measured to be $21 \pm 8 \text{ e}^-/\text{\AA}^2$ and it is ~ 2 times larger than the critical fluence measured at 200 keV on holey-carbon film. The higher accelerating voltage and the relevant type of the TEM support film are both important factors affecting furosemide crystal stability. The available dose budget is, however, not sufficient to acquire a high-quality, low SNR lattice image of furosemide form I by conventional TEM on the microscopes at Leeds.

Standard transmission electron microscopy techniques, e.g. phase-contrast lattice image, require a high electron dose to obtain a suitable SNR in the image for analysis e.g. defects. It was possible to acquire a BF-TEM lattice image of furosemide form I with a total electron fluence $\sim 16 \text{ e}^-/\text{\AA}^2$, however, the low SNR and small sampling area make the interpretation of results subject to major uncertainty.

The low-dose STEM techniques are demonstrated to be an alternative method to analyse the crystal structure of furosemide form I and require a total electron fluence $< 10 \text{ e}^-/\text{\AA}^2$, well below the calculated C_F .

The scanning electron diffraction method was successfully applied to identify disruption in bend contours. This finding suggests the presence of defects in furosemide form I (in particular the (010) lattice plane). Moreover, by analysing structural information from a small volume, it was possible to identify the orientation of individual grains and locate a potential twin boundary that could not be detected using conventional TEM.

BF-STEM scanning moiré fringes were successfully applied to acquire indirect lattice images of furosemide form I in order to inspect two lattice planes, the (001) and (010), known to exhibit different dissolution rates. Some strains are observed within the (001) lattice by SMF, which indicates the presence of a

few defects in this orientation. In contrast, the (010) crystal lattice is highly strained (also confirmed by SED) and this suggests a higher number of defects in the crystal structure. The magnitude of observed disruption in BF-STEM SMFs images is consistent with the difference in dissolution rates as well as with the hydrogen bonding model, which is (001) has a lower dissolution rate than (010) (Adobes-Vidal et al., 2016).

Low-dose STEM techniques are demonstrated here to be a useful complementary method to detect strained faces of furosemide form I and to correlate the results between computational modelling and analysis at the single particle level. Analysis at this scale can contribute to understanding crystal dissolution kinetics and might enable the prediction of the effect of defects during sample preparation or storage. Moreover, the low-dose STEM techniques can be applied to other beam-sensitive materials. Further work will require the development of a methodology for the quantification of defects and the first steps of this are reported in Pham et al. (2023).

Chapter 5 Investigation of Microporous Structure of Sodium Zirconium Cyclosilicate Hydrate

In this chapter, a study of the microporous structure of a highly selective inorganic cation-exchanger, sodium zirconium cyclosilicate hydrate, laboratory synthesized sample is presented. The samples supplied by AstraZeneca as part of this study were taken from development batches manufactured in laboratory conditions not consistent with the commercial manufacturing method. Therefore, any conclusions drawn based on these samples cannot be considered directly transferable to the commercially produced product.

Crystalline sodium zirconium cyclosilicate hydrate has an atomic structure incorporating wide ion channels of $\sim 3 \text{ \AA}$ and substantial micropore volume and has the potential for modification by partial protonation to vary its $\text{Na}^+ - \text{H}^+$ ratio and enhance potassium binding in solution. Two test samples with different $\text{Na}^+ - \text{H}^+$ ratios were investigated: AZ1 (small fraction of sodium cations exchanged for hydrogen) and AZ1-2 (larger fraction of sodium cations exchanged for hydrogen). This study aims to investigate the crystal structure, morphology, identify any micro-strains and investigate the distribution of Na^+ within crystals of AZ1 and AZ1-2 using transmission electron microscopy techniques. pXRD was also used as a “bulk” method to provide complementary analysis of crystallinity and the crystal phases of samples.

5.1 Commercial Product Background

A patented preparation of sodium zirconium cyclosilicate hydrate (Lokelma) is an orally administered, non-absorbed, highly selective potassium binder used for the treatment of hyperkalaemia (Rafique et al., 2015). Hyperkalaemia is a common electrolyte abnormality in which serum potassium ions (K^+) exceed >5.0 mmol/L and occurs in people with diabetes mellitus, chronic kidney disease and heart failure (Linder et al., 2016; Skoyles et al., 2017). Current management of hyperkalaemia is limited because, until 2015, only organic polymer resins such as sodium polystyrene sulfonate (SPS) have been used in therapy. In 2015, two new drugs: Patiromer and Lokelma were reported (Linder et al., 2016; Skoyles et al., 2017). Stavros et al. (2014) characterised the selectivity for K^+ ions by a multi-ion exchange study and found that Lokelma was 125-fold more selective compared to SPS, suggesting an improved ability to lower potassium levels with Lokelma (1 hour in comparison to 2 hours in SPS) (Linder et al., 2016; Stavros et al., 2014). Therefore, Lokelma is a promising and available drug for the treatment of people experiencing hyperkalaemia.

The chemical name of the active substance is hydrogen sodium zirconium (IV) silicate hydrate, with an empirical formula of $Na_2ZrSi_3O_9 \cdot 2-3H_2O$ (European Medicines Agency, 2018). The finished product is a white crystalline powder containing the active substance only, made with a specific particle size distribution profile above $3 \mu m$ in length (Keyser, 2015) and classed as a cubic crystal system (point group $Pa\bar{3}$) with an unit cell lattice parameter of 12.7 \AA . The three-dimensional sodium zirconium cyclosilicate hydrate framework is composed of zirconium, Zr, in octahedral and silicon, Si, in tetrahedral oxygen-coordination units (in a 1:3 ratio) that interconnect through Zr-O-Si and Si-O-Si oxygen bridges (Figure 5.1). This results in regular, non-linear microporosity of cation-binding pores (Stavros et al., 2014). Microporous compositions can incorporate positive ions (sodium, Na^+ , and hydrogen, H^+), which act as exchangeable counter cations and provide electrical neutrality to the structure to balance the negative charge from the octahedral fractions of $[ZrO_6]^{2-}$ (Linder et al., 2016).

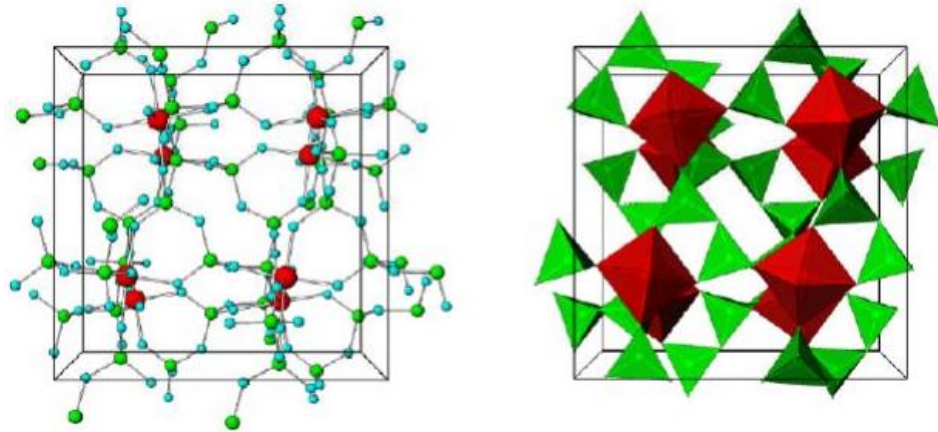


Figure 5.1 Stick-and-ball (left) and polyhedral (right) unit cell structural model of the microporous sodium zirconium cyclosilicate hydrate. Red = zirconium, green = silicon, blue = oxygen atoms. Counter cations (Na^+ and H^+). Taken from European Medicines Agency (2018).

The specific opening pore diameter of $\sim 3 \text{ \AA}$ allows preferential trapping of monovalent cations when crystals are present throughout the gastrointestinal (GI) tract, specifically excess potassium K^+ ions and ammonium ions, which have similar unhydrated ionic diameters (Figure 5.2) (Stavros et al., 2014). It is considered that sodium zirconium cyclosilicate hydrate uses a negatively charged selectivity filter similar to that of physiologic K^+ channels in cellular membranes to effectively select and trap K^+ ions (Figure 5.3). In order to pass through this selectivity filter, an ion must first shed its hydration shell to interact with the carbonyl-bonded oxygens at the pore entrance. The unhydrated ionic diameter of potassium K^+ ions of 2.98 \AA and is of sufficient size to interact effectively with the ion channel carbonyl bonded oxygens (Stavros et al., 2014). However, this process is irreversible, as the energy to dehydrate the K^+ is balanced by the energy of interaction with the oxygen atoms (Stavros et al., 2014). Other cations, i.e. Na^+ and Ca^{2+} , have larger hydrated ionic diameters, therefore require more energy to shed their hydration shell than K^+ . As shown in Figure 5.3, an unhydrated Na^+ ion is too small to interact effectively with the oxygen cages, thus making it energetically unfavourable for it to pass through the filter (Stavros et al., 2014). Therefore, the high specificity of appropriately processed sodium zirconium cyclosilicate hydrate to entrap K^+ is related to the size and possibly the chemical configuration of the micro-pores (European Medicines Agency, 2018).

Cation	Unhydrated Ionic Diameter (Å)	Hydrated Ionic Diameter (Å)
H ₃ O ⁺	2.30	5.60
K ⁺	2.98	6.62
NH ₄ ⁺	2.96	6.62
Na ⁺	2.34	7.16
Ca ²⁺	2.00	8.24
Mg ²⁺	1.44	8.56
Zn ²⁺	1.48	8.60

Figure 5.2 Diameters (Å) of monovalent and divalent cations (both unhydrated and hydrated). Taken from Stavros et al. (2014).

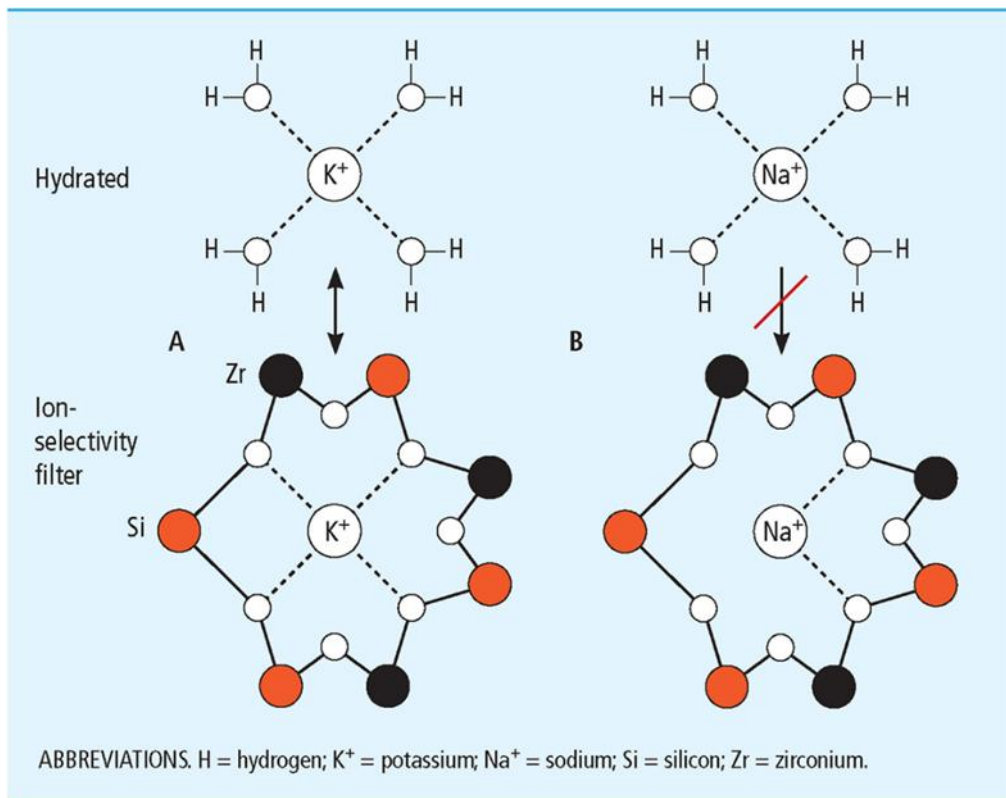


Figure 5.3 Mechanism of ion exchange system in sodium zirconium cyclosilicate hydrate. Potassium K⁺ ions are preferentially trapped in pores due to the size of the pore matching the unhydrated ion diameter. Other cations, e.g. Na⁺, have smaller unhydrated diameters, therefore, require more energy to shed their hydration shell than K⁺ and this action is energetically unfavourable. Taken from Skoyles et al. (2017).

Sodium zirconium cyclosilicate hydrate has been shown to reduce serum potassium concentration, its unique structural properties, especially wide channels and substantial micro-pore volume allow potential chemical composition modifications by partial protonation to varying degrees (i.e. altering Na^+/H^+ ratios). Structural modification of sodium zirconium cyclosilicate hydrate can lead to the development of a novel agent with equivalent efficacy or even increased potassium exchange capacity upon protonation. This allows to achieve of desirable clinical outcomes for a specific target group of patients, for example, avoiding an undesirable increase of pH and excessive release of sodium in a patient's body after administration which is particularly important for patients at risk for congestive heart failure (Keyser, 2015).

Transmission electron microscopy with a combination of spectroscopy techniques can characterise these modified products at the single particle level in order to investigate the crystal structure, morphology, micro-strains and the distribution of Na^+ within laboratory synthesized samples provided by AstraZeneca (AZ1 and AZ1-2).

5.2 Materials and Methods

5.2.1 Sample Preparation

Two test samples with different Na^+/H^+ ratios were prepared by laboratory synthesis and supplied by AstraZeneca, Macclesfield. These samples will be referred to as: (i) AZ1 (a small fraction of sodium cations exchanged for hydrogen) and (ii) AZ1-2 (a larger fraction of sodium cations exchanged for hydrogen) in this chapter.

Albite, a mineral sample, was provided by Dr Richard Walshaw (School of Earth and Environment, University of Leeds).

A grinding method was used to prepare the samples for TEM analysis. AZ1/AZ1-2 crystals were lightly crushed in a pestle and mortar and two methods were used: (i) a few drops of ethanol were added, then the solutions were pipetted onto a TEM grid and allowed to evaporate, and (ii) dry, ground powder was carefully transferred directly onto a TEM grid. Two types of TEM

grids were used: (i) holey-carbon films on 400 mesh copper and (ii) continuous carbon film.

5.2.2 (S)TEM Operating Condition

For initial imaging and diffraction collection, all TEM analyses were carried out using bright-field (BF) mode with a 40 μm objective aperture and a 1-second exposure time for the camera. A monochromator was used to control beam intensity in order to achieve the desired observational signal and appropriate value of an electron fluence in the range of $0.08 - 2 \text{ e}^-/\text{\AA}^2$.

Scanning transmission electron microscopy characterisation was carried out using a 10 mrad convergence semi-angle for the probe (giving a resolution of 0.14 nm in HAADF STEM at probe currents of 70 pA) and a 5.5 mrad collection angle for the bright field detector. The probe current was reduced by using the monochromator focusing lens in order to achieve the desired electron fluence (typically set to 5 pA for imaging). The pixel dwell times (t) were set as 10-20 μs .

STEM-EDX was undertaken using a probe current of 5 pA and a 20 μs dwell time and the magnification was limited to 57 - 80 kX giving a total accumulated fluence of 60-115 $\text{e}^-/\text{\AA}^2$ per pixel for each acquired scan.

Both, the double-tilt holder and cryo-transfer holder were used for STEM-EDX acquisition.

5.2.3 SEM and FIB

The powder samples were coated with iridium for SEM imaging to reduce charging effects and images were acquired at different magnifications for morphology and particle size distribution analysis. Thin FIB-TEM lamella of AZ1 and AZ1-2 were prepared in a standard and cryo condition using a FEI Helios G4 CX DualBeam microscope. This process is summarised in Figure 5.4. After rough-cutting thick lamella ($\sim 1.5 \mu\text{m}$) in-situ, they were lifted out and attached to a specific TEM grid via platinum (Pt) deposition. Two windows of 4-5 μm width were further thinned down to electron transparency (thickness varies between 60 – 110 nm). 2-3 μm thick areas were kept in order to ensure the stability of the sample. The ion current was reduced to 3 nA to prevent damage to the sample.

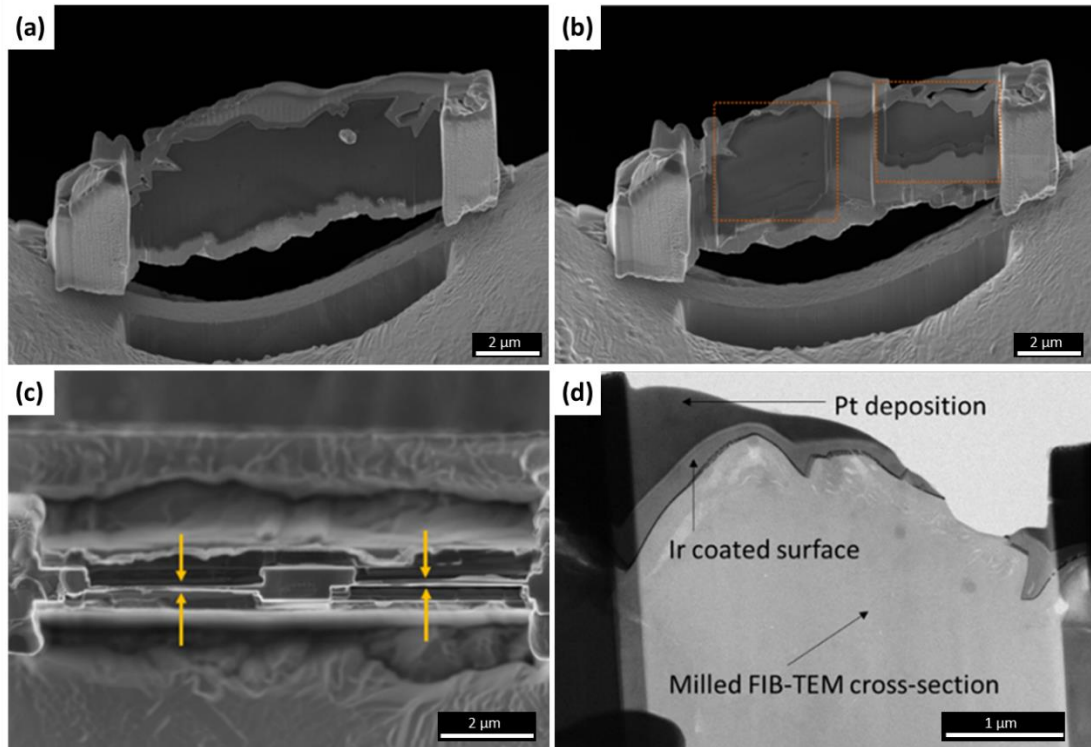


Figure 5.4 Preparation of FIB-TEM lamella: (a) thick lamella attached to the TEM grid via Pt deposition, (b) two windows were further milled until a desired thickness was reached i.e. (c) usually below 100 nm (marked by orange arrows), (d) BF-TEM of the fabricated lamella.

5.2.4 Data Analysis

BF-TEM micrographs and diffraction patterns were acquired and further processed using Digital Micrograph (Gatan Microscopy Suite). Particle size distributions (PSDs) were performed in ImageJ using the 'freehand selection' tool and manually selected representative particles. A number of shape and size descriptors were chosen for PSD measurement:

- Minimum and maximum Feret diameter (d_{\min} and d_{\max}) - the shortest and the longest distance between any two points along the selection boundary of a particle
- Area - an area of the selection boundary of a particle
- Perimeter - the length of the outside boundary of the selection boundary of a particle

- Aspect ratio (AR) - describes the ratio of the longest distance between any two points of a particle (d_{\max}) and the longest distance between any two points of a particle perpendicular to this distance (d_{\min})
- Roundness (R) - a measure of how closely a projected image of a particle resembles a circle and has a value between 0 and 1, a perfect circular particle projection would result in an R equal to 1 (the formula is $4\text{Area}/\pi d_{\max}^2$)
- Solidity (S) - solidity is the area of a particle divided by its convex hull area and provides information about properties such as surface roughness.

BF-STEM, HAADF-STEM and STEM-EDX were acquired and further processed using Velox Software (Thermo Scientific).

CrystalMaker Package and Mercury (v. 2022.2.0) were used for structure simulation and indexing SAED patterns.

5.3 Chemical Composition Modifications and Pore Structure Investigation of Test Samples

5.3.1 Provision of Test Samples and Powder XRD

Powder X-ray Diffraction (pXRD) of AZ1 and AZ1-2 was performed at AstraZeneca in order to account for any changes in crystalline structure during the protonation process. The experimental pXRD patterns of AZ1 and AZ1-2 are shown in Figure 5.5 and 5.6, respectively, along with the corresponding simulated pXRD pattern which was generated using CrystalDiffract software (simulations were undertaken at Leeds, see Appendix B for full 2θ range). The horizontal axis refers to the measured 2θ diffraction angle, and the vertical axis represents the relative detection intensity. Both experimental patterns demonstrated good agreement with the simulated pattern from structure files provided by AstraZeneca (.cif files of AZ1: 391173-ICSD and AZ1-2: ZS140021; personal communication, Dr Helen Blade). Moreover, all the samples show strong characteristic crystalline peaks for the (111), (002), (021), (123), (041) and (142) planes of the cubic phase. Apart from characteristic pXRD peaks of AZ1 and AZ1-2, no other peaks are detected, therefore AZ1 and AZ1-2 are single phases. A minor peak shift towards higher

diffraction angles is observed for the (224) and (143) planes of the AZ1 sample relative to the simulation (marked by red arrows in Figure 5.5). This may indicate the presence of strains (tensile stress) in these crystal planes or a change in chemical composition (upon protonation).

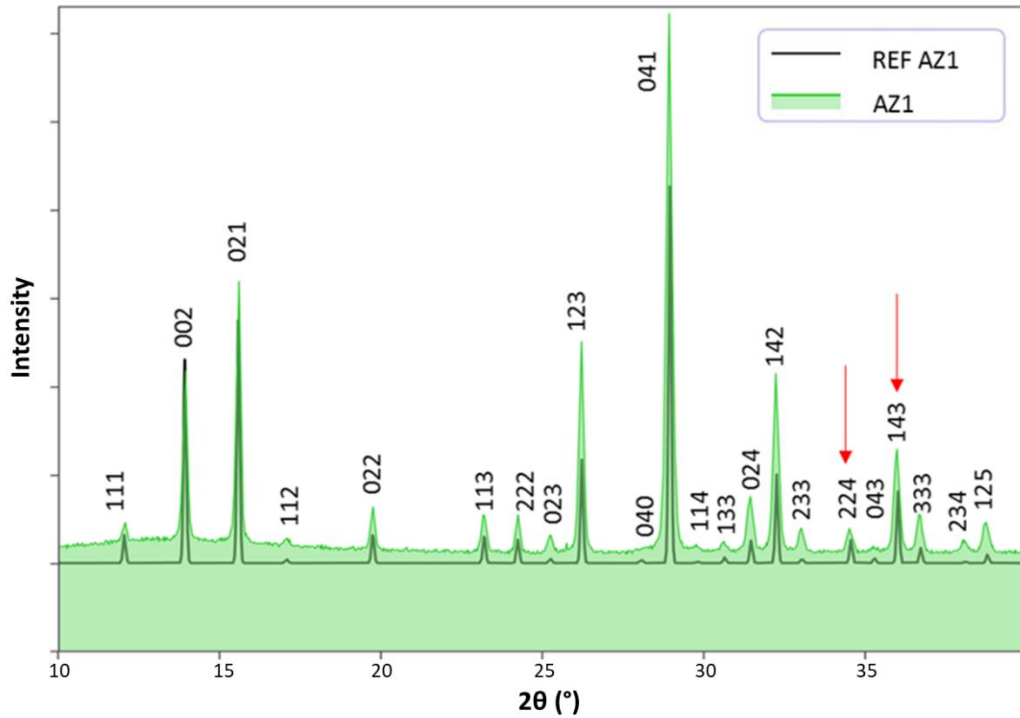


Figure 5.5 Measured (green) and simulated (black) pXRD patterns of AZ1. A minor peak shift is marked by red arrows.

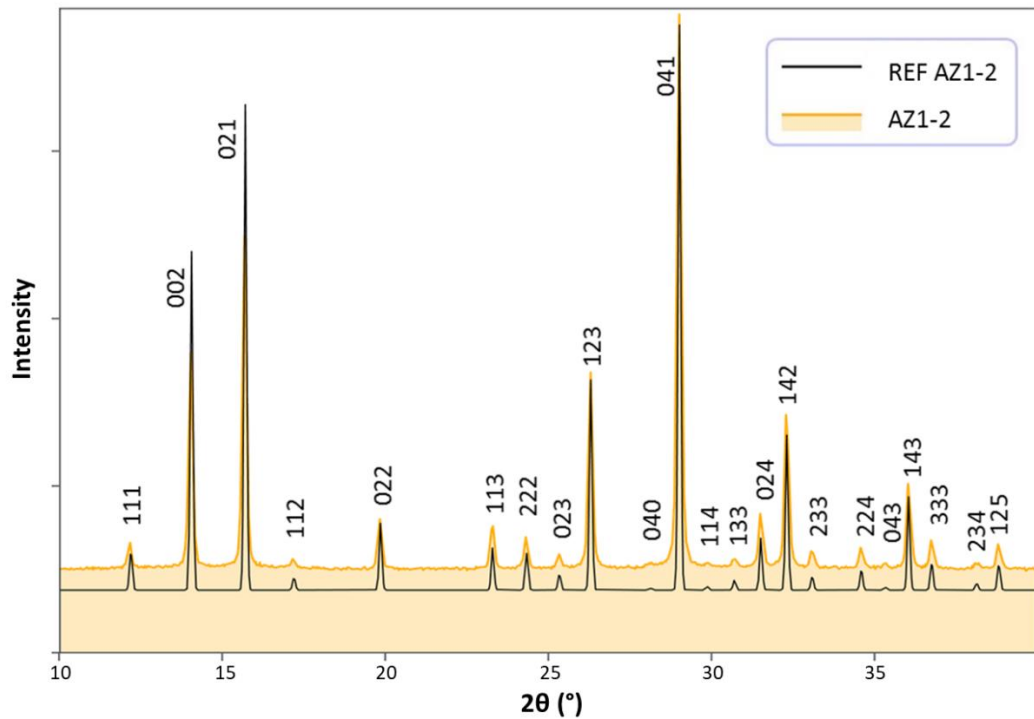


Figure 5.6 Measured (orange) and simulated (black) pXRD patterns of AZ1-2.

Superimposed experimental pXRD patterns for AZ1 and AZ1-2 are shown in Figure 5.7. The pXRD pattern of AZ1-2 is slightly shifted to lower diffraction angles. The characteristic (002) peak value for AZ1 is 6.35 Å and 6.38 Å for AZ1-2 (vertical dashed lines). The protonation process used for the test samples to vary in Na⁺-H⁺ ratio resulted in a marginal difference in unit cell edge of 12.7024 Å for AZ1 compared to AZ1-2 edge length of 12.7620 Å. This suggests lattice relaxation for AZ1-2, which had a larger fraction of sodium cations exchanged for the smaller counter cations, hydrogen, compared to AZ1.

The unit cell parameters of AZ1 and AZ1-2 are summarized in Table 5.1. Table 5.1 also shows the nominal composition of AZ1 and AZ1-2 along with the calculated size and volume of the unit cell based on the supplied structure files.

Both test samples are considered to be strained because higher-angle planes show a larger displacement. There is no significant change in phase besides the minor differences in unit cell parameters (12.7024 Å theoretical vs 12.5610 Å experimental for AZ1, 12.7620 Å theoretical vs 12.6056 Å experimental for AZ1-2).

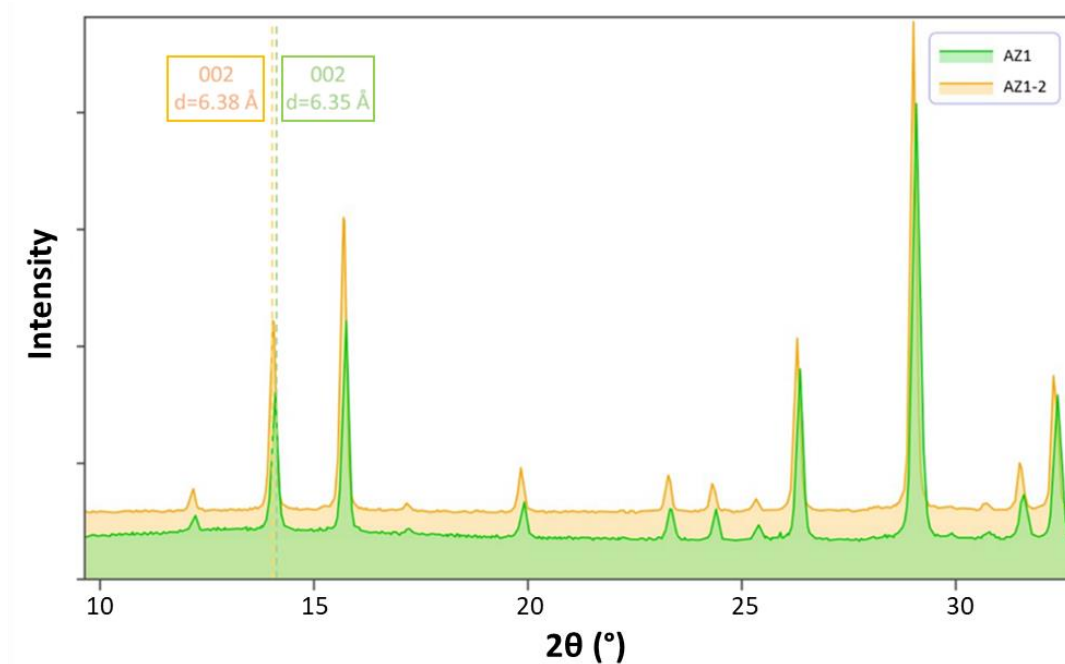


Figure 5.7 Superimposed experimental pXRD patterns for AZ1 and AZ1-2. The dashed lines correspond to the characteristic (002) peak position.

Table 5.1 AZ1 and AZ1-2 structure parameters (calculated in CrystalMaker from the .cif files supplied by Helen Blade, AstraZeneca).

Sample	AZ1	AZ1-2
<i>Chemical formula</i>	$\text{Na}_2\text{ZrSi}_3\text{O}_9 \cdot 2-3\text{H}_2\text{O}$	$\text{Na}_{1.5}\text{H}_{0.5}\text{ZrSi}_3\text{O}_9 \cdot 2-3\text{H}_2\text{O}$
<i>Cell parameters (Å)</i>	12.7024	12.7620
<i>Cell volume (Å³)</i>	2050.416	2078.535
<i>Density (g/cm³)</i>	2.6275	2.5800
<i>Unit cell</i>	164 sites/unit cell	160 sites/unit cell
	0.0683 atoms/Å ³	0.0672 atoms/Å ³
<i>Na⁺ occupancy</i>	0.67	0.62

5.3.2 Pore Structure Simulation

Preliminary analysis of the internal pore structure in the test protonated sodium zirconium cyclosilicate hydrate samples was simulated in CrystalMaker and Mercury software based on the structure file of AZ1. In Figure 5.8a, it can be seen that the pore opening in the AZ1 framework is composed of an asymmetrical seven-member ring (oxygen atoms are not considered in the count) with an average pore size of 3 Å (~ 2.4 x 3.53 Å). The pore network within the three-dimensional crystalline structure has been presented in Figure 5.8b and c, indicating a non-linear pore arrangement that is consistent with the report by Stavros et al. (2014). The counter cations and some of the oxygen sites were excluded in each simulation to make the internal pore structure more visible. However, this simulation does not give a clear explanation of the type of pore network connection. Therefore, a simulated model of sodium sites and cavities above 2.4 Å (representing unoccupied sites/H⁺ sites) in the AZ1 crystal structure was proposed. Figure 5.9 shows a simulation for single and extended (2x2) crystal units along [111] and [010] directions. It can be seen that if the crystal is oriented in the [010] direction, the sodium sites and cavities form a wave or bimodal placement pattern. Considering that the sodium sites and cavities represent the internal pore arrangement in the structure, it can be concluded that the pore channel system is non-linear. TEM analysis through a projected thin structure to identify sodium sites and pore occupancy could prove difficult unless the structure is < 6 Å thick (half of the size of the unit cell).

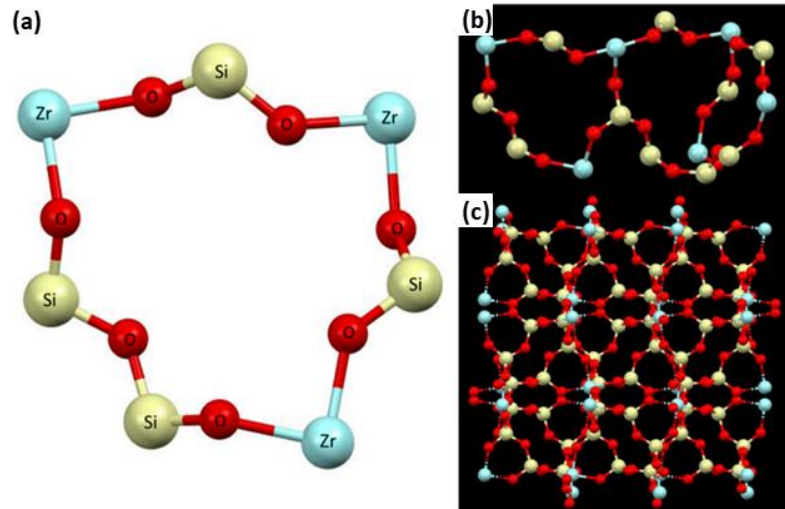


Figure 5.8 Model of (a) a single pore opening in AZ1, (b) selected three connected internal pores and (c) pores across a unit cell of AZ1 simulated in Mercury software. Red spheres = oxygen atoms; blue spheres = zirconium atoms; yellow spheres = silicon atoms. Counter cations are not pictured.

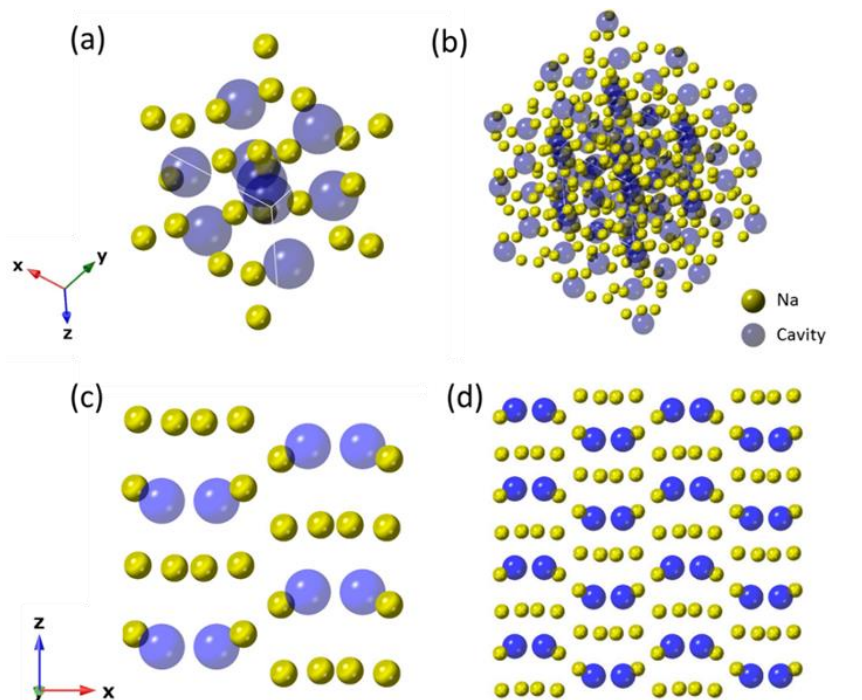


Figure 5.9 Simulated model of sodium sites and cavities (unoccupied sites/pores) of AZ1 for single and extended (2x2) crystal units along (a-b) [111] and (b-c) [010] directions, respectively.

5.4 Crystal Morphology Observation and Particle Size Distribution Analysis by SEM

Morphology

The SEM micrographs of AZ1 and AZ1-2 taken at 10 kX magnification (Figure 5.10a and c, respectively) show particles of non-uniform size distribution, regardless of the type of sample. Each particle is an aggregate of cubic-shaped crystallites and the primary cubic crystallite size is $\sim 1\text{-}2\ \mu\text{m}$ across. The aggregate particle surfaces are not simply planar, therefore reducing the particle size, or preferably separating individual cubic-shaped crystallites, is needed for TEM sample preparation. At higher magnification, significant differences in surface morphology can be observed. SEM micrographs of AZ1 particles taken at 100 kX show that the crystallites surface is rather smooth, with only micro-cracks and signs of crystal growth steps in the form of additional layers on the surface (Figure 5.10b). In contrast, the AZ1-2 crystal surface is covered with numerous spherical particles ranging in size from a few to two hundred nm (Figure 5.10d). The presence of numerous spherical particles on AZ1-2 may be related to the protonation process in which a large fraction of sodium was replaced with hydrogen compared to AZ1. One of the possible second phases that have been reported before for a commercial product is organosilicate moieties grafted through reacting active groups (covalent bonding) e.g. silanols ($\equiv\text{Si}-\text{O}-\text{H}$) (Keyser, 2015). However, AZ1-2 was prepared by a different laboratory synthesis route so the particles on the surface of this test material may be organosilicate or they may be a product of internal out-diffusion and primary crystal fracture during ion exchange and strain. To determine the exact composition of the spherical particles, additional STEM-EDX experiments were carried out and described in Section 5.6.3.

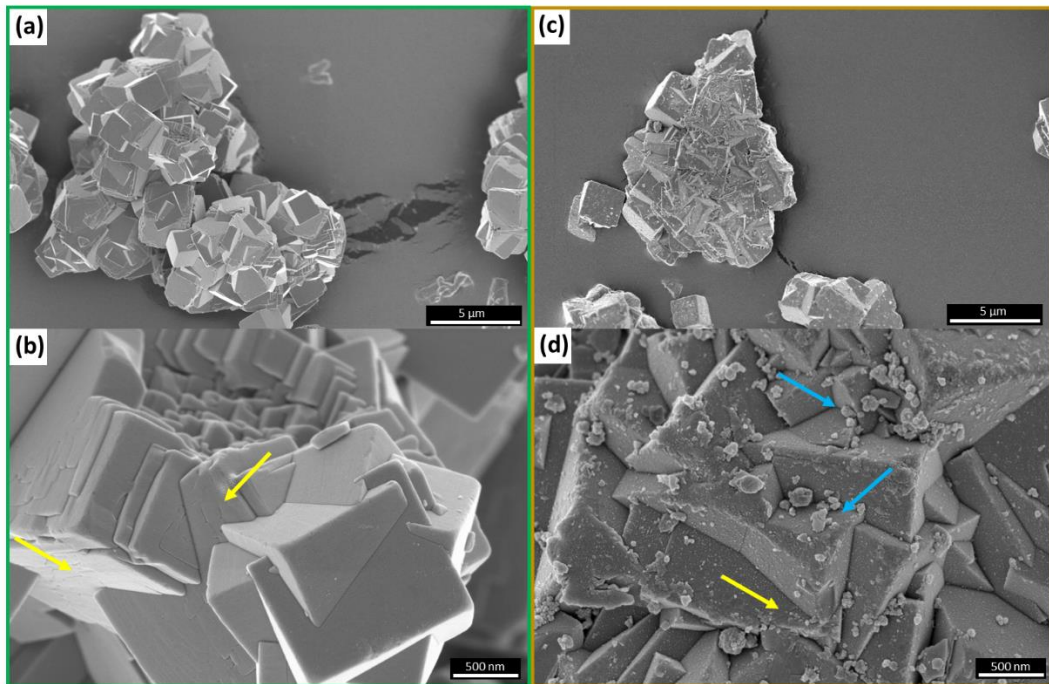


Figure 5.10 SEM micrographs of crystal morphology of (a)-(b) AZ1 and (c)-(d) AZ1-2 taken at 10 kX and 100 kX magnification, respectively. Yellow arrows indicate micro-cracks on the crystal surface in both AZ1 and AZ1-2. Blue arrows indicate the additional spherical particles on the surface of AZ1-2.

The FIB cross sections of the inside surface of AZ1 and AZ1-2 demonstrate a uniform inner morphology with only a few larger voids (up to 500 nm in size) (Figure 5.11). The pores of $\sim 3 \text{ \AA}$ cannot be resolved in SEM due to the limit of resolution (1 nm at best).

A few particles of AZ1 with different structural morphology could be seen in SEM. As shown in Figure 5.12, elongated, tapering fragments with rough textures were identified. Given the shape of these particles, it can be deduced that the chemical composition may differ from the main particles. EDX analysis indicates the elongated parts consist mainly of sodium and oxygen, although a low content of zirconium is present and there is a complete absence of silicon. These particles may be formed in the reaction process, but must be low in volume fraction ($< 5\%$) since they are not detected by pXRD.

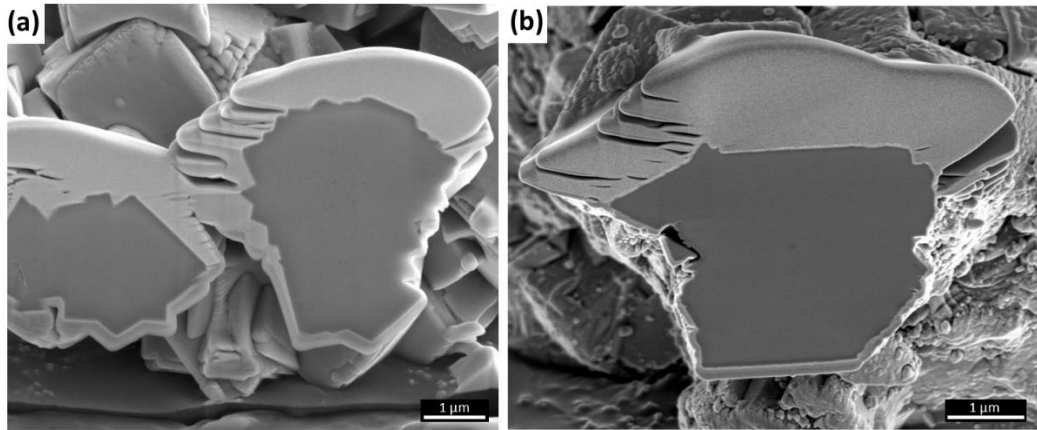


Figure 5.11 FIB cross-sections of (a) AZ1 and (b) AZ1-2 demonstrating no evidence of the internal pore structure.

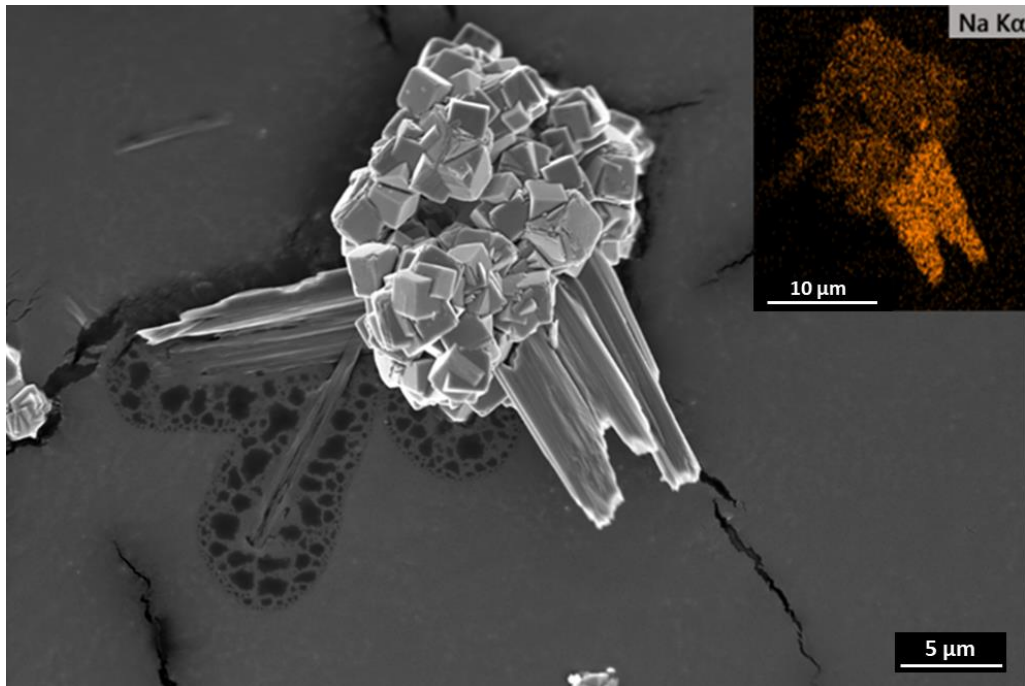


Figure 5.12 Examples of different AZ1 particle morphology. Inset shows the EDX elemental map (Na-K) of the particle.

Particle size distribution

Particle size, shape and distribution analysis of AZ1 and AZ1-2 samples (the term ‘particle’ is ‘aggregate particle’ here) was performed based on the image analysis of the SEM micrographs taken at a low magnification of 1 kX (Figure 5.13). From the low magnification images, it can be seen that AZ1-2 contains a number of particles that appear larger, smoother and more solid than AZ1. It should also be noted that AZ1-2 contains a very large number of small

particles (1-10 μm) relative to AZ1. AZ1-2 was formed from AZ1 by an additional protonation process, which could cause some of the particle aggregates or primary crystallites of AZ1 to break up into the smaller particles seen in AZ1-2.

The average particle size distribution parameters i.e. maximum Feret diameter and area, are presented in Table 5.2 and the histogram is shown in Figure 5.13(c)-(d). The reported standard error in the measurement was calculated by dividing the standard deviation by the square root of the number of particles measured. The average maximum Feret diameter for AZ1 of $22.5 \pm 1.0 \mu\text{m}$ indicates that the particles of AZ1 are significantly larger (~double) than the particles of AZ1-2 with an average particle size of $12.5 \pm 0.5 \mu\text{m}$. The same trend is observed for the average particle area where the mean area of AZ1 ($239.2 \pm 11.4 \mu\text{m}^2$) is more than twice the mean area of AZ1-2 ($98.1 \pm 7.3 \mu\text{m}^2$). The micrographs taken at the low magnification do not suggest by eye that the differences between AZ1 and AZ1-2 are so significant, therefore, a particle size histogram was plotted for each sample with a bin size of 5 μm . Figure 5.13(c)-(d) shows the experimental histograms fitted by distributions of frequency of specific size of particles and the insets show the cumulative average of maximum Feret diameters, where the latter can indicate the minimum number of particles that need to be measured in order to obtain an accurate measurement of particle size. As expected, there is a significantly higher frequency of small particles in AZ1-2 compared to AZ1 and this size fraction dominates the size and area of counted particles to significantly lower the average particle size of AZ1-2 compared to AZ1. It should also be noted that in order to obtain a consistent average (as suggested by the cumulative frequency plots), it is necessary to measure a minimum of 50 particles for AZ1 and a minimum of 100 particles for AZ1-2, likely due to the differences in frequency and size ranges of particles in AZ1-2 versus AZ1.

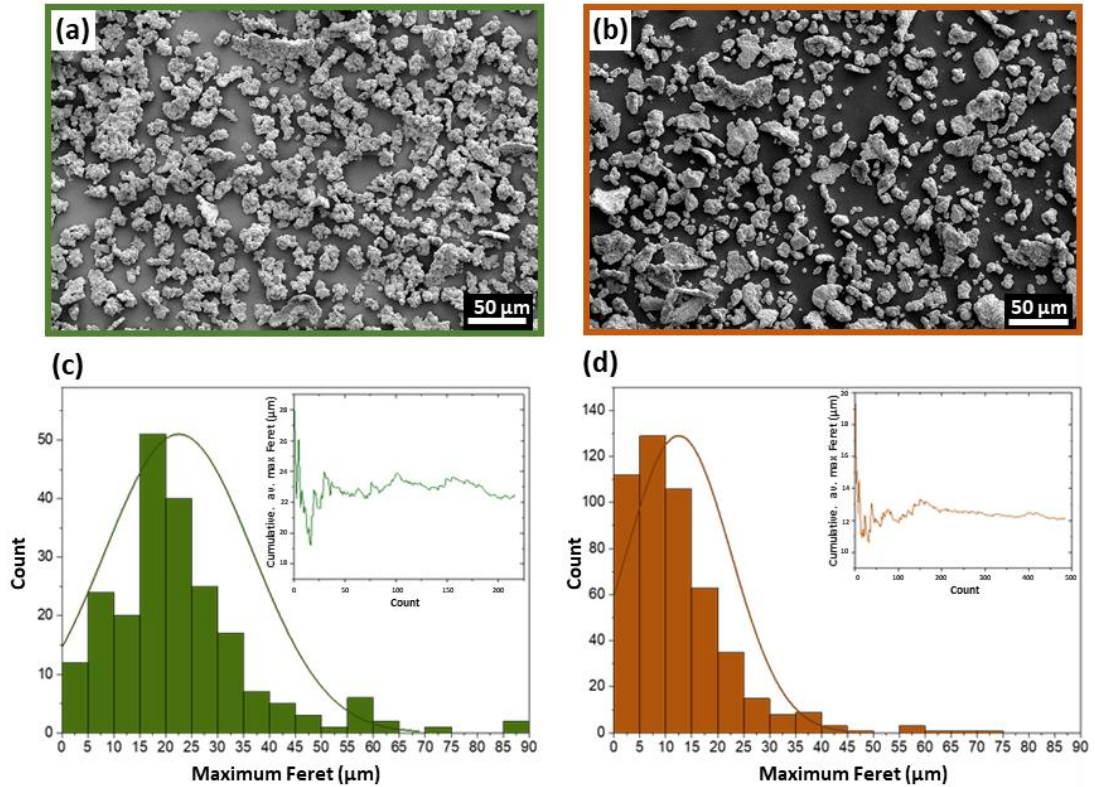


Figure 5.13 (a)-(b) SEM images of AZ1 and AZ1-2 taken at 1 kX with (c)-(d) corresponding histograms of the particle size distribution of AZ1 and AZ1-2, respectively. The inset in (c)-(d) shows the cumulative average of the maximum Feret's diameter.

Table 5.2 The average particle size distribution parameters.

Parameter	AZ1	AZ1-2
<i>Max Feret [μm]</i>	22.5 ± 1.0	12.5 ± 0.5
<i>Area (A) [μm²]</i>	239.2 ± 11.4	98.1 ± 7.3
<i>Number of particles</i>	216	486

Characterisation of irregularly shaped particles requires information on particle shape because a single particle size value is insufficient to properly describe a sample with a non-rounded particle shape. Therefore, more specific shape descriptors such as Feret's min and max diameter, to give an aspect ratio, solidity, and circularity, were also measured. The parameters for determining particle size and shape are summarised in Table 5.3. The same

parameters have been also calculated for the narrowed range of medium and large particle sizes of 30 - 70 μm , due to a higher number of small particles in AZ1-2. As mentioned before, the average maximum Feret diameter for AZ1 of $22.5 \pm 1.0 \mu\text{m}$ indicating that the particles of AZ1 are significantly larger than particles of AZ1-2 with an average particle size of $12.5 \pm 0.5 \mu\text{m}$. However, within the narrowed range the average maximum Feret diameter is similar ($41.5 \pm 1.6 \mu\text{m}$ for AZ1 and $42.4 \pm 2.3 \mu\text{m}$ for AZ1-2). Very interesting results are obtained for the average area of particles, where in the narrowed large particle size range, the average area for AZ1-2 of $619.6 \pm 60.5 \mu\text{m}^2$ is larger than for AZ1 of $549.4 \pm 36.4 \mu\text{m}^2$, which suggests that the particles are more regular and more 'solid' within the similar average maximum Feret diameters of the two samples.

Particle shape analysis (Table 5.3) shows that the aspect ratio (AR) for both size ranges is higher for AZ1 than for AZ1-2. The AZ1-2 particles are more solid than AZ1 in both ranges (by 5-8%). An important parameter is circularity, which indicates that AZ1-2 is much more circular than AZ1 in both ranges (by 24-26%). This means that a factor such as a perimeter is of great importance here, as has been observed on the micrographs, AZ1 particles have more irregular shapes than AZ1-2, which results in a larger perimeter and thus less circularity. Detailed particle size measurements suggest the disintegration of AZ1 particles on processing to AZ1-2.

Table 5.3 Size and shape parameters of AZ1 and AZ1-2 (\pm SD).

<i>Parameter</i>	<i>AZ1</i>		<i>AZ1-2</i>		
	<i>All range</i>	<i>30 – 70 μm</i>	<i>All range</i>	<i>30 – 70 μm</i>	
<i>Size</i>	<i>Max Feret [μm]</i>	22.5 ± 1.0	41.5 ± 1.6	12.5 ± 0.5	42.4 ± 2.3
	<i>Min Feret [μm]</i>	13.7 ± 0.5	22.8 ± 1.1	8.0 ± 0.3	22.8 ± 1.2
	<i>Area [μm^2]</i>	239.1 ± 19.5	549.4 ± 36.4	98.0 ± 7.3	619.6 ± 60.5
<i>Shape</i>	<i>Aspect Ratio (AR)</i>	1.73 ± 0.04	2.16 ± 0.10	1.55 ± 0.02	2.09 ± 0.09
	<i>Solidity</i>	0.85 ± 0.01	0.77 ± 0.01	0.89 ± 0.00	0.83 ± 0.01
	<i>Circularity</i>	0.59 ± 0.01	0.39 ± 0.02	0.73 ± 0.01	0.49 ± 0.02

5.5 Critical Fluence Measurements

An initial TEM study of AZ1 and AZ1-2 was based on the determination of a critical fluence (C_F), to provide a 'dose budget' for future experiments to maximize the information content during TEM experiments. The value of critical fluence of zeolites diverges between 500 and 5000 $e^-/\text{Å}^2$ (Wang et al., 2000). Because of this uncertainty in the selection of optimal experimental conditions, the critical fluence for AZ1 and AZ1-2 was determined. In all cases, the characteristic critical fluence, defined by the accumulated electron dose at which the relative intensity of diffraction spots decreases to $1/e$ (~37%), was measured by the same method as that used for furosemide in Chapter 4.

The first analysis was carried out on a holey-carbon support film, as this type of support grid is commonly used in zeolite and silicate studies. However, again as in the furosemide sample, the particles deposited on a narrow part of the carbon layer were more prone to mechanical reorientation. It was difficult to select representative reflections in order to calculate accurate critical fluence for AZ1. The average C_F of AZ1, measured at 300 kV and using holey-carbon film, was calculated as $300 \pm 100 e^-/\text{Å}^2$.

Additional diffraction pattern series were therefore acquired using continuous carbon film TEM grids, as it was believed to stabilise the crystals in the same way as in the case of furosemide. The corresponding critical fluence of $700 \pm 300 e^-/\text{Å}^2$ is more than twice that of the C_F of the AZ1 sample prepared on holey-carbon film. Therefore, the relevant type of TEM support film is an important factor affecting AZ1 crystal stability under the electron beam. However, some variations due to crystal movement were still observed in the following diffraction patterns series, which can be seen from a larger standard deviation of the data collected (reported as the uncertainty in the C_F value). This might be related to the particle morphology (not planar) or mass loss upon irradiation.

Considering the different compositions of AZ1-2, due to a lower content of sodium ions being replaced by hydrogen, the predicted C_F value may be slightly lower than for AZ-1. The interaction of sodium and hydrogen cations located within the pores with the framework is considered to be ionic, therefore those counter cations can be easily removed during electron irradiation,

particularly hydrogen atoms, as hydrogen has a lower displacement threshold energy than sodium. The critical fluence for AZ1-2 at 300 kV and on continuous carbon film was determined to be $500 \pm 150 \text{ e}^-/\text{\AA}^2$, slightly lower than the critical fluence for AZ1, as expected. It should be noted that most of the diffraction patterns showed that both AZ1 and AZ1-2 crystals to be randomly orientated, therefore this value is only an indication of a range of 'dose budgets' to select optimum conditions to minimize electron irradiation damage to the specimen.

Assessing a characteristic C_F for a specific interplanar spacing (i.e. tilting the particular area of interest into a preferred zone axis) was difficult. However, with care, it was possible to identify some areas of AZ1-2 initially orientated on a low-ordered zone axis. A critical fluence for AZ1-2 orientated on-zone was calculated as $2000 \pm 1600 \text{ e}^-/\text{\AA}^2$, four times higher than the previously calculated C_F for randomly orientated AZ1-2. This may suggest that the sample oriented close to a low zone axis can withstand longer electron beam irradiation, however, this phenomenon requires further investigation (e.g. if there is a type of channelling or diffractive spreading of the beam that can lead to less damage or a recovery process). However, the high standard deviation in C_F values may be a result of the inconsistency in crystal thickness, as thicker samples are generating larger C_F values as a result of less scattering-induced heating. This may also be attributed to preferential rotation or damage along defined crystal planes.

Overall C_F results are shown in Figure 5.14. The relevant type of TEM support film, i.e. continuous carbon TEM grid, proved to be an important factor affecting AZ1 crystal stability. The calculated critical fluence for AZ1 -2 (on the same type of TEM support film) is slightly lower than for AZ1, nonetheless, within a similar range of 'dose budget'. Interestingly, a different, but promising trend was observed for the AZ1-2 crystals initially orientated close to a low-index zone axis, which is characterized by one higher order of magnitude C_F , however, low-dose conditions are still required to avoid electron beam damage.

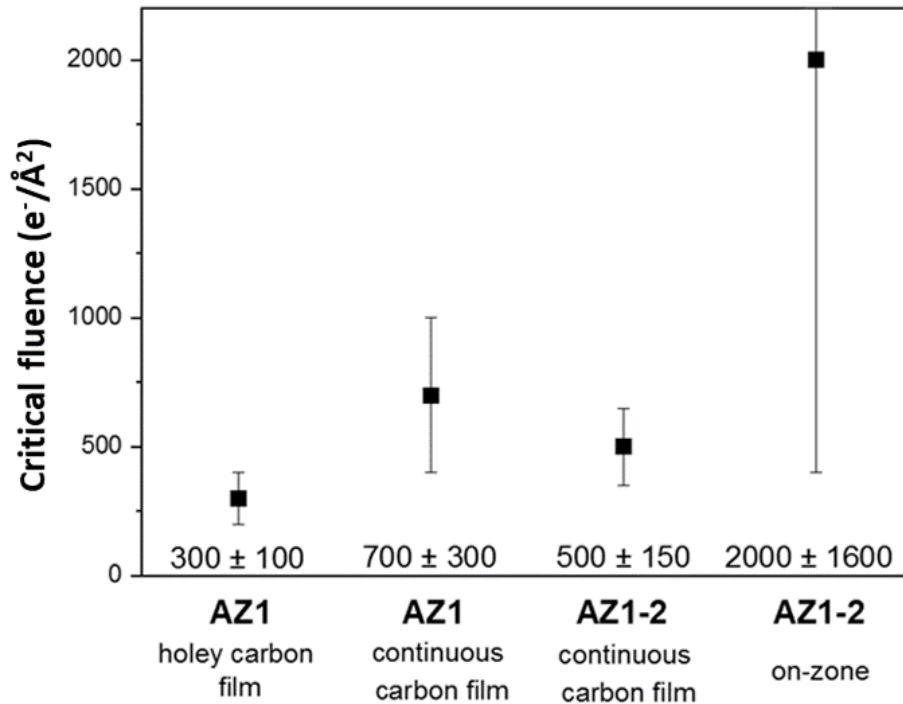


Figure 5.14 Mean C_F and standard deviation of each measurement calculated from diffraction pattern series of AZ1 and AZ1-2 (\pm SD).

5.6 Direct Comparison Between Experimental and Theoretical Predictions of Sodium Content by STEM EDX

5.6.1 Standard – Albite

Prior to the sodium content investigation of AZ1 and AZ1-2 by STEM-EDX, there is a need to perform analysis with a standard reference sample to examine the possibility of Na^+ loss during electron beam irradiation and to apply absorption correction to reduce the overall error in quantitative EDX analysis (Appendix A.6). Difficulties with choosing an appropriate reference sample are related to its composition (same composition as the analysed sample), purity (single phase present) and capability to be thinned for electron beam transparency (without inducing any chemical changes) (Williams and Carter, 2009). Moreover, the standard needs to be relatively stable under electron beam irradiation.

As the sodium distribution within AZ1 and AZ1-2 particles will be calculated based on Na/Si ratio, the chosen reference standard sample is albite, a sodium aluminium silicate, $\text{Na}(\text{AlSi}_3\text{O}_8)$. Albite belongs to the Plagioclase Feldspar group and is one end member, containing sodium and no calcium.

The nominal Na/Si ratio is 0.33. However, the silicate minerals can contain more than one phase and often radiolysis damage can occur.

STEM-EDX spectral maps were acquired and quantified using the standard Cliff-Lorimer method and the default k -factors available in Velox. Plus, the Brown-Powell ionisation cross-section model, absorption correction (density and thickness applied where known) and a multi-polynomial background correction model were used to further reduce the error in quantification.

The spectrum image acquisition was performed under the following conditions: 50 pA probe current, 20 μ s dwell time, 7.473 nm pixel size and 150 frames, giving the total accumulated fluence of $\sim 17 \times 10^3 \text{ e}^-/\text{\AA}^2$. These conditions are needed to increase the number of counts (signal to background), particularly for light elements, in order to further improve quantification. However, the full quantification is complicated as other factors i.e. (i) electron beam damage, (ii) counter ion mobility/loss in vacuum and during the acquisition, (iii) detector resolution and (iv) holder and grid shadowing. Therefore, STEM-EDX of the known standard sample, albite, might help to measure experimental k -factors and compensate for irradiation losses (if similar to those for albite) on quantification of Na/Si in AZ1 and AZ1-2.

As mentioned in Section 5.4, the AZ1/AZ1-2 primary particle size is 1-2 μ m. Therefore, the sample thickness has an additional impact on the STEM-EDX quantification of element ratios and any measurement should be done at the projected edges of the particle. In order to experimentally evaluate the effect of absorption correction and the accuracy of the standard Cliff-Lorimer method, a wedge-shaped FIB-TEM section of albite of controlled thickness was prepared (Figure 5.15). The calculation of the Na/Si ratio against the thickness of the wedge shape sample is summarised in Table 5.4. As the density and thickness of the FIB-TEM section are known, the Na/Si ratio is measured using the standard Cliff-Lorimer method and with and without absorption correction. The accuracy of the quantitative analysis of EDX, especially for light elements i.e. Na-K X-rays that are strongly absorbed, can be significantly improved for the thicker part of the wedge-shaped FIB-SEM by applying an absorption correction within the range of 400-700 nm (by

~10%). For samples with thickness ranging 700-1000 nm, the improvement is even higher i.e. up to 17%, however, the Na/Si ratio remains below the nominal composition. This can be related to (i) beam damage during ion beam milling, (ii) the non-uniform composition of the mineral sample and (iii) sodium loss during the EDX acquisition.

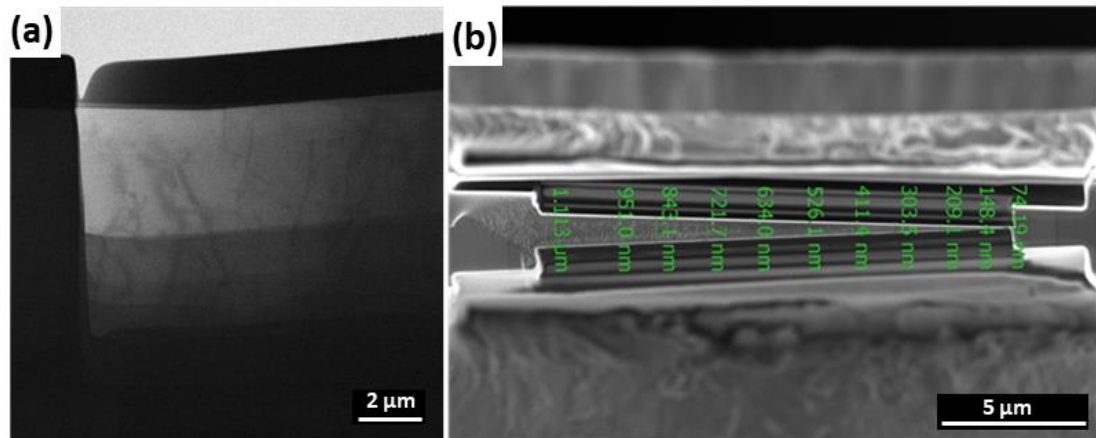


Figure 5.15 (a) Wedge-shaped FIB-TEM section of reference mineral, albite, with measured thickness in (b).

Table 5.4 STEM-EDX of FIB-TEM wedge sample of albite. Na/Si is calculated without and with absorption correction based on the sample thickness at each range. Grey backgrounds indicate accurate Na/Si prediction.

Thickness range (nm)	75 – 200	200 – 303	411 – 526	526 – 634	634 – 721	721 – 843	843 – 951	951 – 1113
Median thickness (nm)	138	252	469	580	678	782	897	1032
NO absorption correction	31.29	31.53	28.62	27.62	26.97	25.33	25.00	22.96
Na/Si ratio	31.98	32.75	30.83	30.26	29.99	28.70	28.78	27.03
% improvement	+2.2 %	+3.9 %	+7.7 %	+9.6 %	+11.2 %	+13.3 %	+15.1 %	+17.7 %

In order to evaluate the effect of ion beam damage, two other methods of sample preparation were used: (a) dispersing a drop of ground powder suspension (in ethanol) and drop casting or (b) directly placing ground powder, onto a TEM copper grid coated with an amorphous carbon film (also to exclude the effect of solvent on the potential sodium removal from channels). Figure 5.16 shows a typical elemental mapping of Na and Si elements in the albite particle. STEM-EDX analysis confirmed that albite is a relatively beam-stable mineral since no decrease in sodium content was observed with increased electron fluence. If the experimental imaging conditions remain the same, the thickness of the thinnest parts of the albite particles can be estimated from the contrast gradient in the FIB section. Surprisingly, regardless of the sample preparation method (ground in solvent or dry), the experimental Na/Si ratio is in accurate agreement with the nominal mineral value. This suggests that ion beam damage during milling or thinning of a section affects the sodium ratio. However, the good correlation between standard and experimental Cliff-Lorimer is promising but it can be used accurately for powder samples only. Thus, the variation in the sample thickness will be the key effect on the EDX quantification of AZ1 and AZ1-2 powder samples.

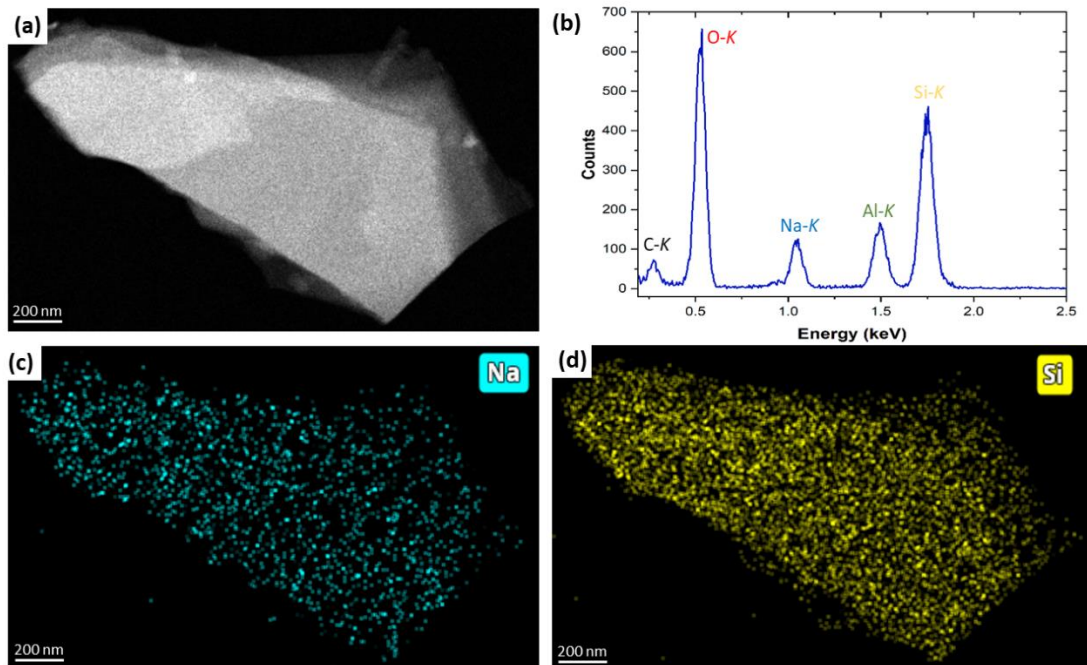


Figure 5.16 (a) HAADF-STEM of albite, (b) typical EDX spectra from isolated particle, (c) sodium and (d) silicon EDX elemental mapping.

Table 5.5 Measured Na/Si ratio of albite standard sample (\pm SD).

Sample	Albite – Na/Si ratio
<i>Ethanol</i>	0.34 \pm 0.02
<i>No solvent</i>	0.34 \pm 0.02
<i>Nominal</i>	0.33

5.6.2 Effect of Sample Preparation Method on STEM-EDX Measurement

Spectrum image acquisition and powder sample preparation were performed under the same conditions and method as for albite analysis in Section 5.6.1 for direct comparability. The structure of AZ1 and AZ1-2 incorporate wide channel systems and substantial micro-pore volume, therefore, there is a possibility that the solvent used may lead to partial removal of sodium ions. Moreover, two types of TEM holders were used, 'standard' and 'cryo-holder' to further prevent potential sodium loss during EDX acquisition.

Typical AZ1 and AZ1-2 STEM-EDX spectra and elemental maps for Si-K (yellow), Na-K (blue), O-K (red) and Zr-K (green) are shown in Figure 5.17 and 18. Superimposed EDX spectra for AZ1 and AZ1-2 show the expected high levels of O and Si, as well as significant Na-K peaks (Figure 5.17). Spectra for the two samples were normalised to the Si-K peak as lighter elements (i.e. oxygen) can be more variably absorbed by a sample, resulting in potentially important errors in quantification analysis. The Cu peak comes from the TEM grid. The EDX spectra for AZ1 show increased levels of Na-K compared to AZ1-2, as expected. The distribution of sodium appears to be relatively uniform across each sample (Figure 5.18).

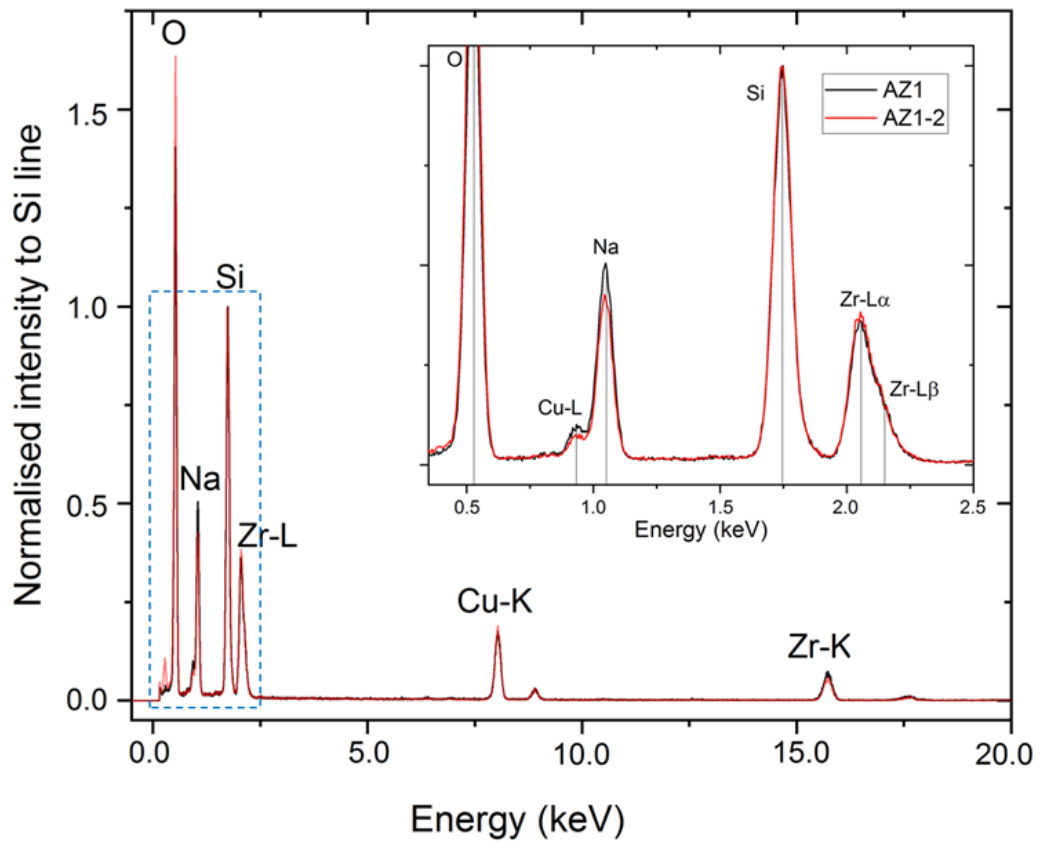


Figure 5.17 Typical STEM-EDX spectra for AZ1 (black) and AZ1-2 (red). The inset shows an enlarged region within the dashed area and the increased Na-K content of AZ1.

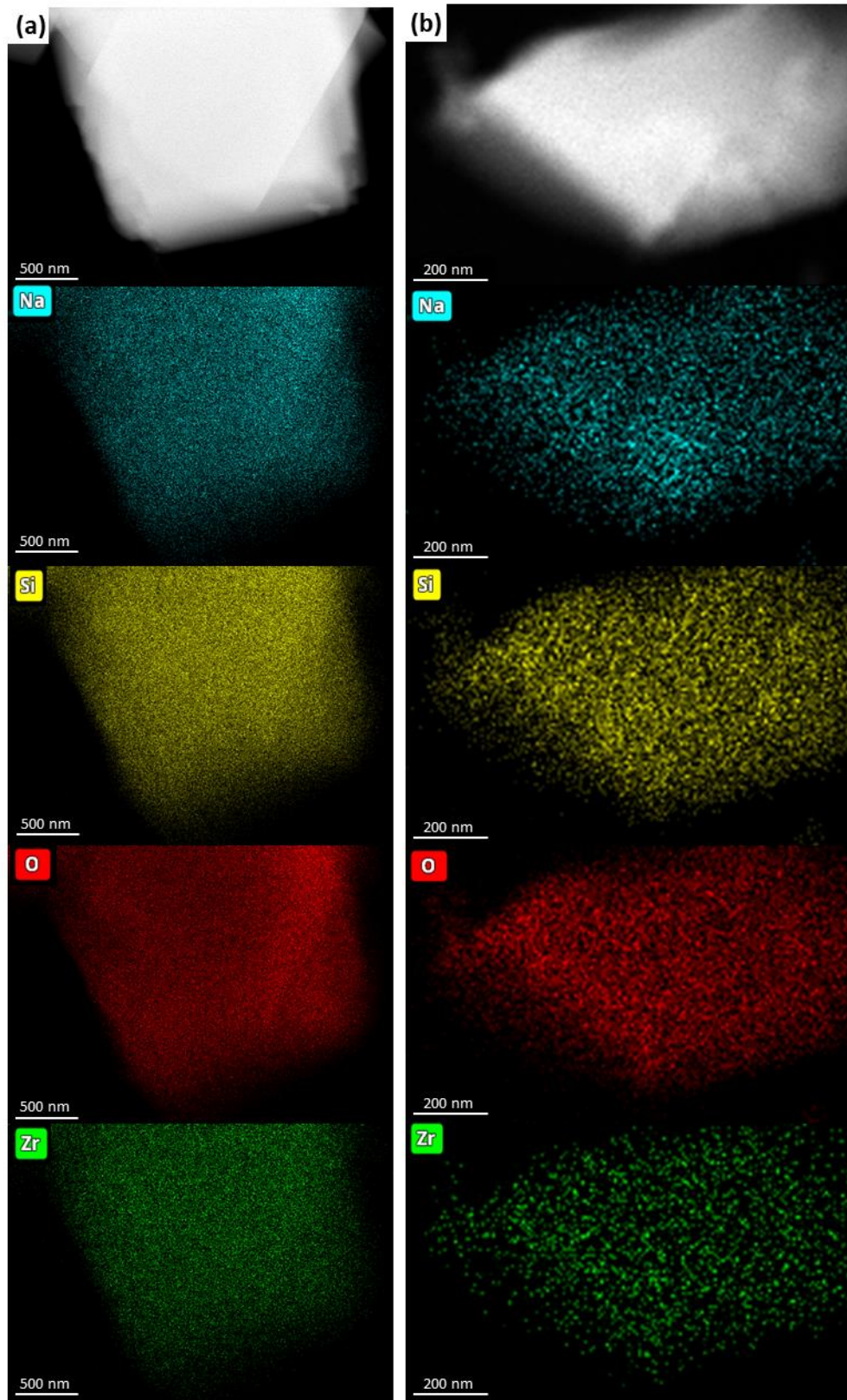


Figure 5.18 STEM-HAADF micrograph showing the area scanned to obtain the EDX spectrum for Si-K, Na-K, O-K and Zr-K elemental maps of (a) AZ1 and (b) AZ1-2.

Sodium content was determined based on the quantified atomic Na/Si ratio using the standard Cliff-Lorimer method with absorption correction (the average thickness value was estimated from the contrast gradient in the albite FIB section) and background correction. According to the pXRD quantification, the nominal atomic Na/Si ratio was calculated as 0.67 and 0.5 for AZ1 and AZ1-2, respectively. The experimental Na/Si ratio by EDX for each sample and different methods of preparation are presented in Table 5.6. STEM-EDX results acquired using a total electron fluence of $\sim 17 \times 10^3 \text{ e}^-/\text{\AA}^2$ from AZ1 and AZ1-2 show that the average Na/Si ratio for samples prepared by dispersing a powder in ethanol is 0.53 ± 0.04 for AZ1 and 0.37 ± 0.06 for AZ1-2. STEM-EDX results from the samples prepared by directly placing a ground powder on a TEM grid show that the average Na/Si ratio is slightly higher of 0.55 ± 0.07 for AZ1 and 0.43 ± 0.04 for AZ1-2, suggesting the ethanol solvent penetrates through the channels reducing Na content by a small 4% fraction for AZ1 and a higher, 14% fraction for AZ1-2. More importantly, the data suggest that AZ1-2 contains less sodium than AZ1. Using a cryo holder for the same type of powder sample preparation, the ratios are again slightly increased, however, both experimental Na/Si ratios are still below the nominal value in Table 5.6. It should be noted that STEM-EDX results calculated based on a reduced number of frame series (50 frames - corresponding to a total electron fluence of $5600 \text{ e}^-/\text{\AA}^2$) from AZ1 and AZ1-2 (powder samples) show that the average Na/Si ratio is slightly higher again at 0.58 ± 0.08 for AZ1 and the same 0.47 ± 0.04 for AZ1-2. Increasing the number of counts collected reduces the noise and uncertainty of the measurement. As mentioned in Section 5.5, sodium and hydrogen atoms are easily removed from their sites during electron beam irradiation, and it is clear that sodium can be continuously removed during EDX mapping. Despite this, STEM-EDX can still be used to confirm the variation in sodium level between AZ1 and AZ1-2 and semi-quantitatively confirm sodium composition.

Table 5.6 Experimental Na/Si ratio of AZ1 and AZ1-2 acquired using a total electron fluence of $\sim 17 \times 10^3 \text{ e}^-/\text{\AA}^2$ (\pm SD).

Method	AZ1	AZ1-2
<i>Cryo</i>	0.57 \pm 0.04	0.46 \pm 0.04
<i>No solvent</i>	0.55 \pm 0.08	0.43 \pm 0.04
<i>Ethanol</i>	0.53 \pm 0.04	0.37 \pm 0.06
<i>Nominal</i>	0.67	0.50

STEM-EDX analysis shows that Na/Si ratio varies between grains (0.45 – 0.71 for AZ1; 0.34 – 0.62 for AZ1-2). This variation might be related to the sample thickness and orientation. Some (relatively few) areas within the grain are very high with sodium (0.7 – 1.1) (Figure 5.19). Sodium levels within these hot spots are 56-107% above levels throughout the rest of the crystal.

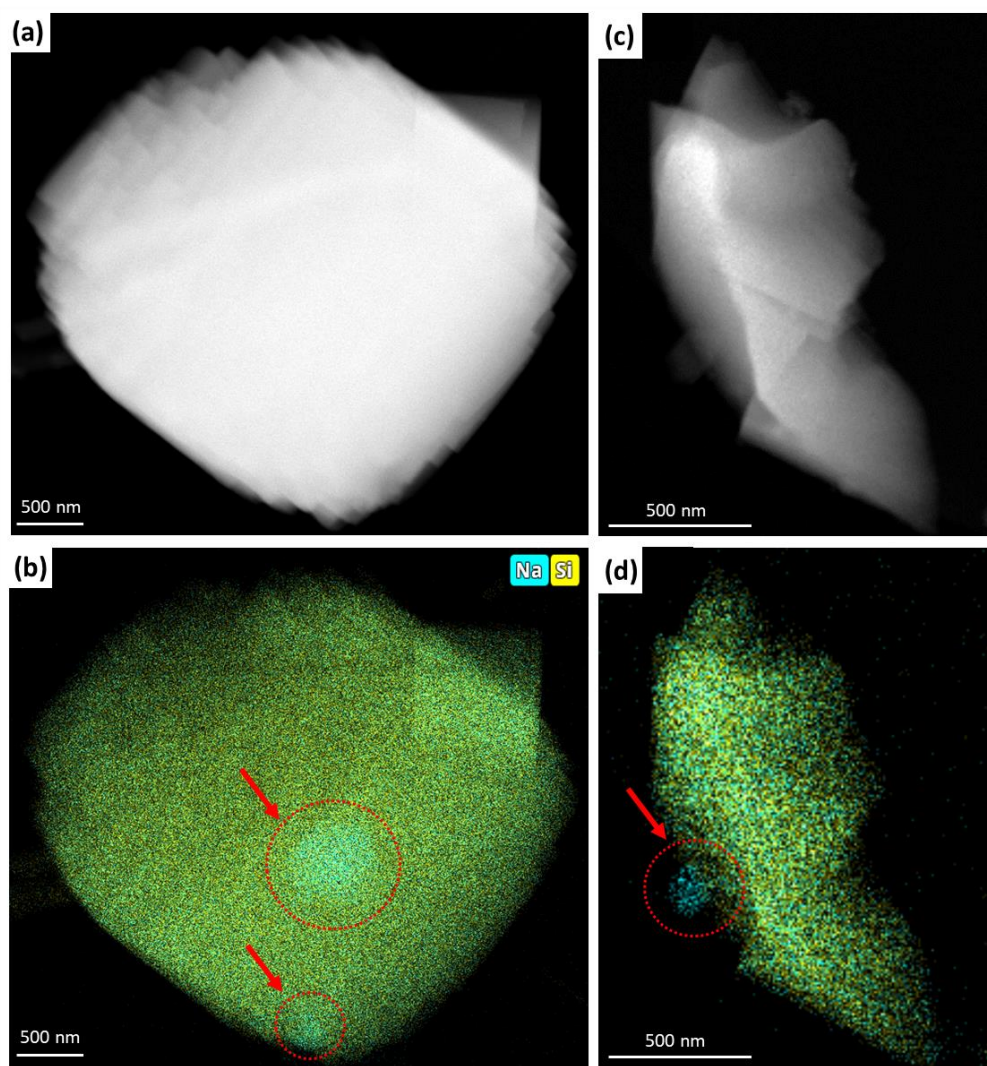


Figure 5.19 Particles with highlighted hotspot region rich with sodium: (a) AZ1, (b) AZ1-2.

STEM-EDX elemental intensity line profiles were performed in order to clarify the typical distribution of sodium and silicon across particles, including one sodium hot spots area (Figure 5.20). The selected vertical and horizontal Na and Si intensity profile boxes for AZ1 and AZ1-2 confirm that Na/Si composition is uniform within both samples and indicate a homogeneous chemical distribution apart from the small number of hot spot areas identified before.

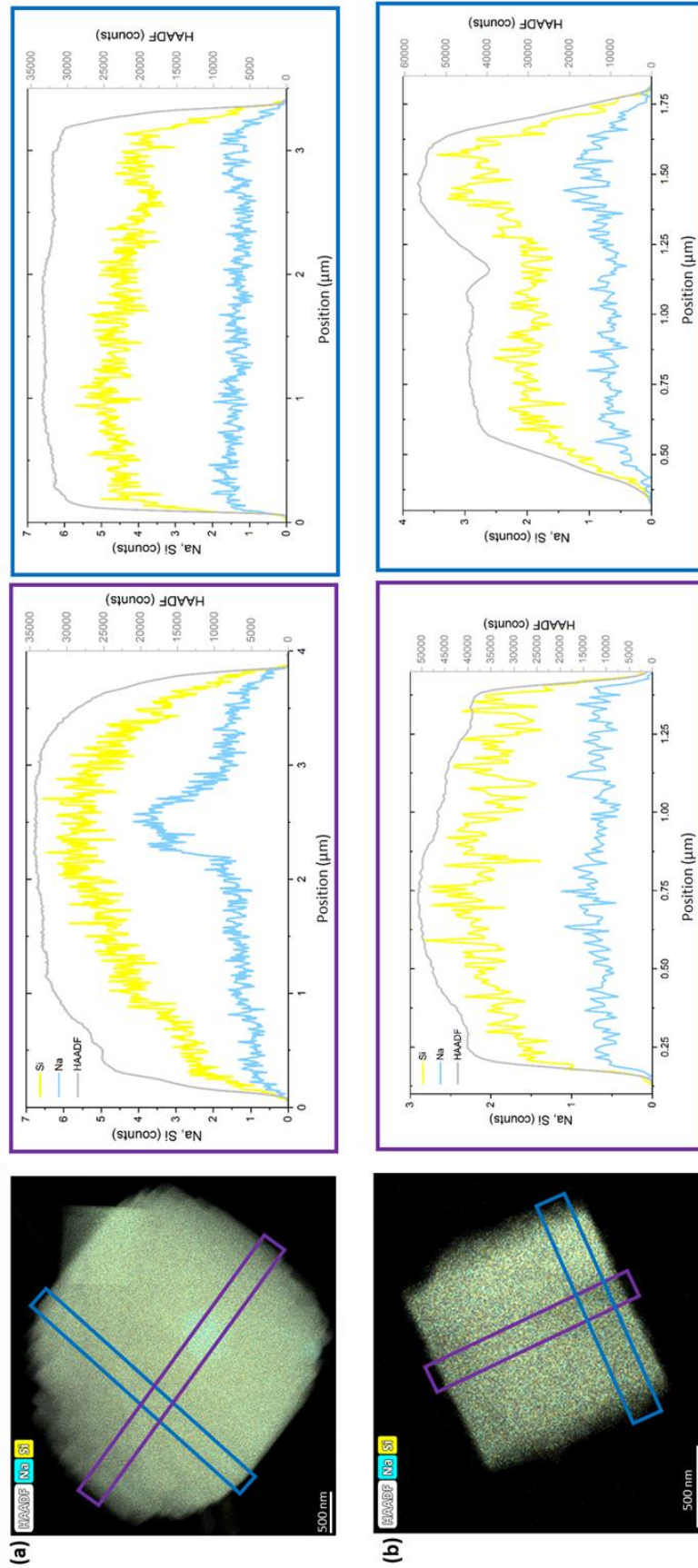


Figure 5.20 STEM-EDX line profile across (a) AZ1 and (B) AZ1-2 indicate Na/Si composition is uniform within both samples.

Although the STEM-EDX of the FIB section of albite demonstrated a slight sodium loss due to ion beam damage, cryo-FIB was used here to better preserve the structure and sodium content of AZ1 and AZ1-2 in order to investigate the internal sodium distribution of AZ1/AZ1-2 by STEM-EDX. However, the results demonstrate high sodium re-deposition on the top surface of each fabricated lamella. Furthermore, the calculated Na/Si ratios deviate from the nominal values (0.41 for AZ1 and 0.32 for AZ1-2) and cannot be considered consistent with the previous STEM-EDX values (Table 5.6).

5.6.3 Investigation of AZ1-2 Surface Particles

SEM morphology observation at high magnification reveals that the AZ1-2 crystal surface is covered with numerous spherical particles compared to AZ1 (Figure 5.10). STEM-EDX mapping of projected surfaces of AZ1-2 was used to confirm the elemental content of the spherical particles observed in BF-TEM images (areas 2-4) and compared to the main region of the AZ1-2 particle (area 1) (Figure 5.21). Noisy STEM-EDX data from smaller particles at the surface of AZ1-2 suggests these particles are silicates (Table 5.7) and is consistent with other reports by US Patent (Keyser, 2015).

EDX analysis showed that the spectra taken from a single spherical particle (using a fine spot electron beam) and from a neighbouring part of the cubic-shaped crystallites suggest a lack of Na and Zr in the surface particles.

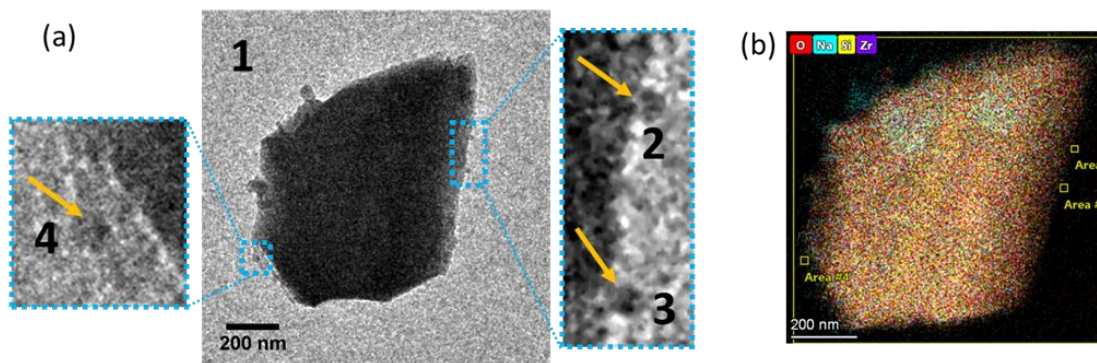


Figure 5.21 (a) BF-TEM image of AZ1-2 with highlighted region for STEM-EDX elemental mapping (b) STEM-EDX mapping of selected areas.

Table 5.7 Elemental composition of areas selected on STEM-EDX mapping.

Element	Atomic Fraction (± 2)			
	<i>Area 1 - all</i>	<i>Area 2</i>	<i>Area 3</i>	<i>Area 4</i>
<i>O</i>	58.0	66	58	61
<i>Na</i>	10.8	0	5	0
<i>Si</i>	24.2	24	36	39
<i>Zr</i>	7.0	9	0	0

5.6.4 EDX Conclusions

The key findings from this compositional study are as follows. By the use of EDX spectroscopy, accurate quantitative composition analysis was difficult due to the ion and electron beam sensitivity leading to mobility/loss of Na^+ , however, it was confirmed that AZ1 contains more sodium than AZ1-2 by approximately 24%. STEM-EDX quantification of Na/Si levels in drop-cast powders is 15% lower than the nominal composition (derived by XRD; Table 5.1), despite similar quantification analysis of a mineral standard giving accurate measures of Na^+ content. TEM and STEM-EDX should be conducted at a maximum electron fluence of $\sim 17 \times 10^3 \text{ e}^-/\text{\AA}^2$. Regardless of actual composition, the distribution of sodium was relatively even in both samples, although a few nanoscale hot spots were present in some particles of both AZ1 and AZ1-2. Cryo-FIB lamellar preparation for TEM causes significant ion beam damage and additional preferential loss of Na^+ in thin sections making them redundant for compositional analysis.

5.7 Lattice Imaging and Strain Analysis

BF-STEM is a potential technique to acquire a crystal lattice image and can provide information about the presence of strains, particularly for samples exhibiting large variability in shape and size or that have some degree of overlapping crystals (Chapter 4). One of the problems during the acquisition of a lattice image is the difficulty obtaining proper focusing. While in a high-resolution image in BF-TEM, a large region of a crystal would have to be sacrificed to focus an image, STEM offers the possibility to focus the probe close to the area of interest without unnecessarily exposing this whole area to the beam by using the

Ronchigram of a static probe (explained in detail in Methodology Chapter 3). Thus, STEM might be particularly advantageous for imaging beam-sensitive particles, despite the lower efficiency of the BF-STEM detector (Methodology Chapter 3).

The schematic shown in Figure 5.22a suggests that a $> 1\text{-}2\ \mu\text{m}$ cubic-shaped isolated crystallite of AZ1, orientated down $\langle 001 \rangle$ would be unlikely to transmit any significant electron beam through it. Therefore, lattice imaging might best be done at the edges of the slightly tilted crystallite e.g. oriented $\langle 011 \rangle$ where it is thinnest at the edges. The contrast gradient in BF-STEM can give an idea of the thickness (Figure 5.22b), and generally, edges showing some electron transparency are sufficient for lattice imaging. Based on the preliminary AZ1 pore structure simulation (section 5.3.2), the direct observation of the non-linear channels is almost impossible to observe in the image, because the open part of the pores is blocked from view unless the sample is less than $6\ \text{\AA}$ thick. Moreover, the average opening size of the pores of $3\ \text{\AA}$ can overlap with the size of spaces related to crystal site vacancies and other crystal defects, therefore it requires careful analysis. However, it is possible to acquire lattice images and apply geometric phase analysis (GPA) to investigate the presence of and quantify the number of strains in the crystal structure of AZ1 and AZ1-2.

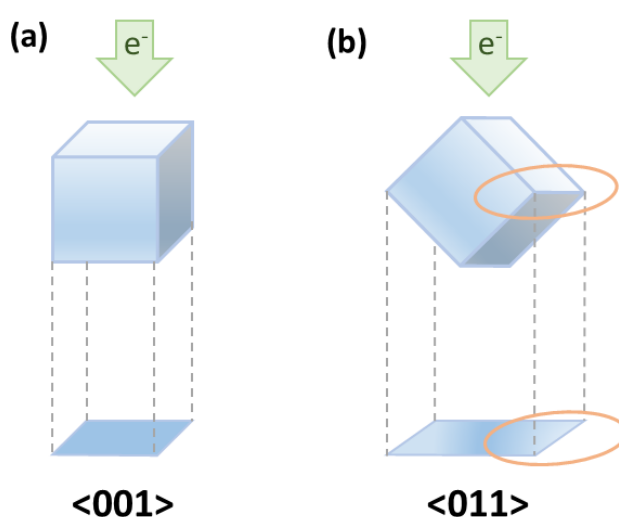


Figure 5.22 Schematic of a profile view of a cubic structure down the (a) $\langle 001 \rangle$ and (b) $\langle 011 \rangle$ zone axis. The contrast gradient in the projected image in (b) (orange ellipses) gives an idea of the thickness, with areas towards the top and bottom edges showing some electron transparency sufficient for lattice imaging.

Based on Table 3.2 (Methodology Chapter 3) and the C_F measured here, the potential magnification which can be used to directly lattice image AZ-1 in BF-STEM mode using a pixel dwell time of 20 $\mu\text{s}/\text{pixel}$ and ~ 5 pA probe current, is 450 kX and 640 kX, giving an electron fluence per image of 230 and 467 $\text{e}^-/\text{\AA}^2$, respectively. Furthermore, the resolution limit for this magnification is 3.2 \AA and 2.3 \AA , respectively. This assumption is based on the Nyquist limit of having at least twice the spatial frequency of the feature i.e. twice the pixel size in BF-STEM imaging. Generally, an increase in magnification would decrease pixel size leading to a bigger increase in the electron dose (pixel size squared) during image acquisition in STEM. Thus, in order to acquire a BF-STEM image at higher magnification without exceeding the critical fluence of the sample, the most straightforward way is to reduce the pixel dwell time, e.g. 10 $\mu\text{s}/\text{pixel}$ gives an electron fluence per image reduced by half. Nonetheless, this is closely related to a reduction in the signal-to-noise ratio (SNR) and difficulties with image interpretation, thus specific image processing methods for noisy low-dose images can be applied i.e. image filtering. Further reduction in the pixel dwell time can cause a streaking artefact parallel to the scan direction (resulting from the scan coils being unable to bring back the beam quickly enough during scanning). In addition, a lower beam current itself also reduces the SNR in the image. Therefore, the lowest possible imaging conditions found here to yield an image with sufficient SNR are a probe current of ~ 5 pA and a pixel dwell time of 20 $\mu\text{s}/\text{pixel}$.

BF-STEM lattice images of AZ1 crystals were acquired and then analysed based on selected areas exhibiting diffraction contrast and confirmed by corresponding SAED patterns by TEM. During initial analysis in TEM an electron flux of 0.08 $\text{e}^-/\text{\AA}^2\text{s}$ was used, making it possible to tilt the particular area of interest close to a preferred zone axis without exceeding the critical fluence; this process typically exposes the sample to less than 10 $\text{e}^-/\text{\AA}^2$. One of the more successful attempts to lattice image AZ1 orientated close to $[\bar{3}1\bar{2}]$ direction is presented in Figure 5.23. Crossed lattice fringes can be observed in the area highlighted by the dotted blue square. These are produced by the intersection of two sets of lattice fringes as the crystal is oriented close to a zone axis. Lattice spacings can be identified, equal to 0.73 nm (blue) indexed as $(11\bar{1})$ and 0.57 nm indexed as (021) (yellow), from the corresponding SAED pattern. The lattice image was collected at a STEM

magnification of 450 kX providing a pixel size of 0.165 nm with the total electron fluence of $230 \text{ e}^-/\text{\AA}^2$ per image. It should be noted that the potential pore opening size using this magnification is only two pixels i.e. on the Nyquist limit, therefore the pores might be difficult to observe. In addition, the SAED pattern and the FFT can be indexed and compared with a simulated diffraction pattern of the nominal crystal structure (.cif file) orientated appropriately in SingleCrystal software (Figure 5.23d-e).

The BF-STEM lattice image from Figure 5.23b was further investigated and corresponding FFTs were taken from four areas marked by orange, green, blue and yellow squares (Figure 5.24). The (021) reflection of 0.57 nm lattice spacing from the bottom areas (blue and yellow) have the same relative angle of -33° , however, there is a small shift in the top areas and the (021) lattice plane is displaced by $1-2^\circ$, suggesting the presence of strains.

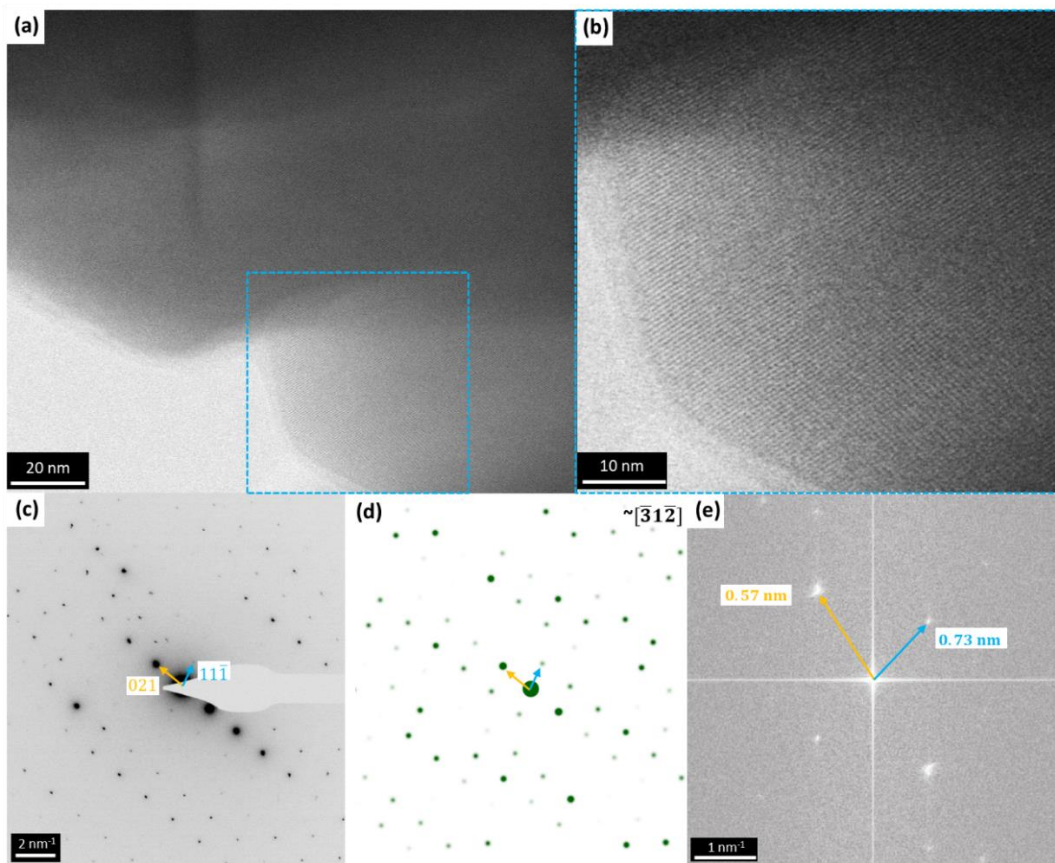


Figure 5.23 (a) BF-STEM crossed lattice image of AZ1 taken in 450 kX magnification, (b) enlarged area taken from the highlighted dotted box, (c) SAED pattern from the crystal in (a) initially orientated close to $[\bar{3}1\bar{2}]$ direction, (d)-(e) simulated electron diffraction pattern of crystal orientation along $[\bar{3}1\bar{2}]$ direction and the FFT from (b).

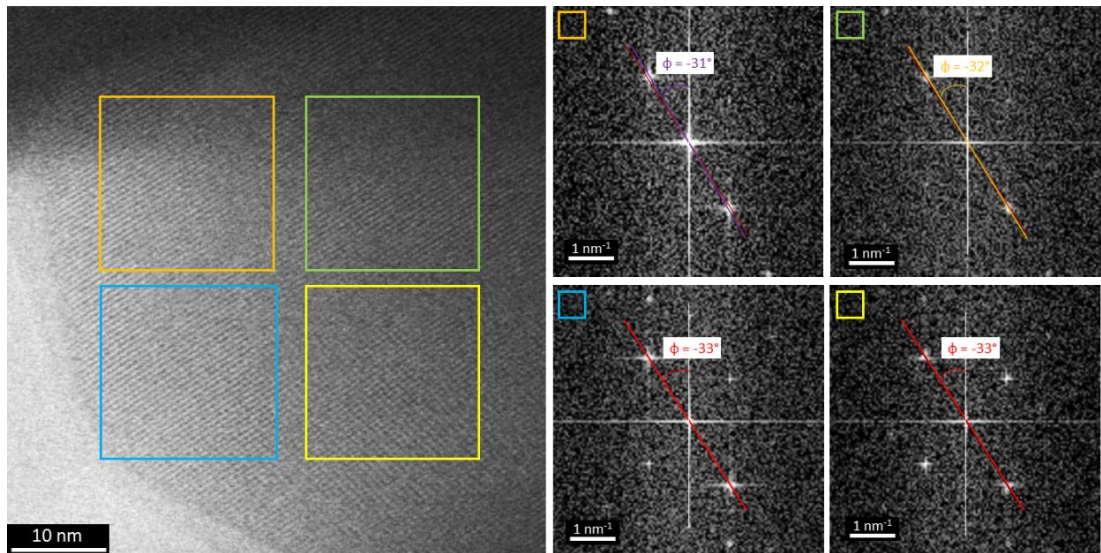


Figure 5.24 BF-STEM lattice image of AZ1 and corresponding FFTs were taken from areas marked by orange, green, blue and yellow squares indicating the slight displacement of the (021) reflection of 0.57 nm lattice spacing by 1-2 degrees suggesting the presence of strains.

The radial Wiener filter, often used to improve SNR for HRTEM images (Lin et al., 2013), can be used here to generate de-noised lattice images. However, this method requires careful noise estimation of the power spectra to restore something close to the original image and avoid artefacts. Here, the noise (i.e. contribution from amorphous/non-periodic area) and signal frequency domains were estimated from the FFT of the image presented in Figure 5.23b. Two cropped lattice images of the experimental BF-STEM of AZ1 and their corresponding Wiener-filtered images are presented in Figure 5.25. The Wiener-filtered images demonstrate substantial improvement in extracting periodic, lattice information making these features more clearly visible in the filtered image. The line intensity profiles were taken from marked areas of the corresponding raw BF-STEM and Wiener-filtered image. The line overlays show good agreement and the average lattice spacing can be measured and match the value calculated from the SAED and FFT. The line profile of the $(11\bar{1})$ reflection shows some variations (average spacing of 0.73 nm) and spacing of 0.90 nm and 0.66 nm can be measured suggesting strains in the $(11\bar{1})$ lattice plane. However, due to: (i) the variation of thickness, (ii) non-linear pore propagation and (iii) the need for the image multi-slice simulation (e.g. μ STEM software package), the direct interpretation of the lattice images is not possible here.

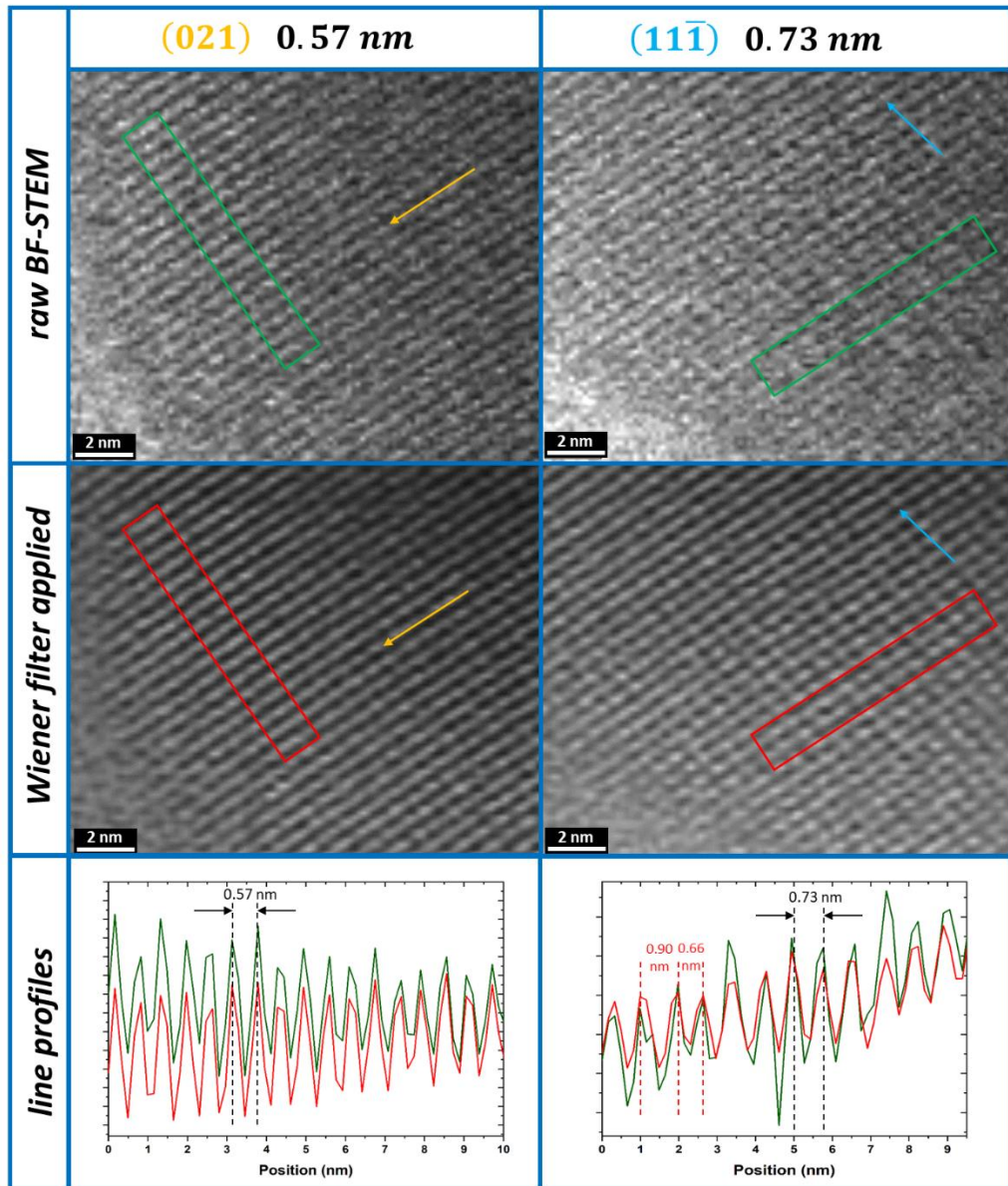


Figure 5.25 Experimental BF-STEM, corresponding Wiener filtered images and line profiles of AZ1.

Next, the pre-protonated AZ1-2 was analysed in order to investigate any difference in lattice images. In some cases, producing lattice images was unsuccessful, possibly due to sample thickness, crystal reorientation or the sample being out of focus. The results demonstrated in Figure 5.26 show that with care it is possible to achieve real-space lattice information at the same 450 kX as used for AZ1 lattice image. An AZ1-2 crystal was orientated close to $[012]$ direction and crossed lattice spacings are measured to 0.61 nm indexed as (200) (orange) and 0.57 nm indexed as $(0\bar{2}1)$ (blue), from FFT. Again, the crossed lattice fringes can be observed in the area highlighted by the dotted blue square

as the crystal is oriented close to a zone axis (Figure 5.26a-b). While the AZ1-2 crystal was orientated close to one of the preferable $\langle 0vz \rangle$ direction of $[012]$, it was possible to acquire a number of lattice images across the particle, because of the higher critical fluence obtained for AZ1-2 on-zoned particles (Figure 5.14).

Corresponding FFTs from two different areas of the BF-STEM crossed-lattice image of AZ1-2 (Figure 5.26a) are presented in Figure 5.27. The (200) reflection of 0.61 nm lattice spacing from the yellow square is displaced by -2° when compared with the red square suggesting the presence of strains.

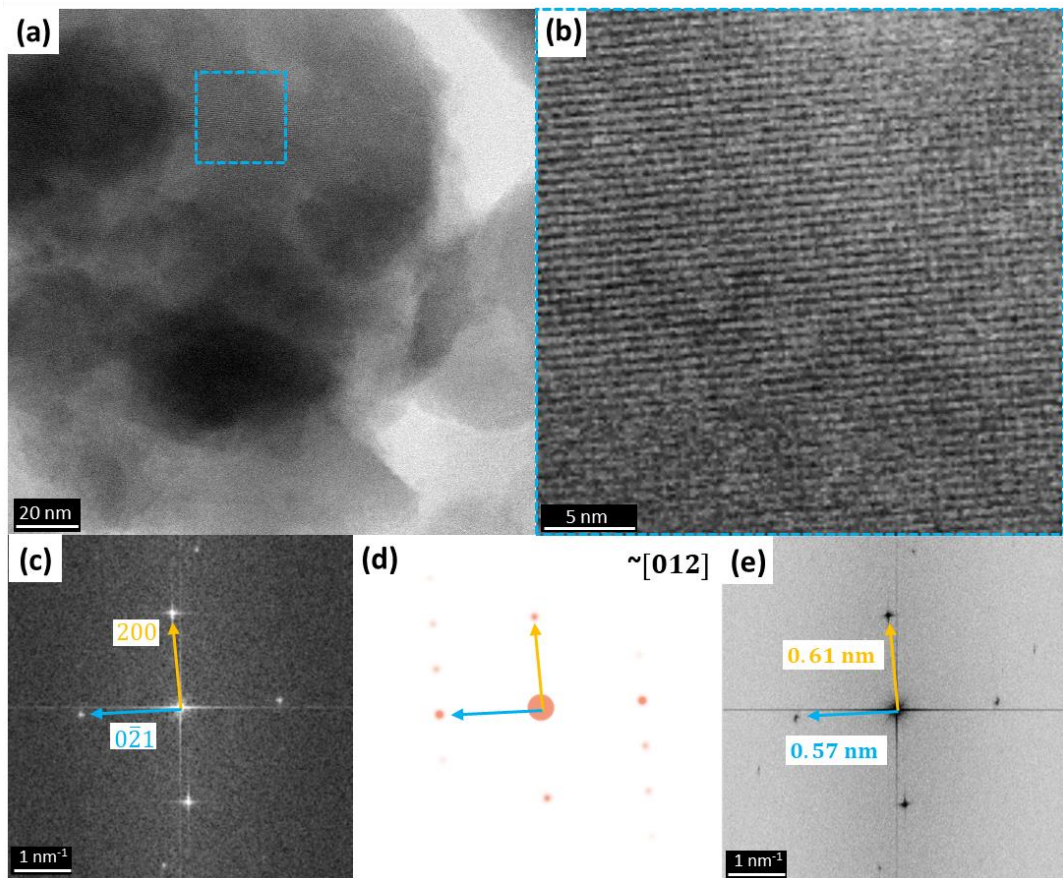


Figure 5.26 (a) BF-STEM crossed lattice image of AZ1-2 taken in 450 kX magnification, (b) enlarged area taken from highlighted dotted box (c) FFT from crystal (A) of which zone axis was indexed of $[012]$ direction, (d)-(e) simulated electron diffraction pattern and crystal orientation along $[012]$ direction. Orange circles correspond to (200) reflection of 0.61 nm lattice spacing, green circles correspond to $(02\bar{1})$ reflection of 0.57 nm lattice spacing.

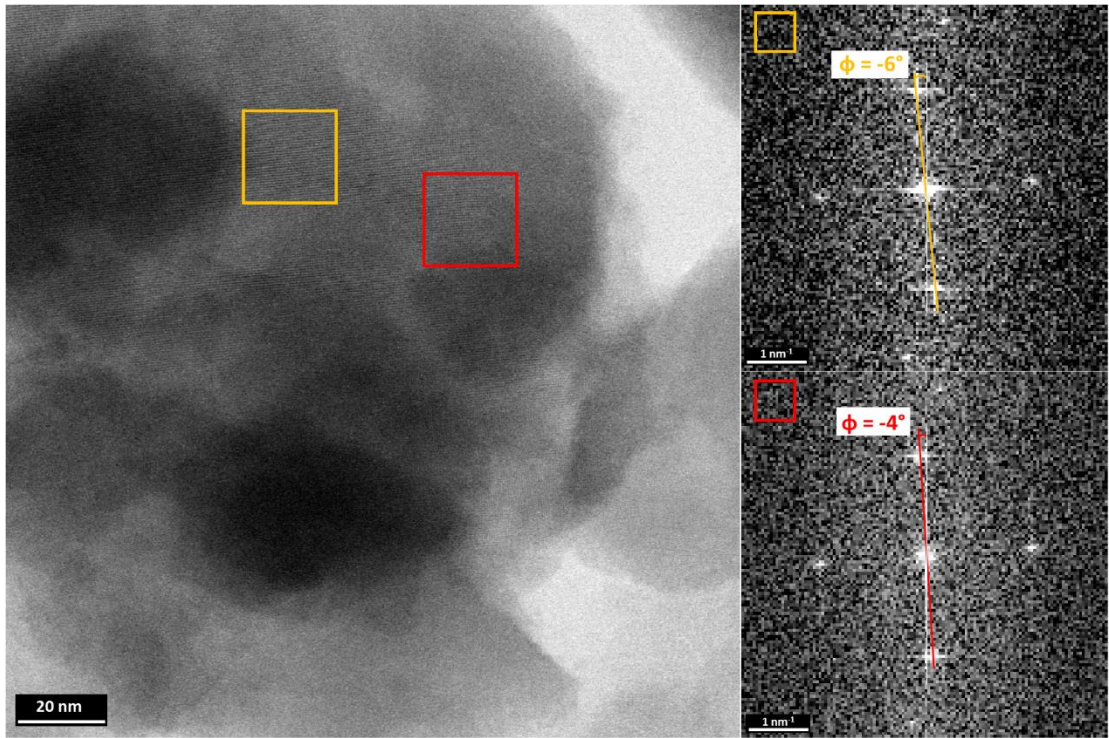


Figure 5.27 BF-STEM lattice image of AZ1-2 and corresponding FFTs were taken from areas marked by yellow and red squares indicating the slight displacement of the (200) reflection of 0.61 nm lattice spacing by 2 degrees suggesting the presence of strains.

The cropped BF-STEM lattice image of AZ1-2 from Figure 5.26b and its corresponding Wiener-filtered image are shown in Figure 5.28. The lattice image restored with the Wiener filter effectively enhances image components at high frequencies and defects in the crystalline lattice are more clearly visible and marked by yellow and red lines/arrows. However, these defects are also visible in the raw image. Furthermore, some more successful attempts show lattice fringes can be observed from different crystals in two magnifications: (i) same 450 kX with the image pixel size of 0.165 nm (area 1) and (ii) at higher, 640 kX magnification with the image pixel size of 0.116 nm (giving electron fluence of 467 e⁻/Å², area 2) and presented in Figure 5.29. Enlarged areas taken from highlighted red boxes show defects in lattice planes i.e. (i) distortion of the lattice planes and presence of line defects in area 1 and (ii) highly distorted lattice planes in area 2.

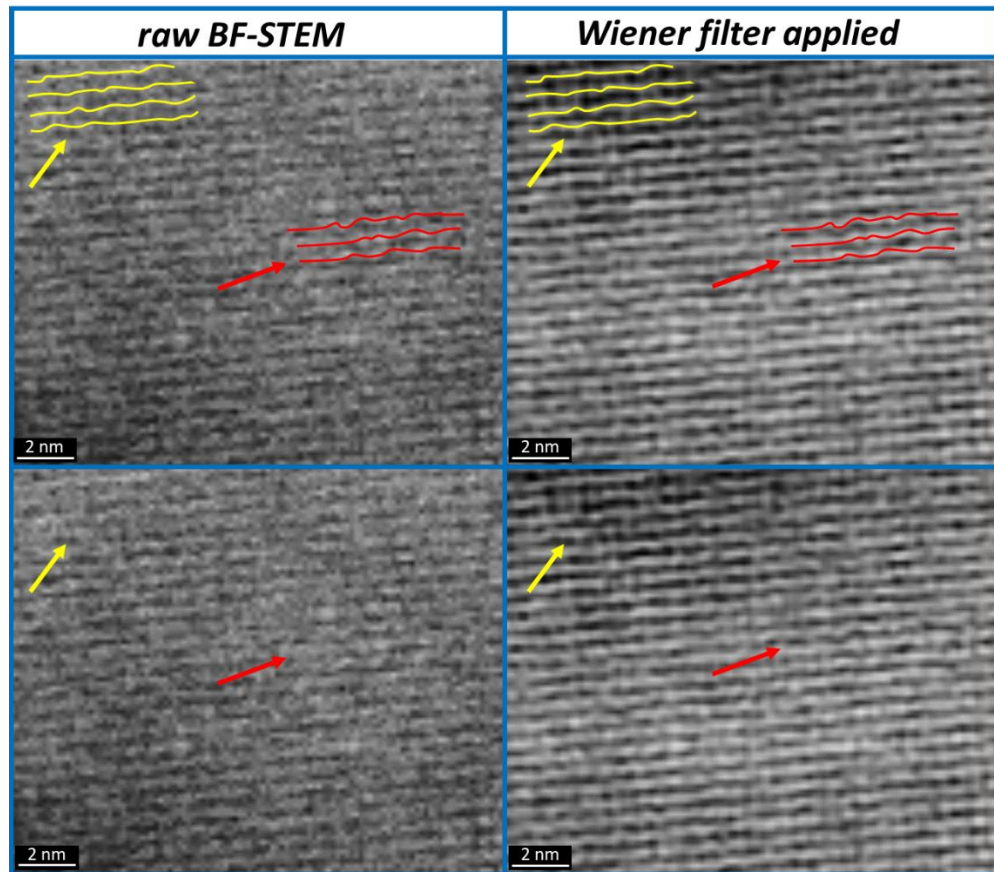


Figure 5.28 Experimental BF-STEM and corresponding Wiener-filtered images of AZ1-2. Defects are marked by yellow and red lines/arrows.

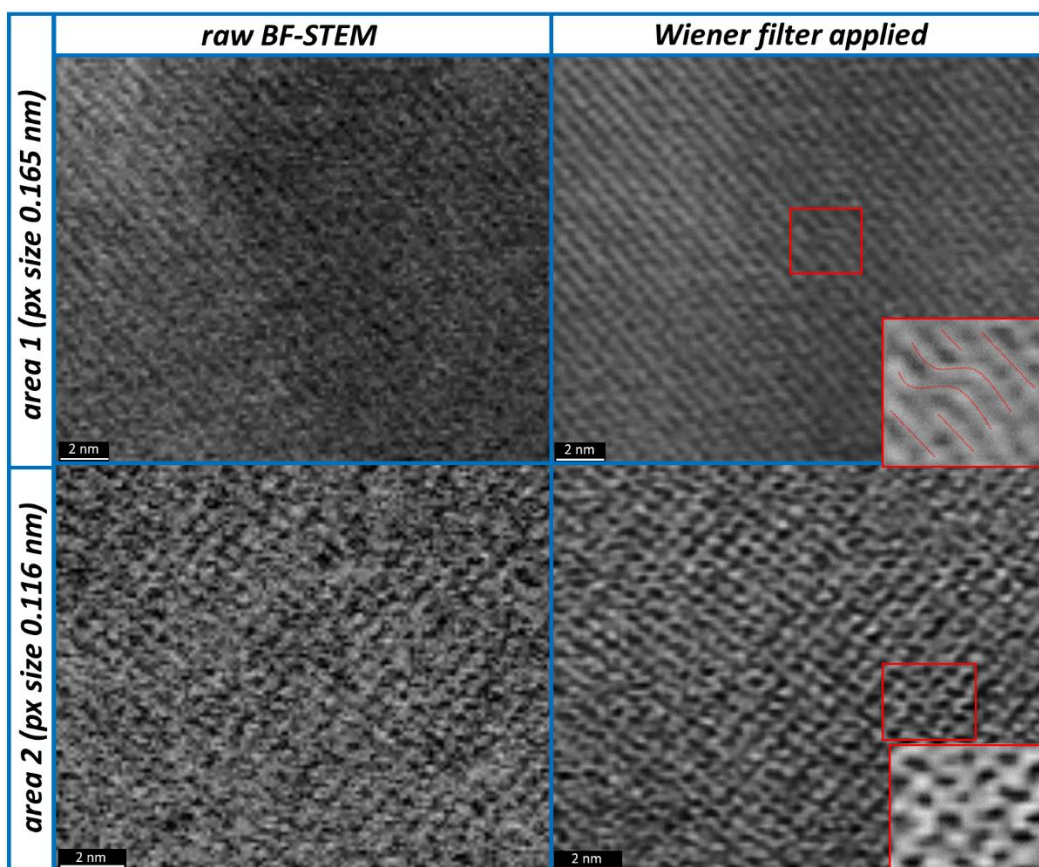


Figure 5.29 BF-STEM crossed lattice image and Wiener filtered images of AZ1-2 taken in 450 kX (pixel size of 0.165 nm) and 640 kX magnification (pixel size of 0.116 nm). Enlarged areas taken from highlighted red boxes show defects in lattice planes.

Based on the presented crossed-lattice images of AZ1 and AZ1-2, it was possible to apply a geometric phase analysis (GPA) plug-in in GMS software (Du H., 2018) in order to investigate the presence of strains in these atomic lattices. GPA is performed by comparing the phase of a set of perfect planes to the planes measured from an image. Results shown in Figure 5.30(c)-(d) and (g)-(h) suggest the presence of strains for each sample; however, the number of distorted atomic planes is higher for AZ1-2. From the XRD pattern of AZ1-2 (Figure 5.7), it can be seen that lattice parameter a is slightly higher than for AZ1 indicating lattice expansion. This may be related to the protonation process and suggests there are defects or distortions as a result of sodium replacement. Quantitative distortion analysis can be performed by comparison to an unstrained image. In the case of beam-sensitive samples, such a reference image can be obtained by computer-simulated variations of the BF-STEM micrographs.

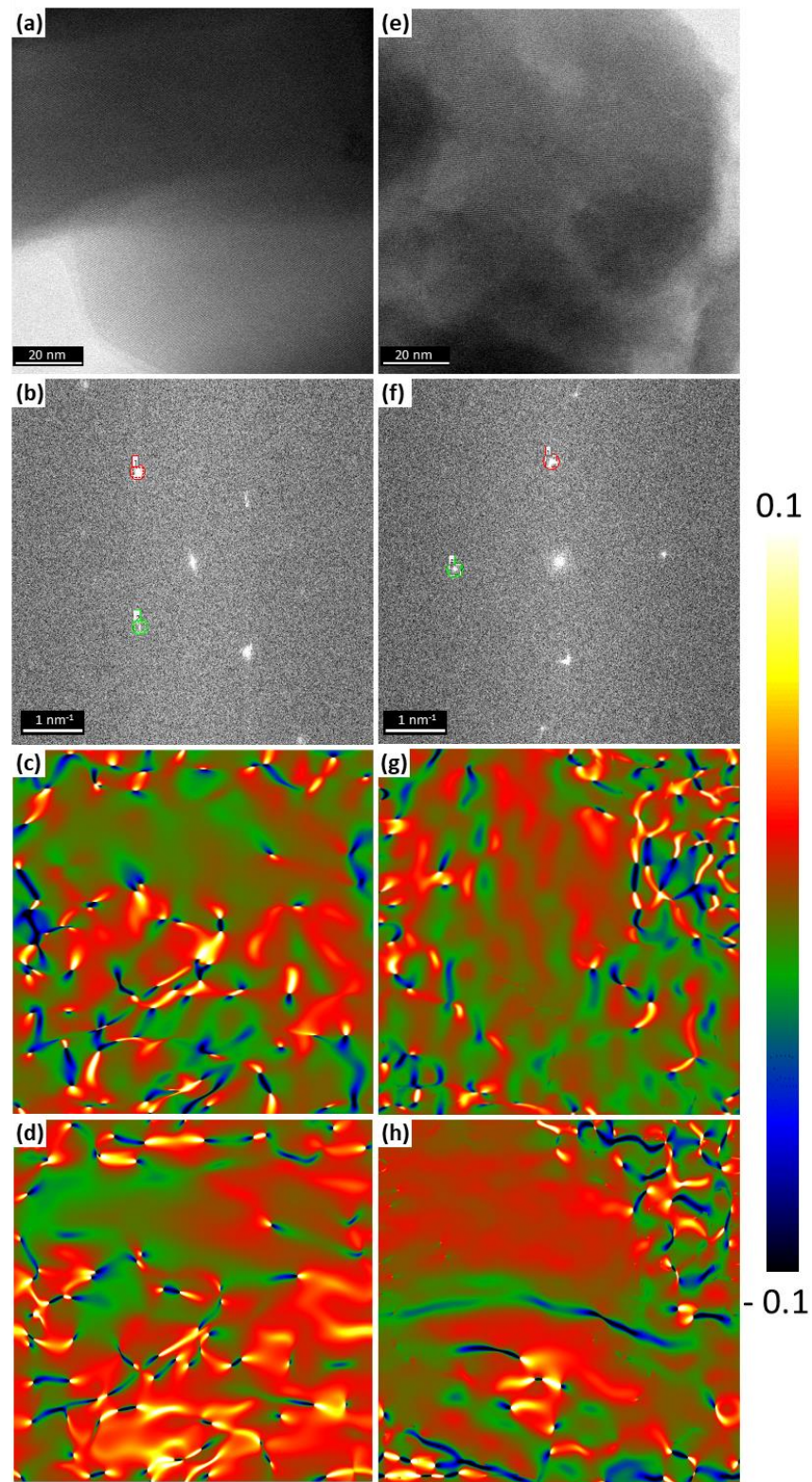


Figure 5.30 Geometric phase analysis of AZ1 (a)-(d) and AZ1-2 (e)-(h): BF-STEM image, FFT, GPA strain image ϵ_{xx} component of the strain tensor and GPA strain image ϵ_{yy} component of the strain tensor.

5.8 Chapter Summary

The study presented in this chapter aimed to demonstrate the possibilities of using electron microscopy techniques for the analysis of inorganic microporous crystalline sodium zirconium cyclosilicate hydrate. This was undertaken on two laboratory synthesized test samples of sodium zirconium cyclosilicate hydrate with varying Na^+/H^+ ratios as-provided by AstraZeneca, AZ1 (containing a small fraction of sodium cations exchanged for hydrogen) and AZ1-2 (containing a larger fraction of sodium cations exchanged for hydrogen).

Surface morphology was investigated by SEM. The particles of AZ1 and AZ1-2 are crystalline aggregates of cubic-shaped crystallites and the primary cubic size is $\sim 1\text{-}2\ \mu\text{m}$ and the particle size of aggregated crystals is 10s of μm . Significant differences in surface morphology were observed at high magnification. The crystallites surface of AZ1 was rather smooth, with only several micro-cracks while the AZ1-2 crystal surface was covered with numerous spherical particles ranging in size from a few to two hundred nanometers. The average maximum Feret diameter for AZ1 of $22.5 \pm 1.0\ \mu\text{m}$ indicates that the particles of AZ1 are significantly larger than particles of AZ1-2 with an average particle size of $12.5 \pm 0.5\ \mu\text{m}$. AZ1 particles have more irregular shapes than AZ1-2, which results in a larger perimeter and thus less circularity and solidity.

The calculated critical fluence for AZ1 and AZ1-2 was determined as $700 \pm 300\ \text{e}^-/\text{\AA}^2$ and $500 \pm 150\ \text{e}^-/\text{\AA}^2$, respectively. However, C_F for AZ1-2 orientated on-zone was calculated as $2000 \pm 1600\ \text{e}^-/\text{\AA}^2$, four times higher than C_F for randomly orientated AZ1-2.

STEM-EDX analysis of a mineral standard (albite) proved the experimental Na/Si ratio is in accurate agreement with the nominal mineral value. Then, STEM-EDX was performed under the same conditions to investigate the distribution of Na^+ within crystals of AZ1 and AZ1-2. Nominal atomic ratios of Na/Si were calculated as 0.67 and 0.5 for AZ1 and AZ-2, respectively. Quantitative composition analysis is difficult because of damage and mobility/loss of sodium under both the ion and electron beam plus in any solvent suspensions used to prepare a sample for TEM. Semi-quantitative STEM-EDX analysis of drop-cast powders at an estimated fluence of $\sim 17 \times 10^3\ \text{e}^-/\text{\AA}^2$ shows that the Na/Si ratio is 0.57 ± 0.04 for AZ1, 0.46 ± 0.04 for AZ1-2 under cryo-acquisition conditions. AZ1 does indeed have more sodium than AZ1-2, however, Na^+ content is below the expected value

in both samples. Based on the line profile analysis, the Na/Si composition is uniform within the crystals of both samples; however, some nanoscale hot spots of sodium are present. STEM-EDX data from the smaller particles at the surface of AZ1-2 suggests these particles are silicates rather than fragments of the primary AZ1 particles.

BF-STEM was applied to acquire crystal lattice images and provide an indication of the presence of strains in AZ1 and AZ1-2. Within the image dose budget, crossed lattice images of AZ1 and AZ1-2 were collected at a STEM magnification of 450 kX and 640 kX (giving 0.165 nm and 0.116 nm probe size), respectively. Lattice spacings were measured to be 0.73 nm indexed as $(11\bar{1})$ and 0.57 nm indexed as (021) for AZ1 which correspond to viewing along $[\bar{3}1\bar{2}]$ crystal direction. AZ1-2 crystal is orientated close to a different viewing direction of $[012]$ and crossed lattice spacings are measured to be 0.61 nm and indexed as (200) and 0.57 nm indexed as $(0\bar{2}1)$. Wiener filter effectively enhances BF-STEM cross-lattice images and allows for the identification of distortion in the crystal lattice. The preliminary results of geometric phase analysis suggest the presence of strains for each sample; however, strain in AZ1-2 might be marginally higher than for AZ1.

Overall, TEM analysis of sodium zirconium cyclosilicate hydrate is challenging because it is both sensitive to sodium loss on irradiation (and solvation) and its pores are not linear throughout any one crystal direction. Indirect effects of protonation such as a change in particle size and shape, contamination by fine silicate particles and an increase in strain have been detected.

Chapter 6 Investigation of Structural Changes During Hydration and Dehydration of a Model Channel Hydrate, Theophylline

This chapter demonstrated the possibility to use (scanning) transmission electron microscopy, especially phase contrast BF-TEM and scanning electron diffraction, to (i) probe structural information at the unit cell level of theophylline crystals and (ii) investigate the structural changes during the hydration and dehydration of this model channel hydrate. The implemented strategy for low-dose imaging allows for the first-time acquisition of atomically resolved lattice images, both of anhydrous theophylline form II and monohydrate. It was possible to identify defects in the crystalline lattice of the monohydrate form. Hydration of theophylline anhydrous form II does not occur in the solid state and it is a solution-mediated route with a dissolution-re-precipitation phase transformation profile. Theophylline anhydrous form II crystals changed their orientation upon contact with water or on storage in high relative humidity conditions (> 90% RH). On prolonged exposure, the particles can break up and transform into highly distorted crystals of form II. The monohydrate form is only observed to precipitate via homogenous nucleation and crystal growth. Dehydration of theophylline monohydrate is a slow process starting from surfaces with exposed water channels via surface etching, and finally, water is removed via diffusion from the centre of a particle along water channels.

Dehydration of the monohydrate form, results in the formation of highly disordered metastable form III crystals. In low humidity conditions, theophylline form III can adsorb water and locally transform back to monohydrate form. However, during heating, the monohydrate form transforms gradually to form III and then, at 90-100 °C transforms rapidly to a more stable form II. The analysis presented here at the single particle level with observation of both, morphology and structural changes, offers an in-depth understanding of the phase transformation.

6.1 Background

Identifying and understanding phase transformations of organic drug compounds, especially when exposed to water during processing or storage, is of great importance to the pharmaceutical industry. Hydrated forms of active pharmaceutical ingredients can alter the dissolution profile of a drug. Limiting hydration requires identification and understanding of reaction pathways to develop improved processing, formulation, and storage.

Theophylline, a model channel hydrate, can exist either as an anhydrate form (form I, II, IV, VI, VII) or a monohydrate form. Theophylline anhydrous form II ($C_7H_8N_4O_2$, *A*) is a kinetically stable form at room temperature and this form is used as an active pharmaceutical ingredient (API). Form II rapidly transforms to the monohydrated form ($C_7H_8N_4O_2 \cdot H_2O$, *M*) when placed in contact with water at ambient temperature or during storage in high humidity conditions (Figure 6.1) (De Smidt et al., 1986; Rodríguez-Hornedo et al., 1992; Suzuki et al., 1989). Depending on the conditions, dehydration of form *M* can be a one-step process leading to the formation of form *A* or a two-step process, with the first and second steps leading to the formation of a metastable intermediate form III (similar structure to *M*, *A*^{*}) and the form *A*, respectively (Figure 6.1) (Agbada and York, 1994; Nunes et al., 2006; Paiva et al., 2021). The presence of metastable form III or the monohydrate form in a final product can have serious consequences on performance leading to increased tablet hardness and lower dissolution rate (Phadnis and Suryanarayanan, 1997).

The structures and simulated Bravais–Friedel–Donnay–Harker (BFDH) morphology of the theophylline anhydrous form II and monohydrate are presented in Figure 6.2. The major structural differences between these forms occur in the hydrogen-bonding network, molecular orientation and arrangement and crystal unit size and type. Infinite water chains of form *M* propagate along [100]. Given the significant changes in molecular packing of theophylline anhydrous form II to monohydrate, the conversion is unlikely to occur in the solid state.

However, many studies reported that these phase transformations occur in the solid state by fitting hydration/dehydration experimental data to the solid-state transformation equations and rate-controlling models (Amado et al., 2007; Matsuo and Matsuoka, 2007; Nunes et al., 2006; Paiva et al., 2021; Tantry et al.,

2007) unless there is a clear indication of using the solvent as hydration/dehydration medium (De Smidt et al., 1986; Jørgensen et al., 2004; Rodríguez-Hornedo et al., 1992). Amado et al. (2007) postulated that the hydration of theophylline form II to monohydrate form is a one-step nucleation process, described by the Avrami–Erofeev equation of exponent 0.5 i.e. by heterogeneous nucleation and diffusion-limited growth of monohydrate needles on the existing form II phase. Suzuki et al. (1989) reported that the dehydration under isothermal conditions followed the Avrami-Erofeev equation with the same exponent of 0.5 or with a slightly lower exponent of 0.25 (suggesting more limited growth) (Agbada and York, 1994; Duddu et al., 1995). These studies linearized the experimental data using the best-fit solid-state models assuming these processes occur in the solid state due to rapid transformation. However, if these phase transformations occur in the presence of either solution, high humidity condition or vapour, it is considered that these changes need to occur via solution or vapour-mediated phase transformation. De Smidt et al. (1986) reported the monohydrate form crystallizes on the surface of the anhydrous form and that the transformation kinetics depend on the boundary layer thickness. These observations indicate a solvent-mediated phase transformation. Rodríguez-Hornedo et al. (1992) also observed that anhydrous form II crystals in an aqueous suspension act as a substrate for nucleation and epitaxial crystal growth of the monohydrate phase i.e. a solvent-mediated transformation.

Thus theophylline provides a good model compound for assessing anhydrate/hydrate phase transformation. A (S)TEM study could reveal essential information about the hydration and dehydration mechanism of channel hydrates, as well as providing a mechanistic understanding of the reaction pathway/s.

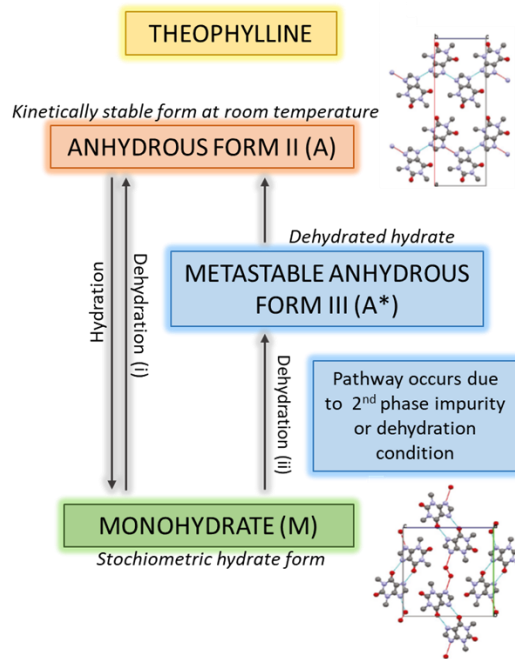


Figure 6.1 Schematic of phase transformation pathways between theophylline form II and monohydrate. Hydration is a one-step process, however, dehydration can be a one or two-step process depending on dehydration conditions (temperature and/or relative humidity).

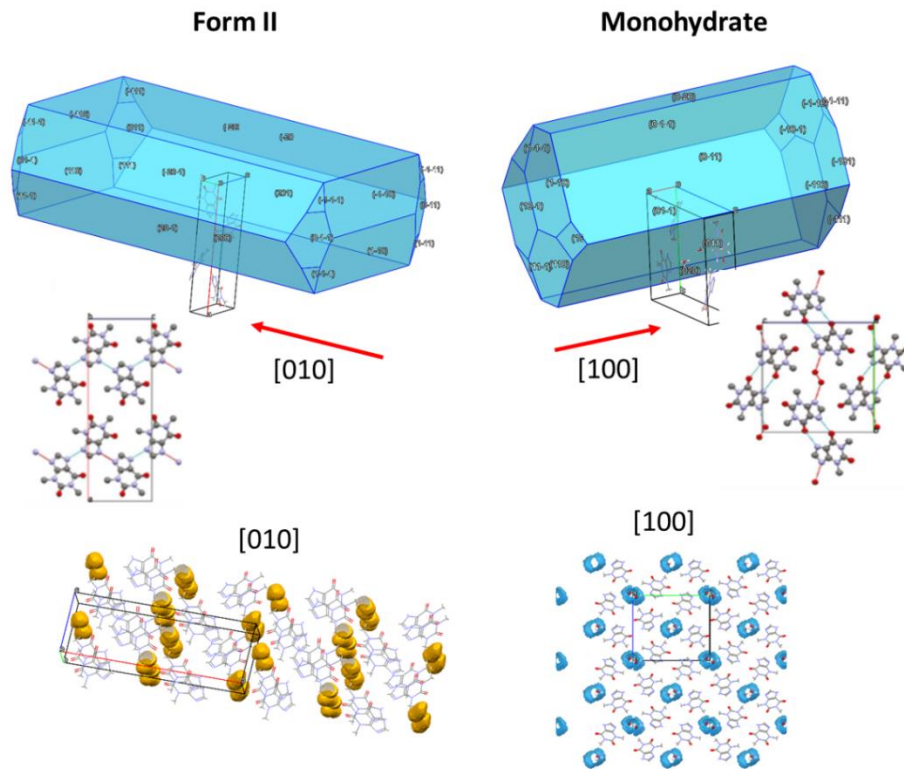


Figure 6.2 Structures with simulated BFDH morphology of the forms of theophylline: (i) form II and (ii) monohydrate calculated in Mercury 2022.2.0. Small voids of form II can be seen when crystals are orientated in [010] and water channels of monohydrate form can be observed in [100].

6.2 Materials and Methods

6.2.1 Sample Preparation

Theophylline anhydrous form II was purchased from Sigma-Aldrich and the samples of form II were prepared for TEM by two different methods:

- *A1* - as-bought powder of anhydrous form II was slightly crushed using a mortar/pestle to reduce the size of crystallites for TEM analysis.
- *A2* - as-bought powder of anhydrous form II was dissolved in nitromethane followed by heating to ~60 °C to obtain a saturated solution. Then, a drop of the solution was drop cast onto a TEM holey or continuous carbon grid and left to evaporate.

Partially hydrated form II plates *A3* were produced after contacting recrystallized form II plates on the TEM grid (i.e. from sample *A2*) with water for 10 minutes and then rapidly plunge frozen into liquid ethane (Leeds) or liquid nitrogen (ePSIC, Diamond), thereby retaining any absorbed water.

Theophylline monohydrate was prepared by three methods:

- *M1* - the TEM grids and a silicon substrate with recrystallized anhydrous form II (sample *A2*) were stored in high humidity conditions in a desiccator maintained at 93% relative humidity over a saturated potassium nitrate solution (KNO_3) and monitored for 7 weeks. (Chang and Sun, 2017)
- *M2* – evaporative recrystallisation from water by dissolving anhydrous form II powder in ultrapure water at ~70 °C under continuous stirring. When fully dissolved, the system was allowed to cool slowly to room temperature (~20 °C) under continuous stirring for a period of 24 h. The precipitate was filtered and allowed to dry at room temperature for 2 days.
- *M3* - evaporative recrystallization from ethanol:water by dissolving anhydrous form II powder in ethanol:water solution at a 3:2 molar ratio and heated to ~55 °C. The solution was allowed to cool slowly to ~35 °C under continuous stirring for a period of 3 h. When the first precipitation occurs, a drop of the solution was pipetted onto a holey carbon or continuous carbon film TEM grid and left to evaporate (Figure 6.3). The precipitate was filtered and analysed by pXRD. The water activity (a_w) of the ethanol:water mixtures is estimated to be >0.68 at 25 °C (Allan and Mauer,

2017), however, due to the volatility of the ethanol during heating, it might reach a higher value.

The dehydration of theophylline monohydrate *M3* was studied *in-situ* by thermally accelerated dehydration using a Gatan heating holder (up to 100 °C) and by vacuum dehydration in the TEM column at room temperature (~20 °C).

Sample IDs, polymorphs, and preparation methods are summarised in Table 6.1. In this chapter, the sample names will be referred to using the proposed IDs for easier identification.

Table 6.1 Type of samples used in the experiments.

ID	Polymorph	Preparation
A1	anhydrous form II	as-bought
A2	anhydrous form II	recrystallisation from nitromethane
A3	anhydrous form II	A2 + contact with water
M1	anhydrous form II + monohydrate	A2 stored in 93% RH
M2	monohydrate	recrystallisation from water
M3	monohydrate	recrystallisation from ethanol:water

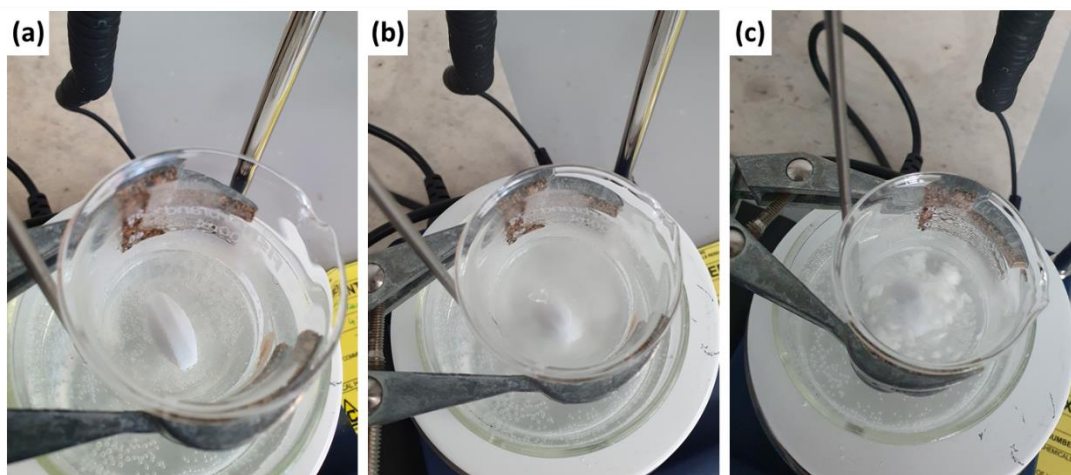


Figure 6.3 Recrystallisation of theophylline monohydrate: (a) form II powder was dissolved in water/ethanol solution and heated to ~55 °C; (b) the solution was allowed to cool slowly to ~35 °C and precipitation occurs and (c) the solution is cooled to room temperature and then precipitates were filtered out for pXRD measurement.

6.2.2 Powder X-Ray Diffraction

The powder X-ray diffraction (pXRD) patterns of all prepared samples were measured on a D8 Advance diffractometer using copper radiation (Cu $K\alpha$) at a wavelength of 1.54180 Å. For a fast collection of data, especially for the monohydrate form to avoid dehydration, the diffraction pattern was recorded using a 0.5 s/0.02° scanning speed over 2θ range from 5° to 40°. All powder samples were placed into a sample holder and pressed by a glass slide to produce flush surfaces between the powder and the sample holder. Samples: A2, A3, and M1 were prepared directly onto a silicon substrate. The experimental pXRD patterns of theophylline phases were compared with the theoretical pXRD patterns calculated from crystal structure files (.cif) of: (i) theophylline anhydrous form II (REF code: BAPLOT01), (ii) theophylline monohydrate (REF code THEOPH01 and SI from Paiva et al. (2021)), (iii) theophylline metastable form IIIa and IIIb (SI from Paiva et al. (2021)) in CrystalDiffract software. Crystallographic parameters are summarised in Table 6.2.

Table 6.2 Crystallographic parameters for anhydrous theophylline form II (REF code: BAPLOT01), monohydrate (REF code: THEOPH01 and from Paiva et al. (2021)) and metastable forms III (from Paiva et al. (2021)).

	anhydrous form II (REF code: BAPLOT01)	monohydrate (REF code: THEOPH01)	monohydrate (from Paiva)	metastable form IIIa (from Paiva)	metastable form IIIb (from Paiva)
Space group	Pna2 ₁	P2 ₁ /n	Pc	P2 ₁ /n	P2 ₁ /n
Crystal system	Orthorhombic	Monoclinic	Monoclinic	Monoclinic	Monoclinic
a (Å)	24.6120	4.468	4.35589	4.25667	4.48328
b (Å)	3.8302	15.355	15.0368	15.23611	13.82268
c (Å)	8.5010	13.121	13.39735	13.78663	12.71439
α (°)	90	90	90	90	90
β (°)	90	97.792	101.9574	97.43541	97.38406
θ (°)	90	90	90	90	90

6.2.3 (S)TEM Operating Condition

TEM analysis was mainly performed on the Titan Themis³ operated at 300 kV and coupled with a monochromator to control electron dose. For initial imaging and diffraction collection, all TEM analysis was carried out using bright-field (BF) mode with the electron fluence of 0.08-0.09 e⁻/Å². Phase contrast lattice imaging was acquired at a total electron fluence of 31 e⁻/Å² (sum of fluence during searching particles, initial BF-TEM and SAED pattern acquisition and phase-contrast lattice image acquisition) and an image pixel size of 0.076 nm. Focusing was performed on a sacrificed part of the particle and this fluence is not counted in the total electron fluence. Additional high-resolution imaging was performed on JEOL ARM300CF 300 kV TEM at ePSIC (Diamond Light Source) using a direct electron detector (DE16) within the same electron dose budget and the image pixel size of 0.06 nm.

Low-dose scanning electron diffraction (SED) was performed within the total electron fluence of ~ 8 e⁻/Å² using a Merlin/Medipix pixelated electron counting detector at ePSIC.

Double-tilt holders (Gatan and JEOL), single-tilt cryo-transfer holders (Gatan and Fischione) and a heating holder (Gatan) were used for (S)TEM acquisition.

6.2.4 Polarised Light Microscopy

Optical images were collected on an Olympus BX51 microscope with a polarising filter on *A3* and *M1* samples. Samples were prepared directly on glass slides.

6.2.5 Data Analysis

BF-TEM micrographs and SAED patterns were acquired and further processed using Digital Micrograph (Gatan Microscopy Suite) and ImageJ. Colour coding is implemented in this chapter. Red refers to theophylline anhydrous form II and green to theophylline monohydrate. SED data were processed using HyperSpy and pyXem. Structural .cif files were downloaded from the Cambridge Structural Database and reported structure files available in the Supporting Information (Paiva et al., 2021) and further analysed using CCDC Mercury 2022.2.0 (Macrae et al., 2020) and CrystalMaker package. Water space and water interaction maps were simulated using the 'Hydrate Analyser' tool in Mercury 2022.2.0.

6.3 Crystallisation of Anhydrous Theophylline Form II and Theophylline Monohydrate

All anhydrous theophylline form II samples, *A1-A3* and theophylline monohydrate samples, *M1-M3* were analysed by powder XRD and TEM to obtain information about the desired phase and to confirm suitable morphology and orientation for further TEM experiments. To obtain the most accurate information, *A2*, *A3*, and *M1* were recrystallized on a TEM grid and on a silicon substrate for pXRD at the same time.

Figure 6.4 shows a comparison between the 'as-bought' anhydrous form II (*A1*) and form II recrystallized from nitromethane solution (*A2*). BF-TEM image of *A1* shows a random particle morphology, thickness, and orientation (that also might result from the sample grinding). This sample is not suitable for further TEM analysis, even though the presented SAED pattern shows a low index [110] zone axis, it took ~2 h to find this particle.

Sample *A2* shows a significant change in morphology and theophylline form II (*A2*) is recrystallized as thin, large, plate crystals oriented to [100] zone axis - ideal for TEM analysis.

The experimental powder XRD pattern of A1 was shown to have equivalent distinct peak positions to those listed in the structure file for anhydrous theophylline form II (ref code: BAPLOT01) at 7.17° (200), 12.64° (201), 14.38° (400), 17.78° (401), and 20.88° (002) 2θ . The powder XRD pattern of A1 shows the relative intensities of peaks more closely resemble that of the simulated form II pattern which assumes a random orientation of particles. However, higher angle peaks and especially $\{x1z\}$ peaks move toward lower 2θ , and a significant variation in relative peak intensity is observed. This discrepancy is quite common in the literature and can be explained by variations in sample preparation, packing characteristics, and/or preferred orientation (Chang and Sun, 2017). Powder XRD experimental pattern of A2 shows the significant increase in $\{200\}$ peak intensities suggesting a preferred orientation of crystallites in the [100] and corresponds with the simulated pXRD of form II plates with preferred [100] orientation calculated in CrystalDiffract (Figure 6.4b, purple trace). An additional peak at 6.49° 2θ cannot be indexed to any theophylline polymorph and might indicate other crystalline phases or (200) of different crystal unit sizes. The peak at 12.64° 2θ can be indexed to the (201) plane and suggests that not all crystallites are oriented to the [100] zone axis.

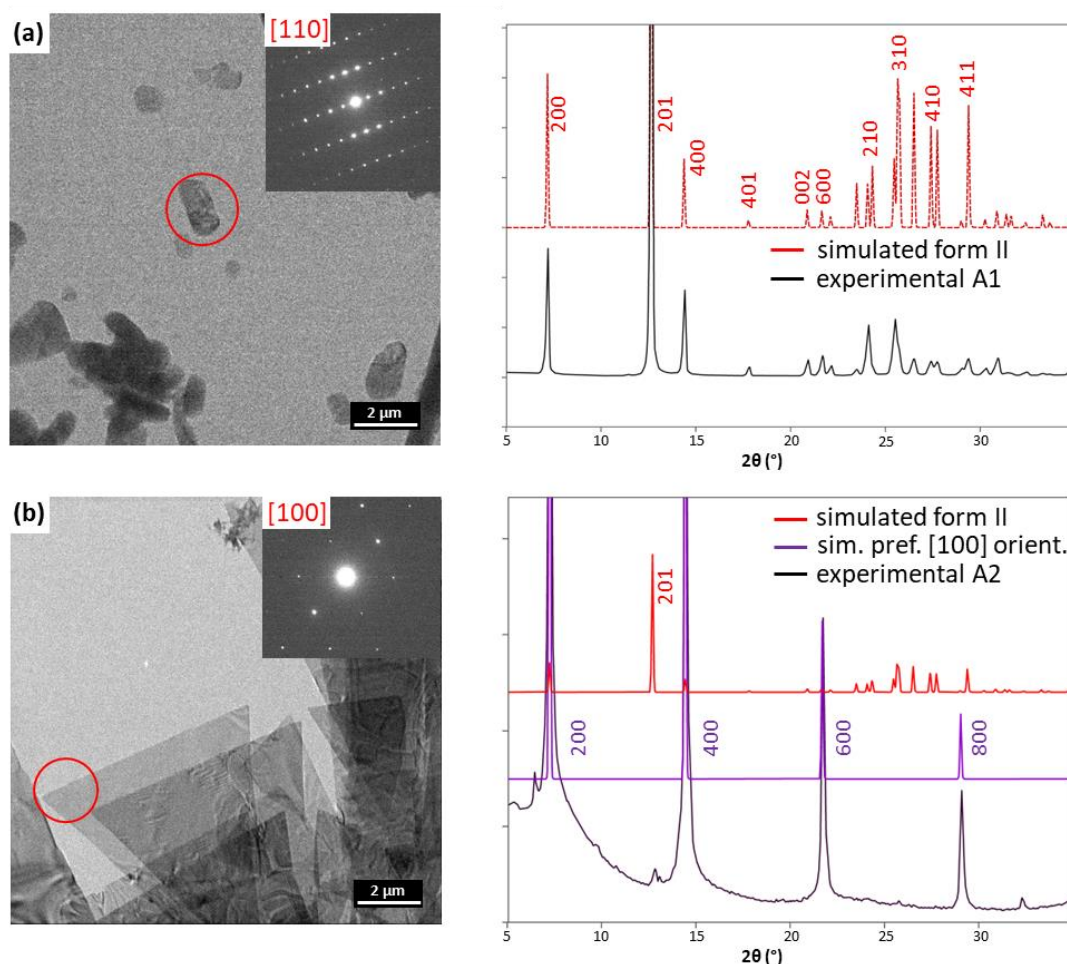


Figure 6.4 BF-TEM images with corresponding indexed SAED patterns (taken from areas marked by red circles) and overlay of corresponding experimental and simulated powder XRD patterns of: (a) ‘as-bought’ anhydrous theophylline form II (A1) and (b) anhydrous theophylline form II recrystallised from nitromethane solution (A2). The strong, distinct Bragg peaks of theophylline anhydrous form II are labelled with corresponding Miller indices.

BF-TEM, a polarised light microscopy image and a SAED pattern of theophylline form II plates after contact with water (A3) indicate a significant change in morphology and orientation of theophylline. The presence of the strong periodic contrast fringes in BF-TEM and the SAED pattern indexed to [131] suggest that A2 plates changed orientation after contact with water. De Smidt et al. (1986) stated that form II rapidly converts to monohydrate form after contact with water, however here after 10 min of water immersion, there is no observation of any new hydrated phase. Moreover, the powder XRD pattern of A3 was still in good agreement with the simulated pattern of form II with preferred [100] or [131] orientation (Figure 6.5). An additional peak at 13.75° 2θ cannot be indexed to

theophylline form II or monohydrate (Figure 6.5b, marked by an asterisk). The closest matching theophylline peak is at 13.61° 2θ and corresponds to the (002) plane of theophylline monohydrate. Figure 6.5c shows a comparison between A2 and A3. There is an observable decrease in peak height and increase in FWHM of A3 compared to A2 suggesting loss of crystallinity with the reduction in sample amount (red arrows). However, the relative peak height from [100] towards [131] at 12.64° (201) 2θ increased and suggests a change in orientation (blue arrow).

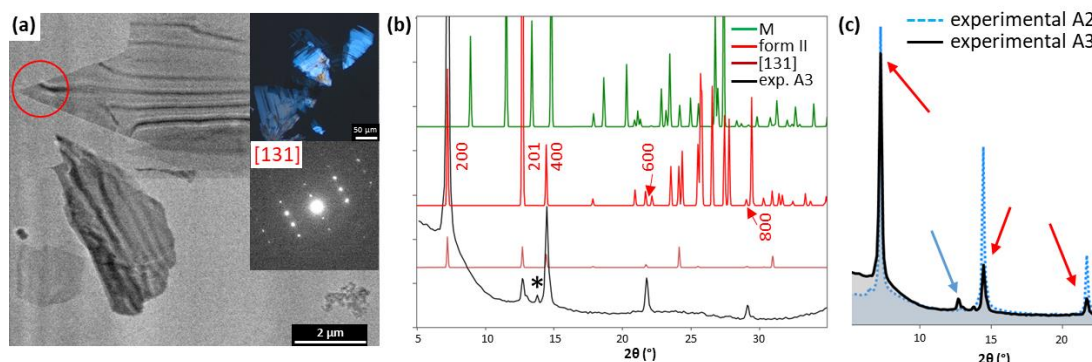


Figure 6.5 (a) Cryo-BF-TEM, polarised light microscopy image and SAED pattern taken from the area marked by a red circle of theophylline form II plates after contact with water (A3); (b) overlay of experimental A3 and simulated powder XRD patterns (green – theophylline monohydrate, red – form II, burgundy – preferred [131] orientation of form II). Unindexed peak is marked by an asterisk; (c) overlay of experimental patterns of A2 and A3. The red arrows indicate a decrease in the peak intensities and the blue arrow indicates an increase in peak intensity at 12.64° (201) 2θ .

The results of the storage of A2 plates in high humidity conditions show that the conversion of anhydrous form II to monohydrate form M1 is a slow process, which might be related to the specific morphology and orientation of the A2 plates (Figure 6.6). Otsuka et al. (1991) stated that anhydrous theophylline of different morphologies has different hydration kinetics. BF-TEM and corresponding SAED patterns of M1 stored in 93% RH for 1-week show that both phases are present, a majority of anhydrous form II with different orientations and morphology to the original A2 plates and a minority of monohydrate crystallites present as separate particles on the TEM grid (Figure 6.6a and b). Polarised light microscopy images of M1 after storage in 93% RH for 3 weeks show significant fragmentation of the original, triangular form II plates and growth of new monohydrate phases as needles (Figure 6.6c). The powder XRD pattern of the 1-week storage in 93% RH does not reveal any trace of the monohydrate form, however, the monohydrate form was found by TEM (Figure 6.6d). The first XRD detectable level of

theophylline monohydrate was found after 3 weeks of storage in 93% RH, and the characteristic peaks at 8.90° (011), 11.51° (020), and 18.61° (031) 2θ of monohydrate form were resolved. A powder XRD pattern after 7 weeks of storage in 93% RH showed still incomplete conversion, however, it did reveal a significantly larger fraction of monohydrate form than for earlier weeks.

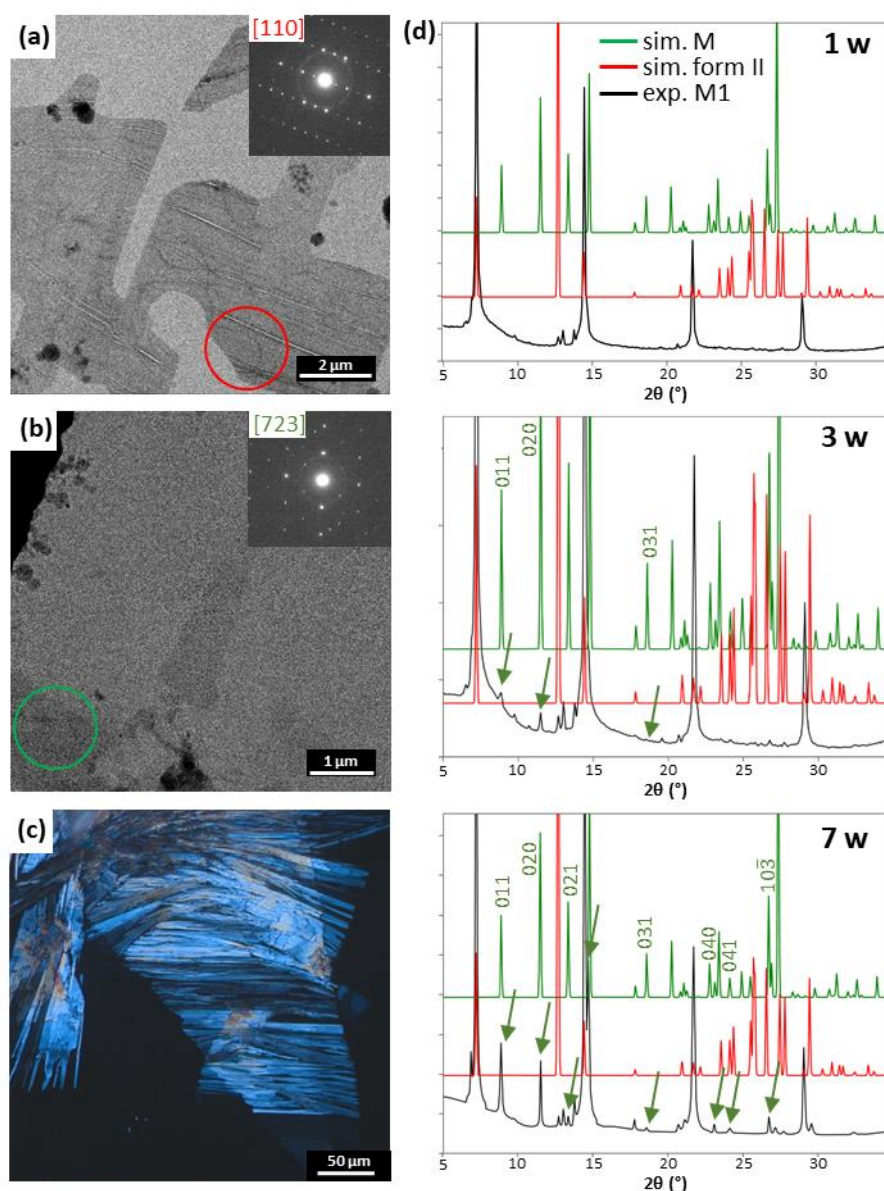


Figure 6.6 (a)-(b) BF-TEM and SAED pattern of *M1* stored in 93% relative humidity for 1 week, identifying both: mainly form II (a) and some monohydrate phases (b), respectively; (c) polarised microscopy image of *M1* after 3 weeks showing significant fragmentation of the original triangular form II plates or growth of new monohydrate phases; (d) powder XRD patterns of *M1* taken after 1, 3 and 7 weeks of storing *A2* in 93% RH condition. Characteristic peaks of theophylline monohydrate are marked by green arrows.

Figure 6.7 shows the comparison between theophylline monohydrate recrystallized from water (*M2*) and theophylline monohydrate recrystallized from ethanol:water solution (*M3*). BF-TEM and the corresponding SAED pattern of *M2* indicate random morphology and orientation which might be related to sample preparation (grinding) (Figure 6.7a). However, the *M3* sample shows some promising morphology for TEM analysis (relatively thin and faceted particles). Most crystallite shapes follow the same trend as for *M2*, however, it is possible to find rod-shaped particles that can be ambiguously indexed to theophylline monohydrate (Figure 6.7b). Experimental powder XRD patterns of *M2* and *M3* are in good agreement with the simulated structure file of theophylline monohydrate (ref code: THEOPH01). However, the peaks at 14.72° and 17.80° of the *M2* sample are slightly shifted towards lower 2θ as compared to experimental peaks at 14.79° (031) and 17.86° (022) 2θ . Higher angle peaks are also moved toward lower 2θ and the variation in relative peak intensity and increase in FWHM can indicate some loss of crystallinity and variation in molecular arrangement.

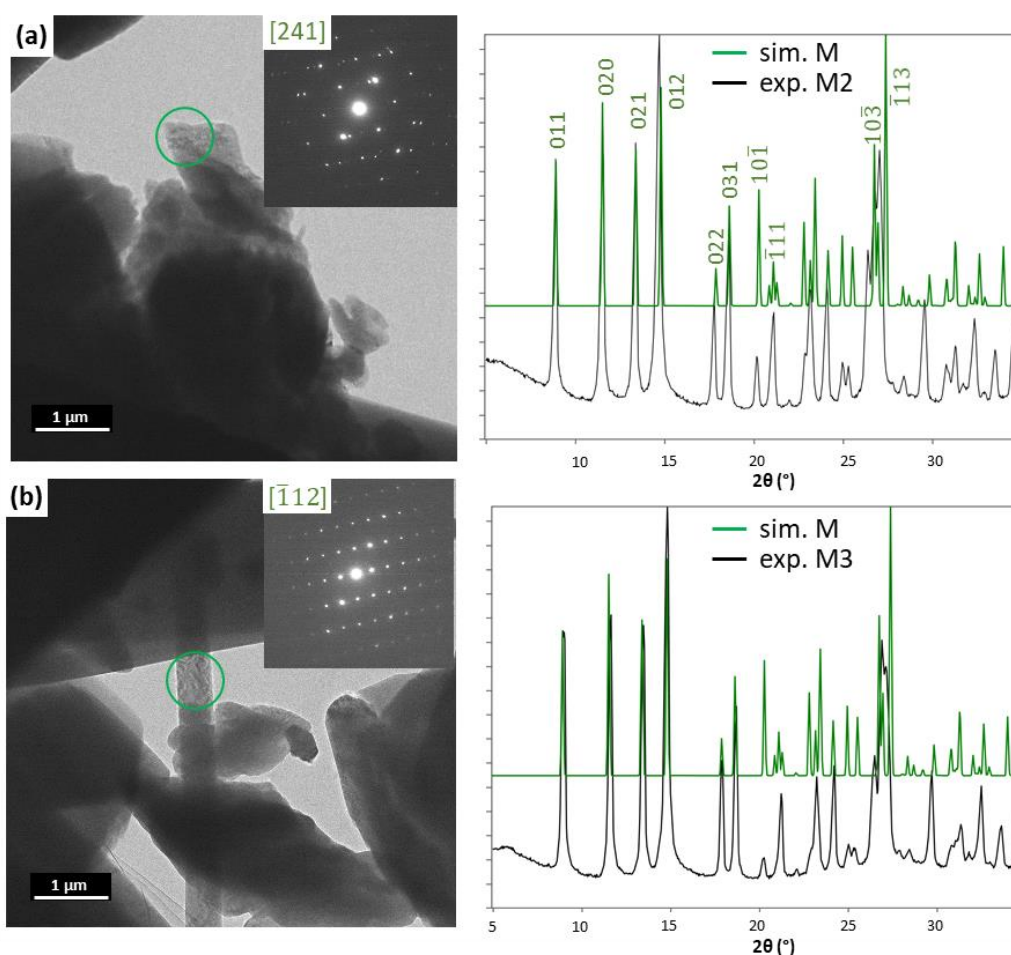


Figure 6.7 BF-TEM image with corresponding indexed SAED pattern (taken from areas marked by the green circle) and overlay of corresponding experimental and simulated powder XRD patterns of: (a) theophylline monohydrate recrystallised from water (*M2*) and (b) theophylline monohydrate crystallised from ethanol:water (*M3*). The distinct form *M* peaks are labelled with corresponding Miller indices.

6.4 Critical Fluence Measurement

The critical fluence (C_F) of theophylline form II has been extensively investigated for different variables, determining the effect of sample and experimental conditions (Cattle et al., 2016; Cattle, 2019). The two largest values of C_F were identified using: (i) a 300 keV accelerating voltage ($\sim 36 \pm 8 \text{ e}^-/\text{\AA}^2$) and (ii) a 200 keV, a graphene support substrate and 93 K sample temperature ($\sim 42 \pm 4 \text{ e}^-/\text{\AA}^2$). However, for optimisation of phase-contrast lattice imaging in this study, it is important for a sample to be well-orientated to a low zone axis, therefore a double tilt holder needs to be used. The cryo holder available in Leeds only allows a single (α) tilt. A graphene substrate is $\sim 5x$ more expensive than a typical holey/continuous carbon film and only provides an additional few $\text{e}^-/\text{\AA}^2$ in C_F so does not provide significant improvement in the signal-to-noise (SNR) ratio of

images. However, C_F benefits most significantly ($23 \text{ e}^-/\text{\AA}^2$ at 200 kV compared to $36 \text{ e}^-/\text{\AA}^2$ at 300 kV) by increasing acceleration voltage due to lower inelastic scattering cross-section and this condition will be used here for optimising lattice imaging of theophylline form II and monohydrate.

Figure 6.8a and b show a BF-TEM image of a tip of a triangular plate of theophylline form II before and after acquiring a series of electron diffraction patterns at increasing fluence. The loss of Bragg contours indicates a loss of crystallinity over the exposure period. The majority of the diffraction patterns of theophylline form II (sample A2) were indexed to the [100] zone axis (Figure 6.8c). Therefore, it was possible to assess a characteristic C_F for a specific interplanar spacing (Figure 6.8d-f). The average C_F , defined by the accumulated electron dose at which relative intensity decreases to $1/e$ ($\sim 37\%$), was measured from an exponential decay fit to all spots and was calculated to be 38 ± 8 (\pm SD) $\text{e}^-/\text{\AA}^2$. Generally, the outer spots that correspond to smaller d -spacing values, decrease in intensity faster than the inner spots that represent larger d -spacing values. Although a spot indexed to the $(0\bar{1}1)$ plane (3.49 \AA) exhibits a C_F more than two times higher than the (002) plane (4.25 \AA). This variation might be related to the different molecular groups present in particular planes, however, this requires further investigation to develop a more complete understanding. The decay profile of $(0\bar{1}1)$ exhibits an unusually long initial plateau up to $\sim 60 \text{ e}^-/\text{\AA}^2$ followed by a linear decay in spot intensity (Figure 6.8e). A plateau is generally observed at cryogenic temperatures (Wade and Pelissier, 1982), however, S'ari et al. (2018) observed this phenomenon in a room temperature measurement.

Diffraction spots have been grouped into two d -spacing ranges: (i) $> 2 \text{ \AA}$ and (ii) $< 2 \text{ \AA}$ and a summary of C_F values is presented in Table 6.3. To acquire lattice images, the cumulative electron fluence should be below the calculated C_F indicated by green shading ('safe zone') in Figure 6.8d-f and stated in the last column in Table 6.3 (on average $\sim 30 \text{ e}^-/\text{\AA}^2$). This is related to the fact that by exposing the sample to higher electron fluence (even not exceeding the average C_F), the fine spacings of the specimen are at the exposure where they are damaged more rapidly, and amorphous parts are formed making the interpretation of lattice imaging difficult. Simply reducing the electron dose rate reduces the SNR in the image. Therefore, a combination of the highest possible dose rate (within the 'dose budget'), reducing pre-exposure irradiation time of the

area of interest, and decreasing the noise level (e.g. using a direct electron detector when possible) should be implemented.

The critical fluence of theophylline monohydrate was measured to be similar to that of form II (29 vs 38 $e^-/\text{\AA}^2$). This may be due to a tight packing of water molecules within the narrow channels of form M and a BFDH morphology prediction suggests preferred crystal growth along these channels thereby minimising their surface exposure.

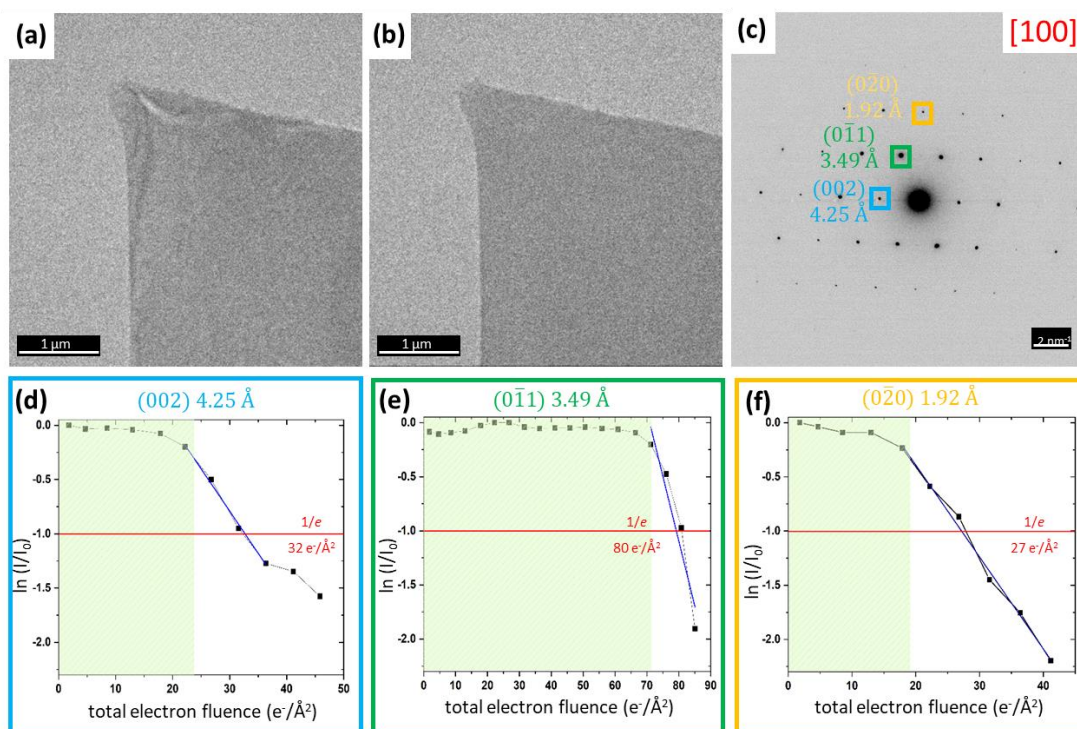


Figure 6.8 BF-TEM image of theophylline form II plate (A2) (a) before increasing fluence (b) after acquiring a series of electron diffraction patterns. (c) Typical diffraction pattern of A2 indexed to [100] zone axis and corresponding decay profiles of (d) (002) plane, (e) (011) and (f) (020). Green shading indicates a suggested 'safe zone' of C_F to acquire lattice imaging.

Table 6.3 Mean critical fluence (\pm SD) and optimal total electron fluence for d -spacing ranges of $> 2\text{Å}$, $< 2\text{Å}$ and an average C_F calculated from the series of electron diffraction pattern data.

Spacings	Mean critical fluence ($e^-/\text{Å}^2$) \pm SD	Optimal total electron fluence ($e^-/\text{Å}^2$)
$> 2\text{Å}$	60 ± 17	40
$< 2\text{Å}$	25 ± 7	15
average	38 ± 8	30

6.5 Lattice Imaging

The initial purpose of lattice imaging was to explore the feasibility of imaging water channels in theophylline monohydrate. The size of the water molecule is $\sim 3\text{Å}$ and water channels run along the a -axis of form M's crystal structure. Therefore, theophylline monohydrate particles need to be orientated to the [100] zone axis. The resolution limit for the maximum magnification that can be used here within the 'dose budget' of theophylline (image pixel size of 0.076 nm for OneView and 0.06 nm for DE16 is 1.52 Å and 1.20 Å, respectively. This assumption is based on the Nyquist limit of having at least twice the spatial frequency of the feature to be resolved i.e. twice the pixel size to the pore size in BF-TEM imaging.

All attempts to recrystallize theophylline monohydrate on or close to the [100] zone axis were unsuccessful. Based on the structure information and the predicted BFDH morphology of the theophylline monohydrate form, the smallest a -axis of form M is the fastest growth direction, dominated by π - π stacking. Aromatic solvents, that can prevent π - π stacking of the molecule and stunt growth along the a -axis direction, are miscible with water. However, a mixture of solvent and water is required to recrystallize the monohydrate form (to increase the water activity of the solution). Alcohol solvents can mix with water but do not block π - π interactions effectively. Water-soluble polymer additives might be an alternative here, but this requires extensive study.

Sample M3 did show a distinct morphology by TEM, in the form of the rod-shaped particles (Figure 6.7b). It was assumed the water channels might run along or close to the longest axis of these rods. Therefore, a FIB-TEM cross-section was

prepared from the specific site of a rod i.e. perpendicular to the longest face (Figure 6.9a). The disruption in the Bragg contour in the BF-TEM image confirms the retention of crystallinity on milling and indicates the presence of defects in the crystal structure (Figure 6.9b). Diffraction patterns from regions (i) and (ii) confirm that the sample is still crystalline, however, the orientation of the channels is not parallel to the viewing direction. The diffraction pattern of area (i) can be indexed to \sim [985] zone axis, and the crystal unit with water channels is simulated using Mercury 2022.2.0 (Figure 6.9(i)). To be normal to the channels in this orientation a cross-section should be taken diagonally across the rod axis (e.g. around $-70^\circ\alpha$ and $+5^\circ\beta$ here), however, this is more of a trial and error method as it is difficult to estimate the orientation of the crystal and channels in the FIB without prior orientation knowledge.

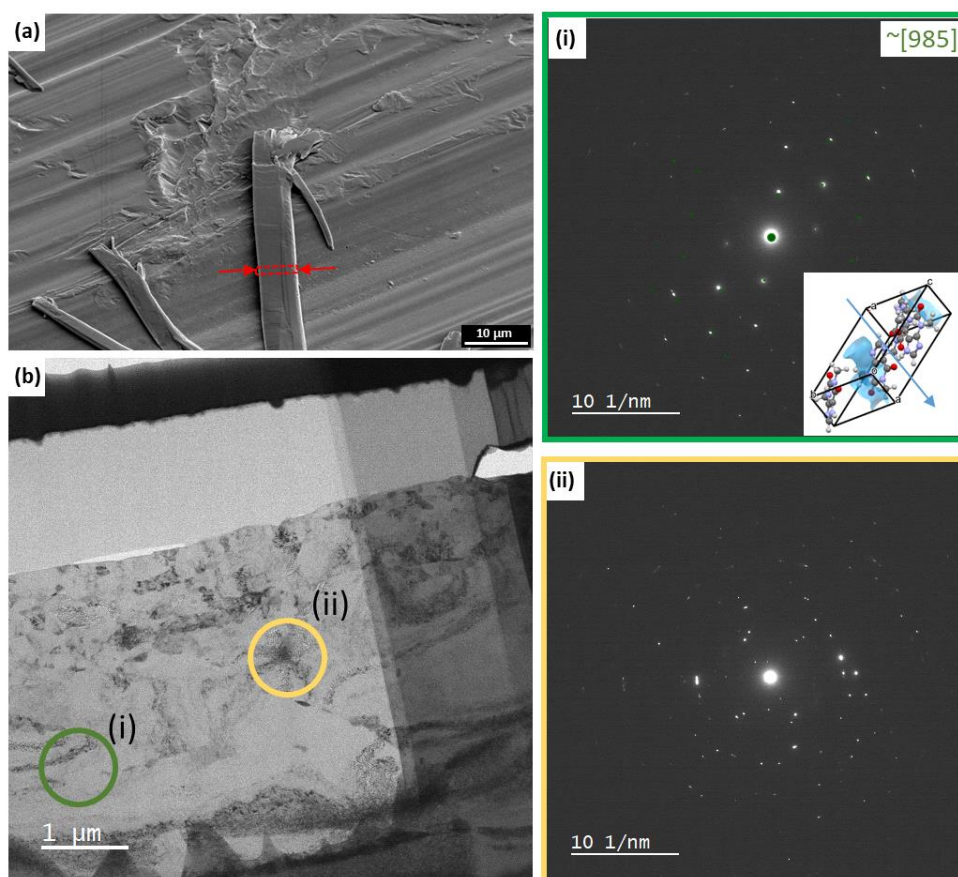


Figure 6.9 (a) SEM image of theophylline monohydrate (*M3*) with distinct morphology; (b) FIB-TEM cross-section from the area marked by red in (a). Corresponding diffraction patterns from regions (i)-(ii) confirm that the sample is still crystalline, however, channels are not orientated parallel to the view direction.

Lattice imaging of theophylline anhydrous form II and monohydrate orientated to a different zone axis than [100] was however performed to explore the potential

for detecting defects in the crystal structure. Defects or the presence of disordered regions within a solid can initiate polymorphic phase transformation e.g. surface nucleation often starts in distorted areas (Amado et al., 2007; Khoo et al., 2010). Lattice imaging can provide direct information on the type and distribution of defects in APIs, however, the identification of these defects depends primarily on the orientation of the crystallites to appropriate directions that show the projected image of a defect core as well as any distortion it causes and requires a SNR > 3-5 in the acquired images (Rose criterion).

One of the many successful attempts for lattice imaging of theophylline form II (A2) oriented to the [100] zone axis is presented in Figure 6.10. Focussing of the beam was done in an area nearby but separate from the area to be imaged (Figure 6.10a, yellow square). For the first time, lattice fringes of theophylline are observable in the real image (Figure 6.10c). The total electron dose used was ~ 31 e⁻/Å². The FFT and lattice image show visible spots resolving 0.35 nm *d*-spacing corresponding to the (011) lattice plane.

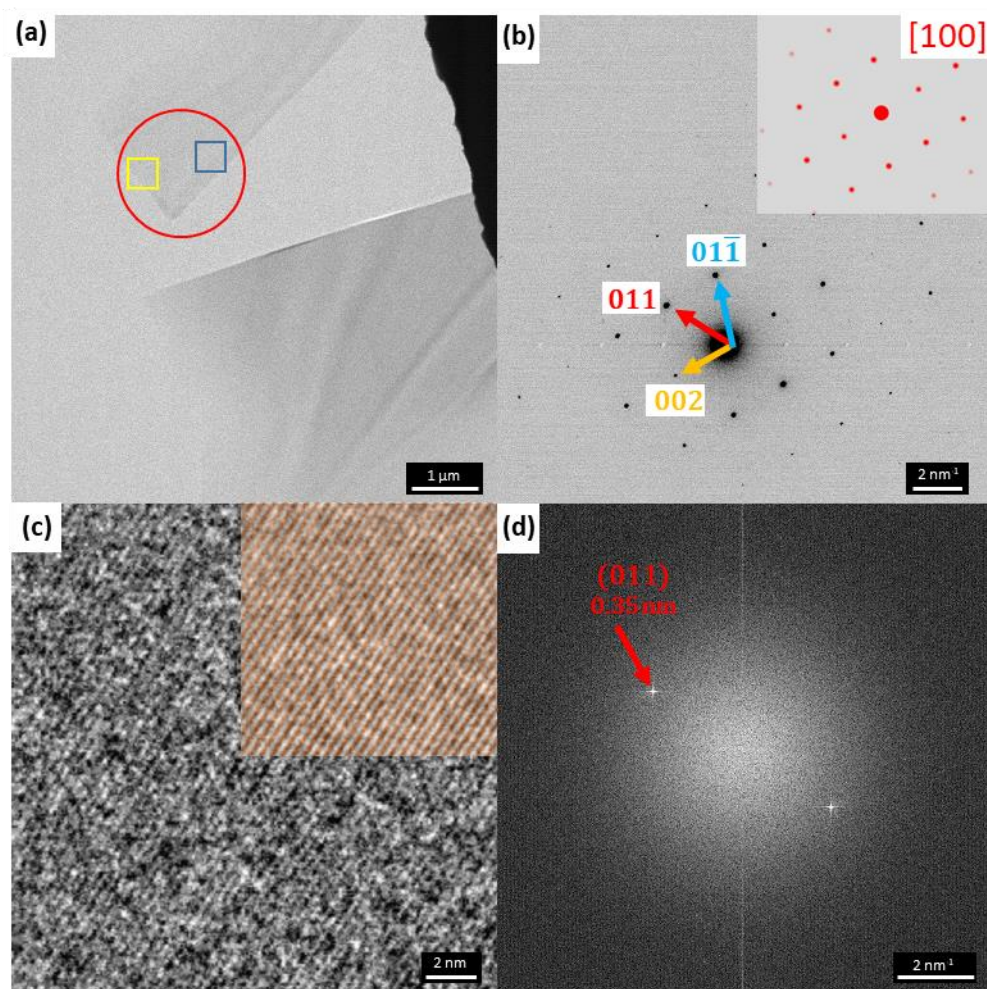


Figure 6.10 (a) Low-magnification BF-TEM image of theophylline form II (A2); (b) SAED pattern indexed to $[100]$ zone axis and taken from the area marked by the red circle in (a); (c) cropped phase-contrast lattice image from the area marked by the blue square in (a). Yellow square in (a) indicates a sacrificed area for focusing. The inset shows an inverse FFT of the image. (d) FFT from the area in (c) and 0.35 nm d -spacing indexed to (011) lattice plane can be resolved.

Further improvement in lattice imaging is presented in Figure 6.11. The crossed lattice fringes formed by the intersection of three sets of lattice fringes corresponding to (011) , $(0\bar{1}1)$ and (002) lattice planes of theophylline form II (A2) oriented to $[100]$ zone axis. The inset in Figure 6.11c shows the inverse FFT image for easier identification of crossed lattice fringes in the raw image. There is no obvious indication of the presence of defect sites, however, the imaged area represents a fraction of the available crystallite area.

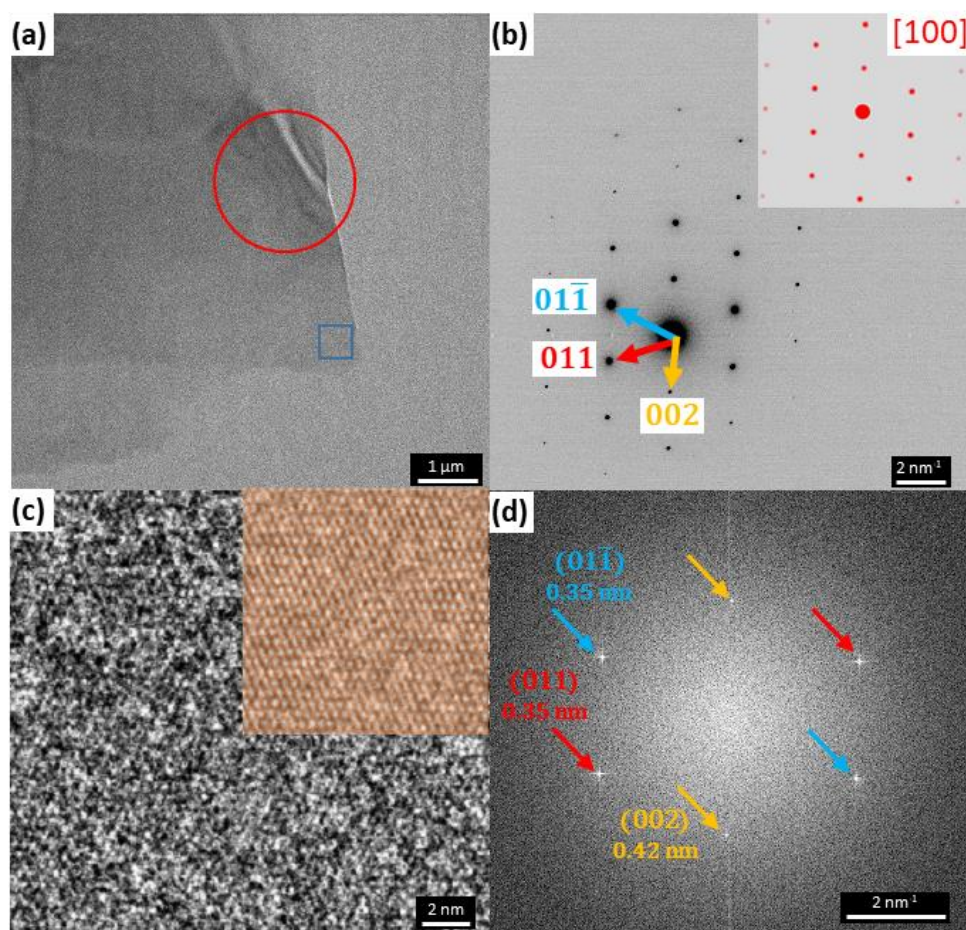


Figure 6.11 (a) Low-magnification BF-TEM image of theophylline form II (A2); (b) SAED pattern indexed to [100] zone axis and taken from the area marked by the red circle in (a); (c) cropped phase-contrast lattice image from the area marked by the blue square in (a) resolving cross-fringes. The inset shows an inverse FFT image. (d) FFT from the area in (c) and 0.35 nm *d*-spacing indexed to (0 $\bar{1}$ 1) and (011) lattice planes and 0.424 nm *d*-spacing indexed to (002) can be resolved.

Powder XRD confirmed the presence of the monohydrate phase in *M1* (Figure 6.6b-c). The particles found on the TEM grid that can be indexed to monohydrate form are very thin and suitable for lattice imaging. Therefore, phase contrast lattice imaging procedures were also successfully applied to the image, for the first time, lattice planes of theophylline monohydrate (*M1*) (Figure 6.12). The particle can be indexed to the [531] zone axis, however, the crystal unit simulation performed in CrystalMaker and Mercury 2022.2.0 shows that the water channels run perpendicular or slightly diagonal to the viewing direction (Figure 6.12b). Therefore, the water channels cannot be resolved in that orientation. Phase contrast lattice image from the area marked by the blue square in Figure 6.12a resolves 0.34 nm lattice spacing and corresponds to ($\bar{1}2\bar{1}$) lattice plane. However,

the FFT resolves three sets of lattice fringes corresponding to $(\bar{1}2\bar{1})$, $(\bar{1}12)$ and $(0\bar{1}3)$ lattice planes, but $(\bar{1}12)$ and $(0\bar{1}3)$ are not visible in the image. This can be explained by the fact that the power spectrum (FFT) spatially averages the weak images the lattice spacings of the many unit cells from the noisy image and any periodicity present in the field of view can be observed in the FFT (Kuo and Glaeser, 1975). Without a clear indication of $(\bar{1}12)$ and $(0\bar{1}3)$ in the raw image, an inverse FFT is not implemented here, as applying a periodic mask to the FFT can artificially introduce a periodic feature in the inverse FFT image (Ishizuka et al., 2018). As the diffraction pattern between theophylline anhydrous form II oriented to $[100]$ zone axis (Figure 6.11b) looks similar to the diffraction pattern of the monohydrate form oriented to $[531]$ zone axis (Figure 6.12b), the comparison between simulated diffraction patterns between the two phases was presented in Figure 6.12e. The differences in d -spacings and the relative angles between the planes allow for the unambiguous identification of the area in Figure 6.12a as the monohydrate phase.

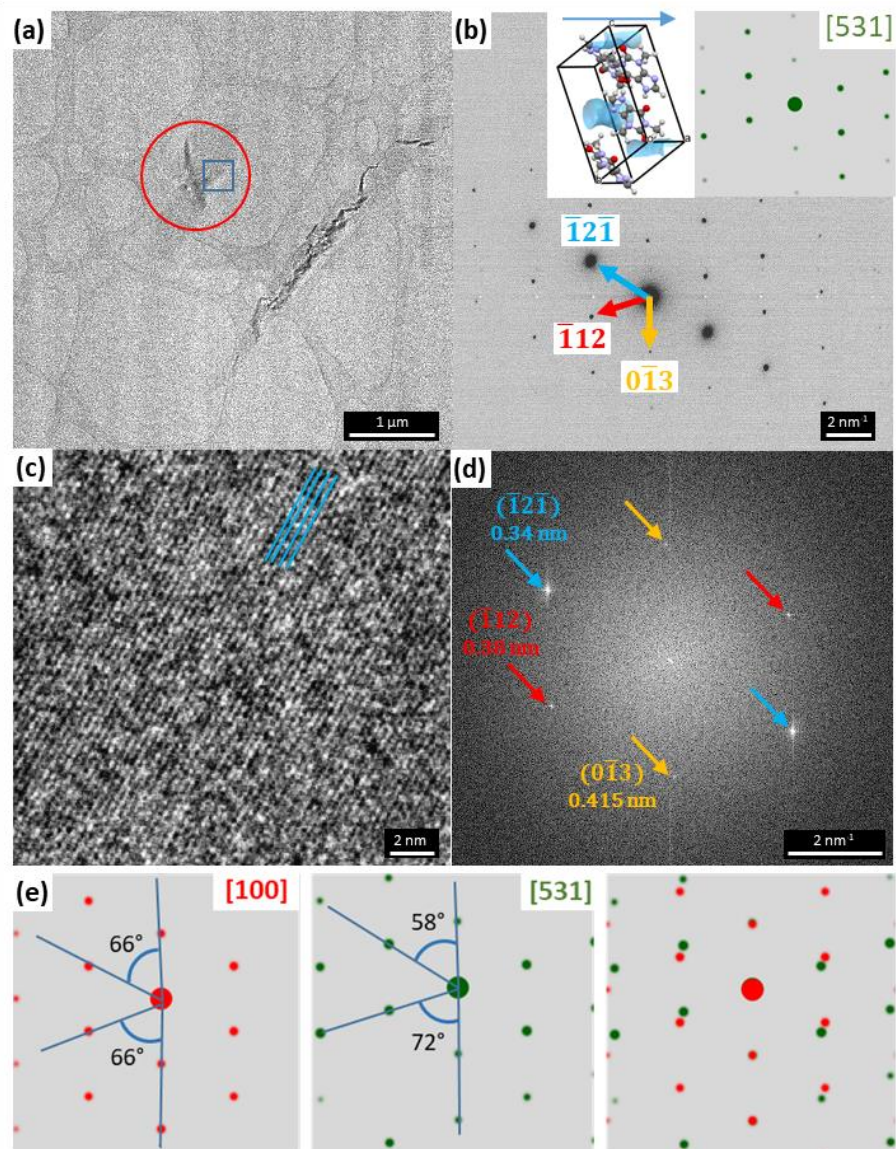


Figure 6.12 (a) Low-magnification BF-TEM image of theophylline monohydrate (*M1*); (b) SAED pattern indexed to $[531]$ zone axis and taken from the area marked by the red circle in (a). The inset represents the orientation of the unit cell and the direction of water channels is marked by a blue arrow; (c) cropped phase-contrast lattice image from the area marked by the blue square in (a) resolving cross-fringes. 0.34 nm lattice spacing is marked by blue lines. (d) FFT from the area in (c) and 0.34 nm d -spacing indexed to $(\bar{1}2\bar{1})$ 0.38 nm d -spacing indexed to $(\bar{1}1\bar{2})$ and 0.415 nm d -spacings indexed to $(0\bar{1}3)$ lattice planes can be resolved. (e) comparison between simulated diffraction pattern of theophylline form II oriented to the $[100]$ zone axis and monohydrate oriented to the $[531]$ zone axis. The differences in d -spacings and the relative angles between the planes allow for the unambiguous identification of the area in (a) as a monohydrate phase.

Further improvement with the image resolution can be obtained using a direct electron detector DE16 at ePSIC with higher detector quantum efficiency (DQE)

compared to the Gatan OneView 4K CMOS camera at Leeds and ePSIC. The comparison between the two types of cameras and two different modes for DE16 is presented in Figure 6.13. The images of gold particles were acquired at similar image pixel sizes between the two cameras (0.076 nm for OneView and 0.06 nm for DE16) with approximately $\sim 20 \text{ e}^-/\text{\AA}^2$ total electron dose per image. The dose was calculated from the beam profile and calibrated current measurement at ePSIC. The counting mode on the DE16 provides substantial improvement in the SNR and resolving lattice fringes within the same total electron dose compared to the low dose mode on the OneView. Moreover, the information transfer is improved to $<0.2 \text{ nm}$ as revealed from the corresponding FFT.

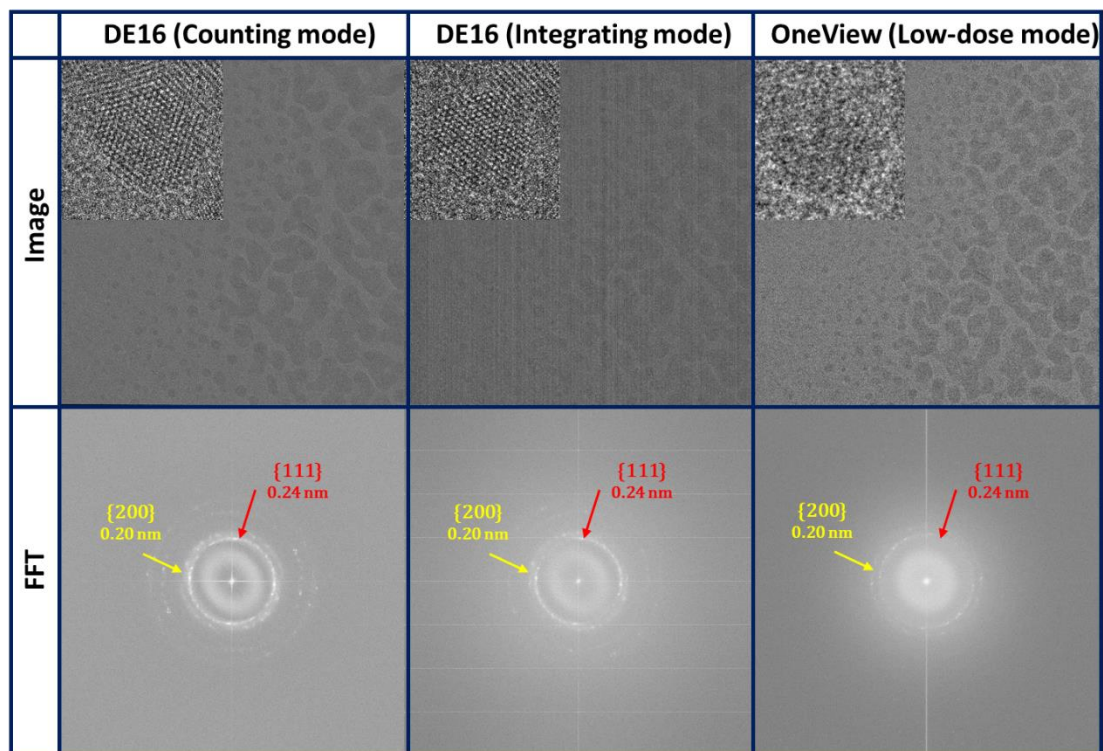


Figure 6.13 Comparison between different cameras and modes i.e. direct electron detector DE16 (counting vs integrating mode) and OneView (low dose mode) within the same total electron dose range of $\sim 20 \text{ e}^-/\text{\AA}^2$ on the model sample of gold particles. DE16 in counting mode provides substantial improvement in resolving lattice planes. Data acquired by Dr Thomas Slater, ePSIC, Diamond Light Source, UK.

However, the JEOL ARM300CF aberration-corrected microscope at ePSIC does not have an objective aperture to enhance contrast when the particle is in focus. This causes difficulties with navigating to an area of interest. Therefore, the lattice imaging procedure was adjusted and the following steps were implemented: (i) identifying the approximate minimum contrast z-height (this value needs to be

noted), (ii) dropping the stage significantly with the beam spread to enhance the contrast of the particle, (iii) moving to the sacrificed area of the particle to correct to Scherzer defocus, (iv) blanking the beam, (v) returning the stage to the noted z-height, (vi) re-set condenser lens to the saved setting for illumination using a OneView at 200 kX (pixel size of 0.076 nm) for easier correction of Scherzer defocus (vii) un-blank the beam, then acquiring multiple images and checking the FFT of the image (note the z-height of the image with the best Scherzer defocus), blank the beam (viii) dropping the stage again significantly with the beam spread to enhance the contrast of the particle, (ix) moving to the area of interest and returning the stage to the noted final z-height, (x) re-set condenser lens to the saved setting for illumination using DE16 (pixel size of 0.06 nm), (xi) un-blank the beam and acquire immediately, (xii) blank again after acquisition complete and repeat the procedure acquiring images along the particle.

A successful attempt to acquire phase-contrast lattice imaging of theophylline monohydrate (*M3*) using the direct electron detector DE16 is presented in Figure 6.14. Low-magnification BF-TEM image shows that the particle is electron transparent and orientated to $[\bar{4}1\bar{1}]$ zone axis of the monohydrate form, however, it exhibits unusual contrast that might be related to a highly defective crystal structure due e.g. to rapid crystallisation. Diffraction mode is not available on the JEOL ARM300CF, but the crystal orientation was extracted by indexing the spots in the FFT of the phase contrast lattice images. Cropped phase contrast lattice imaging in Figure 6.14c shows highly distorted lattice planes and resolves 0.33 nm lattice spacing corresponding to $(\bar{1}\bar{3}1)$ lattice plane.

Phase contrast lattice image from the area in Figure 6.14b was further investigated and corresponding FFTs were taken from four areas (i)-(iv) marked by purple (entire area), yellow, red and orange (cropped areas) squares (Figure 6.15). All planes $(\bar{1}\bar{3}1)$, $(\bar{1}\bar{2}1)$ and $(\bar{1}\bar{1}3)$ are marked in the phase contrast lattice image. The $(\bar{1}\bar{3}1)$ reflection of the 0.33 nm lattice spacing from the entire area (i) and cropped area (ii) have the same relative angle of -56° , however, there is a split in the spot intensity in area (iii) and the $(\bar{1}\bar{3}1)$ lattice plane is displaced by -2° and $+1^\circ$. There is also a small shift in area (iv) by -1° . The $(\bar{1}\bar{2}1)$ reflection of 0.35 nm lattice spacing changes the position between the areas by $\pm 1-2^\circ$. However, the position of the $(\bar{1}\bar{1}3)$ reflection of 0.33 nm lattice spacing remains the same across all (i)-(iv) areas, suggesting that the observed variations are

caused by the presence of distortion likely due to defects in the lattice planes and/or in the variation in the sample thickness or orientation.

The cropped raw phase contrast lattice image from the bottom part of Figure 6.15 indicates the presence of defects (Figure 6.16a and c). The lattice image was restored using a non-linear filter algorithm reported elsewhere (Du, 2015) and efficiently denoised to a clearer phase contrast lattice image (Figure 6.16b and d) without noticeable artefacts (Figure 6.16e and f). Defects in the crystalline lattice are more clearly visible e.g. short extra half plane is present suggesting point defects edge on, however, it is difficult to determine the exact nature of these defects.

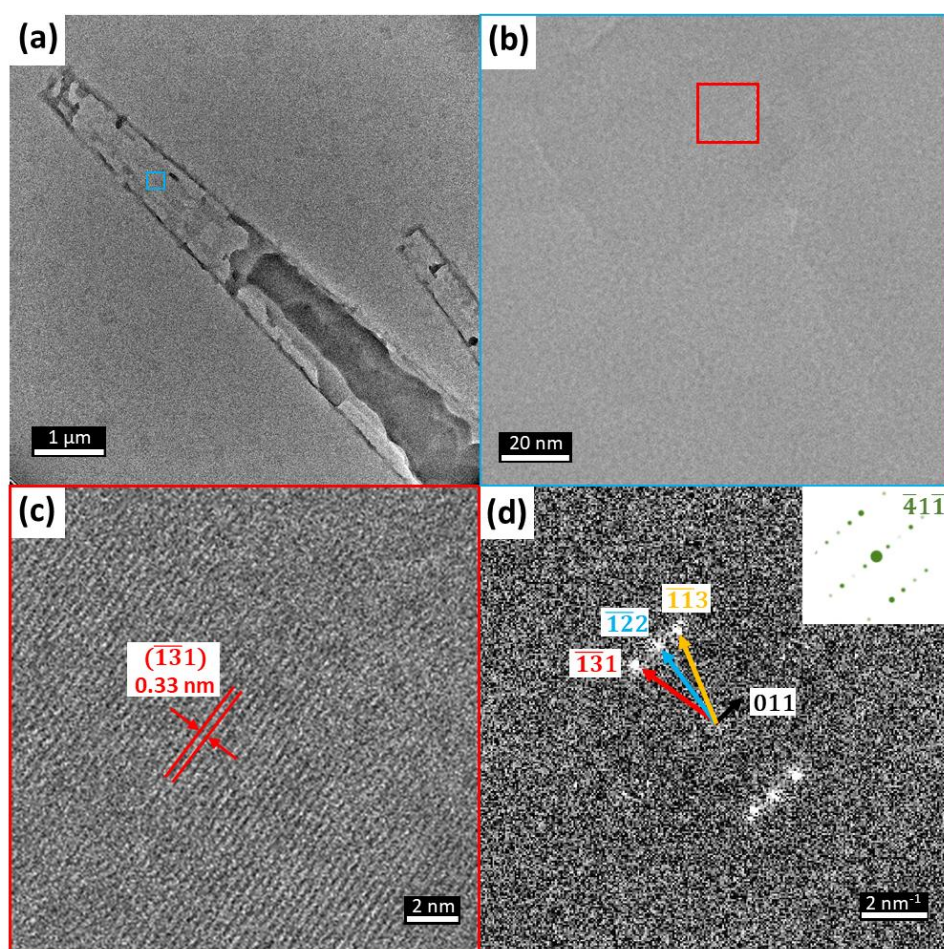


Figure 6.14 a) Low-magnification BF-TEM image of theophylline monohydrate ($M3$) acquired at ePSIC using the direct electron detector DE16; (b) phase contrast lattice imaging of the area marked by the blue square in (a); (c) cropped phase contrast lattice image from (b) and 0.34 nm lattice spacing corresponding to $(1\bar{3}1)$ lattice plane are marked by red lines; (d) FFT from the area in (a) that can be used for indexing the crystal orientation to $[\bar{4}1\bar{1}]$ zone axis.

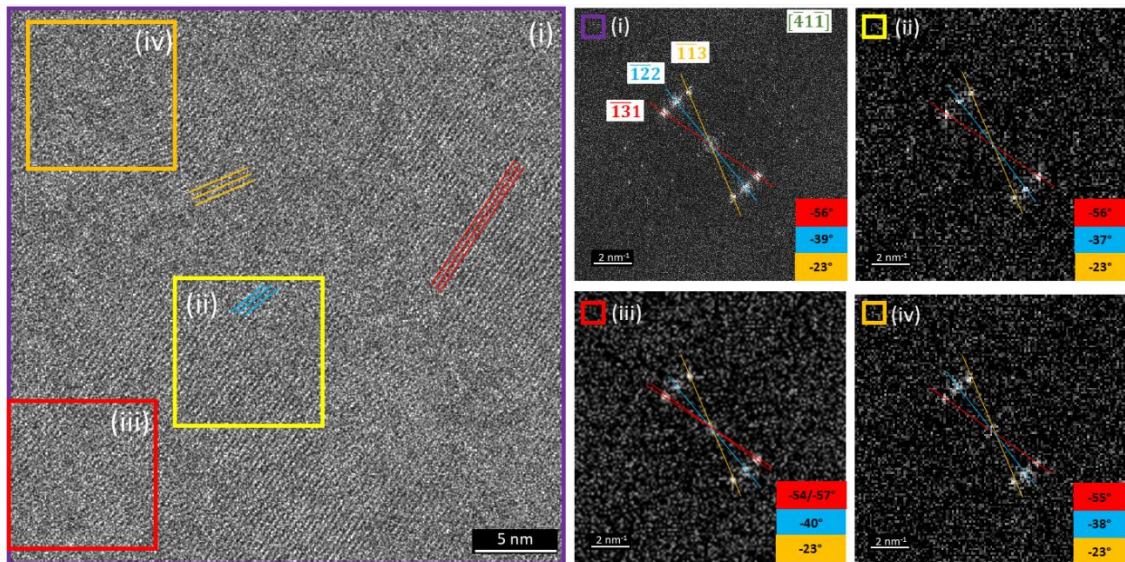


Figure 6.15 Phase-contrast lattice image of the area presented in Figure 6.14. Corresponding FFTs from the different parts of the image (i)-(iv) indicate the change in the position (a relative angle to a vertical line) of spots corresponding to $(\bar{1}31)$ and $(\bar{1}22)$ planes but the position of a spot corresponding to $(\bar{1}13)$ plane is constant.

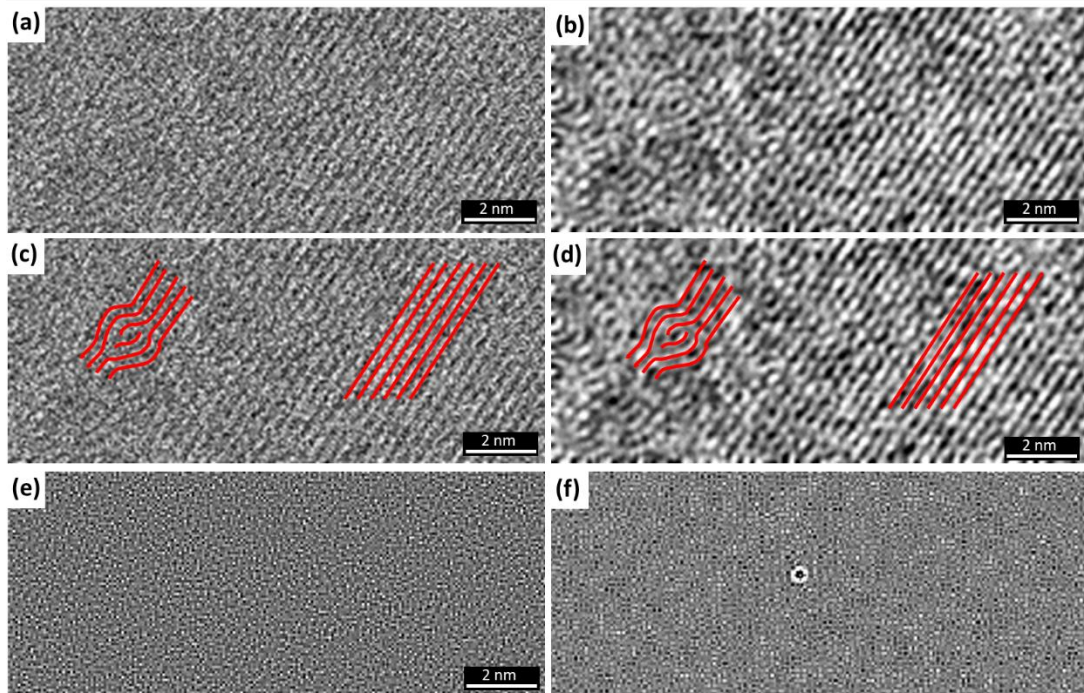


Figure 6.16 Cropped (a) the raw phase contrast lattice image and (b) the effect of applying a non-linear filter reported elsewhere (Du, 2015) to the same area from Figure 6.14. Lattice planes are marked by red in the corresponding: (c) - raw and (d) – filtered images; (e) residual image and (f) its auto-correlation.

In conclusion, it was possible to acquire phase contrast lattice imaging of theophylline form II and monohydrate with a total electron fluence not exceeding $31 \text{ e}/\text{\AA}^2$. Defects in the crystal structure are visible for theophylline monohydrate (*M3*, Figure 6.9b and Figure 6.16) but are not detected for theophylline anhydrous form II (*A2*) and another theophylline monohydrate sample (*M1*). However, low-dose phase contrast lattice imaging is not an efficient method for detecting defects due to low SNR and small sampling area. In the subsequent sections 6.6 and 6.7, another method of virtual dark field (VDF) imaging using scanning electron diffraction (SED) datasets will be demonstrated to be more effective to (i) detecting the disruption in the Bragg contours that can indicate the presence of defects and (ii) analyse these to identify defect character and displacement vector ((i) is reported in a manuscript currently in draft).

6.6 Investigation of Structural Changes During Hydration

To determine structural changes during the hydration of theophylline anhydrous form II (*A2*), two independent conditions were applied: (i) full water immersion for 10 min (thereafter *A3*) and (ii) storage in high humidity conditions (93% RH) (thereafter *M1*). By combining the results of pXRD, BF-TEM, SAED and SED analysis (i.e. both changes in morphology as well as phase and defect identification of *A3* and *M1*), it can be postulated that hydration is a solution-mediated route and thus it is a dissolution - re-precipitation phase transformation and this is consistent with some previous studies (Chen et al., 2010; Rodríguez-Hornedo et al., 1992). The following steps in the hydration mechanism of theophylline form II have been identified (Figure 6.17) and are presented here first so that the results and detailed analysis confirming these steps that will be shown after are easier to follow:

- (i) Step 1 – ‘*water interaction with (100) surface*’. The water interaction with the (100) surface is strong due to the presence of the C(2) carbonyl group on the surface of form II which can lead to the formation of a surface solution from water adsorption (water exposure or storage in high RH). This increases the mobility or detachment of theophylline molecules on/from the surface and can facilitate further phase transformation. However, there appears to be a long induction time to nucleate the hydrate phase suggesting a significant activation energy barrier for monohydrate phase nucleation and transition (at a critical

RH from 25% to 82%) (Amado et al., 2007; Chen et al., 2010; Otsuka et al., 1990; Zhu et al., 1996).

- (ii) Step 2 – '*changing orientation*'. SAED and SED of both samples, A3 and M1, show a re-arrangement of theophylline form II plates (A2) oriented initially to [100] zone axis to [131] for sample A3 and similar, [130] for sample M1. This re-arrangement might act as the pre-transformation phase and facilitate further phase transformation.
- (iii) Step 3 – '*crystal breakage*'. The SED of both samples, A3 and M1, indexed to re-arranged theophylline form II shows a number of breaks in the bend contours indicating the presence of defect sites. More defects were found in M1 than in A3, which is related to the longer exposure time of the sample to water adsorption. A greater amount of lattice disorder leads to increased surface free energy and reactivity that can facilitate crystal breakage (Ohta and Buckton, 2004).
- (iv) Step 4 – '*dissolution*'. The indication of dissolution was observed in both samples. A3 particles exposed to longer water interaction dissolved completely (see Figure 6.3). However, re-orientated and distorted crystals of M1 have etching side surfaces and reduced particle size compared to A2, without any evidence of the monohydrate phase nucleating on the surface of the anhydrous form. The monohydrate phase is seen to re-precipitate and grow only under a highly supersaturated environment that is presumably induced by the dissolution of the A2 phase.
- (v) Step 5 – '*re-precipitation as monohydrate form*'. Monohydrate form was identified in the sample M1 and only in areas indicating homogeneous nucleation and crystal growth of the hydrated phase. The long induction period suggests that crystallisation is a nucleation-controlled process and might depend on the local degree of supersaturation.

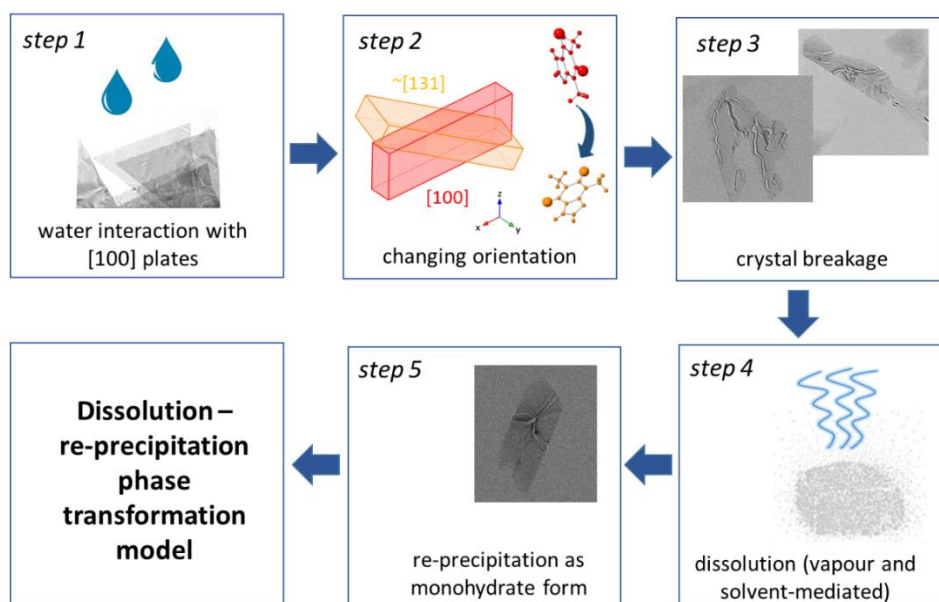


Figure 6.17 Proposed dissolution – re-precipitation phase transformation model for hydration of theophylline form II (A2).

Samples *A3* and *M1* were investigated mainly by scanning electron diffraction, which can provide a wealth of spatially resolved crystallographic data from a selected region and allows the identification of potential nucleation or defect sites. Theophylline anhydrous form II has three main sites binding water molecule strongly, therefore they play an important role in hydration: (i) the C(6) carbonyl group (most favourable site for hydration), (ii) the C(2) carbonyl group and (iii) the N(9) atom (Figure 6.18) (Singh, 2015). Interaction between these specific sites and water molecules can disrupt the hydrogen bonding network in theophylline anhydrous form II. The bonding between theophylline molecules in anhydrous form II is less preferred (due to higher energy) than the bonding between water and theophylline anhydrous form II. Theophylline form II (*A2*) plates oriented to [100] are exposed to water through the (100) top (projected) surface containing the C(2) carbonyl group (Figure 6.18). However, the absence of appropriate size channels or voids in theophylline form II prevents water diffusion into the crystal lattice due to the size of the water molecule ($\sim 2.8 \text{ \AA}$ the van der Waal's diameter) (Chen et al., 2010). Therefore, only the surface of theophylline form II crystals can interact with water and transformation can be a surface solution-mediated process. Otsuka et al. (1990) have observed that theophylline of different morphologies has different hydration kinetics consistent with these surface effects.

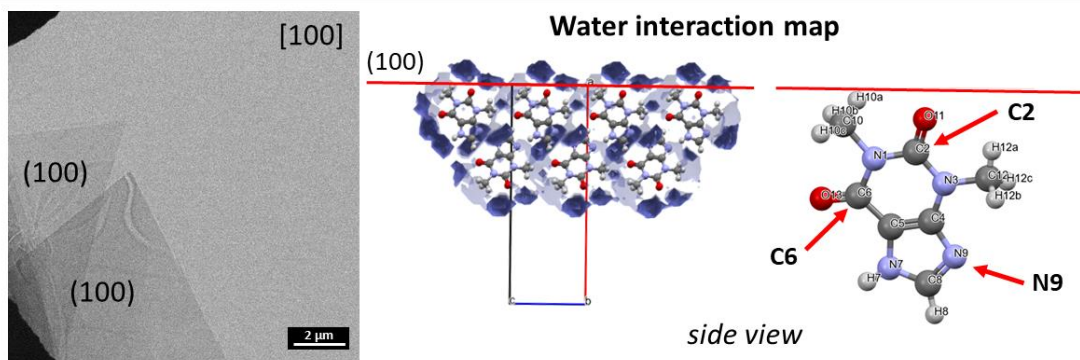


Figure 6.18 Water interaction map of (100) lattice plane of theophylline anhydrous form II (A2) generated in Mercury 2022.2.0. Particles oriented to [100] have the (100) projected surface facet.

Method 1 - full water immersion for 10 min

Figure 6.19 shows SED results for sample (A2) left in direct contact with water for 10 min (thereafter A3). Theophylline particles lost most of the original platelet orientation, however, the particle edges are still faceted and there is no evidence of secondary crystallite formation. SED data reveals two orientations of the same plate that can be indexed to theophylline anhydrous form II: (i) the underlying original [100] (minor) and (ii) the formation of [131] after contact with water. The top, projected edge of the crystal can be indexed to the $\bar{2}02$ plane, which contains the strongest water-binding C(6) carbonyl site on the surface. Light microscopy imaging showed (an experiment of extended water contact time and larger size of plates) that these plates are dissolved completely in the final step (data not shown). The inset in Figure 6.5a shows that there are several cracks in the theophylline form II plates (A3) exposed to water for a prolonged time. It is suggested that surface water contact causes the plates to separate into smaller fragments and thus increases the surface area, which facilitates further dissolution.

Virtual dark field (VDF) of the [131] orientation confirms a number of defects in the structure and a clear connection to the original plate suggesting this disruption may be a precursor to particle break-up (Figure 6.19, orange box). The high density of breaks in the bend contours are marked by the blue circle and line in Figure 6.19 (orange box) and are linked to the presence of defects in the crystal structure.

The theophylline anhydrous form II to monohydrate phase transformation of A3 was not detected by powder XRD (Figure 6.5) and SED (Figure 6.19), however, the reactions were limited to contact with water for 10 minutes so only the initial steps of the phase transformation were detected, i.e. reorientation of theophylline to [131] zone axis and appearance of crystal disorder. The long induction time suggests that theophylline monohydrate crystallization is a nucleation-controlled process and is in agreement with previously reported hydration studies (Ohta and Buckton, 2004).

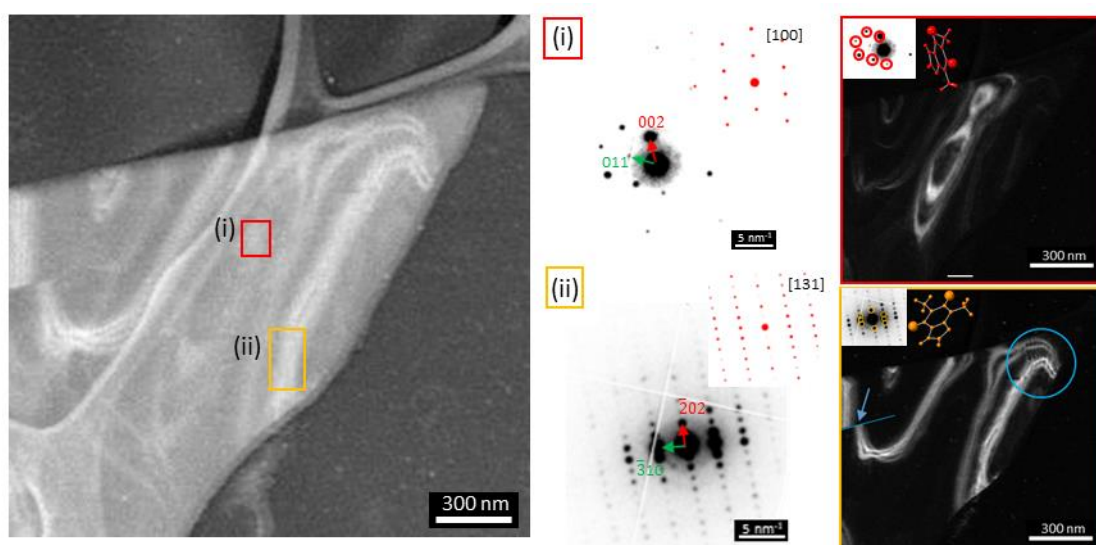


Figure 6.19 ADF-STEM image of theophylline anhydrous form II (A3). SED reveals two orientations: (i) original [100] and (ii) dominant [131]. Corresponding ADF-STEM images are formed by plotting the intensity within the red and orange disks marked in SED patterns as a function of probe position. Disordered sites are marked by blue circle and line.

Method 2 - storage in high humidity conditions (93% RH)

Figure 6.20 and Figure 6.21 show the results for sample A2 exposed to high humidity conditions (93% RH) for 4 weeks (thereafter M1). This sample also has many crystals of altered morphology compared to the theophylline anhydrous form II triangular plates. These plates are crystals of form II that are still electron transparent, but oriented to the [130] zone axis and are highly distorted (Figure 6.20). Similarly to that during contact with water A3, the appears to be a rearrangement of theophylline form II from the original [100]. Moreover, a number of defects and etching surfaces are identified. This high humidity condition can be considered to form a surface layer of condensed water that increases the mobility of theophylline molecules from the surface and facilitates the dissolution

and re-precipitation of the monohydrate phase rather than the solid-state transformation. The slow dissolution of anhydrous theophylline form II crystals leads to a supersaturated solution with respect to the hydrated form. Then, the theophylline monohydrate form can re-precipitate and grow until the concentration reaches the solubility limit of the monohydrate form (Rodríguez-Hornedo et al., 1992). There are no detectable sites of monohydrate heterogeneous phase nucleation on the surface of theophylline form II. However, some isolated (homogeneous) crystals can be indexed to monohydrate form (Figure 6.21). The first signs of homogeneous nucleation of monohydrate form were detected in the first week of high humidity storage by SAED (also with reduced RH of 75%), but this phase is not observable by pXRD (Figure 6.6). The induction time to initiate nucleation and crystallisation of monohydrate form is less than or the order of 7 days, indicating again that the phase transformation is slow and is a nucleation-controlled process. However, the presence of theophylline monohydrate crystals does not promote further nucleation (secondary nucleation) since the final number of crystals is not dependent on the initial number of monohydrate crystal seeds but it is dependent on the supersaturating level of the anhydrous form (Rodríguez-Hornedo et al., 1992).

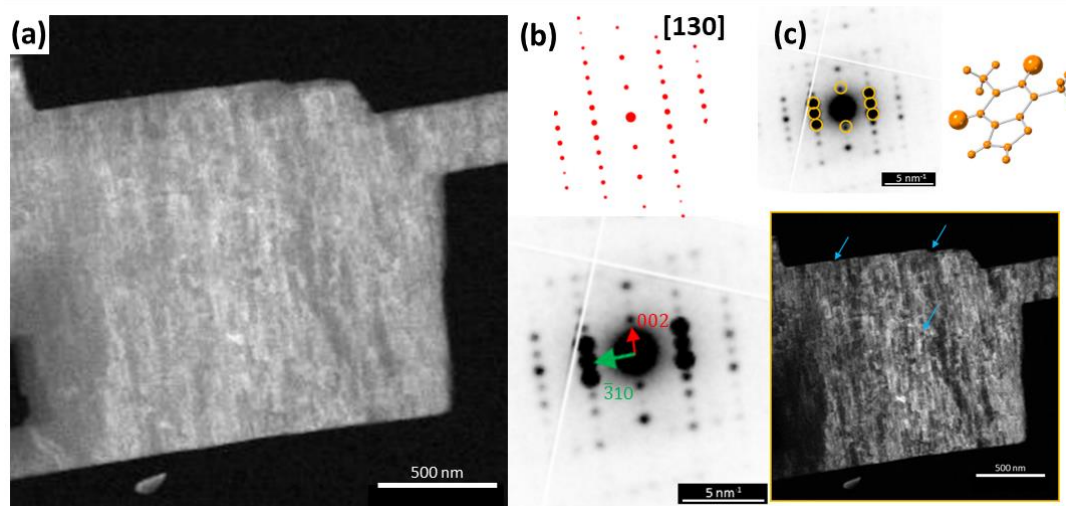


Figure 6.20 (a) ADF-STEM image of theophylline anhydrous form II (*M1*) and (b) corresponding SED indexed to [130] zone axis. (c) Virtual ADF-STEM image was formed by plotting the intensity within the orange disks marked in the SED pattern as a function of probe position.

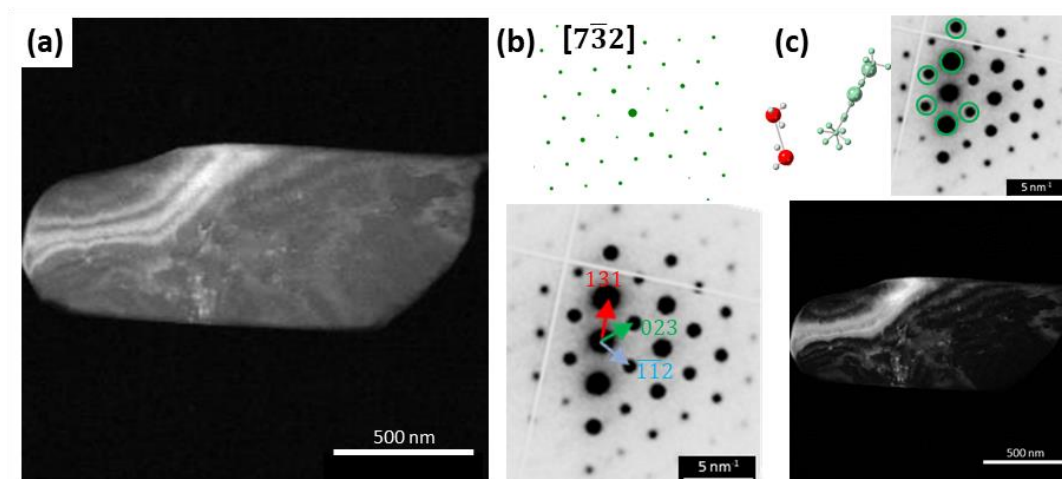


Figure 6.21 (a) ADF-STEM image of theophylline monohydrate (*M1*) and (b) corresponding SED indexed to $[\bar{7}32]$ zone axis. (c) Virtual ADF-STEM image was formed by plotting the intensity within the green disks marked in the SED pattern as a function of probe position.

Conclusions

During the hydration of theophylline form II plates (*A2*), two independent conditions were applied to monitor the phase transformation. Although the monohydrate phase was not detected in sample *A3*, the initial steps of the phase transformation of theophylline form II to the monohydrate form are comparable for both samples *A3* and *M1*. Analysis at this scale, with both morphology and structure changes identified, allows insight into the phase transformation processes and confirms that the hydration of theophylline is a solution-mediated process via crystal disruption, dissolution and re-precipitation phase transformation mechanism.

6.7 Investigation of Structural Changes During Dehydration

The dehydration pathway of theophylline monohydrated was analysed by two methods: (i) vacuum drying from monohydrate crystals (*M3*) in-situ in the TEM (likely to observe dehydration pathway (ii) as per Figure 6.1 due to low RH condition and high vacuum according to the recent study (Paiva et al., 2021) and (ii) using the heating holder (likely to observe dehydration pathway (i) as per Figure 6.1 due to increased temperature). The formation of any metastable intermediate phase and changes in morphology and crystal structure were characterised by SED, SAED and BF-TEM imaging. Transformation of theophylline monohydrate to theophylline anhydrous form II is postulated to

proceed via vapour-mediated phase transformation. Dehydration of theophylline monohydrate can be divided into the following steps (presented schematically in Figure 6.22) and again the identified steps are presented here first before the detailed results and analysis used to obtain these steps are shown:

- (i) Step 1 - '*Anisotropic surface dehydration*'. This step is common for both experimental conditions. Erosion via etching was identified at the surfaces with exposed water channels. These surface etchings do not propagate along the direction of water channels, but they are directed diagonally towards the centre of the particle thereby opening additional channels to a free surface. This might be induced by the removal of water from the molecular columns closer to the sample surface. This can result in the destabilisation of the hydrogen bond network and the formation of voids between theophylline molecules i.e. crystal disruption. If the particle size is smaller or the dehydration temperature increases, the rate of surface dehydration is accelerated. This partial water removal can be related to the first, low-temperature mass loss reported in the published literature (Duddu et al., 1995; Nunes et al., 2006; Paiva et al., 2021).
- (ii) Step 2 – '*Formation of theophylline metastable form III at the surface of the particle*'. Dehydrating particles can be divided into two zones the first or zone 'one' corresponds to areas where there the surface degradation by etching is present, and zone 'two' - the central part of the particle, then form III (which has the same structure as monohydrate form but without water in the channels) is shown to be present in the zone 'one'. Zone 'two' may be still saturated with water in the channels due to the slow out diffusion rate of water from the elongated narrow channels.
- (iii) Step 3 – '*Route 1 (room temperature) – local reabsorption of water and formation of theophylline monohydrate*'. At room temperature, there might be local surface zones with increased water vapour egress. In combination with the mobility of the theophylline molecules at the surface etched zones (zone 'one'), this moisture can be reabsorbed facilitating nucleation and growth of the monohydrate form (Matsuo and Matsuoka, 2007; Vora et al., 2004). Conversion from metastable form III to anhydrous form II is slow at room temperature and was not

observed in this study, however, it is reported to be accelerated in higher RH conditions (complete conversion of metastable III to anhydrous form II occurred in <4 days at 52% RH vs <10 days at 33% RH) suggesting the transformation is vapour mediated (Phadnis and Suryanarayanan, 1997).

- (iv) Step 4 – *'Route 2 (increased temperature) – rapid dehydration from the bulk and recrystallisation of theophylline anhydrous form II in the presence of water vapour'*. At higher dehydration temperatures, water molecules leave the crystal lattice rapidly. Under these conditions, significant dehydration from the centre part of the particle was observed (zone 'two') as were the formation of cracks and altered morphology across whole particles. This is consistent with the second, higher temperature mass loss during dehydration reported in the published literature (Duddu et al., 1995; Nunes et al., 2006; Paiva et al., 2021). At these temperatures, the outgoing water vapour and increased mobility of theophylline molecules followed to enable the rapid rearrangement of the structure to the theophylline anhydrous form II. Paiva et al. (2021) reported that dehydration disrupts the crystal structure of theophylline monohydrate due to the collapse of the dimers and formation of a number of cracked short structures, but stated that theophylline monohydrate to theophylline anhydrous form II is a solid-state transformation. However, if the observed changes only occur in the presence of water vapour, the phase transformation actually proceeds via a vapour-mediated phase transformation.

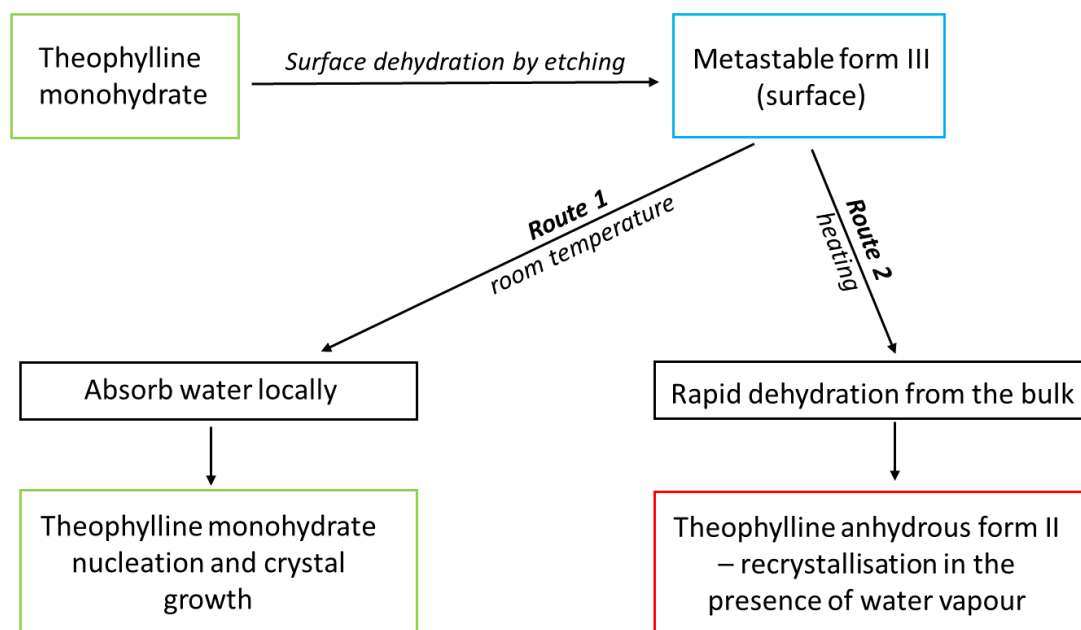


Figure 6.22 Dehydration routes of theophylline monohydrate.

Method 1 - vacuum drying in TEM

Selected crystals of theophylline monohydrate (*M3*) were held in the TEM and two SED datasets were acquired during the vacuum drying – the first one immediately after finding an area of interest (roughly around 30 min in vacuum) and the second one after leaving the sample overnight in the TEM column (~17 h). The double area scan was within the total electron dose budget for theophylline and the electron fluence used for both scans was $<16 \text{ e}^-/\text{\AA}^2$ ($<8 \text{ e}^-/\text{\AA}^2$ per single scan).

Figure 6.23 shows the comparison between ADF-STEM images taken during the first and second vacuum holds. There is observable repeated surface etching on the lower crystal edge indexed to the $(0\bar{1}1)$ plane (marked by a red line) and which terminates with water channels on the surface (based on Mercury BFDH analysis). However, this surface erosion propagated into the crystal diagonally to the water channels. A previous dehydration study on another channel hydrate, carbamazepine dehydrate, also revealed surface etchings, but these propagate along the water channels (Khoo et al., 2010). Similar phenomena were observed on heating thymine hydrate crystals and the macroscopic direction of surface etching corresponded to the crystallographic direction of the water channels in the unit cell (Perrier and Byrn, 1982). However, the water channels and crystal

structure of these compounds have different arrangements and larger diameters than theophylline monohydrate. Different phenomena for freeze-drying of theophylline monohydrate were observed in a recently published report (Ren et al., 2023). Dehydrated theophylline monohydrate, which is assumed to be metastable form III after 2-h freeze-drying dehydration, shows crystals that have many cracks in different directions. Moreover, elongated crystals become opaque, which suggests surface amorphisation that can induce the formation of nucleation seeds and, control further dehydration (Ren et al., 2023). The diagonal surface etching seen here in theophylline monohydrate might be related to the mobility of theophylline molecules and the loss of some water and theophylline to the vacuum, opening up regular surface defects. Further dehydration (time in the vacuum) increases the amount of surface erosion (that intersects with additional water channels) also opening up cracks. The surfaces at the ends of the elongated crystal (not imaged here) may also have open channels but these surfaces are not the largest exposed area, therefore out-diffusion of the water located at the centre of the elongated particle is slow. This slow removal of water might also explain the good stability of theophylline monohydrate during lattice imaging.

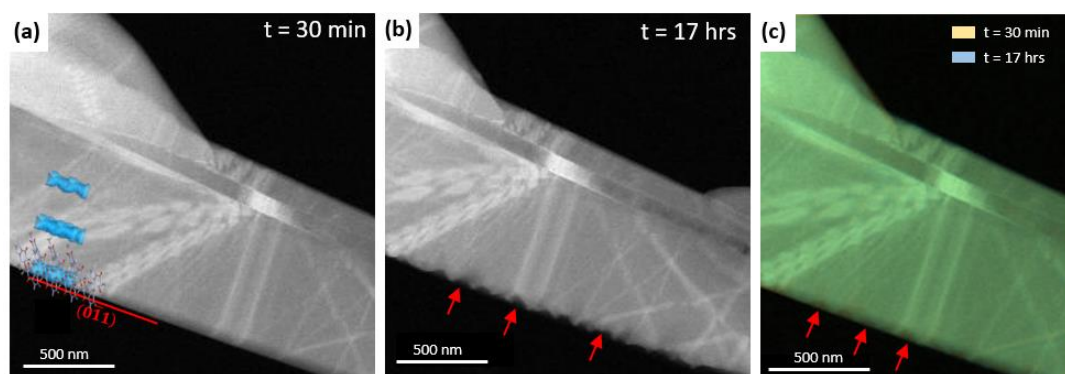


Figure 6.23 ADF-STEM image of theophylline monohydrate (*M3*) after (a) 30 min and (b) 17 hrs in a vacuum. (c) shows the overlay between (a) and (b). Characteristic surface erosion by etching is marked by red arrows in (b) and (c).

Clearly, water removal from theophylline channels is a complex process, and it is not only governed by the diffusion of water along the *a*-axis of the crystal lattice. The structure of form III is reported as having the same dimer structure as the monohydrate (Fucke et al., 2012) therefore, if there is water loss at the edges of the crystal (zone 'one') it may have converted to metastable form III while the centre of the crystal (zone 'two') might remain in the monohydrate form. Ultimately

conversion to theophylline form II is not observable due to the low RH that can hinder phase transformation (Paiva et al., 2021). Moreover, conversion between metastable form III to theophylline anhydrous form II may occur over a period of several months depending on the dehydration condition (Phadnis and Suryanarayanan, 1997).

SED for identification of grain boundary and defect sites

Figure 6.24 shows theophylline monohydrate (*M3*) after 30 min in a vacuum (same area as presented in Figure 6.23a) with corresponding SED patterns from the selected regions (i)-(v). The top (i.e. region (iv)) and bottom (regions (i), (ii) and (v)) parts of the particle can be indexed to theophylline monohydrate (or metastable form III) oriented to the [111] zone axis. However, the middle incline crystal (i.e. region (iii)) can also be indexed to theophylline monohydrate, but with a different orientation \sim [001]. SED patterns of regions (i), (ii) and (v) are taken from different parts of the same particle and show the different intensity of diffraction spots that suggest that this particle is slightly tilted from the [111] zone axis. From the indexed orientation and analysis of the structure file of theophylline monohydrate in Mercury, the direction of the water channels can be specified. Water molecules form channels along the longest part of the particle (i.e. along the *a*-axis) and this direction is marked by a blue arrow in Figure 6.24.

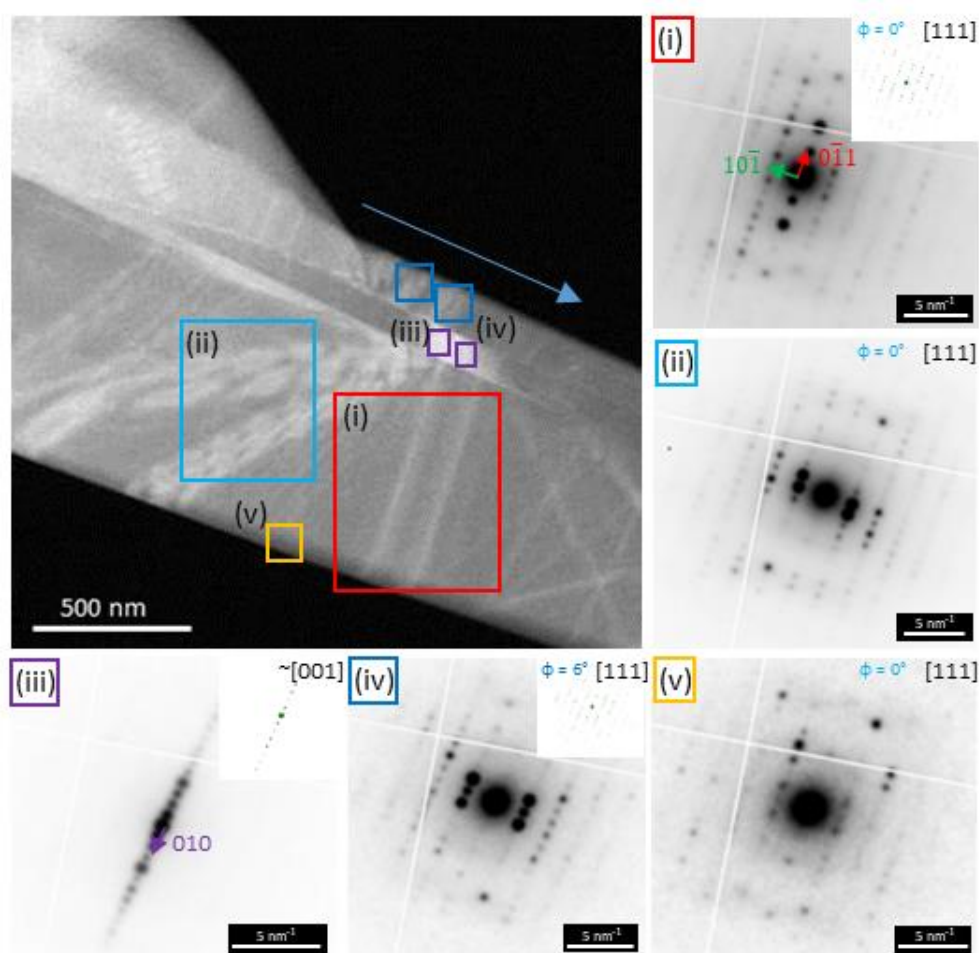


Figure 6.24 ADF-STEM image of theophylline monohydrate (*M3*) and SED patterns from the selected regions (i) – (v). The blue arrow indicates the direction of the water channels.

SED offers the potential to investigate the presence of defects, but also the presence of grain or twin boundaries between different parts of the particle (Figure 6.25). Figure 6.25a-b shows the schematic of three regions present in this particle with their indexation and the difference in the relative angle between the particle edges. Predicted BFDH morphology and channel propagation were modelled in Mercury 2022.2.0 to find a common plane (in the case of the twin boundary) or a relationship between different parts of the crystal (e.g. grain boundary). Area (i) and (iii) are indexed to [111] zone axis, but the bottom and top edge of the area) is shifted by 4° and 6°, respectively to the bottom edge of the area (i). The middle area (ii) is indexed to [001] zone axis, however, there is no common or mirror plane between these two orientations. There is an interesting relationship between these areas in terms of the presence of water channels on the crystal surfaces that run in the same direction. The bottom edge

of area (i) is indexed as the $(0\bar{1}1)$ plane and this plane terminates where the water channels occur on the surface (Figure 6.25c). The top edge can be indexed to $(01\bar{1})$ and terminates where water channels are absent. The bottom edge of area (ii) can be indexed as the (010) plane which terminates without water channels at the surface, whereas the top edge $(0\bar{1}1)$ terminates with water channels at the surface. Based on the predicted morphology, this area (ii) of the crystal is rotated by 132° with respect to area (i). The same pattern of channel propagation can be observed for area (iii). This analysis shows that the imaged particle contains a grain boundary, however, there is a relationship between the grains in terms of the water channel propagation at contact surfaces.

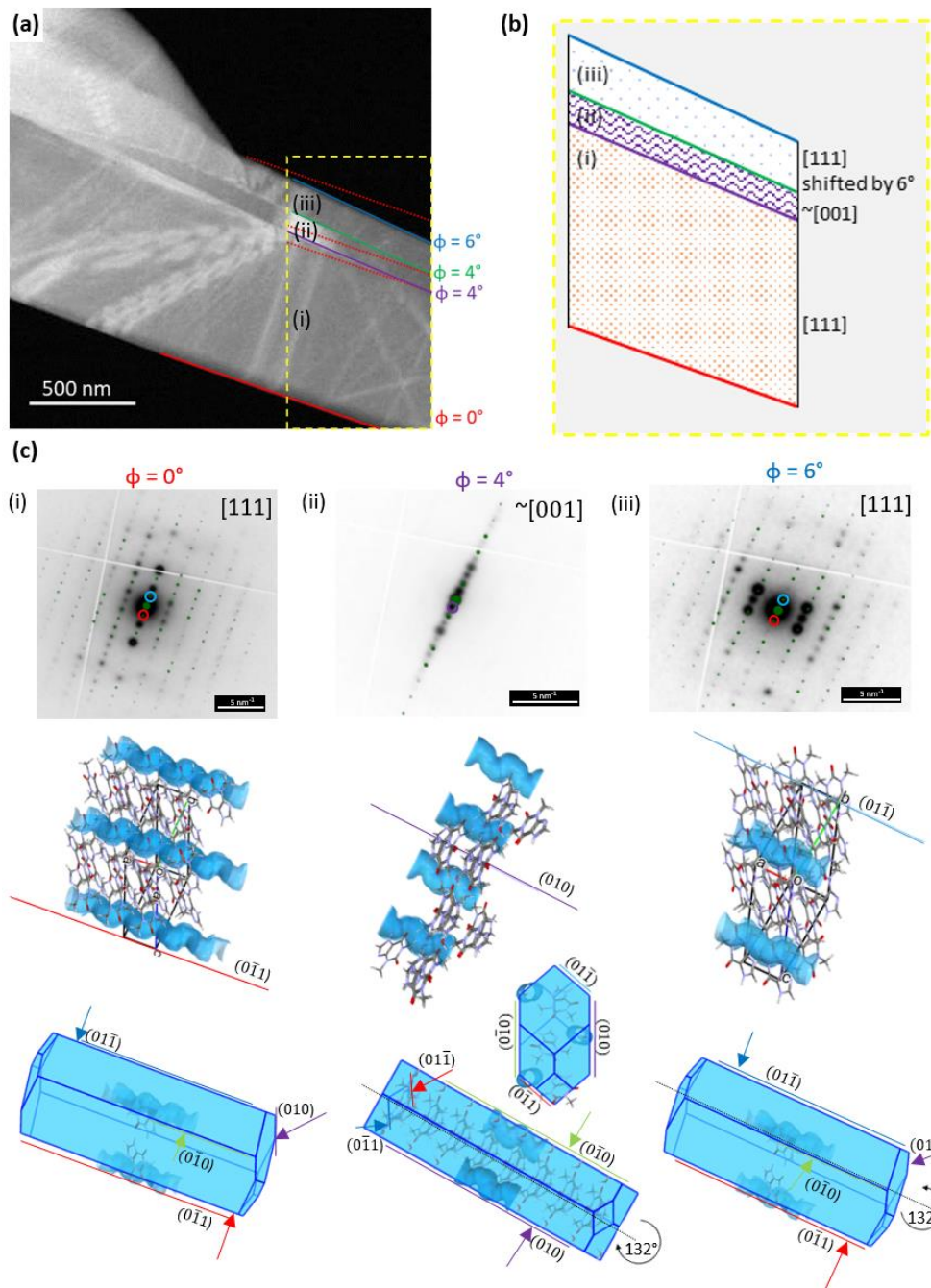


Figure 6.25 (a)-(b) Identification of three different areas within one particle and their relative orientation. (c) the relationship between the orientations of individual areas and the presence of channels on the common surfaces. BFDH morphology and channel propagation were modelled in Mercury 2022.2.0.

Figure 6.26 shows the ADF-STEM image of the particle after 17 h in a vacuum (area presented in Figure 6.23b) and corresponding VDF images formed by plotting the intensity within the disks marked in the SED pattern and SED patterns taken from the same sized two regions: at the surface of the particle and from the inner part of the particle. Diffraction analysis at the surface etching discussed

above may be consistent with the formation of form III in this region and can be demonstrated by more disordered regions and loss of diffraction spots in Figure 6.26e (red box).

In addition, a number of defects can be identified in the ADF-STEM images (shown for clarity in the prolonged vacuum hold image but present at the beginning of the vacuum hold too). There are clear displacements in bend contours that are indicative of in-plane line defects now running through the crystal. The displacements in the bend contours (blue lines in Figure 6.26d) can be used to identify the dislocation type (edge, screw or mixed) and for identification of the displacement Burgers vector directions. These findings are beyond the scope of this work and are presented in a manuscript submitted for publication led by Dr Pham and Dr Collins at Leeds (Pham et al., 2023). This result is achieved using an electron fluence of $< 8 \text{ e}^-/\text{\AA}^2$ per SED scan compared to $\sim 31 \text{ e}^-/\text{\AA}^2$ used for lattice imaging. These defects were likely present throughout the dehydration process but may have facilitated enhanced water transport and dehydration.

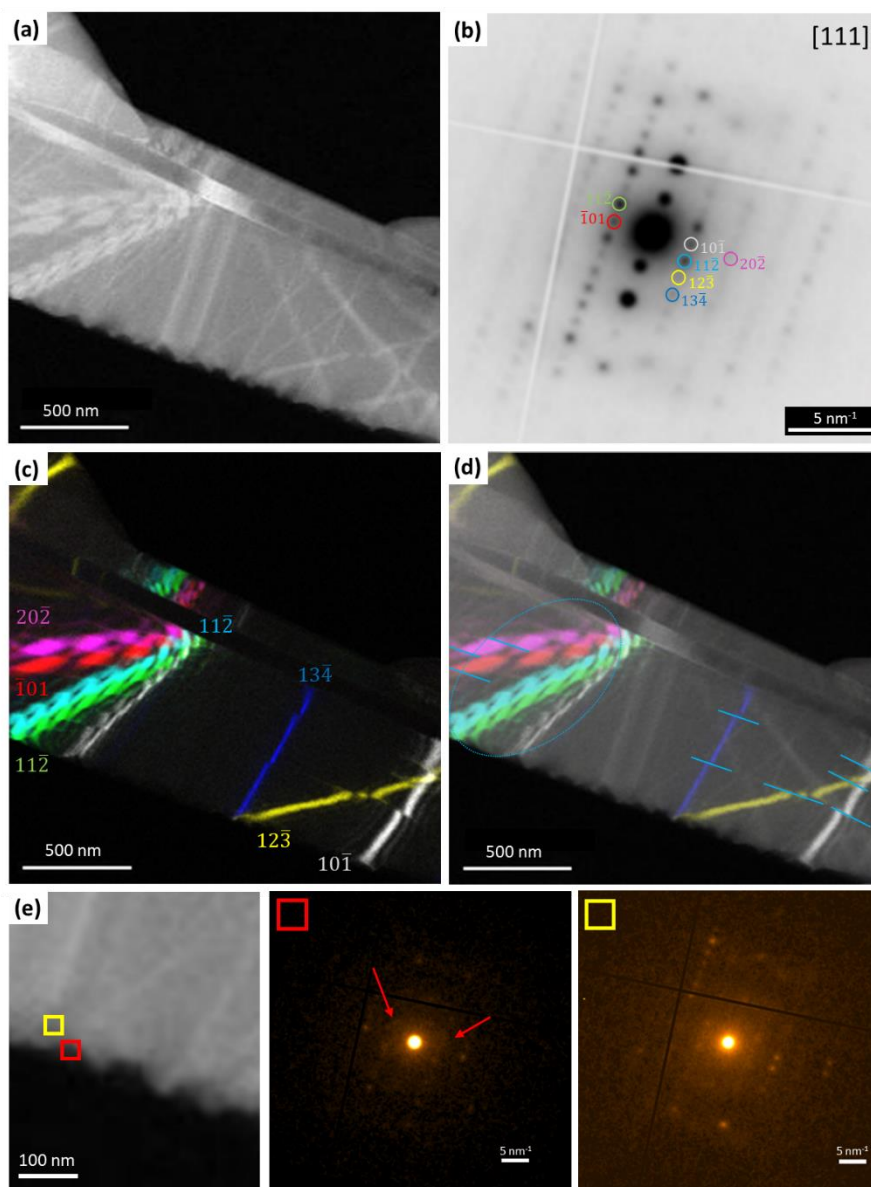


Figure 6.26 (a) ADF-STEM image of theophylline monohydrate (*M3*) and its (b) SED pattern from the bottom part of the crystal. (c)-(d) Virtual ADF-STEM images formed by plotting the intensity within the disks marked in the SED pattern in (b) as a function of probe position. Defect sites are marked by blue lines (dislocation) and a circle in (d). (e) cropped area in (a) and two diffraction patterns from same-sized regions: red- at the edge of the crystal and yellow – slightly above the edge of the crystal. Red arrows indicate disordered regions.

An interesting phenomenon was found at another theophylline monohydrate (*M3*) particle orientated to the $[\bar{1}13]$ zone axis during the same dehydration condition (Figure 6.27). Surface erosion via etching is identified on the face of the particle that corresponds to the plane terminating with water channels on the surface and it is consistent with previous observations. However, on the one end of the elongated particle, where water channels are exposed and water can out-diffuse,

the formation of a new crystal is observed (Figure 6.27b-c). This new crystal can be indexed to theophylline monohydrate on the [310] zone axis (Figure 6.27d). Surface etching confirms the mobility of theophylline molecules while conditions near the open channels can be high in water vapour to facilitate surface growth of a secondary crystal of the monohydrate phase. Vora et al. (2004) revealed that metastable form III can adsorb moisture at the beginning of the transition to an anhydrous form. Matsuo and Matsuoka (2007) also suggested that metastable form III absorbs moisture to form locally the monohydrate before final transformation into anhydrous form II. The diffused water can facilitate structural reorganisation as the water vapour pressure increases.

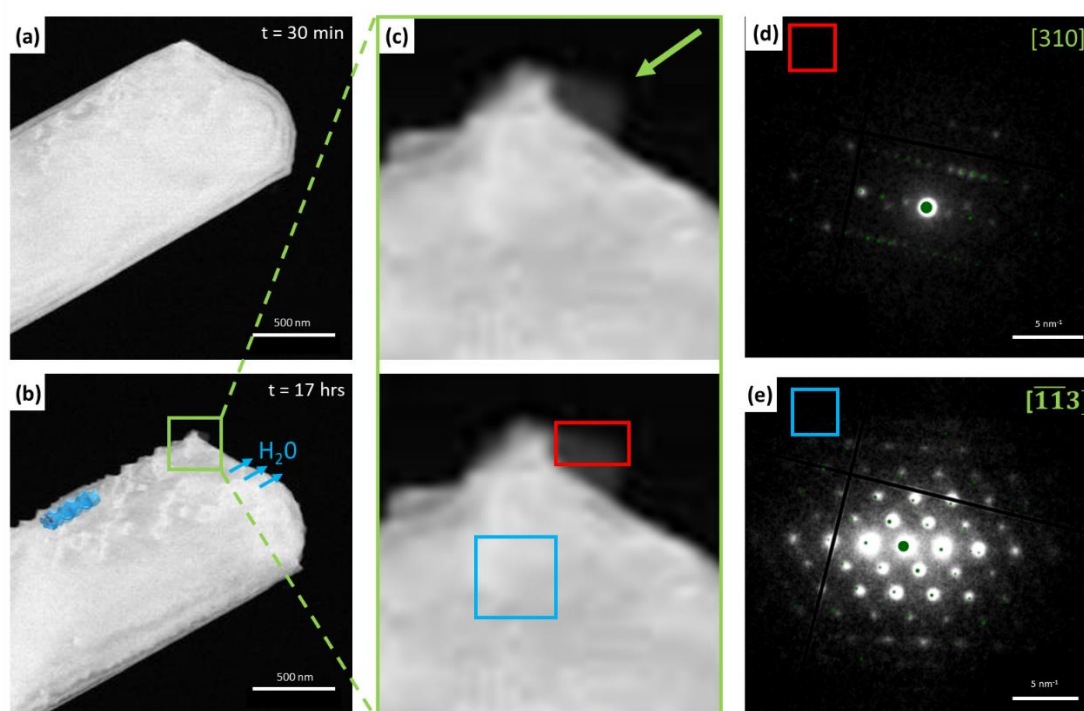


Figure 6.27 (a)-(b) Vacuum dehydration of another area from *M3* also reveals the etching on the surface. (c) New crystal growth in the corner of the main particle during dehydration can be indexed to (d) theophylline monohydrate orientated to [310] zone axis (red square in (c)). (e) Initial particle can be indexed to theophylline monohydrate or metastable theophylline form III upon partial dehydration.

Method 2 - heating in-situ experiment

In the second experiment, a heating holder was used to promote accelerated dehydration of theophylline monohydrate (*M3*) during in-situ heating up to 100 °C (well below the melting point of theophylline monohydrate of 270 – 274 °C) and to detect any trace of phase transformation from theophylline monohydrate to

anhydrous form II. The dehydration time of theophylline monohydrate should be reduced by heating and by small particle size as these conditions enhance the water removal, and theophylline molecule mobility to facilitate nucleation of the anhydrous phase (Khoo et al., 2010).

Figure 6.28a-b shows two areas heated to 60 °C and 100 °C, respectively, and both can be indexed to theophylline monohydrate at the beginning of the experiment. The same surface etching mechanism is observed for both areas and is consistent with the previous vacuum dehydration experiments i.e. some loss of water (Figure 6.23 and Figure 6.27). Gradual surface etching was produced with heating up to 60 °C. As expected, the depth of etching is greater for smaller particles (red arrow) than for larger particles (yellow arrow) (Figure 6.28b).

At 80 °C, a number of cracks can be seen on all the surfaces of the particles. At 90 - 100 °C, significant morphology changes are observed and presented in Figure 6.28b - the overall boundaries of the particle are preserved, however, the formation of numerous thin elongated particles is visible in the direction of the formation of cracks. The SAED pattern can be indexed to theophylline form II oriented to the $[\bar{1}01]$ zone axis. These changes indicate the rapid expulsion of the remaining hydrate water molecules, which results in the presence of significant local water vapour – as per the second step in the two-step water loss report by Nunes et al. (2006). The resulting combination of the highly disordered material (which might be locally amorphous) and the presence of the water vapour can facilitate structural reorganisation and nucleation and growth of the theophylline anhydrous form II. As the observed changes occur in the presence of water vapour/medium (consistent with the second step of mass loss from the bulk), this significant molecular reorganization and phase transformation are unlikely to occur in the solid state and the results suggest vapour-mediated phase transformation.

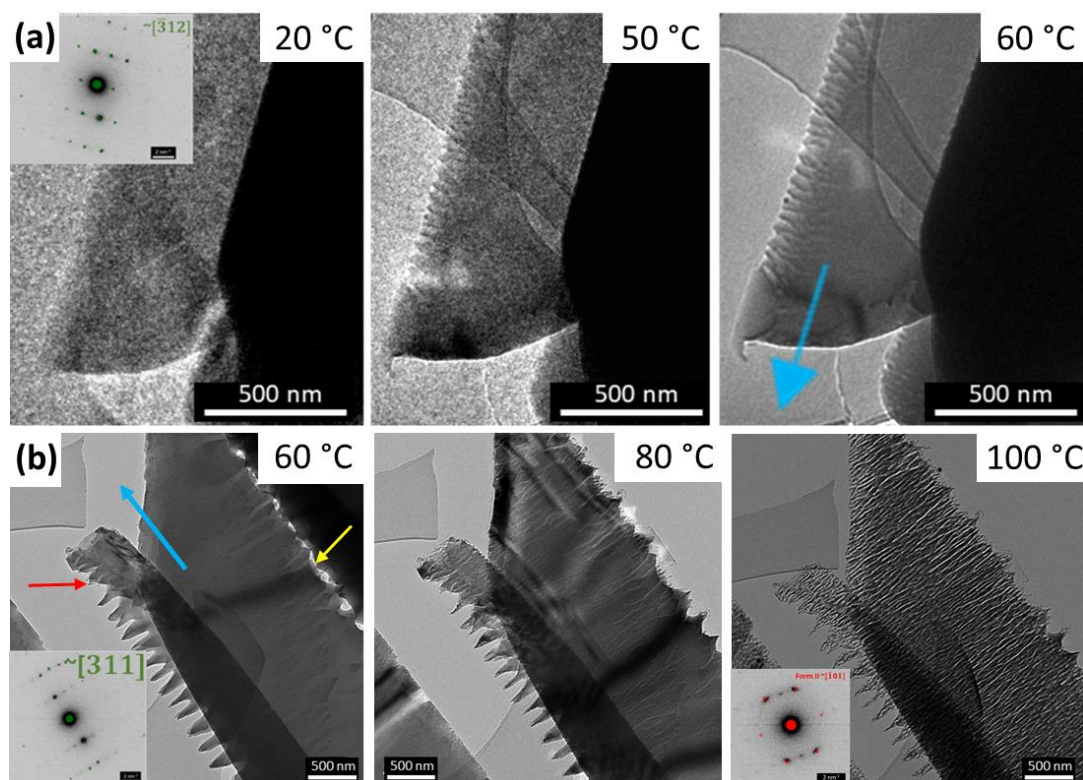


Figure 6.28 Dehydration of theophylline monohydrate *M3* using a heating holder: (a) *M3* particle orientated close to $[\bar{3}12]$ zone axis and heated to 60 °C and (b) *M3* particle orientated close to $[311]$ and heated to 100 °C. There is a significant change in morphology at 100 °C and the resulting SAED can be indexed to the anhydrous form II $[\bar{1}01]$ zone axis. Blue arrows indicate the direction of the water channels, and red and yellow arrows indicate smaller and bigger particle sizes within one area, respectively, with different surface etching rates.

Conclusions

During the dehydration of theophylline monohydrate form (*M3*), two different experimental conditions were applied to monitor phase transformation: (i) vacuum dehydration and (ii) heating in situ. Complete phase transformation from monohydrate form to anhydrous form II was observed only using condition (ii), however initial steps of dehydration are similar for both (i) and (ii) experimental conditions. Data suggest that dehydration of theophylline monohydrate is a continuous, two-step mechanism that consists of both, dehydration from the surface and along water channels to form the metastable form III anhydrate. Transformation of theophylline form III to anhydrous form II is shown to then proceed via a thermally induced restructuring at 90 °C.

6.8 Chapter Summary

The study presented in this chapter aimed to demonstrate the possibilities to use (scanning) transmission electron microscopy to acquire lattice imaging and investigate the structural changes during the hydration and dehydration of a model channel hydrate, theophylline.

The measured critical fluence of theophylline form II was $38 \pm 8 \text{ e}^-/\text{\AA}^2$ at 300 kV when supported on the continuous carbon film TEM grid. The critical fluence of theophylline monohydrate is estimated to be within a similar critical fluence range, due to the relatively small size and closed porosity of the water channels.

Low-dose phase contrast lattice imaging of anhydrous theophylline form II and monohydrate was acquired with a total electron fluence not exceeding $31 \text{ e}^-/\text{\AA}^2$. The counting mode on the DE16 camera provided a substantial improvement in resolving lattice fringes within the same total electron dose compared to the low-dose mode on the OneView camera. It was possible to identify defects in the crystalline lattice of the monohydrate form. Recrystallisation of theophylline monohydrate orientated to [100] zone axis (to image the water channels which run along the *a*-axis) proves to be difficult, however, the resolution obtained in phase contrast lattice images is sufficient for potential imaging of water channels.

SED showed that hydration of theophylline anhydrous form II does not occur in the solid state and it is a solution-mediated route with a dissolution-re-precipitation phase transformation profile. Theophylline anhydrous form II crystals changed their orientation upon contact with water or storage in RH condition, followed by crystal fragmentation. VDFs revealed that the produced form II crystals are highly distorted. Theophylline monohydrate was formed by homogeneous nucleation and crystal growth of the hydrated phase.

Dehydration of theophylline monohydrate was identified to start from surfaces with exposed water channels via surface etching (first step), and finally, water was removed via diffusion from the centre of a particle along water channels (second step). Transformation of monohydrate form/form III to form II depends on the humidity condition and temperature. In low humidity conditions, theophylline form III can adsorb water and locally transform back to monohydrate form. During heating, the monohydrate form transforms gradually to form III and then, starting at 90 °C, transforms rapidly to a more stable anhydrous form II. Form III reassembles the structure of the monohydrate form, however, a number

of defects in the crystal structure can be identified. As the observed changes occur in the presence of water vapour, phase transformation during dehydration needs to proceed via vapour-mediated phase transformation.

This study clearly shows that if the final product i.e. theophylline form II is stored in high humidity conditions or the monohydrate form is present in the final product due to e.g. incomplete drying, there is a potential risk for phase transformation. Hydration of theophylline form II is a slow, surface-driven process and the final product needs to be stored below surface saturation levels (< 66% RH) to avoid local dissolution of form II and re-precipitation of the monohydrate phase. Dehydration of the monohydrate form is also a slow process that can result in a build-up of metastable form III locally. Knowing these pathways of hydration/dehydration of theophylline can help to develop appropriate processes and storage strategies to limit phase transformations during drug manufacturing. The low-dose TEM/STEM setup used here can be used as a good starting point for elucidating the hydration and dehydration mechanism of other pharmaceutical and beam-sensitive samples.

Chapter 7 Investigations into the Physical and Chemical Structure of Tumour-Targeted Polymeric Nanoparticles

This chapter will explore the potential of using multi-modal cryogenic scanning transmission electron microscopy techniques to probe the structure of a model nanoparticle drug delivery system composed of polylactic acid - polyethylene glycol (PLA-PEG) nanoparticles (NPs) where the polymeric matrix encapsulates a hydrophobic ion-pair between an active pharmaceutical ingredient (API) (AZD2811) and a counter ion, pamoic acid, for controlled release of the drug from the polymer matrix. The physical and chemical characterization of the functionalised nanoparticle system is required to measure the drug loading and dispersion but also to understand and provide parameters to model the rate and extent of drug release, to help predict product performance. Cryogenic (scanning) transmission electron microscopy (cryo (S)TEM) imaging in combination with energy-dispersive X-ray and energy loss spectroscopies are used here to provide a multi-modal approach to the characterisation of the self-assembled polymeric nanoparticle. The results show that these core-shell particles form layered structures of different compositions and densities at the nanometre scale and are useful for identifying the typical distribution of the API within the particle layers. Cryogenic conditions can preserve the close-to-native-state structure of these hydrated polymeric nanoparticles.

7.1 Background

Drug delivery via solid formulations such as tablets taken orally can be limited by poor solubility and low bioavailability of active pharmaceutical ingredients (APIs). Encapsulation of an API within a functionalized polymeric nanostructure however has shown potential as an alternative delivery formulation that could improve therapeutic efficacy due to increasing the half-life of drug circulation while reducing side effects (Nimesh et al., 2006; Torchilin, 2006). One promising group of nano-carriers are polymeric core-shell nanoparticles (NPs) because they can encapsulate APIs by accumulation in a hydrophobic polymer matrix, assumed to be at the core (Labhasetwar et al., 1997; Matsumura and Maeda, 1986; Song et al., 2016; Wallace et al., 2012). A hydrophilic shell provides a hydrated steric barrier to increase the dispersion stability of the NPs in aqueous suspension and to protect them from recognition and removal by the reticuloendothelial system (Tang, Y. et al., 2019), and prolonging blood circulation time (Xiao et al., 2010). API delivery then depends on the loading efficiency, the rate of diffusion through the polymeric matrix and any degradation of the polymeric NPs themselves (Lim Soo et al., 2008). An important aspect of understanding the potential of new drug-loaded polymeric NPs is to characterise the particle structure, i.e. identification of the size and morphology of the core-shell nanoparticles and measurement of the distribution of API within the polymer matrix (Mahapatro and Singh, 2011; Mahdavi et al., 2020).

Many techniques can be used, however, difficulties related to structure determination and identifying the precise location and amount of the drug fraction make the characterisation more complex and in many published examples the final conclusions are based on assumptions regarding an expected structure. Cryogenic scanning transmission electron microscopy imaging in combination with energy-dispersive X-ray and energy loss spectroscopies are used here to address this issue and provide a multi-modal approach to the characterisation of a self-assembled polymeric nanoparticle system based upon a polylactic acid - polyethylene glycol (PLA-PEG) block copolymer containing a hydrophobic ion-pair between pamoic acid and an active pharmaceutical ingredient (API).

Establishing accurate measures of product structure enables a link to performance by providing appropriate physical parameters for future mathematical modelling of barriers controlling API release in these nanoparticle formulations.

7.2 Sample Preparation and Methods of Analysis

7.2.1 Nanoparticles and Suspension Preparation

Polymeric nanoparticles were obtained from AstraZeneca Ltd. Polymeric nanoparticles containing polylactic acid - polyethylene glycol (PLA-PEG) block copolymer (a number average molecular weight of approximately 16 kDa for PLA and approximately 5 kDa for PEG, determined via nuclear magnetic resonance, NMR), an active pharmaceutical ingredient (API) (AZD2811, ~20% nanoparticle) and pamoic acid (the functional excipient that forms a hydrophobic ion pair with the API, AZD2811:Pamoic 1:0.5) were prepared following the method of Song et al. (2016) via a nanoemulsion process at an estimated concentration of 137 mg/mL (Figure 7.1). The small molecule API contains 19% nitrogen in its molar mass. As produced suspensions potentially containing excess API and residual Tween (detergents for protein solubilisation) were further diluted with ultrapure water (Synergy® purification systems, Type 1, 18.2 MΩ•cm at 25 °C) to a final concentration of ~1.5 mg/mL and stored at 4°C.

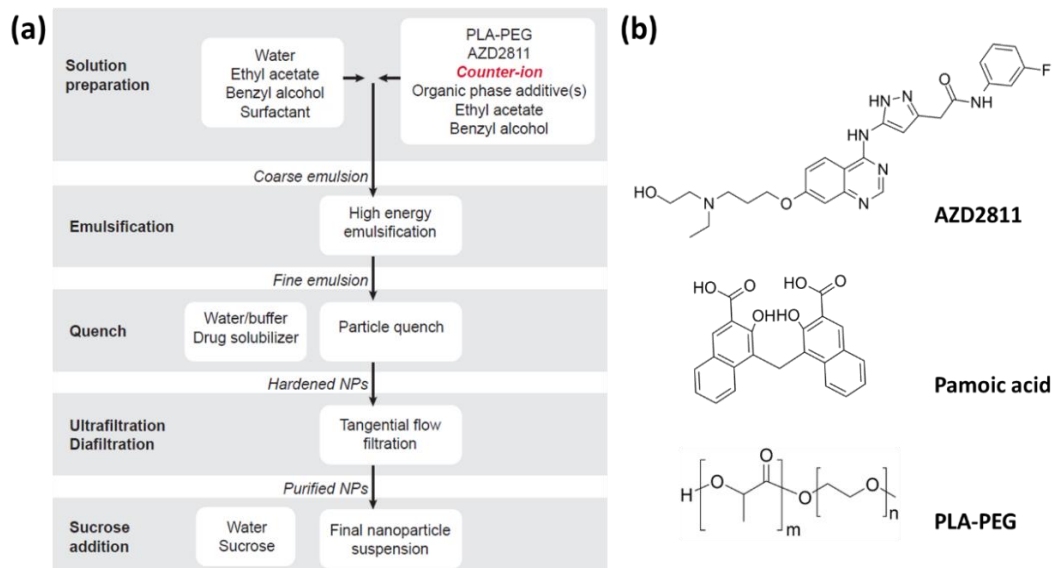


Figure 7.1 (a) Schematic of nanoparticle preparation via the nanoemulsion process. Adapted from Song et al. (2016) and (b) chemical structure of the components: AZD2811, pamoic acid and PLA-PEG co-polymer.

7.2.2 Cryo Sample Preparation

Cryo-TEM specimens were obtained by placing 3.5 μL of the diluted polymeric nanoparticle solution onto plasma-cleaned, lacey carbon TEM grids. Each grid was blotted and rapidly plunge frozen into liquefied ethane using a FEI Vitrobot[®] and transferred into a Gatan 914 TEM cryo-holder under liquid nitrogen. The temperature was kept below $-160\text{ }^{\circ}\text{C}$ during transfer into and subsequent TEM observation.

7.2.3 Cryo-(S)TEM Analytical Microscopy

Cryo-(S)TEM analytical microscopy was performed using a ThermoFisher Titan³ Themis G2 operated at 300 kV, equipped with a monochromator, multiple HAADF/ADF/BF STEM detectors, FEI Super-X 4-detector EDX system, Gatan Quantum 965 ER spectrometer and a Gatan OneView camera. Cryo-bright-field (cryo-BF-TEM) images and selected area electron diffraction patterns (SAED) were acquired in a low dose condition not exceeding a total of $\sim 10\text{-}20\text{ e}^{-}/\text{\AA}^2$ per acquired image. Cryo-annular dark-field STEM (cryo-ADF-STEM) and cryo-bright field STEM (cryo-BF-STEM) were undertaken using a probe current of 40 pA and a 10 - 40 μs dwell time and the magnification limited to 57 kX giving a total accumulated fluence of $\sim 30\text{ - }60\text{ e}^{-}/\text{\AA}^2$ per pixel for each acquired image. The camera length of the ADF-STEM detector was set to 1.15 m giving a minimum and maximum collection angle of 5 and 30.9 mrad.

Cryo-STEM-EDX spectrum imaging was performed using a probe current of 40 pA, reduced dwell time of 20 μs and pixel size of 1.319 nm giving a total electron fluence (for 48 frames) of $\sim 1.4 \times 10^3\text{ e}^{-}/\text{\AA}^2$ per pixel. Cryo-STEM-EELS spectrum imaging was undertaken in the image-coupled mode using a 0.25 eV per channel dispersion on the spectrometer. Dual EELS collection mode enabled zero loss peak (ZLP) energy calibration of core loss spectra. To minimize specimen damage, vitreous ice melting, and subsequent drift, a moderate dose (33 pA probe current and 0.05 s pixel acquisition time) was used to collect spectrum imaging data at 12 nm \times 12 nm pixel size yielding an acquisition fluence of $\sim 715\text{ e}^{-}/\text{\AA}^2$ per pixel.

7.2.4 Data Processing and Analysis

Cryo-TEM micrographs were acquired and further processed using Digital Micrograph (Gatan Microscopy Suite). Particle size distributions (PSDs) were

extracted using the ImageJ 'oval' tool and manually selected, representative nanoparticles. A number of size and shape descriptors were chosen for PSD measurement (i.e. Feret diameter and circularity).

Cryo-STEM micrographs and cryo-STEM-EDX were acquired and further processed using Velox Software (Thermo Scientific). Radial elemental distributions were measured from EDX spectrum imaging datasets of similarly sized nanoparticles using the 'radial plot profile' plug-in in ImageJ. Cryo-EELS mapping and principal component analysis were performed using Digital Micrograph.

All data and statistical analyses were carried out using OriginPro (v.2021).

7.3 Results and Discussion

7.3.1 Imaging Condition Optimisation

Optimal Magnification and De-focus Value

Initial cryo-BF-TEM observation was carried out using 0.85 nm pixel size and 4096 by 4096 pixel image size (Figure 7.2a). To minimise electron beam damage of the irradiated sample the electron intensity at the specimen was limited by the monochromator gun lens. The electron fluence was set to be $\sim 0.8 \text{ e}^-/\text{\AA}^2\text{s}$ giving a cumulative electron fluence of $\sim 2 \text{ e}^-/\text{\AA}^2$ per image. There is no observation of particle overlap in the Z-direction in any of the acquired images allowing interpretation of cryo-(S)TEM results at the single particle level. The similarly sized polymeric nanoparticles self-organise into reasonably regular hexagonal close-packed 2D arrays and most are separated by a constant spacing, suggesting the presence of either significant surface charge on the nanoparticles or a low electron density layer of material between the particles rather than just ice. However, as seen in Figure 7.2a, the polymeric nanoparticles have low contrast in the close-to-focus cryo-BF-TEM images due to their density being similar to that of the vitrified ice background. Therefore, the magnification and contrast of these images are not sufficient to enable the characterisation of the molecular packing and structure of the polymeric NPs. In order to begin to characterise the structure of the NPs, the magnification was increased, giving 0.2 nm pixel size and 4096 by 4096 pixel image size and 4 μm under-focus applied to enhance the particle contrast (Figure 7.2b). The electron fluence for this magnification was set to be $\sim 9.7 \text{ e}^-/\text{\AA}^2\text{s}$ giving the cumulative electron fluence of

$\sim 10 \text{ e}^-/\text{\AA}^2$ per image. The under-focus condition is a commonly used approach for imaging biological samples (Elbaum et al., 2021; Pustulka et al., 2013). The contrast transfer function (CTF), which represents the phase change between the scattered electron wave and the direct beam as modified by the objective lens, is schematically presented in Figure 7.2c for $0 \text{ }\mu\text{m}$ (in-focus condition) and $4 \text{ }\mu\text{m}$ under-focus. Here, the approach is opposite to using Scherzer defocus or increasing the information limit for lattice imaging as used in Chapter 6. At a high defocus value of $4 \text{ }\mu\text{m}$ under-focus, the CTF oscillates strongly and the point resolution (first cross of the CTF across the frequency axis) is shifted towards lower spatial frequencies affecting the resolution. This approach does however increase the contrast obtained which is important for the characterisation of low scattering objects such as the current polymeric NPs. At this condition of $4 \text{ }\mu\text{m}$ under-focus three components of each NPs are easily identified in cryo-BF-TEM images: (i) layer 1 – a core, (ii) layer 2 – a coating of the core and (iii) layer (matrix) 3 – which must be a low density coating or charge-limited space around each particle that is preventing particle aggregation (Figure 7.2d).

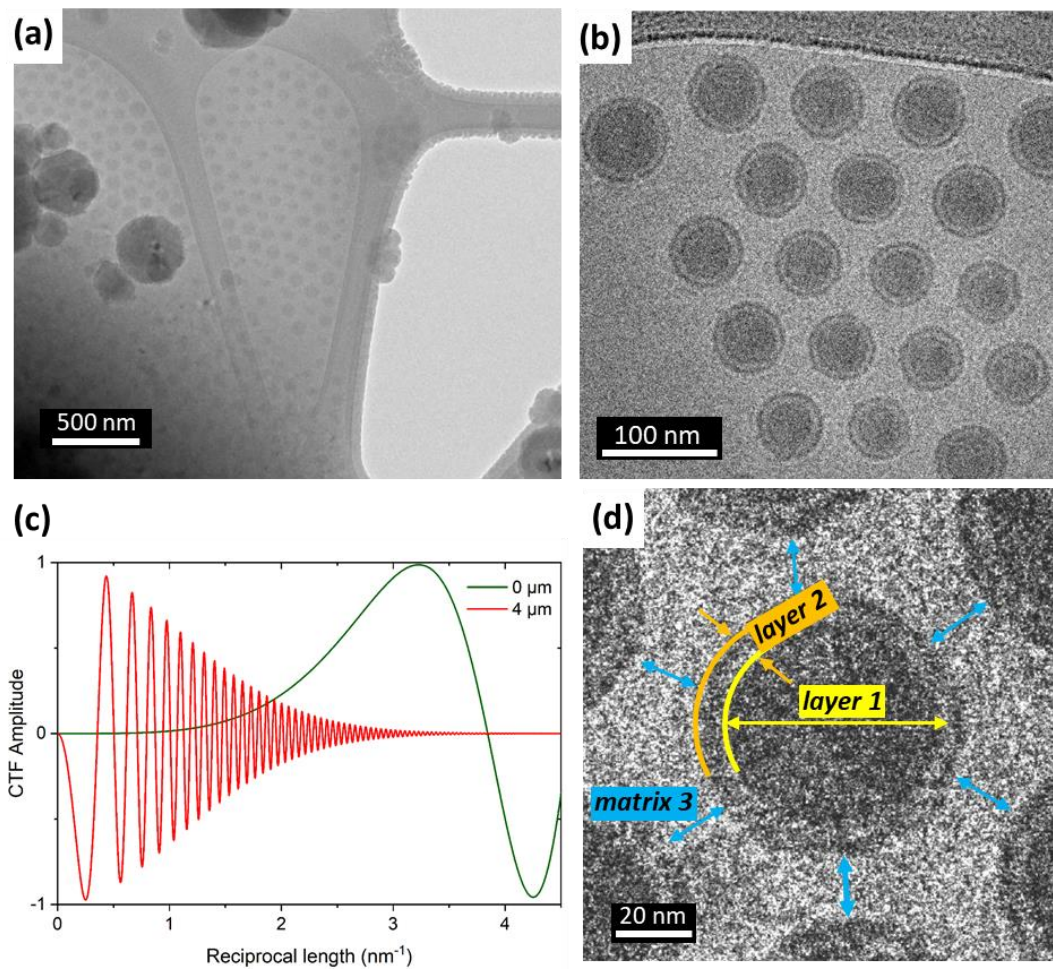


Figure 7.2 Cryo-TEM micrograph of polymeric nanoparticles: (a) Low magnification cryo-BF-TEM image taken close to focus and (b) higher magnification image with 4 μm under-focus applied, (c) CTF comparison between in-focus (green) and under-focus condition (red), (d) identification of three individual layers in each nanoparticle (as labelled in the image).

De-focusing increases the image contrast but might affect the measurable size of the NPs due to the generation of an under-focus Fresnel fringe. In Figure 7.3, the same area was imaged close to Gaussian focus and with 4 μm under focus (bottom) to enhance particle contrast of the cryo-TEM image (Pustulka et al.). The difference between close-to-focus and under-focus image conditions are presented in the power spectrum or fast Fourier Transform- FFT (top left inset at each image) and it is seen that at the under focus-condition, there are more oscillations (rings) in the FFT as predicted by the model of the CTF in Figure 7.2c but that this results in enhanced contrast of the cryo-BF-TEM image. At the under-focus condition, a lower-density surface layer surrounding the particle core becomes more visible (layer 2 in Figure 7.2d). The differences between the mean values of the in- and under-focus particle diameters (outer, low-density layer)

were shown to not differ by more than 0.7 nm. However, determination of the layer boundaries of NPs in the image close to focus is difficult. An estimate of a manual measuring error of ± 2 nm in diameter size (under/over-estimate of the size of the NPs) was used and close to focus values compared to the equivalent under-focus image values (Figure 7.3). A two-tailed P-test run on these measured diameters yielded $P = 0.097$, suggesting that the difference in the measured mean value between the image types is not statistically significant ($P > 0.05$) and diameters measured at $4 \mu\text{m}$ under-focus can be used for further analysis (Table 7.1).

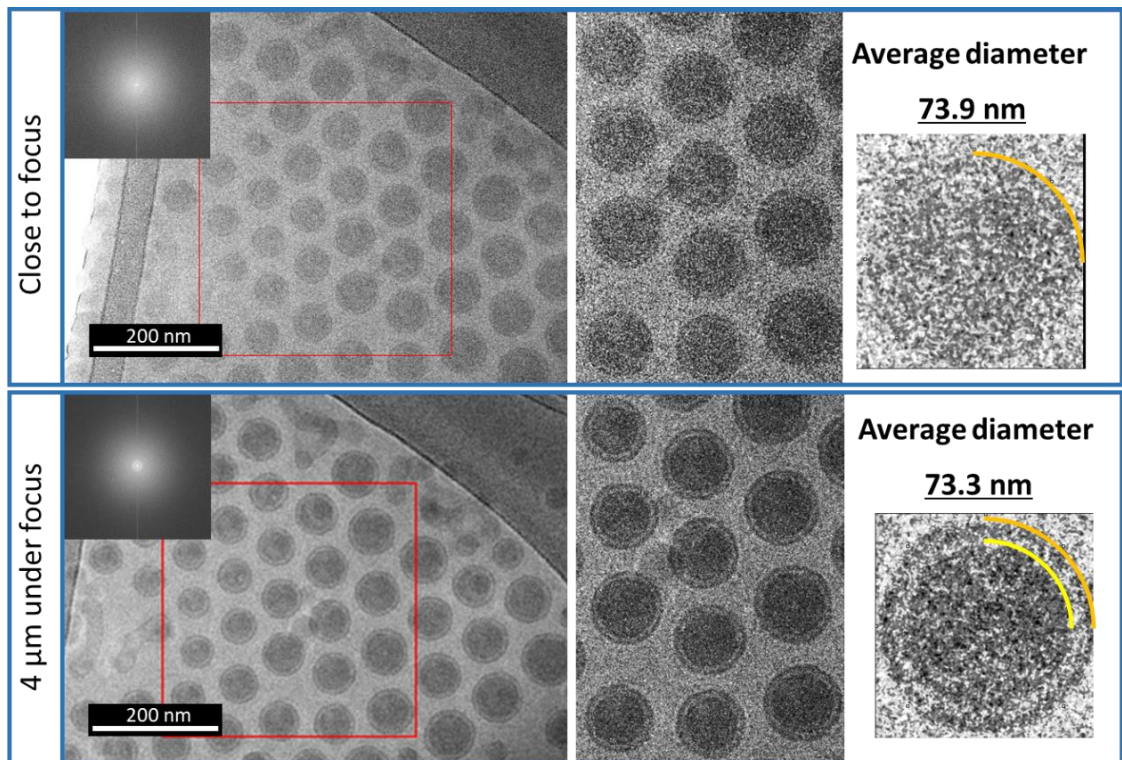


Figure 7.3 Comparison between the high-magnification cryo-BF-TEM images of the same area taken: (a) close to focus and (b) by applying $4 \mu\text{m}$ under-focus to the same area to increase the particle contrast.

Table 7.1 Measurement of corresponding particle diameter from close to focus and 4 μm under-focus images. A two-tail P-test was performed on both datasets.

	Particle	Close to focus	4 μm under-focus
	1	63.9	65.5
	2	70.4	68.5
	3	74.5	73.2
	4	69.6	69.1
<i>Measurement of the corresponding particle diameters (layer 1 + layer 2)</i>	5	75.1	73.8
	6	75.1	73.2
	7	74	71.4
	8	70.4	70.2
	9	72.9	75
	10	78.1	78.5
	11	79.8	79.7
<i>Mean</i>		73.9	73.2
<i>Variance</i>		10.0	12.6
<i>Observations</i>		11	11
<i>P(T\leqt) two-tail</i>		0.097	
		> 0.05	<i>the null hypothesis is not rejected</i>
		P(T>=t)	

Critical fluence measurement

Low-dose selected area electron diffraction and high-magnification images do not reveal any signs of crystallinity in the polymeric NP. Formation of ice and frost contamination can be seen in the cryo-BF-TEM images (e.g. Figure 7.2a) and are seen as rings (or polycrystalline reflections in SAED patterns for highly contaminated areas) that can be indexed to the crystalline lattice of hexagonal ice crystals (Ilett et al., 2019). However, as demonstrated in Chapter 4 and Chapter 6, cryo scanning electron diffraction has the resolution to map amorphous and crystalline structures of soft matter using a low-dose condition and has been recently used to map crystalline regions in an amorphous-crystalline polymer blend (Donohue et al., 2022). However, due to data protection

of any polymeric NPs results, it was not possible to analyse this sample at ePSIC (Diamond Light Source) as open access to data is required when applying for beamtime.

Critical fluence (electron beam sensitivity) cannot be calculated by measuring the change in intensity of diffraction spots in the SAED pattern series for this case (as the material is fully amorphous). Therefore, an electron beam damage threshold was estimated by identifying changes to particle structures in a series of images collected at progressively higher cumulative electron fluence. Figure 7.4 shows electron beam damage observation in a series of cryo-BF-TEM images based on illuminating the same area with the cumulative electron fluences of (a) $20 \text{ e}^-/\text{\AA}^2$, (b) $40 \text{ e}^-/\text{\AA}^2$ and (c) $80 \text{ e}^-/\text{\AA}^2$. Electron beam damage of the particles is identifiable by two characteristic features. First, a decrease in the contrast between layers 1 and 2. Yellow arrows in the higher magnification insets of Figure 7.4 indicate that the layer 1 boundary begins to fade at $40 \text{ e}^-/\text{\AA}^2$. Second, void formation preferentially occurred at the interface between layer 1 and layer 2 (marked by blue arrows in the higher magnification inset). Voids or bubbling in polymeric material can result from restricted diffusion of radiolysis products i.e. formation of gas (e.g. hydrogen H^+) within a vitrified sample (Leapman and Sun, 1995). As cumulative electron dose increases, the bubbling expands in layer 2 and some bubbling can also be observed in layer 1 (although this could be from layer 2 on the top surface of the projected image of the spherical nanoparticles). This suggests a structural difference between layers 1 and 2 consistent with the image contrast difference. Layer 2 is made of the most beam-sensitive component and damaged products may migrate to the interface between layers 1 and 2 where the interface acts as a nucleation point for gas bubble formation. It is not possible to get a robust critical fluence value from the limited image series, however, based on the damage observation, the cumulative electron fluence per image in cryo-TEM should be kept below $40 \text{ e}^-/\text{\AA}^2$.

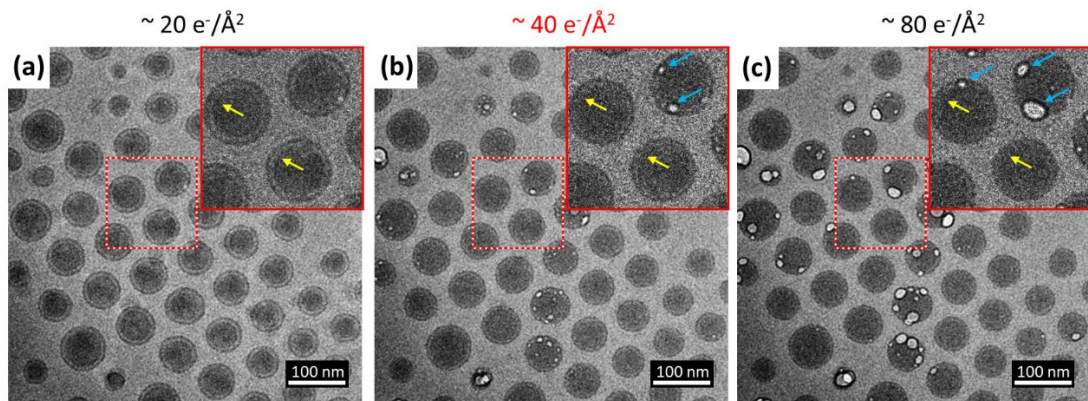


Figure 7.4 Electron beam damage observation in cryo-BF-TEM based on imaging the same area with a total electron fluence of (a) $20 \text{ e}^-/\text{\AA}^2$, (b) $40 \text{ e}^-/\text{\AA}^2$ and (c) $80 \text{ e}^-/\text{\AA}^2$. Yellow arrows indicate the layer 1 boundary which begins to fade at $40 \text{ e}^-/\text{\AA}^2$ indicating damage to the structure of the nanoparticles. The blue arrows indicate bubble/void formation, especially at the interface between layer 1 and layer 2, related to severe radiation damage. Based on this observation of damage propagation, $< 40 \text{ e}^-/\text{\AA}^2$ (marked in red font) is considered as a safe dose for cryo-TEM imaging.

Moreover, the same observation was performed in cryo-ADF-STEM using a 40 pA probe current and 10 μs dwell time giving an image series based on 1, 3, 5, 8, 11, and 14 scans of the same area with the cumulative electron fluences of 29, 86, 144, 230, 317 and 403 $\text{e}^-/\text{\AA}^2$, respectively (Figure 7.5). Based on the observation of the damage propagation, $< 80 \text{ e}^-/\text{\AA}^2$ (marked in red font) is considered as a safe dose for cryo-STEM imaging. The electron beam damage limit at $\sim 80 \text{ e}^-/\text{\AA}^2$ in cryo-ADF-STEM is $\sim 40 \text{ e}^-/\text{\AA}^2$ better than in cryo-BF-TEM. That might be an indication of the inverse dose effect for high current STEM, suggested by Egerton (2019).

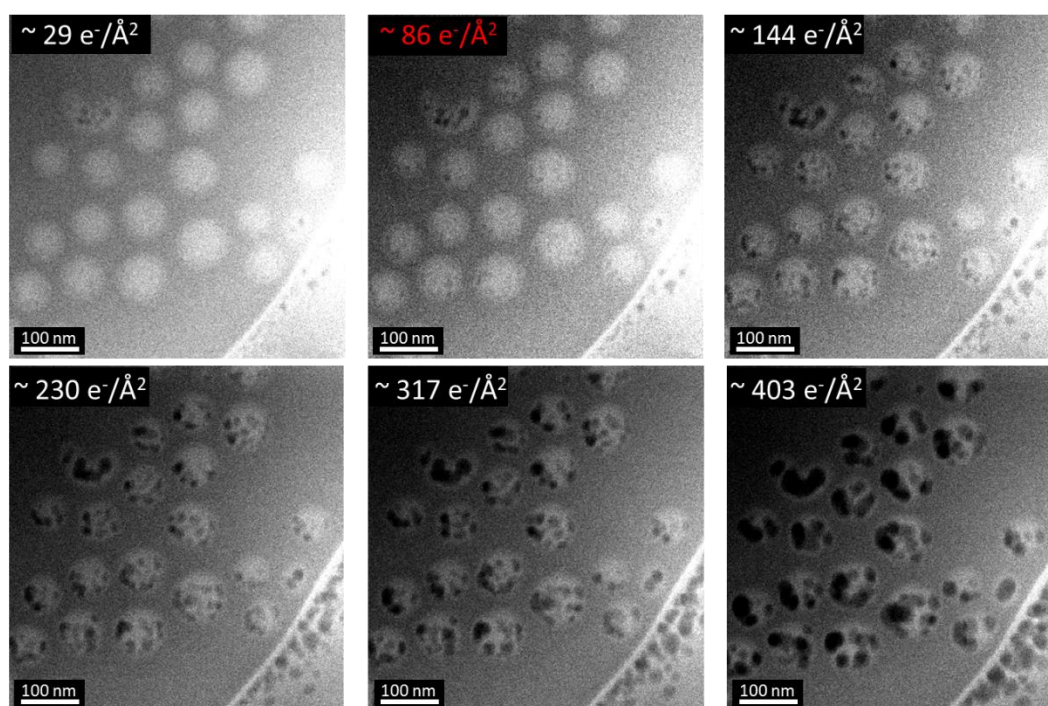


Figure 7.5 Electron beam damage observation in cryo-ADF-STEM based on imaging the same area after total frames of: 1, 3, 5, 8, 11, and 14 scans and using a 40 pA probe current and 20 μ s dwell time. Based on the observation of the damage propagation, < 80 $e^-/\text{\AA}^2$ (marked in red font) is considered as a safe dose for cryo-STEM imaging.

7.3.2 Physical Characterisation

As discussed above, the under-focus cryo-BF-TEM images may be used for representative size distribution measurement, of both the entire nanoparticle size and the thickness of the individual layers. Individual layers were measured by the following procedure (shown schematically in Figure 7.6). (i) Layer 1 - the radius is half the maximum Feret diameter. (ii) Layer 2 – the thickness is half of the difference between the two Feret diameters of layer 1 and layer 1+2. (iii) Layer 3 – the thickness is taken as half of the smallest distance between adjacent particles. The particle size distribution, determined from 100 manually measured nanoparticles in ImageJ (Schneider et al., 2012), is presented in Figure 7.7. The mean radius for layer 1 is 25 ± 4 (\pm SD) nm, and the thickness for layer 2 is 9 ± 1 (\pm SD) nm and for most particles, the thickness of layer 3 is 10 ± 4 (\pm SD) nm. The total mean diameter of the polymeric nanoparticles is 88 ± 9 (\pm SD) nm (layer 1-3), across a size range of 68 – 126 nm. The insets (Figure 7.7a and b) show cumulative mean radius against particle counts and it can be noted that only around 80 particles or more need to be measured for a consistent particle size to

be obtained. The average roundness is calculated to be 0.99 confirming the circular shape of the nanoparticles (1 is a perfect circle).

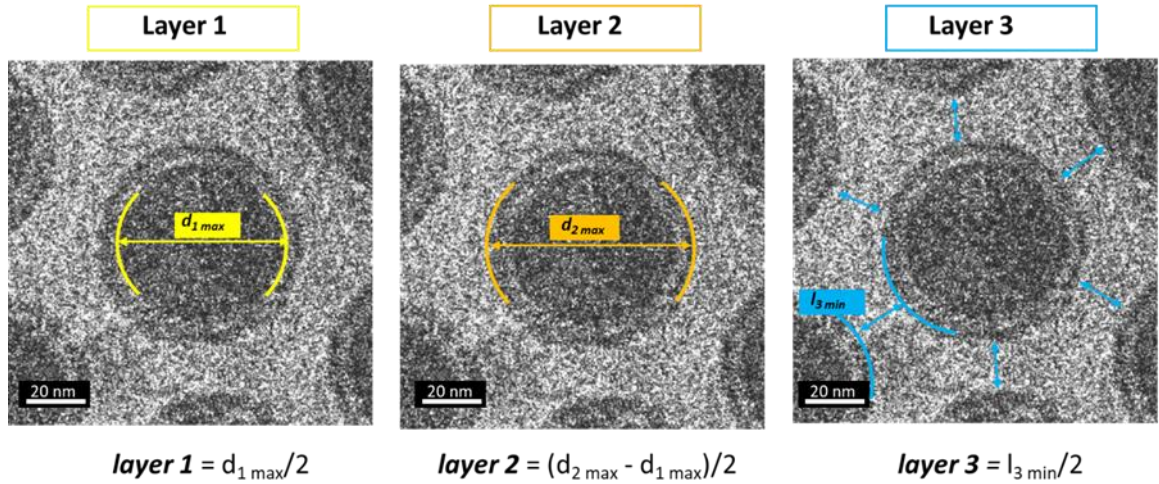


Figure 7.6 Measurement procedure to calculate the radius of individual layers.

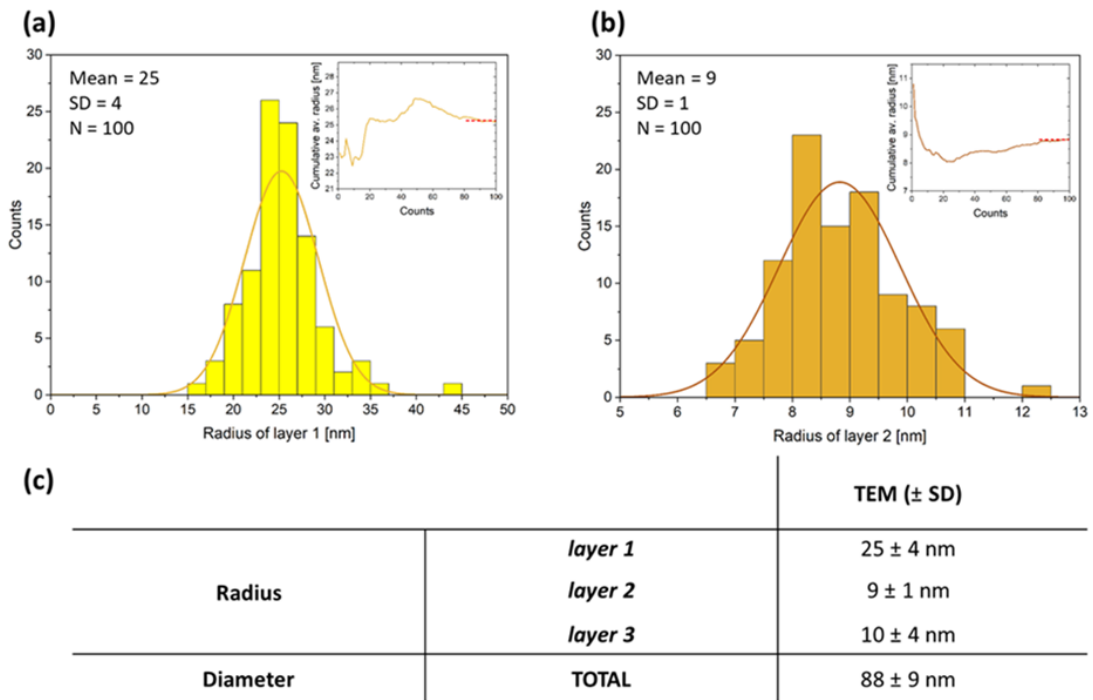


Figure 7.7 Particle size distribution histograms of the radius of (a) layer 1 and thickness of (b) layer 2 measured on the de-focused images. The inserts represent the cumulative mean radius, suggesting that a minimum of 80 particles is required to accurately measure the particle size distribution (since after that number the cumulative radius does not vary significantly). (c) Table with the mean values for layers 1-3. The average diameter of nanoparticles is 88 \pm 9 (\pm SD) nm.

Cryo-STEM Imaging

In the STEM mode, where the probe is scanned across the specimen, focusing the sample is crucial to acquire an in-focus image. Besides the electron beam sensitivity of polymeric NPs, vitrified ice causes an additional complication i.e. different ice thickness, produced by blotting the grid, causes variation in focal heights of NPs and contributes to noise in the image (Glaeser et al., 2016). Focusing the probe using a Ronchigram was performed carefully on the carbon film to not extensively melt the vitrified ice. The comparison between cryo-BF-STEM (used for phase contrast imaging which by reciprocity can be similar to a conventional cryo-BF-TEM image), cryo-ADF-STEM (can be used for imaging materials with different densities and possible imaging lighter elements) and corresponding inversed contrast cryo-ADF-STEM images are presented in Figure 7.8. The difference in the density of the central part of the NPs is seen and marked by green arrows. Contrast arising from the thickness of NPs contributes also to the cryo-ADF-STEM images, however, some particles exhibit slightly different bright contrast in the core of NPs in the cryo-ADF-STEM and their profile slightly differs from the corresponding darker contrast in the cryo-BF-STEM image (analysed in detail in Figure 7.8). As the nanoparticles consist only of light elements, i.e. hydrogen, carbon and oxygen, the additional scattering contribution from nitrogen, that is present in the API, might generate extra contrast in an ADF image of the core. Moreover, when a NP image is properly focused, layers 1 and 2 are visible in cryo-ADF-STEM images (yellow and orange curves). However, as reported by Piepenbrock et al. (2014), the black object on a white background is better suited for the human eye to pick-out, therefore contrast reversal of the ADF-STEM images is used here to enhance the visibility of layers (Figure 7.9). A dark (lower contrast) halo is visible around many particles suggesting layer 3 contains material of lower scattering density than both the particle cores (layers 1 and 2) and the surrounding vitreous ice (the upper boundary of layer 3 is marked by blue curves in Figure 7.8). The thickness of these 'halo' regions is measured to be ~10 nm and this is in good agreement with the previously measured layer 3 thickness from cryo-phase contrast-TEM images.

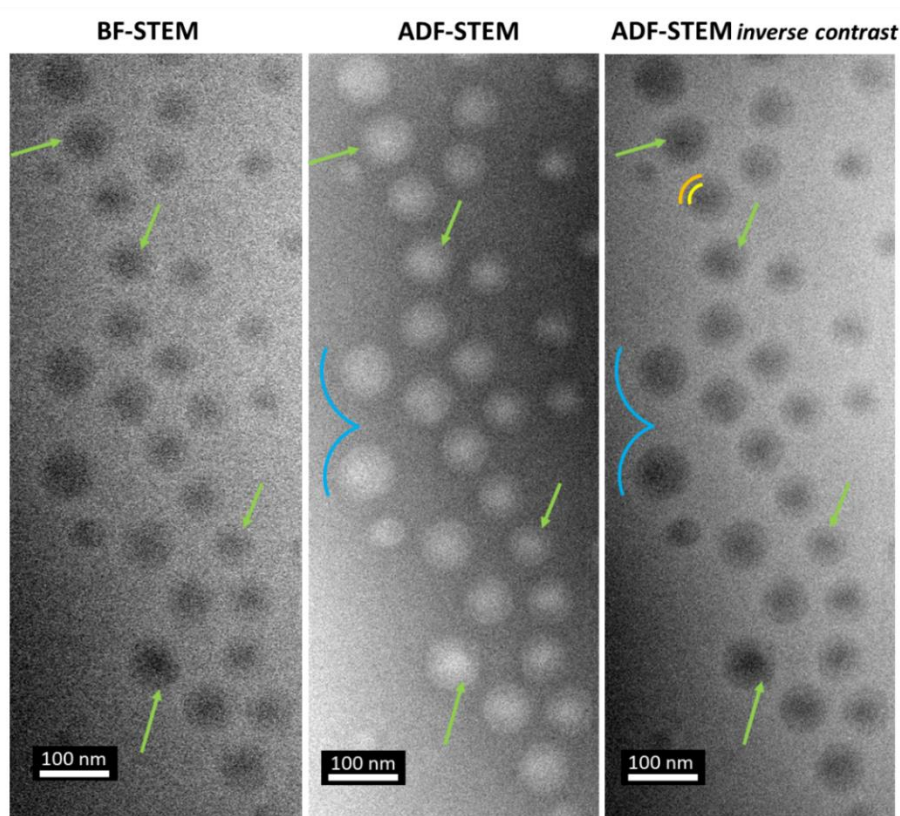


Figure 7.8 Comparison between corresponding cryo-BF-STEM, cryo-ADF-STEM and inversed contrast cryo-ADF-STEM revealing: (i) different contrast within the core (marked by green arrows), (ii) layers 1 and 2 (yellow and orange curves) and (iii) layer 3 (blue curves) components.

A comparison between image modes is presented in Figure 7.9. Conventional cryo-BF-TEM provides better resolution and SNR as defocusing enhances the phase contrast of the NPs. Conversely, layer 3 can be seen in the cryo-ADF-STEM as a dark 'halo' but is not distinguishable in cryo-BF-STEM images. In addition, applying a high-pass filter (Fourier-filtering function to remove low frequencies) to the cryo-ADF-STEM images enhances the contrast in layer 3 significantly (by removing the low-frequency background variation). This confirms a lower electron density for layer 3 than the surrounding ice and inverting the contrast clearly reveals the inner core, layer 1, 2 and 3 in one image i.e., direct identification of a core, shell and corona particle structure (Figure 7.8, 9). A particle corona of lower electron density than vitreous ice could be due to there being a low-density brush of PEG molecules attached to layer 2 only. A 5 kDa PEG chain typically extends out by 10 nm for a dense brush layer (Xu et al., 2015) however this may extend further to 10-20 nm when the brush packing becomes less dense (Pagels et al., 2018; Tian et al., 2020).

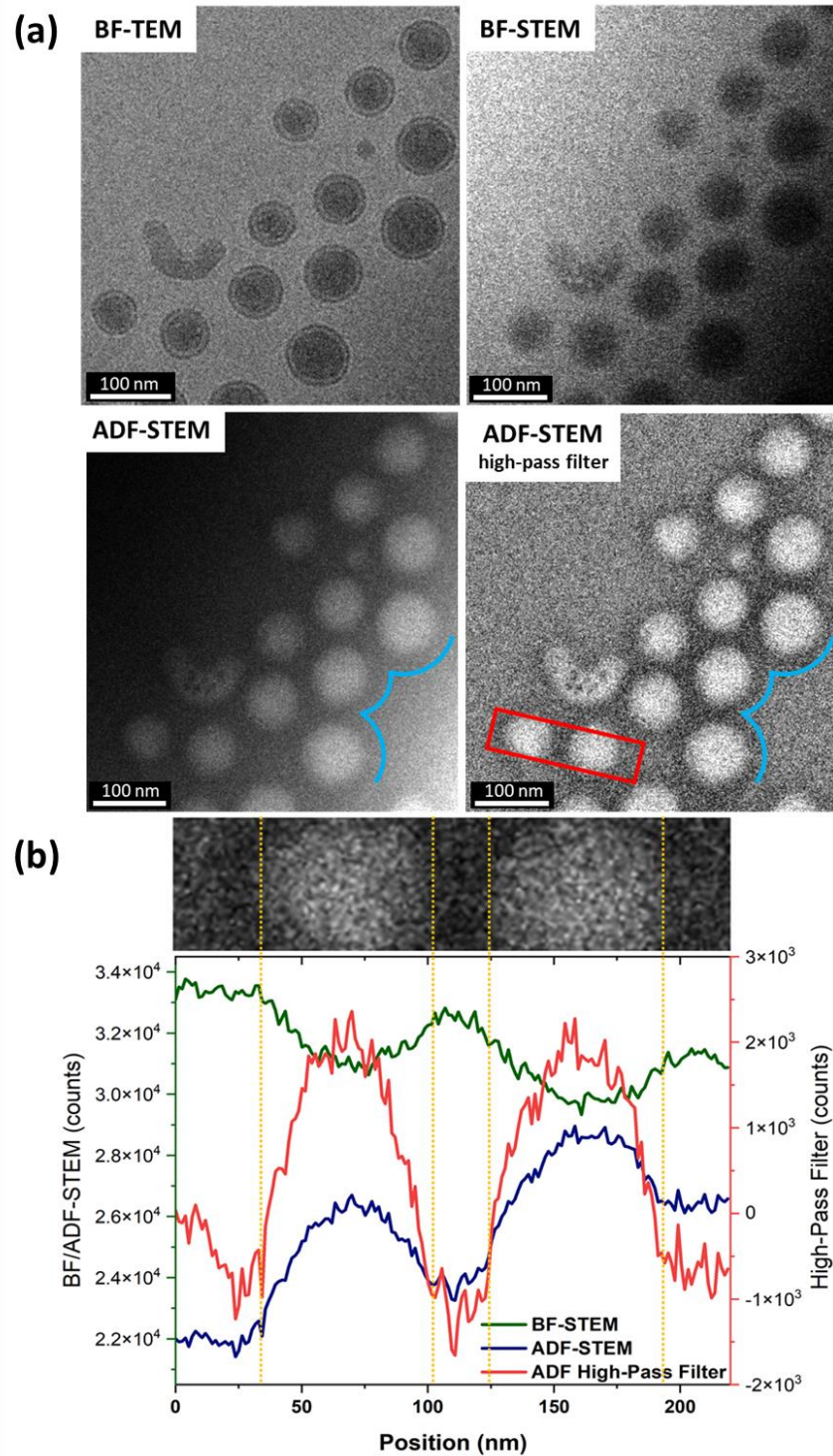


Figure 7.9 (a) Cryo-(S)TEM images of polymeric nanoparticles taken from the same region. A high-pass filter applied to the cryo-ADF-STEM image significantly enhances the contrast of layer 3. (b) The intensity line profile from the region marked by the red rectangle in (a) shows that the particle diameter is the same across all images and high-pass filtering can be used for particle measurement.

The intensity line profile taken across 2 nanoparticles of corresponding STEM images is presented in Figure 7.9, confirming that the diameter of corresponding

nanoparticles is the same in BF/ADF and high-pass filtered ADF-STEM images. This shows that both types of image modes can be complementary and each of them supports the characterisation of particular components of NPs.

7.3.3 Chemical Characterisation

Low-dose EDX and EELS

Cryo-BF-TEM and cryo-ADF-STEM were used to identify the three layers plus an inner core to the polymeric NPs. However, elemental spectroscopy is needed to complete chemical identification and to locate the nitrogen-containing API. Typical energy-dispersive X-ray and electron energy loss spectra from an area containing NPs in the field of view are presented in Figure 7.10. Cryo-STEM-EDX and EEL spectra show the characteristic C-K, N-K and O-K edges from within the area containing several NPs, however, the F-K edge is not distinguishable. This latter point is not surprising due to several reasons: (i) only one F atom is present in each molecule of the API giving ~4% contribution to its molar mass (Figure 7.1b), (ii) Egerton (2019) suggested that substitution of a fluorine atom in place of hydrogen results in rapid F loss and fast radiolysis and (iii) in EELS, there is a domination of O-K edge due to high oxygen content in the cryogenic sample that overlaps with F-K edge.

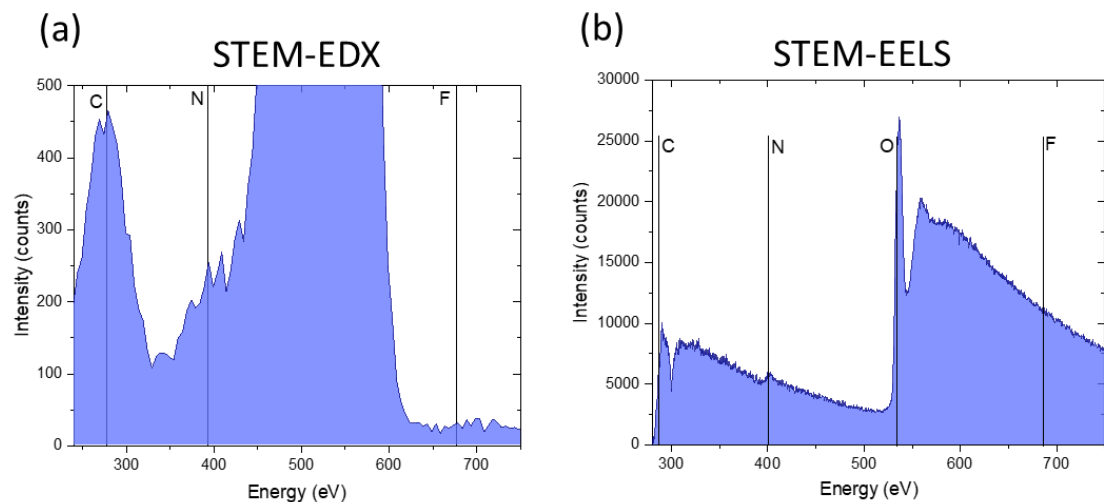


Figure 7.10 (a) Typical cryo-STEM-EDX and (b) background subtracted EEL spectra identifying C-K, N-K and O-K edges from the area containing nanoparticles in the field of view.

Spatially resolved spectrum imaging by EDX and EELS required high probe currents and is therefore highly limited by the potential for electron beam damage

of the polymeric nanoparticles. Initial elemental mapping was performed using cryo-STEM-EDX due to reasonable ease of use and lack of requirement on the sample thickness (Figure 7.11). Figure 7.11a-b shows cryo-ADF-STEM images before and after EDX acquisition, respectively. The electron beam damage is clearly visible in the cryo-ADF-STEM. A total electron fluence of $1.4 \times 10^3 \text{ e}^-/\text{\AA}^2$ per pixel was used for EDX acquisition. The C-K elemental map assembled using a single-pixel average filter does not provide the required resolution for layer identification (Figure 7.11c). Therefore two strategies have been considered: (i) increasing the average pixel filter to 38 pixels in order to increase signal to noise for quantification and (ii) measuring the radial average profile across 8 similarly sized nanoparticles. The images from both strategies are shown in Figure 7.11f. Different individual C-K profiles indicate the need for averaging radial profiles across many nanoparticles or increasing the average filter pixel size. Moreover, a carbon signal is also present at the edge of the nanoparticles (layer 3). Noisy N-K elemental maps and its weak radial profile suggest that the API is located somewhere near the centres of the nanoparticles, but the resolution is not sufficient for complete structure identification by EDX.

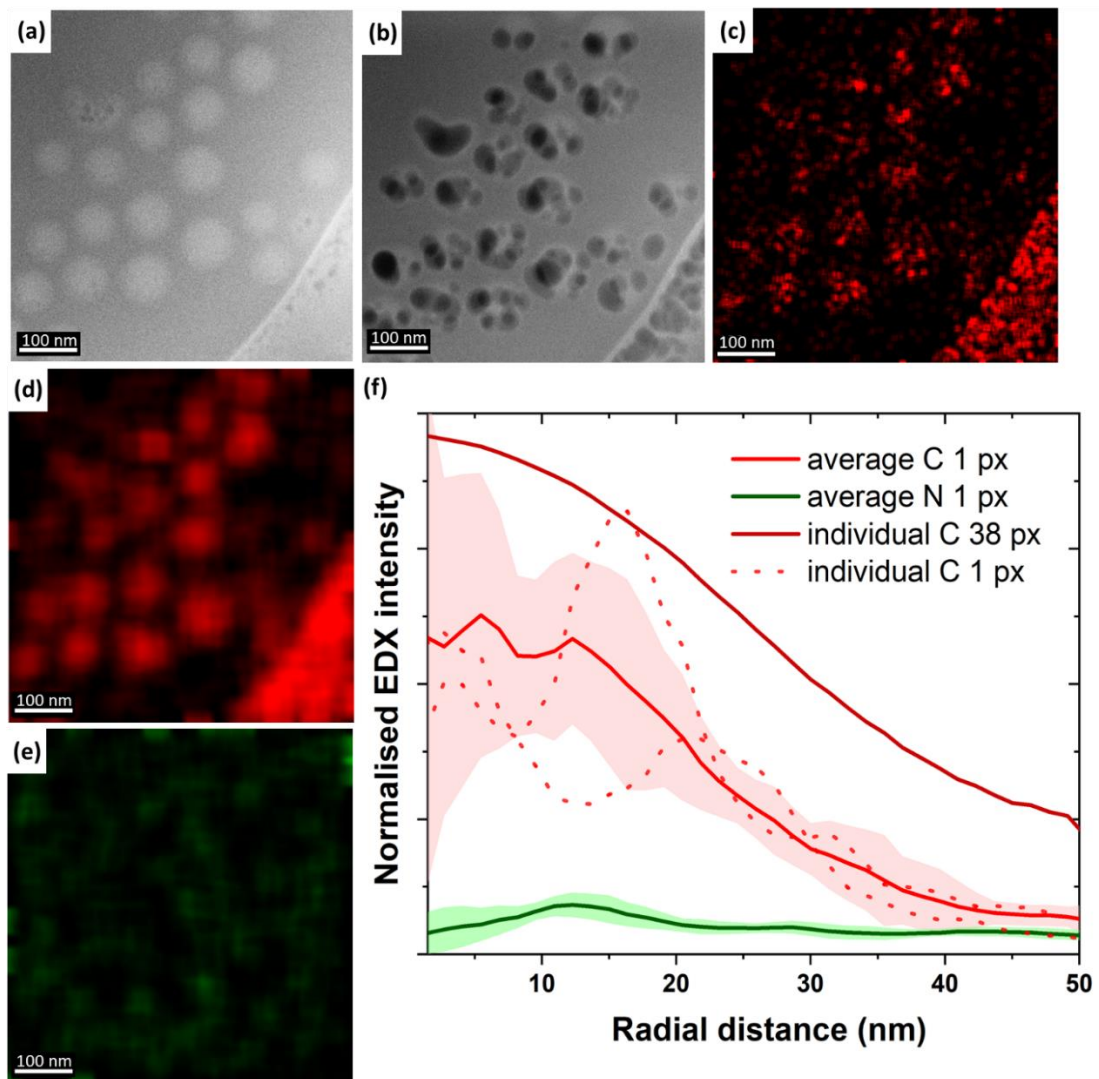


Figure 7.11 (a)-(b) Cryo-ADF-STEM images before and after EDX acquisition, respectively, and corresponding: (c)-(d) C-K EDX elemental maps using 1 and 38 px average filter, respectively and (e) N-K EDX elemental map using 38 px average filter. (f) Radial elemental distribution measured using ‘radial plot profile’ plug-in in ImageJ from the area in (a).

Cryo-STEM-EELS has a greater collection efficiency of elemental scattered electrons, especially for light elements, however, this method also requires a high probe current, and it is dependent on the sample thickness. To maintain a relatively low dose condition, cryo-STEM-EELS elemental maps were acquired with an image pixel size increased to 12 nm and the probe dwell time offset to 0.05 s, resulting in reduced signal-to-noise ratio (SNR) and limiting spatial resolution but an acquisition fluence of $715 \text{ e}^-/\text{\AA}^2$, half of the dose range used in the cryo-STEM-EDX elemental mapping. A 12 nm pixel size is sufficient to identify the thinnest component of the structure identified so far i.e. layer 2. Figure 7.12 presents the cryo-STEM-EEL spectra that reveal the characteristic C-K, N-K and

O-K edges from within the particles, and from which the elemental maps for carbon and nitrogen were gathered. The spatial distribution of the C signal is in good agreement with the scattering contrast from these carbon-rich, polymeric NPs seen in the corresponding cryo-ADF-STEM image. Line profiles along C and N elemental overlay maps confirm that the peak C and N signals within nanoparticles correspond to the bright central region or inner core identified in the cryo-ADF-STEM images, suggesting, that these are where the N-rich API is located. Cryo-STEM-EELS has been shown to be the most efficient method for the structural characterisation of nanoparticles.

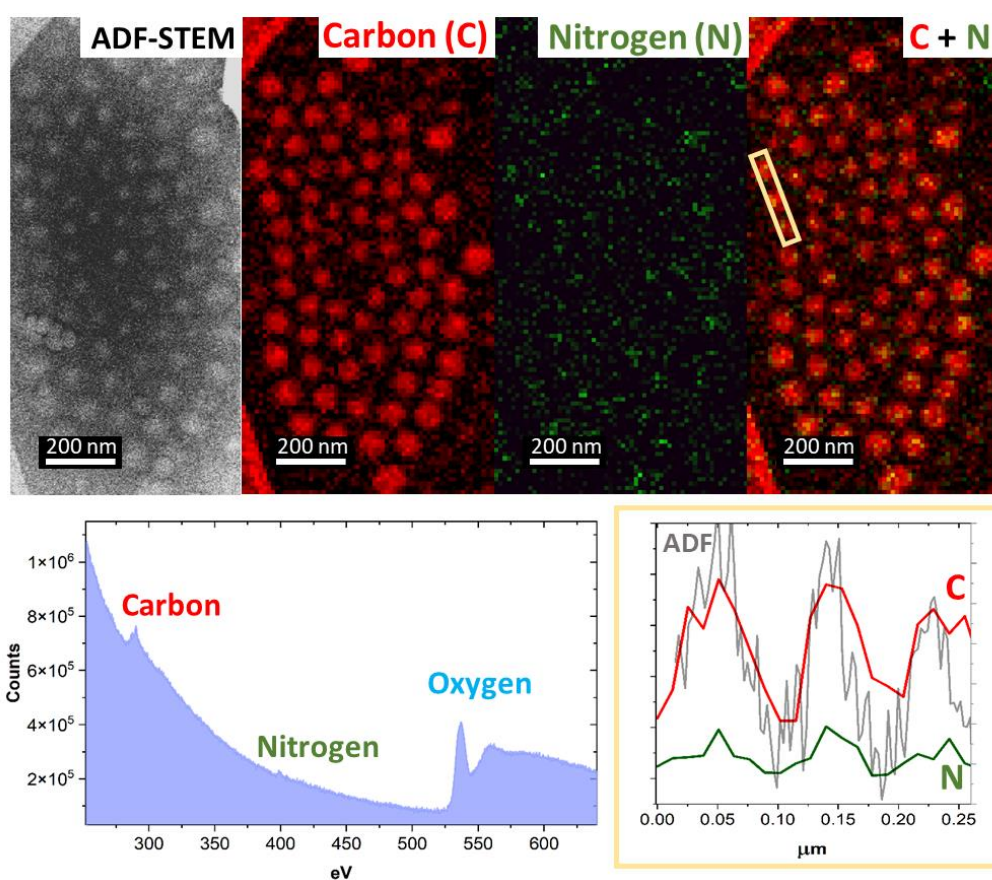


Figure 7.12 Cryo-STEM EELS carbon and nitrogen mapping. A linear intensity profile taken from the C-N overlay map and ADF image indicates that C occurs also between the nanoparticles and N is located approximately in the centre of individual nanoparticles (yellow boxes). Cryo-STEM-EEL spectrum acquired over the whole area shows the presence of C, N and O elements (below and left).

Principal component analysis

Low-dose cryo-STEM-EELS elemental maps can be de-noised by the application of Principal Component Analysis (PCA). Particular attention was made to the

correct identification of significant components in the corresponding scree plots (Figure 7.13). The number of components is commonly related to the known or expected factors i.e. elements in cryo-STEM-EELS mapping in this investigation (Lucas et al., 2013). The first component can consist of the mean cryo-STEM-EELS spectra and it is clearly seen in Figure 7.13b, where C-K, N-K and O-K edges are distinguishable. The second component is clearly related to C-K and O-K edges (Figure 7.13c). The subsequent 3rd, 4th and 5th components can be attributed mainly to O-K as oxygen dominates in the cryogenic specimen, however, these can also be related to minor signals from C-K (4th, 5th) and N-K (4th) (Figure 7.13e). However, the number of components is commonly lower than the expected factors due to the noise present in the data (Lucas et al., 2013). To avoid artefacts related to overestimating the number of components, only the first two meaningful components (Figure 7.13b, c) are used to provide denoised cryo-STEM-EELS mapping.

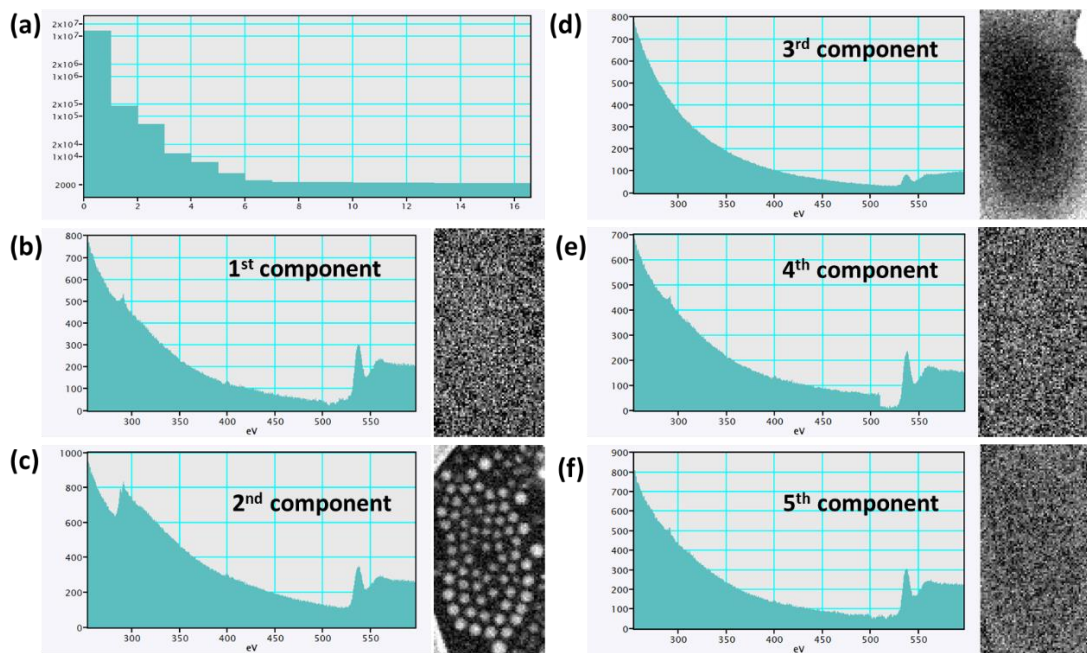


Figure 7.13 Principal component analysis: (a) scree plot used for identification of (b)-(f) first five significant components that are presented as loading (spectra) and scores (image).

An example of a PCA de-noised cryo-STEM-EELS carbon elemental map is shown in Figure 7.14. The corresponding under-focus cryo-BF-TEM, cryo-ADF-STEM and C elemental maps allow for multi-modal interpretation and identification of the structural components of the nanoparticles. The diameter of layer 1 plus layer 2 measured by under-focus cryo-BF-TEM image is in good

agreement with the diameter measured by cryo-ADF-STEM and de-noised C mapping (orange arrow). However, layer 3, which is not directly seen by under-focus cryo-BF-TEM, can be identified by cryo-ADF-STEM and de-noised C mapping (blue arrows) and is consistent with a 10 nm thickness layer containing organic material, as inferred from the spacing of the NPs in BF-TEM. Moreover, layer 2 was significantly damaged during EELS mapping and is seen as a dark rim to the NPs in the post-acquisition cryo-ADF-STEM image (red arrows in Figure 7.14) confirming the higher electron beam sensitivity of this component compared to layer 1 i.e. that layer 2 is of different composition to layer 1. Layer 3 does contain C, but it is at a significantly lower concentration than in layers 1 and 2 and damages at the same rate as the surrounding ice.

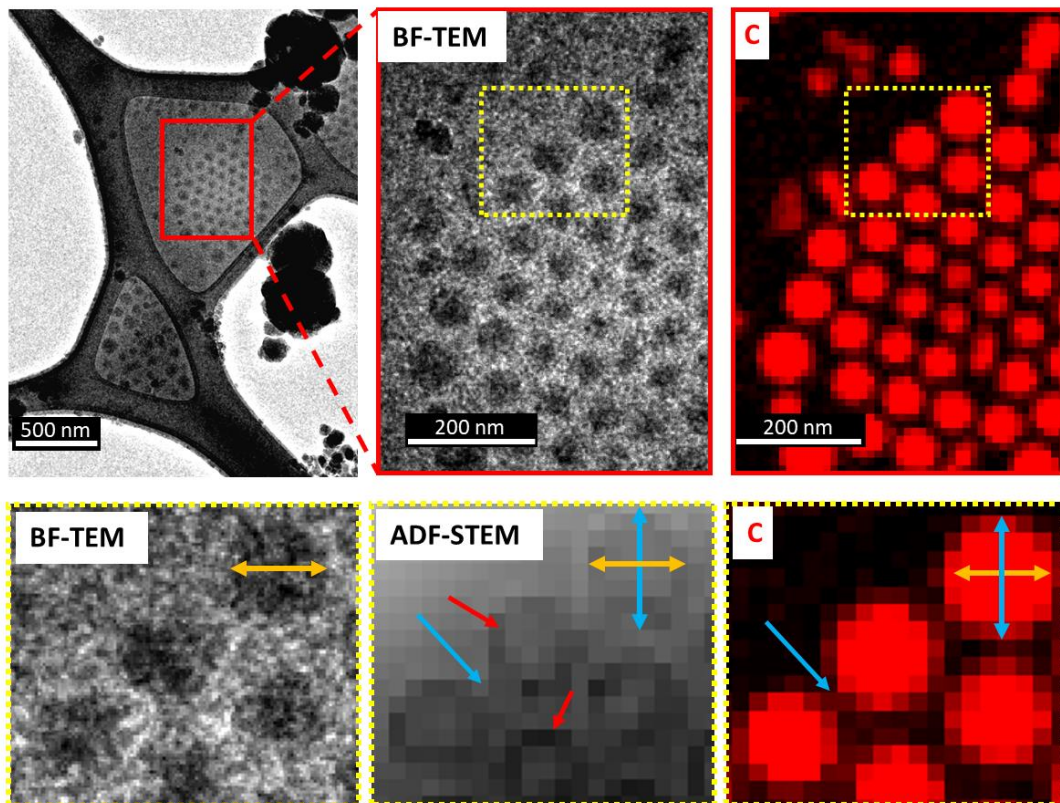


Figure 7.14 PCA treated carbon cryo-STEM-EELS mapping of the area marked in red in the under-focus cryo-BF-TEM image. Below, under-focus cryo-BF-TEM, cryo-ADF-TEM and C EELS mapping of a cropped fragment marked in yellow and showing carbon presence between the particles and confirming the C-content to layer 3. The corresponding diameter of layer 1+2 is identical between cropped under-focus cryo-BF-TEM, cryo-ADF-STEM and C-map images (yellow arrows) and the thickness of layer 3 is consistent with earlier measurements of the spacing between nanoparticles by under-focus cryo-BF-TEM (blue arrow). Red arrows indicate severe electron beam damage in layer 2 visible in a post-EELS acquisition, cryo-ADF-STEM image.

Low-dose EEL spectra from individual layers

Averaged cryo-STEM-EEL spectra were selected from particle layers 1, 2 and 3 and are presented in Figure 7.15. The smoothed spectra show the C-*K* and O-*K* edges are visible in all layers and the N-*K* edge is clear detectable in layer 1 (Figure 7.15a and b; note that trace C may be detected in the amorphous ice but at levels lower than that in layer 3). The maximum C counts in unsmoothed spectra of the measured areas for the spatially separated layers decrease from 600 for layer 1 to 240 for layer 2 and 120 for layer 3. The C:O peak intensity ratio varies from 1 to 0.7 for layer 1, to 1 to 2.1 for layer 2 and 1 to 4.1 for layer 3 (and the absolute O count in layer 3 remains lower than that in the amorphous ice with C:O ratio of 1 to 11.2). These data are consistent with the cryo-BF-TEM and cryo-ADF-STEM results that show the core or layer 1 of the nanoparticles has the densest C packing and contains the majority of the API, and that the very outer layer (3) is the least dense but does indeed contain C. The near-edge fine structure (or shape) of the un-smoothed, background subtracted C *K*-edges are shown in Figure 7.15c. Layer 1 C *K*-edge shows a broad C 1s- π^* peak just above 285 eV suggesting additional transitions to the C 1s- π^* C=C peak. These may result from the formation of unsaturated bonds resulting from electron beam damage during irradiation (Pal et al., 2021). This would be consistent with the C-rich, conjugated C structures of pamoic acid and the API being in layer 1, as also revealed by the N mapping (Figure 7.12). The C 1s- π^* peak is much sharper in layer 2 suggesting a simpler carbon structure than layer 1 consistent with layer 2 being dominated by the simpler PLA and/or PEG structures. The C *K*-edge for layer 3 is noisy but closest in shape to that of layer 2.

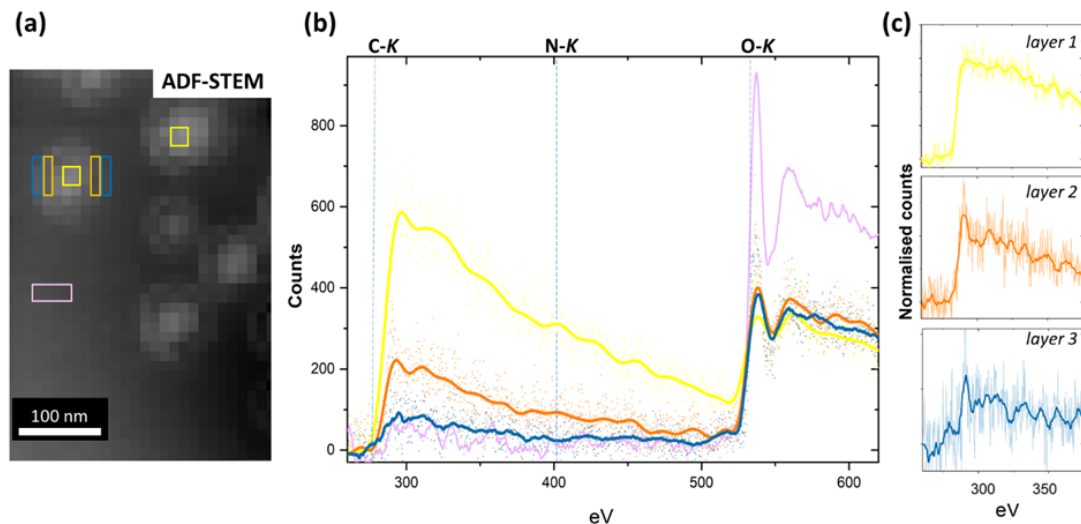


Figure 7.15 (a) Cryo-ADF-STEM image of particles and areas where spectra were extracted from – layer 1 (yellow box), layer 2 (orange boxes), layer 3 (blue boxes) and amorphous ice (purple box). (b) Background stripped, as-acquired (faint dots) and smoothed (bold lines) STEM-EELS from layer 1, layer 2 layer 3 and amorphous ice areas in (a). Layer 1 is C rich and also has a clear N peak identifiable. Layers 2 and 3 have progressively less C and relatively more O per layer and less than that of the amorphous ice. (c) Background stripped, as-acquired (faint lines) and smoothed (bold lines) STEM EELS at the C K-edge reveal that layer 2 and layer 3 have slightly different edge structures to that of layer 1 suggesting a different polymer composition.

7.3.4 Identifying Impurities and Non-Standard Particles

Cryo-STEM-EDX and the background subtracted cryo-STEM-EEL spectra from the amorphous ice area (that does not contain any particles in the field of view), reveal reasonably weak C-*K* and N-*K* edges that can be related to the presence of excess API (C, N, O and F elements) and residual Tween (C and O elements) (Figure 7.16). This is consistent with the noisy spectra extracted from amorphous ice in Figure 7.15b.

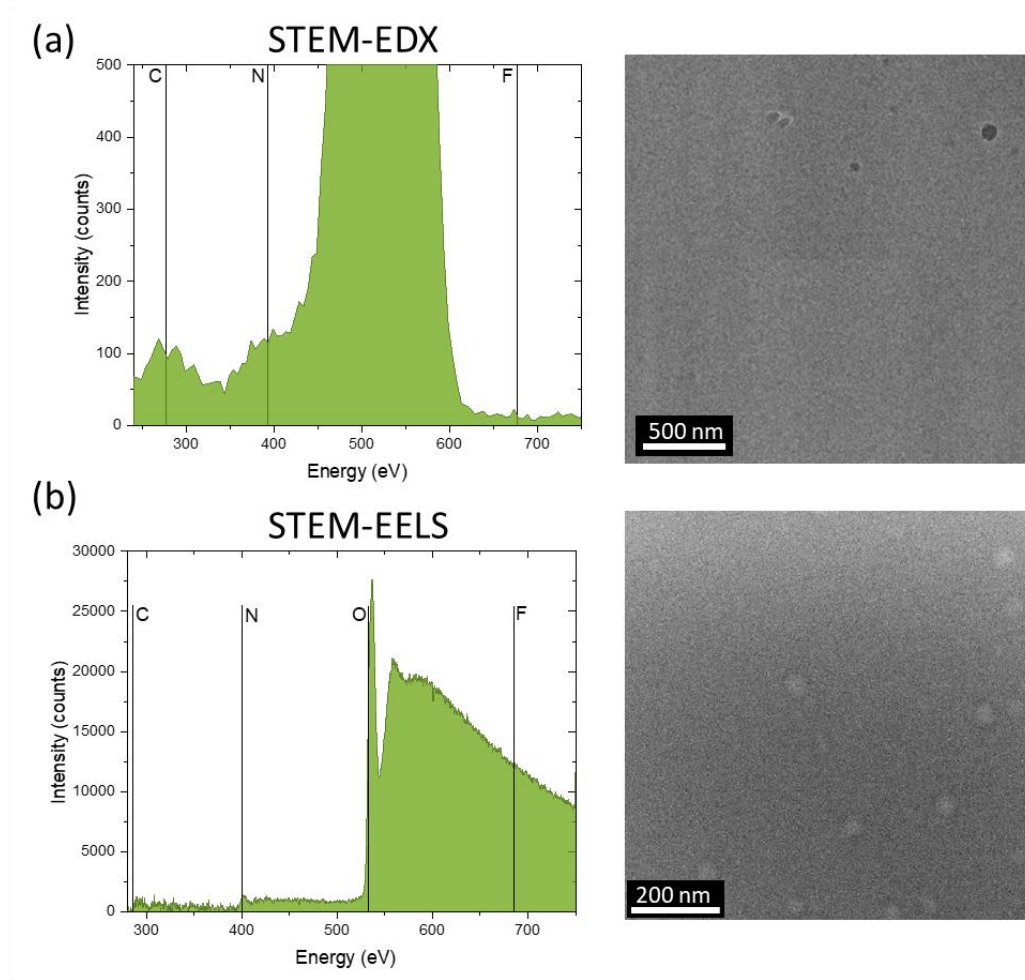


Figure 7.16 Cryo-STEM-EDX and background subtracted cryo-STEM-EEL spectra identifying C-K, N-K and O-K edges from the amorphous ice.

In addition to the major structural layering of the polymeric nanoparticles, two types of distinct, non-standard particles have been identified: (i) 'Blank' - circular particles with no visible layer 2, and (ii) 'Debris' - non-circular particles of various shapes (Figure 7.17). Based on electron beam damage observations of these, it can be seen that in both types, the same damage mechanism operates as that in the case of layer 2, i.e. void or bubble formation throughout these particles. This suggests that these non-standard particles are made of the same, very beam-sensitive material as layer 2 but do not contain significant amounts of the N-rich API. Cryo-STEM-EELS C and N elemental mapping show that the 'Debris' and 'Blank' particles contain only a negligible amount of nitrogen (and so have little or no API content).

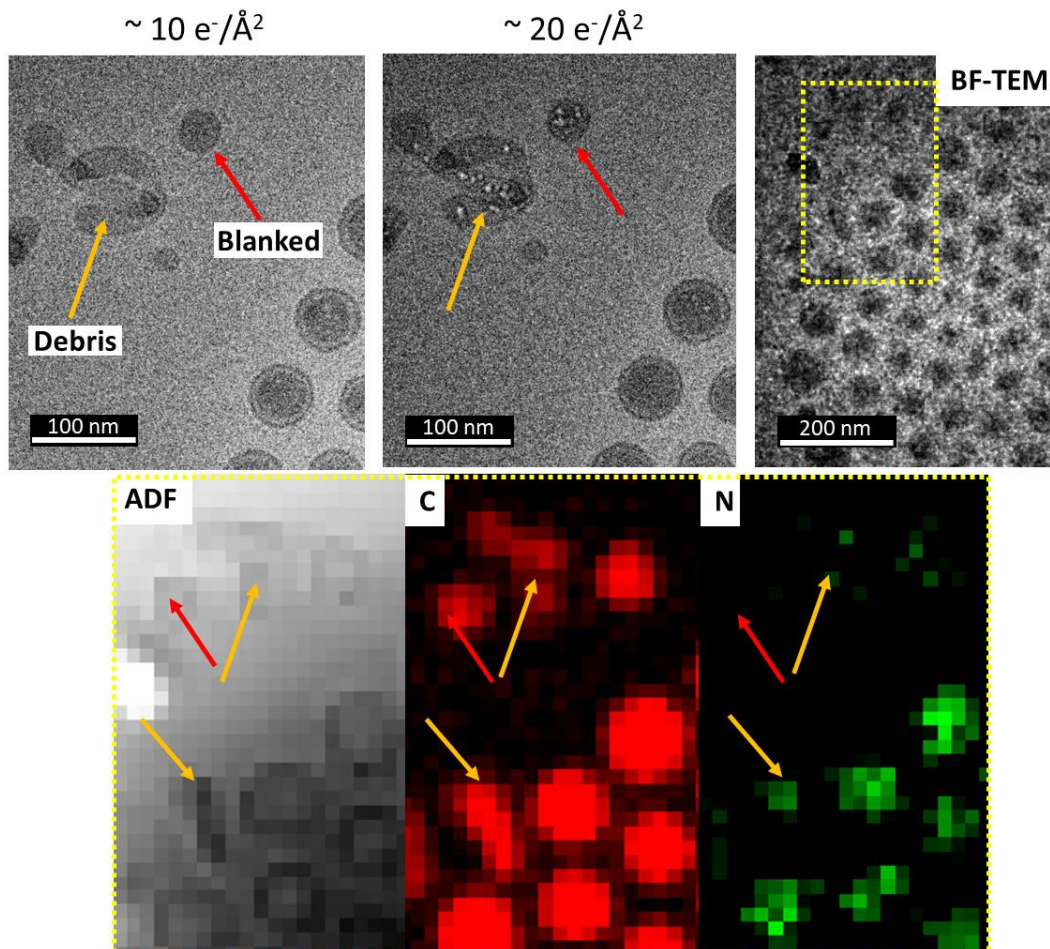


Figure 7.17 Under-focus cryo-BF-TEM and cryo-STEM-EELS mapping of non-standard nanoparticles named as: debris (non-spherical particles, marked as orange arrows) and blank (no visible layer 1, marked as red arrows). Cryo-STEM-EELS mapping suggests that debris and blank particles consist of the same material as layer 2 in the standard particle (i.e. have negligible N content and are highly beam sensitive).

7.3.5 Discussion

Combining the results of the cryo-phase contrast-TEM, cryo-ADF-STEM and cryo-STEM-EELS, a final model of these polylactic acid (PLA), polyethylene glycol (PEG), pamoic acid and active pharmaceutical ingredient (API) polymeric NPs can be obtained (Figure 7.18). Starting from the centre of the polymeric NP, the following structural components have been identified: inner core, layer 1, layer 2 and layer 3. It is known that the nano-emulsion synthesis method will result in the self-assembly of the components such that the hydrophobic material is coated by the hydrophilic PEG when a stable colloid is achieved, as is the case here. Taking only this information, the structure of polymeric nanoparticles can be

identified based on the results from the multi-modal cryo-(S)TEM characterisation.

Cryo-ADF-STEM shows a bright, sometimes off-centre inner core that was confirmed by cryo-STEM-EELS elemental maps to contain N (Figure 7.12) and so can be related to the highest concentration of the API in the nanoparticle. The inner core occupies only a part of layer 1 that was itself identified by cryo-BF-TEM to have a radius of $25 \text{ nm} \pm 4 (\pm \text{SD}) \text{ nm}$ (Figure 7.2, 7). This layer does not show electron beam damage or bubbling at or just above the critical fluence of $40 \text{ e}^-/\text{\AA}^2$ (Figure 7.4). It is the most C-rich and dense of all the layers by cryo-ADF-STEM and EELS mapping (Figure 7.8, 11, 12). It has a broad C $1s-\pi^*$ peak by EELS (Figure 7.15), indicative of a range of carbon bonding in the core. This is consistent with the presence of the C-rich pamoic acid and API throughout layer 1 because both contain conjugated carbons that are more resistant to electron beam damage than polymer chains (S'ari et al., 2018). It is known however that the self-assembly will occur around a hydrophobic polymer blend and so the PLA part of the PLA-PEG co-polymer is expected to be attracted to the hydrophobic ion-paired pamoic acid and API in layer 1.

A layer 2 of different contrast to layer 1 is identified around the NPs by under-focus BF-TEM and its thickness is $9 \pm 1 (\pm \text{SD}) \text{ nm}$ (Figure 7.2, 7). Layer 2 is made of a more beam-sensitive component than layer 1 (Figure 7.4) and is of slightly lower density than layer 1 (because of lower contrast in the de-focussed BF-TEM images that is also seen by inverted contrast, high pass-filtered ADF-STEM; Figure 7.8, 9). Cryo-STEM-EELS confirms this layer is less C-rich and has a simpler C structure than layer 1 (Figure 7.15). Thus, this layer contains little or no pamoic acid-API pairing, i.e. no HIP material. This is consistent with the increased beam sensitivity of this layer (Figure 7.4; (Weiss et al., 2019)). Thus, layer 2 could consist of a layer of PLA or a layer of mixed PLA-PEG or even a layer of PEG. Both PEG and PLA polymers damage by the bond scission and release of free radicals that could lead to gas formation and bubbling as seen here (Pal et al., 2021). It is not clear if the PLA-PEG co-polymer remains intact during self-assembly but if it does then one would expect the hydrophobic PLA to phase separate or align to the HIP material during synthesis to form a distinct layer. It suggests that layer 2 could be richer in PLA or alternatively layer 2 is a mixed PLA-PEG layer or even a dense PEG layer bonded to the PLA-HIP core

on self-assembly. Ultimately PEG is the hydrophilic component and will assemble at the surface of the NPs. A PEG layer however is generally shown to be difficult to directly visualise by cryo-TEM due to low density packing of the PEG at the surface (Claes et al., 2018).

The final layer 3 was identified by all methods to have a nominal thickness of $10 \text{ nm} \pm 4$ ($\pm \text{SD}$) nm however it was not directly visible by cryo-BF-TEM (Figure 7.2) but was identified in high-pass filtered ADF-STEM images and was shown to be of lower electron density than both the NP cores and vitreous ice by cryo-ADF-STEM (Figure 7.8, 9). Layer 3 was also shown to contain only some C and of the same bonding structure as layer 2 by cryo-STEM-EELS (Figure 7.14, 15). This suggests that this layer contains some loosely packed, brush of hydrophilic PEG chains that provide the main steric dispersion of the NPs at a regular, minimum physical distance of 20 nm (Figure 7.2). The 5 kDa PEG chains would be anchored to layer 2 and so could extend out 10-20 nm depending on their packing density (Pagels et al., 2018; Tian et al., 2020; Xu et al., 2015).

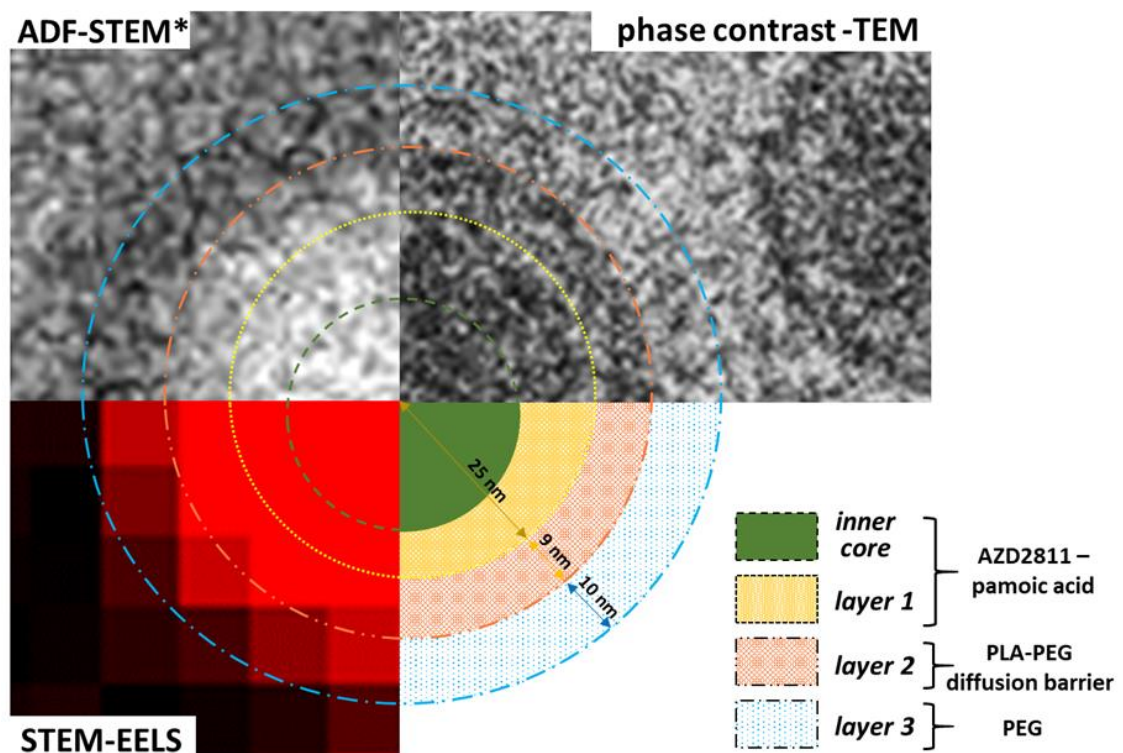


Figure 7.18 Final multi-modal data-driven model of the polymeric nanoparticles based on phase contrast-TEM, ADF-STEM (*high-pass filtered) and STEM-EELS analysis. The likely content of each layer is HIP and some PLA material in layer 1 with a core enriched in HIP material. Only PEG and PLA are in layer 2 and diffuse PEG packing is in layer 3.

It is possible to link these structural findings back to prior reports on the performance of these nanoparticle formulations. For example, Song et al. (2016) suggest that the key factor in loading and API release is the counter ion pairing and presented findings confirm here the co-localization of the two within the 50 nm diameter core of these particles (layer 1). They also suggest steady-state co-diffusion and co-release of the pamoic acid and API without an initial burst release of surface adsorbed material from these formulations. Cryo-(S)TEM results provide a mechanistic understanding of these release kinetics as it has been shown that the majority of the pamoic acid and API is located within an inner core in layer 1 and so release will require diffusion through or degradation of the outer edges of the core and through the dense, 9 nm thick layer 2, which is rich in PLA-PEG. Thus, knowing the size of the API-rich inner core plus the thickness of layer 2 and the molecular weight of the PLA-PEG copolymer give starting parameters for future mathematical modelling of the diffusion barrier inhibiting API release (Kamaly et al., 2016). Making the link between nanoparticle structure and product performance enables the structure of the nanoparticles to be optimised and for robust control strategies to be established to ensure that product quality and performance is maintained for the life-time of the drug.

7.4 Chapter Summary

This chapter has provided evidence that a multi-modal cryo-(S)TEM approach can be used for physical and chemical characterisation that can be linked to the release kinetics of a model polylactic acid - polyethylene glycol (PLA-PEG), and hydrophobic ion-pair between pamoic acid and an active pharmaceutical ingredient (API) polymeric nanoparticle system. Low-dose cryo-(S)TEM, without staining or chemical fixation, is shown to provide characterisation in the native state. Cryo-phase contrast-TEM in combination with cryo-STEM imaging and elemental analysis reveals a multi-layer structure to these self-assembled particles consisting of a 25 nm radius hydrophobic core of PLA and pamoic acid-API material with additional enrichment of the pamoic acid-API material within the core (that can be off-centre), surrounded by a 9 nm thick, dense PLA-PEG layer all with a low-density PEG surface coating of around 10 nm thickness. This structure suggests that release of the API can only occur by diffusion through or degradation or both processes simultaneously acting on the 9 nm thick, dense PLA-PEG layer, with diffusion being the process most consistent with the

previously reported steady release kinetics of API and counter ion from these nanoparticle formulations. Establishing the link between product structure and performance provides appropriate physical parameters for future mathematical modelling of the PLA-PEG diffusion barrier controlling API release in these nanoparticle formulations.

Chapter 8 Final Conclusions and Future Work

8.1 Conclusions

The aim of this thesis was to demonstrate the use of (scanning) transmission electron microscopy to characterise a range of beam-sensitive pharmaceutical compounds at the molecular length scale. Particular attention was paid to optimising strategies to mitigate electron beam damage in order to have an insight into key structure-property challenges faced by the pharmaceutical industry i.e. identifying defects in a small molecule crystal structure, providing characterisation of structure and porosity plus composition in small molecule compounds, inorganics and polymeric materials, and monitoring hydrate/anhydrate formation in a channel hydrate.

Chapter 4 demonstrated the possibilities of using low-dose scanning transmission electron microscopy techniques to acquire crystal lattice images and to inspect defects in the crystal structure of furosemide form I. It was possible to acquire a BF-TEM lattice image of furosemide form I within the measured electron fluence budget, however, the low SNR and small sampling area make the interpretation of results subject to major uncertainty. The low-dose STEM techniques of scanning electron diffraction (SED) and scanning moiré fringe (SMF) imaging were successfully applied to identify defects in different lattice planes of furosemide form I, particularly (001) and (010) which are known to exhibit different dissolution rates (Adobes-Vidal et al., 2016). The magnitude of observed disruption in BF-STEM SMFs images was consistent with the difference in dissolution rates of furosemide (001) and (010) crystal habits measured by optical microscopy ((010) is more strained and undergoes faster dissolution), as well as with the hydrogen bonding model of these specific planes. Low-dose SED holds the most promise for in-plane dislocation analysis of small molecule compounds.

Chapter 5 demonstrated the possibilities of using (S)TEM and elemental analysis techniques for the investigation of the structure and composition of development batches of inorganic microporous crystalline sodium zirconium silicate with varying Na^+/H^+ ratios due to laboratory induced protonation (any conclusions drawn based on these samples cannot be considered directly transferable to the commercially produced product). Surface morphology and particle size

distribution were investigated by SEM. Samples were found to be crystalline aggregates of cubic-shaped, micrometre size crystallites, however, the pre-protonated (partially H⁺ exchanged) samples were smaller in size and covered with numerous spherical nanoparticles. Quantitative composition analysis by TEM, even using a mineral standard, was found to be difficult because of damage and mobility/loss of Na under both the ion and electron beam plus in any solvent suspensions used to prepare a sample for TEM. Semi-quantitative STEM-EDX analysis showed that Na⁺ content does decrease on exchange with H⁺ ions however this was already established by XRD. The Na/Si composition was found to be mostly uniform throughout the crystals of both samples although some nanoscale hot spots of Na were identified. STEM-EDX data from the smaller nanoparticles at the surface of the H⁺ exchanged sample suggested these particles are pure silicates rather than fragments of the primary sodium zirconium silicate phase. Moreover, BF-STEM was successfully applied to acquire crystal lattice images and provide an indication of the presence of strains in these materials (suggesting greater strain on protonation), but direct visualisation of 0.3 nm micro-pores was not possible due to these not being aligned along channels in these materials.

Chapter 6 examined the possibilities of acquiring crystal lattice images and exploring the structural changes during hydration and dehydration of a model channel hydrate, theophylline. The resolution obtained in phase contrast lattice images was found to be sufficient for potential imaging of water channels, however, recrystallisation of theophylline monohydrate orientated to the appropriate [100] zone axis to see down these channels proved to be difficult. SED showed that hydrate formation from theophylline anhydrous form II does not occur in the solid state and is a solution-mediated route with a dissolution-re-precipitation phase transformation profile. Dehydration of theophylline monohydrate was identified to start from surfaces with exposed water channels via surface etching (first step), and finally, water was removed via diffusion from the centre of a particle along water channels (second step) to form metastable form IIIa and or IIIb (that can then convert to anhydrate form II via a thermally induced restructuring, as observed here at 90 °C). As the observed changes occurred in the presence of water vapour (released from the channel hydrate itself), phase transformation during dehydration likely proceeds via vapour-mediated phase transformation. This study clearly showed that if the final product

i.e. theophylline form II is stored in high humidity conditions or the monohydrate form is present in the final product due to e.g. incomplete drying, there is a potential risk for phase transformation and a change in solubility.

Chapter 7 demonstrated the multi-modal cryo-(S)TEM approach to provide a complete physical and chemical characterisation of an example of a new modality, polylactic acid - polyethylene glycol (PLA-PEG), and hydrophobic ion-pair between pamoic acid and an active pharmaceutical ingredient (API) polymeric nanoparticle system. This sample was characterised in a near-native state without staining or chemical fixation. Cryo-phase contrast-TEM in combination with cryo-STEM imaging and cryo-STEM-EELS/EDX elemental analysis revealed a multi-layer structure to these self-assembled particles consisting of a 25 nm radius hydrophobic core of PLA and pamoic acid-API material with additional enrichment of the pamoic acid-API material within the very inner of the core, surrounded by a 9 nm thick, dense PLA-PEG layer all with a low-density PEG surface coating of around 10 nm thickness. This finding suggests that release of the API can only occur by diffusion through or degradation of (or both processes simultaneously acting on) the 9 nm thick, dense PLA-PEG layer, with diffusion being the process most consistent with the previously reported steady release kinetics of the API and counter ion from these nanoparticle formulations.

8.2 Final comments

In summary, this thesis demonstrates that low-dose (S)TEM techniques along with elemental analysis are useful in investigating the structure, composition and defects of different pharmaceutical compounds. Defect analysis at this scale can contribute to the understanding of crystal dissolution kinetics and might enable the prediction of the impact of processing routes or storage on the kinetics. Identification of strain in small molecule drugs and inorganic materials is possible and may again help explain dissolution or cation-exchange profiles. Hydration/dehydration transformation pathways have been identified in a channel hydrate and this knowledge can help to develop appropriate processing and storage strategies. While drug loading and release barriers have been identified in new modality polymer nanoparticles such that parameters for accurate mathematical modelling of release kinetics are now known.

The knowledge of API structure and composition shown to be obtainable here by S/TEM demonstrates the potential of the technique for the development of pharmaceutical drugs and for the improvement of manufacturing processes and storage conditions.

8.3 Future Work

To develop the work presented in this thesis, there are several future extensions as follows:

Development of a methodology for quantification of defects

Further work will require the development of the SMF and SED methodology for quantification of defects in pharmaceutical materials. Some dislocation analysis using SED has already contributed to a Nature Materials submission by Pham et al. (2023) (also see Appendix C). Further work can address improvement in the data analysis of the strains and defects in a crystal structure to give quantitative measures e.g. Geometric Phase Analysis (GPA). Data analysis techniques should be applied to easily measure these defects automatically and the effect on the type of defect on the SMF images could be modelled to provide information regarding the defect type. In a recent review, Ke et al. (2022) stated that SMF images can play an important role in the characterisation of a range of beam-sensitive materials over a larger field of view than direct lattice imaging, however, optimisation of sample preparation and data acquisition needs to be considered to improve the quality of SMF images.

Monitoring processing-induced defects and their impact on the dissolution

Experiments utilising SMF and SED could be carried out on samples prepared by different crystallisation routes and also before and after processing e.g. milling or hot-melt extrusion to monitor any change in structure and identify how process conditions can affect the type and density of defects. This study can be also employed to understand the effect of these defects on dissolution by performing in-situ dissolution studies. Moreover, identifying defect types and slip direction opens the possibility for computational work to model mechanical behaviour on tableting or dissolution by etch pitting.

Acquiring lattice imaging of water channels

The results in this thesis (Chapter 6) showed that it is possible to acquire phase contrast lattice images of a channel hydrate. However, recrystallisation of theophylline monohydrate to the [100] zone axis (to image along the water channels which run parallel to the *a*-axis) proved to be difficult. A combination of solvent-controlled precipitation and FIB sectioning could be a route to prepare this or other channel hydrates in that orientation to then image the water channels in cryogenic conditions and dehydrate in situ to observe changes in the structure (e.g. defects, polymorphic transition).

Monitoring phase transformation of other channel hydrates

The hydration and dehydration study presented in Chapter 6 can be used as a good starting point for elucidating the phase transformation mechanism of other channel hydrates. Moreover, it would be interesting to combine experimental results with computational modelling of hydration/dehydration mechanism (e.g. modelling lattice energy, structure prediction, stability of these pseudo-polymorph forms). These findings can contribute to the development of different pathways and processes for the preparation of polymorphs with desired physical properties. Moreover, the knowledge of these phase transformations can then be utilised in the optimisation of the drug processing and storage conditions.

Investigating other polymeric nanoparticles and developing mathematical modelling of release kinetic

The study presented in Chapter 7 and published in Heliyon (Koniuch et al., 2023) shows the potential of using multi-modal (S)TEM as a fundamental technique for polymeric nanoparticle characterisation. Further study can be performed on other polymeric nanoparticle systems to get the appropriate physical parameters (such as polymer density as well as layer thickness and polymer type) that will help to develop mathematical model of API release kinetics. Moreover, further studies can focus on the development of automated imaging and auto-measurement of different components of polymeric nanoparticles. By combining experimental data and computational models, it will be possible to better predict the physicochemical properties of polymeric nanoparticles before the clinical phase trial stage.

Ultimately, this thesis has shown that low dose (S)TEM really does have the potential to become a commonly used characterisation technique in pharmaceutical drug development.

Appendix A Methods of Data Acquisition and Data Analysis

A.1 Apparatus

Transmission electron microscopy (TEM) characterisation was performed at room temperature by using a FEI Tecnai TF20 and a FEI Titan³ Themis 300 operated at 200 and 300 keV acceleration voltages, respectively. The FEI Tecnai TF20 is equipped with a Field emission gun FEGTEM/STEM and a Fischione HAADF detector and a Gatan Orius SC600A CCD camera. The FEI Titan³ Themis 300 microscope is supplied with an X-FEG 300 kV S/TEM with S-TWIN objective lens, monochromator (energy spread approx. 0.25 eV), multiple HAADF/ADF/BF STEM detectors and Gatan OneView 4K CMOS digital camera.

Scanning electron microscopy of the development batches of a model inorganic cation exchanger samples, sodium zirconium silicate, was performed using a FEI Helios G4 CX DualBeam - High-resolution monochromated FEGSEM with precise Focused Ion Beam (FIB) microscope with capabilities of in-situ TEM sample preparation and Slice&View acquisition of multi-signal 3D data sets using an SE or BSE detector.

All low-dose operating conditions will be given in a specific section in each experimental chapter.

A.2 Calculation of Critical Fluence (C_F)

The critical (characteristic) fluence C_F is commonly measured from diffraction pattern series and indicates the radiation resistance of the sample as well as the radiation mechanism (Egerton, 2019). The C_F can be measured as a fluence at which diffraction spot intensity decreases to 1/e of the initial intensity as a function of an accumulated electron fluence. This beam sensitivity or radiation resistance depends on the type of sample, morphology and experimental condition (e.g. cryo condition can increase C_F).

Figure A.1 shows bright field (BF) images acquired before and after taking a diffraction pattern series of furosemide and confirms the loss of crystallinity upon irradiation. Knowledge of the critical fluence value of an analysed compound is very important prior to conducting any further experiment and allows for the choice of the right operating condition to ensure that significant crystallinity will not be destroyed before it can be detected by TEM.

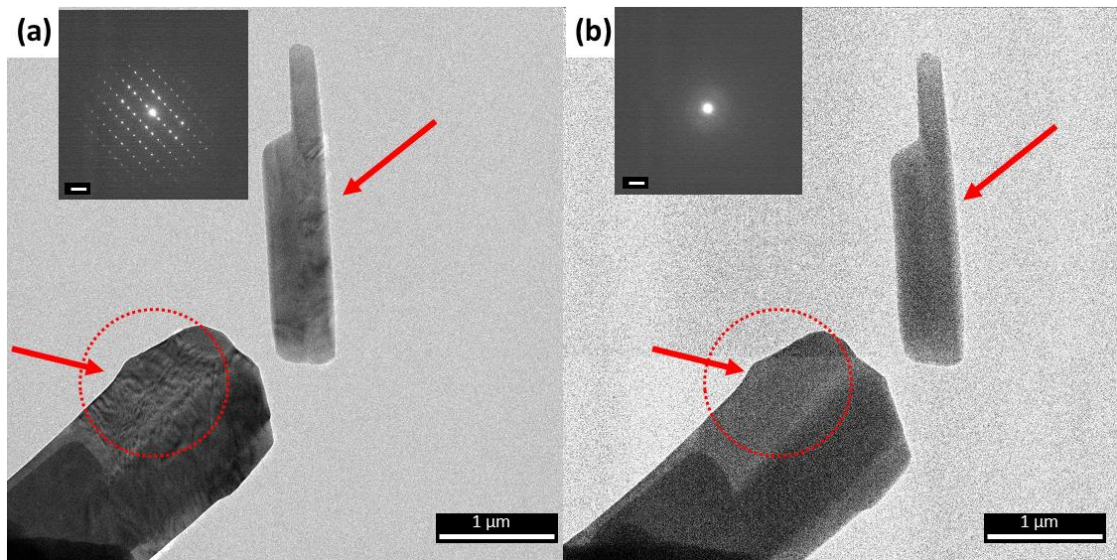


Figure A.1 (a) BF-TEM initial image and (b) BF-TEM image after taking diffraction series confirm loss in diffraction contrast and therefore crystallinity. The scale bar represents 2 nm^{-1} .

The decay in the intensity of diffraction spots during irradiation is assumed to fit an exponential profile. This gives the characteristic fluence for the decay intensity. Therefore, a series of diffraction patterns at increased cumulative fluence needs to be acquired. The general workflow and detailed description of electron fluence (electrons per nm^2 or \AA^2) calculation are presented below:

- 1. Acquisition of electron diffraction series.** The series of electron diffraction patterns acquired at constant fluence rate (electrons per nm^2 or \AA^2 per s) at intervals of 20-30 s were performed based on selected areas of single crystals showing diffraction contrast in BF images (SAED aperture of $20 \mu\text{m}$ diameter equating to approx. 200 nm diameter in the image plane) in order to characterise the relationship between cumulative electron fluence and loss of crystalline structure, and also the effect of different accelerating voltage on critical fluence value for damage.
- 2. Measure the changes in diffraction spot intensities.** The decay in diffraction spot intensities with increasing electron fluence was measured from the intensity (I) value of each spot for each diffraction pattern in an exposure series (in ImageJ) and then normalised against the maximum intensity (I_0) for each diffraction spot (I/I_0).

- 3. Measure the d -spacing for each diffraction spot.** The distance between each pair of the most distant diffraction spots whose intersection crosses the zero-order spot was measured in ImageJ. Then, the measured value was divided by the number of lattice planes given by the reflections (in order to minimise the measurement error) and converted to d -spacing.
- 4. Index diffraction pattern.** The electron diffraction patterns were indexed to Miller indices and directions of the expected structures by comparison with known crystal structures available in the Cambridge Structural Database (CSD). The distance and the angle between the two diffraction spots closest to the zero-order spot were measured, converted to a d -spacing and matched to reference values for the known structures using the CrystalMaker SingleCrystal software. A comparison of an experimental and a simulated diffraction pattern of a given zone axis pattern was performed in order to confirm correlation with crystal structure parameters in CSD. Some diffraction patterns from high index zone axes can be only compared with a pXRD trace as they could not be precisely indexed. An example of an indexed experimental and simulated diffraction pattern of furosemide crystal in a low index zone is shown in Figure A.2.

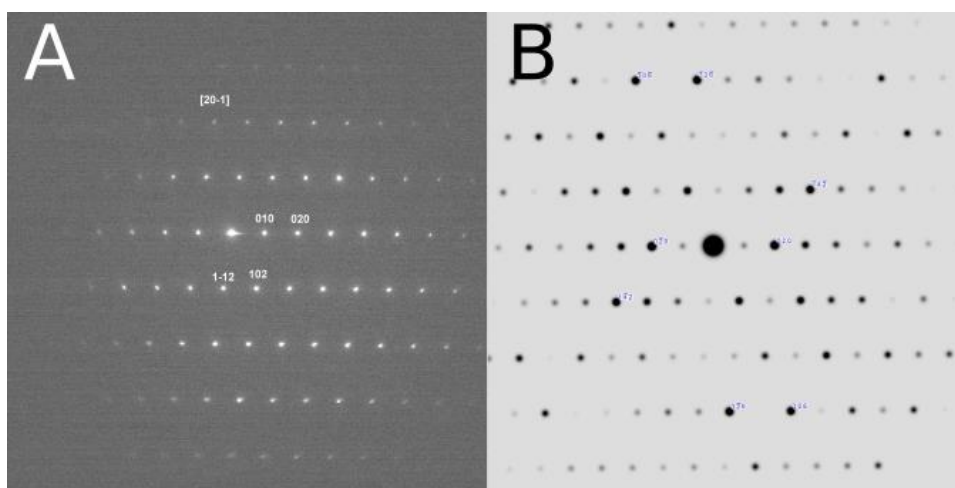


Figure A.2 Example of (A) indexed experimental and (B) simulated diffraction pattern of furosemide form I orientated along the $[20\bar{1}]$ zone axis.

- 5. Calculate an electron flux and an electron fluence.** An electron flux (for Tecnai FEI calibration) from the screen exposure time read (when exposed to the beam) can be calculated from Equation A.1 (S'ari et al., 2018):

$$J (e^{-}/(\text{\AA}^2s)) = \frac{a \times b \times \epsilon}{T_e \times C_s \times e} \times \frac{M^2 \times 10^{-20}}{\pi \times r^2} \quad \text{A.1}$$

where for using the Tecnai, the parameters are as follows: a is a calibration constant (1.875×10^{-15}), b is a constant relating to the accelerating voltage (1.3 at 200 kV), ϵ is the emulsion setting (equal to 2), C_s is the screen correction factor (equal to 1.2), T_e is an exposure time (read from the exposure meter on the TEM phosphor screen), e is the elementary charge of an electron (1.6×10^{-19} C), M is the magnification at the viewing screen and r is the radius of the projected electron beam on the screen [m]. The value of an electron flux (J) using the Titan was provided by a flu-cam current reading which was pre-calibrated using a Faraday cup. The cumulative electron fluence (F) can then be calculated by multiplying the time the sample has been exposed to the electron beam (in [s]) by an electron flux (J) (Equation A.2) (S'ari et al., 2018):

$$F (e^{-}/\text{\AA}^2) = J \times (t_0 + t) \quad \text{A.2}$$

where J is an electron flux, t_0 is the time for the initial exposure and the time taken to record the first diffraction pattern [s] and t is the subsequent acquisition time of the following diffraction patterns [s].

6. **Calculate the critical fluence (C_F).** Critical fluence for each diffraction spot was calculated by plotting an exponential decay fit to $\ln(I/I_{\max})$ against cumulative electron fluence (F) and measuring C_F at which the normalised intensity drops to $1/e$ (Figure A.3). Measured diffraction spots from several patterns have been grouped into d -spacing ranges (<2, 2–4, 4–6, and >6 Å) with assigned values of cumulative electron fluence for each group. The mean critical fluence (C_F) value with corresponding standard deviation for each group and experiment were calculated and compared.

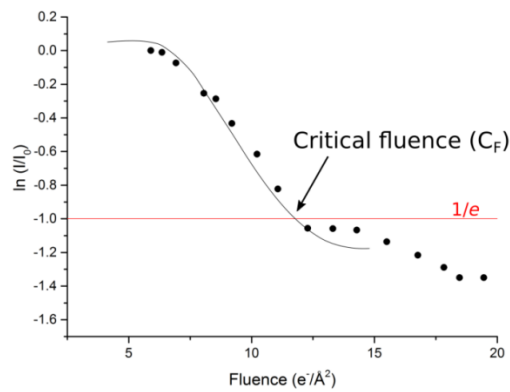


Figure A.3 Explanation of critical fluence C_F calculation for a specific site of diffraction spot in the furosemide diffraction pattern.

A.3 Acquisition of Scanning Moiré Fringes

The general workflow and detailed description of scanning moiré fringe acquisition are presented below:

- 1. Identify crystals orientated close to the low zone axis required to acquire SMF lattice images.** Crystals were analysed based on the BF-TEM of selected areas exhibiting diffraction contrast and the orientation confirmed by a corresponding SAED pattern. In all experiments, a double-tilt holder was used and allowed the sample to be oriented to a low zone axis using an α and/or β tilts (i.e. in all directions). Based on critical fluence calculations, this reorientation procedure uses up electron irradiation and could be performed only for a compound with a sufficiently high value of critical fluence i.e. AZ1. Alternatively, for the more beam-sensitive materials many areas are checked in order to identify one on or close to a zone axis.
- 2. Measure the angle from the vertical of a selected spacing from the acquired diffraction pattern.** The angle from vertical of a selected spacing in the acquired TEM diffraction pattern was measured, which allows calculation of the change in rotation to the STEM scan direction in order to align the crystal and scanning lattice to acquire translational moiré fringes. The STEM lattice is an additional angle of 6.4° off vertical compared to the TEM camera used for diffraction (S'ari et al., 2019).
- 3. Measure the d -spacing for each diffraction pattern.** The distance between the corresponding pair of the most distant diffraction spots whose intersection passes through the zero-order spot was measured in a Digital

Micrograph, then divided by the number of reflections that appear for the corresponding lattice plane (in order to minimise the measurement error) and converted to d -spacing to get d_l (Equation 3.1 in section 3.2.4.2).

4. **In STEM mode, choose magnification relevant to calculated d -spacing.** For STEM the electron fluence can be calculated by Equation A.3 (S'ari et al., 2019):

$$F (e^-/\text{\AA}^2) = \frac{I \times t}{e \times d_s^2} \quad \text{A.3}$$

where I is probe current (here 5 pA), t is dwell time (here 10 μ s or 20 μ s), e is the charge of an electron and d_s is the STEM pixel size. Based on Table A.1, where the size of the pixels assigned to the corresponding magnification is presented, the selection of appropriate magnification should be made on the criterion of the closest match of d -spacing to the pixel size.

5. **Acquire the SMF image at the appropriate magnification to match d_s to d_l .**
6. **Measure the scanning moiré fringes.** The measurement of scanning moiré fringes can be done either by measuring the distance based on the line profile taken across the acquired fringes and dividing by the number of fringes or by measuring the distance of corresponding spots to the central spot in a fast Fourier transform (FFT).
7. **Calculate the theoretical value of scanning moiré fringes.** The size and orientation of the generated SMFs depend on the magnification (determined by the pixel size d_s), the size of the crystal lattice d_l and the angle β between fringes d_s and d_l . If β is equal to zero, translational moiré fringes can be calculated from Equation 3.1. If β is different from zero then it affects the size of the fringe and therefore can be calculated by Equation 3.2.
8. **Compare the measured and calculated value of scanning moiré fringes.** Accurate rotational angle measurement is very important prior to acquiring scanning moiré fringes images as small fluctuations significantly affect the size of the resulting SMFs. Moreover, the scanning magnification

should be carefully selected. If the relative difference between d_s and d_i increases, then the size of SMFs decreases and it can be unobservable.

Table A.1 Calculated electron fluence in STEM mode using 5 pA probe current.

Magnification in STEM (kX)	Pixel size [pm]	Electron Fluence [$e^-/\text{Å}^2$]	
		dwelt time 10 μs	dwelt time 20 μs
57	1319	1.8	3.6
80	933	3.6	7.2
115	659.7	7.2	14.3
160	465.8	14.4	28.8
225	329.4	28.8	57.5
320	232.9	57.5	115.1
450	164.7	115.1	230.1
640	115.6	233.6	467.1
910	81.73	467.2	934.5

A.4 Image Filtering of lattice (phase contrast) images.

When using low-dose conditions, the directly interpretable crystal lattice images are difficult to obtain due to reduced signal-to-noise ratio (SNR). Image filtering can enhance image quality, however, these methods require careful image processing and interpretation due to the risk of introduction of the artefacts. The most common filtering techniques are: Fast Fourier Transform processing (FFT), Wiener filtering, Low and High-Pass filtering.

Fast Fourier Transform (FFT)

The Fast Fourier Transform, commonly referred to as FFT, is a mathematical tool used to transform an image from its spatial domain into its frequency domain. This transformation provides valuable insights into an image's spectral composition, making it possible to isolate and manipulate specific frequency components such as crystal lattice fringes. The FFT represents the image as a combination of sinusoidal waves of different frequencies and orientations. High-

frequency components typically represent fine details and edges, while low-frequency components represent smoother regions and overall structure.

Wiener Filtering

Wiener filtering is a deconvolution technique used to restore images by minimizing the impact of the distortions due to e.g. noise and degradation during (S)TEM acquisition. The Wiener filter operates in the frequency domain and estimates the power spectral density of both the original, uncorrupted image and the noisy, degraded image. By understanding how noise affects different frequencies, the Wiener filter can attenuate noise and enhance signal components during the restoration process.

Low and High-Pass Filtering

Low-pass and high-pass filters allow the passing of specific signals with a certain frequency cut-off that can preserve or attenuate specific frequency components in an image. A Low-pass filter allows low-frequency components to pass through and removes high-frequency noise resulting in an enhanced image quality e.g. lower noise lattice image (smoother and cleaner image). This is particularly useful when dealing with images affected by Gaussian noise or other high-frequency distortions. A High-pass filter allows high-frequency components to pass through and block low-frequency details enhancing the contrast of fine details in the image e.g. images affected by the noise related to the specimen thickness such as in cryo-ADF-STEM images.

A.5 SED Data Processing

SED acquires a two-dimensional diffraction pattern at each point (X, Y) of a probe position resulting four-dimensional dataset. Therefore, SED provides valuable structural and crystallographic information at the nanoscale and data processing requires a software package for data processing and interpretation.

The general workflow and detailed description of SED acquisition and SED data processing are presented below:

1. **Instrument setup for low-dose SED acquisition.** This includes adjusting the beam conditions, changing probe convergence semi-angle (below 1 mrad), and camera settings. Low-dose scanning electron diffraction (SED) was performed using a 1 pA probe size within the total electron fluence of

$\sim 8 \text{ e}^-/\text{\AA}^2$ per scan using a Merlin/Medipix pixelated electron counting detector at ePSIC.

2. **SED scan parameters.** After finding the area of interest, the scan area (256x256 probe positions) and magnification were defined. In case this area needs to be scanned again (e.g. to observe dehydration of theophylline monohydrate in a vacuum), immediately after the first scan the beam is blanked. The stage X and Y coordination of this area is saved allowing the stage position recall for the second scan.
3. **Data Storage and Binning.** The recorded data are saved as .mib files (around 16 GB in size each). Therefore, these data are binned using HyperSpy software (a ratio of 4 - each pixel in the binned SED is 4x the size of the pixels in the original SED) significantly reducing the file size (saved as _binned2.hdf5). This procedure allows for data processing using a typical laptop with 8 GB RAM.
4. **Data Processing in Python (HyperSpy and pyXem).**
 - (a) **Data Import.** Loading the binned SED dataset into pyXem using supported file formats of .hdf5.
 - (b) **Data Calibration and Centring.** Gold diffraction cross-grating (500 nm) was used for image and diffraction calibration data and elliptical distortion correction. Molybdenum oxide was used to calculate the rotation angle between the diffraction pattern and the image. This calibration is essential for subsequent analysis steps.
 - (c) **Virtual selected area diffraction image.** This function allows one to obtain the sum of diffraction images from all or selected real space probe positions (pixels).
 - (d) **Virtual dark field image.** This function allows one to extract the image intensities of all or selected spots from the SED pattern.
 - (e) **Data saving.** Generated images and diffraction patterns are saved as 32-bit .tiff files that can be processed further using ImageJ or GMS Digital Micrograph.
 - (f) **Indexing Diffraction Patterns.** Obtained diffraction patterns are indexed in a similar way to the methodology presented in section 3.4.2. Indexing allows to determine the orientation and lattice parameters of each crystal in the field of view.

A.6 EDX Absorption Correction

EDX in scanning transmission electron microscopy is a powerful technique for elemental analysis at the nanoscale and allows for the collection of elemental or chemical maps at each probe (pixel) position (X, Y). However, one common challenge in quantitative EDX-STEM analysis is the absorption of X-rays by the sample itself, which can lead to inaccurate results. Absorption effects in EDX occur when X-rays generated by the electron beam within the sample are partially absorbed before reaching the detector. This absorption is influenced by several factors, including: (i) sample thickness (thicker samples absorb X-rays more than thinner samples), (ii) sample density (denser materials absorb X-rays more effectively than less dense materials) and (iii) X-ray energy (the energy of the emitted X-rays affects their penetration depth, with higher-energy X-rays penetrating deeper into the sample). One widely used approach to improve elemental quantification is the Cliff-Lorimer (CL) method, which compensates for specimen thickness and density-related absorption effects. The CL sensitivity factor (k_{AB}) between two elements can be calculated, but it varies with microscope conditions (e.g. accelerating voltage) and depends on the materials, therefore standards of similar composition are required.

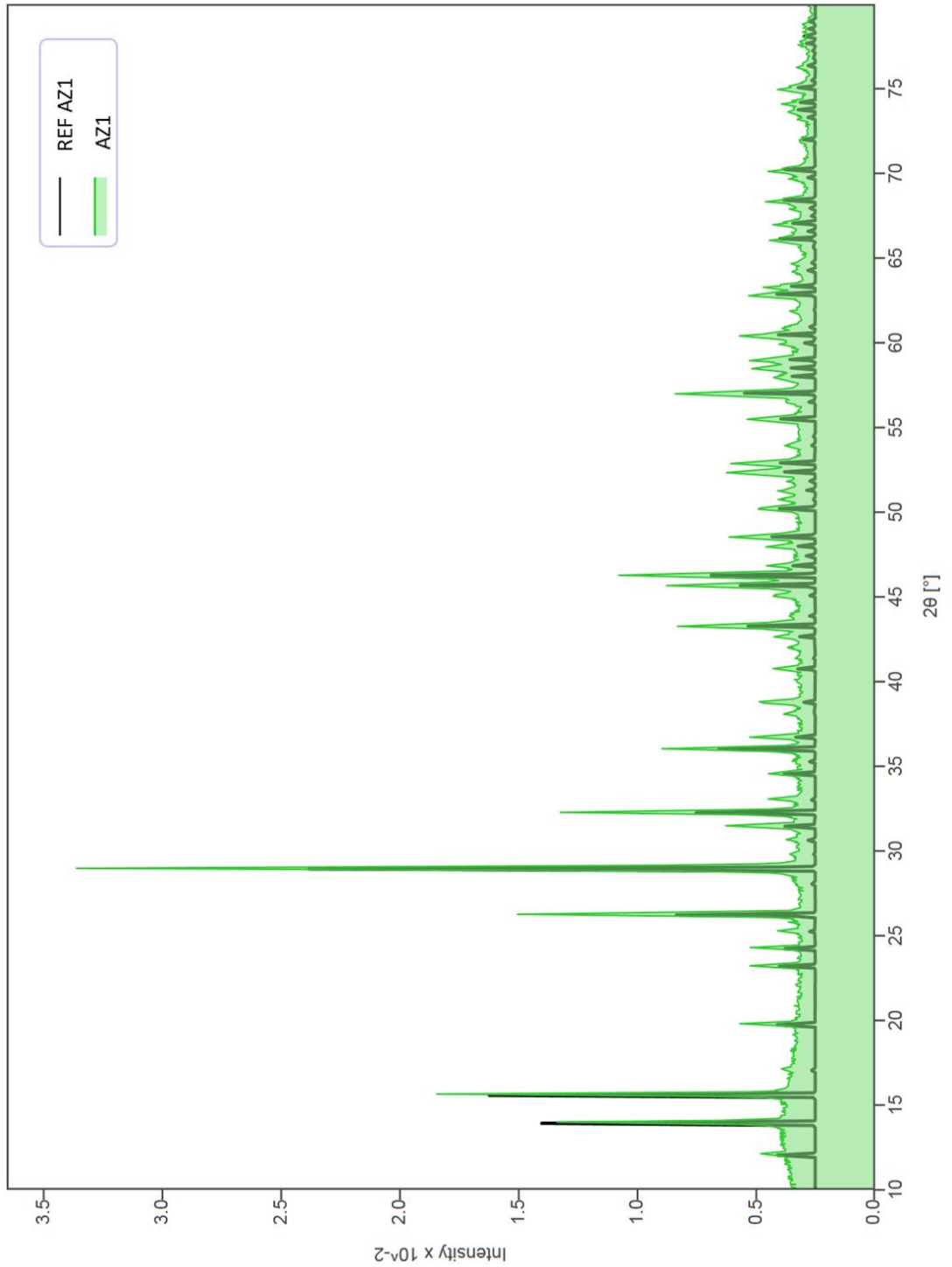
The general workflow and detailed description of EDX acquisition and data processing steps using the CL method are presented below:

1. **Validation of CL method in Velox using a standard.** A standard reference sample of similar composition to AZ1/AZ1-2 (similar sodium to silicon ratio) was selected to be albite, a sodium aluminium silicate, $\text{Na}(\text{AlSi}_3\text{O}_8)$. A FIB/TEM cross-section was prepared and analysed by EDX-STEM.
2. **Region of Interest (ROI) Selection.** The selected ROI is chosen within the STEM image and areas are selected based on the greyscale contrast in HAADF images (i.e. less bright regions are thinner). The sample needs to be relatively thin to apply the CL method.
3. **Thickness Measurement.** The average grey scale values of HAADF images can be measured from the selected areas within the wedge-shaped FIB/TEM cross section (the width between 150 nm to 1350 nm). In EDX-STEM data of AZ1/AZ1-2, the thickness was estimated based on the grey scale and manually provided for the chosen ROI in Velox.

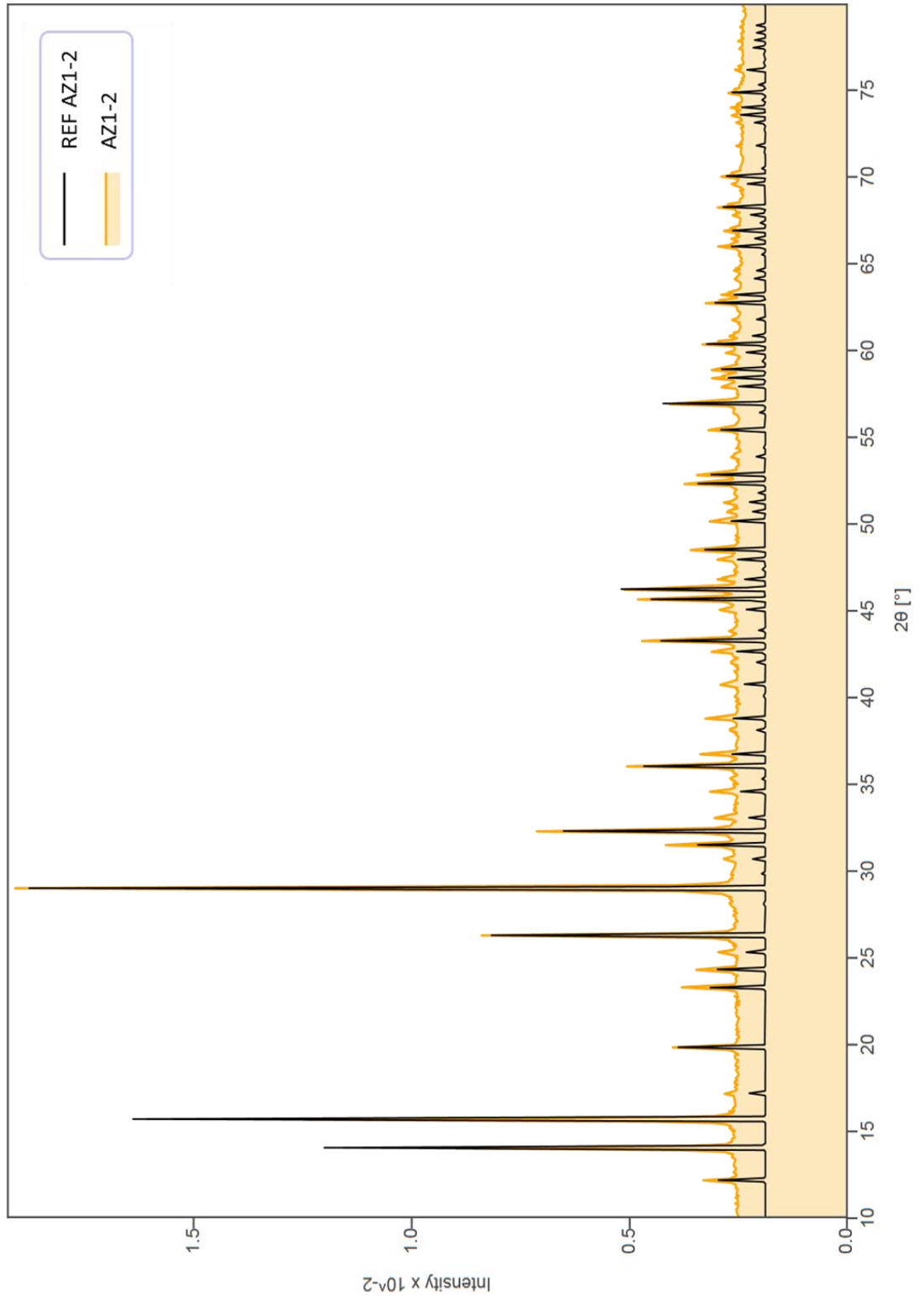
4. **Sample density.** The density of the samples was manually provided based on the information from structure files.
5. **Absorption Correction.** The CL absorption correction is applied using Velox built-in correction algorithms. These algorithms utilize the thickness measurement and the composition information to correct absorption effects in the EDX spectrum data.
6. **Semi-quantitative Analysis.** As the thickness of the sample is estimated based on the thickness greyscale, the absorption-corrected data can perform only semi-quantitative analysis in Velox. The CL method can be applied to elemental mapping, line scans or composition quantification.

Appendix B XRD plots of AZ1 and AZ1-2

B.1 XRD plot of AZ1



B.2 XRD plot of AZ1-2



Appendix C SED of Theophylline Form IIIb

One TEM grid with theophylline monohydrate form (*M3*) was plunge frozen straight in liquid nitrogen (LN_2) to preserve the water in the channels, as the access to e.g. a Vitrobot and plunge freezing in liquid ethane was not possible in ePSIC. LN_2 has low heat capacity, therefore upon contact with the TEM grid, it starts to boil, and an insulation layer of nitrogen gas can be produced on the surface of the TEM grid preventing fast freezing. Despite the known risk of water crystallisation in the channels, this experiment was carried out and interesting results are presented in Figure C.1. This particle has a different morphology (plate-like shape) and cannot be indexed to either monohydrate form, metastable form III (i.e. form III which has similar packing as monohydrate) or anhydrous form II. The only matching structure is metastable form IIIb oriented to the [211] zone axis, which was recently reported by Paiva et al. (2021). This metastable IIIb structure slightly differs from the typical form III i.e. molecule arrangement is slightly shifted resulting in a 12.4% reduction in the cell volume. This structure file was calculated by the full unconstrained geometry optimisation method of form III and proved experimentally. However, the structure of form III depends on different experimental factors e.g. RH and temperature (Paiva et al., 2021). Given the zone axis of the [211], arrangements of channels in the initial monohydrate form had to be at an angle to the largest surface. Given the small thickness of the plate-like particles, the length of the water channels was not long compared to the elongated particles presented earlier. Therefore, the insulating layer might produce a local pressure around the particle. This pressure could destabilise the weak hydrogen bond and push the water out from the channels. The structure of this particle shows a number of breaks in the bend contour suggesting the presence of defects (Figure C.1c-d). Moreover, the slower freezing rate may allow the theophylline molecule to rearrange to form a more energy-optimised metastable form. If the water would be frozen in the channels, the size of the water channels in theophylline monohydrate is not large enough to accommodate ice crystals. This would result in an expansion of the structure and increase of the unit cell, which is not observed here according to Table 6.2.

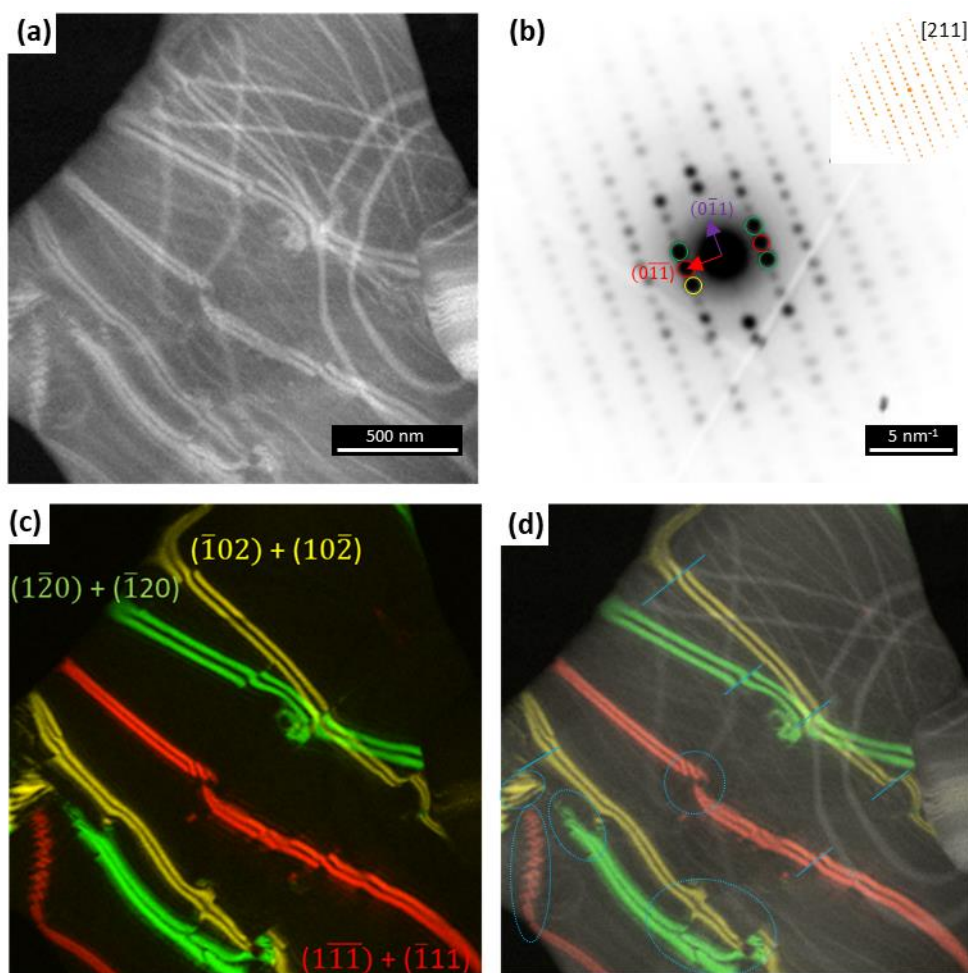


Figure C.1 (a) ADF-STEM image of metastable theophylline form IIIb (structure file reported by Paiva et al. (2021)) that was found in sample *M3* immersed in liquid N₂. (b) SED pattern that can be indexed to [211] zone axis. (c)-(d) Virtual ADF-STEM images formed by plotting the intensity within the disks marked in the SED pattern in (b) as a function of probe position. Defect sites are marked by blue lines (dislocation) and circles in (d).

References

- Aceves, J.M., Cruz, R. and Hernandez, E. 2000. Preparation and characterization of Furosemide-Eudragit controlled release systems. *International Journal of Pharmaceutics*. **195**(1), pp.45-53.
- Adobes-Vidal, M., Maddar, F.M., Momotenko, D., Hughes, L.P., Wren, S.A.C., Poloni, L.N., Ward, M.I.D. and Unwin, P.R. 2016. Face-Discriminating Dissolution Kinetics of Furosemide Single Crystals: In Situ Three-Dimensional Multi-Microscopy and Modeling. *Crystal Growth & Design*. **16**(8), pp.4421-4429.
- Adrjanowicz, K., Kaminski, K., Grzybowska, K., Hawelek, L., Paluch, M., Gruszka, I., Zakowiecki, D., Sawicki, W., Lepek, P., Kamysz, W. and Guzik, L. 2011. Effect of cryogrinding on chemical stability of the sparingly water-soluble drug furosemide. *Pharmaceutical Research*. **28**(12), pp.3220-3236.
- Afsharzadeh, M., Yazdian-Robati, R., Ataranzadeh, A., Ramezani, M. and Hashemi, M. 2019. Formulation and evaluation of anticancer and antiangiogenesis efficiency of PLA-PEG nanoparticles loaded with galbanic acid in C26 colon carcinoma, in vitro and in vivo. *Journal of Cellular Physiology*. **234**(5), pp.6099-6107.
- Agbada, C.O. and York, P. 1994. Dehydration of theophylline monohydrate powder — effects of particle size and sample weight. *International Journal of Pharmaceutics*. **106**(1), pp.33-40.
- Allan, M. and Mauer, L.J. 2017. Dataset of water activity measurements of alcohol:water solutions using a Tunable Diode Laser. *Data in Brief*. **12**, pp.364-369.
- Amado, A.M., Nolasco, M.M. and Ribeiro-Claro, P.J.A. 2007. Probing Pseudopolymorphic Transitions in Pharmaceutical Solids using Raman Spectroscopy: Hydration and Dehydration of Theophylline. *Journal of Pharmaceutical Sciences*. **96**(5), pp.1366-1379.
- Ambroggi, V., Perioli, L., Pagano, C., Latterini, L., Marmottini, F., Ricci, M. and Rossi, C. 2012. MCM-41 for furosemide dissolution improvement. *Microporous and Mesoporous Materials*. **147**(1), pp.343-349.
- Amidon, G.L., Lennernäs, H., Shah, V.P. and Crison, J.R. 1995. A theoretical basis for a biopharmaceutic drug classification: the correlation of in vitro drug product dissolution and in vivo bioavailability. *Pharmaceutical Research*. **12**(3), pp.413-420.
- Andima, M., Costabile, G., Isert, L., Ndakala, A.J., Derese, S. and Merkel, O.M. 2018. Evaluation of β -Sitosterol Loaded PLGA and PEG-PLA Nanoparticles for Effective Treatment of Breast Cancer: Preparation, Physicochemical Characterization, and Antitumor Activity. *Pharmaceutics*. **10**(4), p232.
- Avgoustakis, K. 2004. Pegylated poly(lactide) and poly(lactide-co-glycolide) nanoparticles: preparation, properties and possible applications in drug delivery. *Current Drug Delivery*. **1**(4), pp.321-333.

- Babu, N.J., Cherukuvada, S., Thakuria, R. and Nangia, A. 2010. Conformational and Synthon Polymorphism in Furosemide (Lasix). *Crystal Growth & Design*. **10**(4), pp.1979-1989.
- Banik, M., Gopi, S.P., Ganguly, S. and Desiraju, G.R. 2016. Cocrystal and Salt Forms of Furosemide: Solubility and Diffusion Variations. *Crystal Growth & Design*. **16**(9), pp.5418-5428.
- Bassim, N.D., De Gregorio, B.T., Kilcoyne, A.L.D., Scott, K., Chou, T., Wirick, S., Cody, G. and Stroud, R.M. 2012. Minimizing damage during FIB sample preparation of soft materials. *Journal of Microscopy*. **245**(3), pp.288-301.
- Behme, R.J. and Brooke, D. 1991. Heat of Fusion Measurement of a Low Melting Polymorph of Carbamazepine That Undergoes Multiple-Phase Changes During Differential Scanning Calorimetry Analysis. *Journal of Pharmaceutical Sciences*. **80**(10), pp.986-990.
- Békés, M., Langley, D.R. and Crews, C.M. 2022. PROTAC targeted protein degraders: the past is prologue. *Nature Reviews Drug Discovery*. **21**(3), pp.181-200.
- Beloborodova, A.A., Minkov, V.S., Rychkov, D.A., Rybalova, T.V. and Boldyreva, E.V. 2017. First Evidence of Polymorphism in Furosemide Solvates. *Crystal Growth & Design*. **17**(5), pp.2333-2341.
- Bhalani, D.V., Nutan, B., Kumar, A. and Singh Chandel, A.K. 2022. Bioavailability Enhancement Techniques for Poorly Aqueous Soluble Drugs and Therapeutics. *Biomedicines*. **10**(9).
- Bootz, A., Vogel, V., Schubert, D. and Kreuter, J. 2004. Comparison of scanning electron microscopy, dynamic light scattering and analytical ultracentrifugation for the sizing of poly(butyl cyanoacrylate) nanoparticles. *European Journal of Pharmaceutics and Biopharmaceutics*. **57**(2), pp.369-375.
- Bortun, A.I., Bortun, L.N. and Clearfield, A. 1996. Ion Exchange Properties of a Cesium Ion Selective Titanosilicate. *Solvent Extraction and Ion Exchange*. **14**(2), pp.341-354.
- Bortun, A.I., Bortun, L.N. and Clearfield, A. 1997. Hydrothermal Synthesis of Sodium Zirconium Silicates and Characterization of Their Properties. *Chemistry of Materials*. **9**(8), pp.1854-1864.
- Boyd, G.E., Adamson, A.W. and Myers, L.S., Jr. 1947. The Exchange Adsorption of Ions from Aqueous Solutions by Organic Zeolites. II. Kinetics1. *Journal of the American Chemical Society*. **69**(11), pp.2836-2848.
- Braidy, N., Béchu, A., de Souza Terra, J.C. and Patience, G.S. 2020. Experimental methods in chemical engineering: Transmission electron microscopy—TEM. **98**(3), pp.628-641.
- Brydson, R., Brown, A., Benning, L.G. and Livi, K. 2014. Analytical Transmission Electron Microscopy. *Reviews in Mineralogy and Geochemistry*. **78**(1), pp.219-269.

- Buban, J.P., Ramasse, Q., Gipson, B., Browning, N.D. and Stahlberg, H. 2010. High-resolution low-dose scanning transmission electron microscopy. *Journal of Electron Microscopy*. **59**(2), pp.103-112.
- Bugay, D.E. 2001. Characterization of the solid-state: spectroscopic techniques. *Advanced Drug Delivery Reviews*. **48**(1), pp.43-65.
- Burt, H.M. and Mitchell, A.G. 1981. Crystal defects and dissolution. *International Journal of Pharmaceutics*. **9**(2), pp.137-152.
- Cattle, J. 2019. *Transmission electron microscopy of organic crystalline material and zeolites*. thesis, University of Leeds.
- Cattle, J., S'ari, M., Abellán, P., Ramasse, Q., Hondow, N., Brown, A. and Brydson, R. 2016. Quantitative analysis of a model pharmaceutical material, theophylline, by transmission electron microscopy. *European Microscopy Congress 2016: Proceedings*. pp.752-753.
- Censi, R. and Di Martino, P. 2015. Polymorph Impact on the Bioavailability and Stability of Poorly Soluble Drugs. *Molecules (Basel, Switzerland)*. **20**(10), pp.18759-18776.
- Chamarthy, S.P. and Pinal, R. 2008. The nature of crystal disorder in milled pharmaceutical materials. *Colloids and Surfaces A: Physicochemical and Engineering Aspects*. **331**(1), pp.68-75.
- Chan, E.J., Gao, Q. and Dabros, M. 2014. Understanding the structure details when drying hydrate crystals of pharmaceuticals - interpretations from diffuse scattering and inter-modulation satellites of a partially dehydrated crystal. *Acta Crystallographica Section B, Structural Science, Crystal Engineering and Materials*. **70**(Pt 3), pp.555-567.
- Chang, S.-Y. and Sun, C.C. 2017. Superior Plasticity and Tabletability of Theophylline Monohydrate. *Molecular Pharmaceutics*. **14**(6), pp.2047-2055.
- Chen, D., Haugstad, G., Li, Z.J. and Suryanarayanan, R. 2010. Water Sorption Induced Transformations in Crystalline Solid Surfaces: Characterization by Atomic Force Microscopy. *Journal of Pharmaceutical Sciences*. **99**(9), pp.4032-4041.
- Chieng, N., Rades, T. and Aaltonen, J. 2011. An overview of recent studies on the analysis of pharmaceutical polymorphs. *Journal of Pharmaceutical and Biomedical Analysis*. **55**(4), pp.618-644.
- Claes, N., Asapu, R., Blommaerts, N., Verbruggen, S.W., Lenaerts, S. and Bals, S. 2018. Characterization of silver-polymer core-shell nanoparticles using electron microscopy. *Nanoscale*. **10**(19), pp.9186-9191.
- Crewe, A.V. 1966. Scanning Electron Microscopes: Is High Resolution Possible? **154**(3750), pp.729-738.
- Das, P.P., Guzzinati, G., Coll, C., Gomez Perez, A., Nicolopoulos, S., Estrade, S., Peiro, F., Verbeeck, J., Zompra, A.A. and Galanis, A.S. 2020. Reliable Characterization of Organic & Pharmaceutical Compounds with High Resolution Monochromated EEL Spectroscopy. *Polymers (Basel)*. **12**(7).

- De Smidt, J.H., Fokkens, J.G., Grijseels, H. and Crommelin, D.J. 1986. Dissolution of theophylline monohydrate and anhydrous theophylline in buffer solutions. *Journal of Pharmaceutical Sciences*. **75**(5), pp.497-501.
- De Souza Guimarães, M., Cachumba, J.J.M., Bueno, C.Z., Torres-Obreque, K.M., Lara, G.V.R., Monteiro, G., Barbosa, L.R.S., Pessoa, A., Jr. and Rangel-Yagui, C.O. 2022. Peg-Grafted Liposomes for L-Asparaginase Encapsulation. *Pharmaceutics*. **14**(9).
- De Yoreo, J.J. and Sommerdijk, N.A.J.M. 2016. Investigating materials formation with liquid-phase and cryogenic TEM. *Nature Reviews Materials*. **1**(8), p16035.
- Doktorovova, S., Souto, E.B. and Silva, A.M. 2014. Nanotoxicology applied to solid lipid nanoparticles and nanostructured lipid carriers – A systematic review of in vitro data. *European Journal of Pharmaceutics and Biopharmaceutics*. **87**(1), pp.1-18.
- Donohue, J., Zeltmann, S.E., Bustillo, K.C., Savitzky, B., Jones, M.A., Meyers, G.F., Ophus, C. and Minor, A.M. 2022. Cryogenic 4D-STEM analysis of an amorphous-crystalline polymer blend: Combined nanocrystalline and amorphous phase mapping. *iScience*. **25**(3), p103882.
- Du, H. 2015. A nonlinear filtering algorithm for denoising HR(S)TEM micrographs. *Ultramicroscopy*. **151**, pp.62-67.
- Duddu, S.P., Das, N.G., Kelly, T.P. and Sokoloski, T.D. 1995. Microcalorimetric investigation of phase transitions: I. Is water desorption from theophylline · HOH a single-step process? *International Journal of Pharmaceutics*. **114**(2), pp.247-256.
- Eddleston, M.D., Bithell, E.G. and Jones, W. 2010. Transmission electron microscopy of pharmaceutical materials. **99**(9), pp.4072-4083.
- Eddleston, M.D., Hejczyk, K.E., Bithell, E.G., Day, G.M. and Jones, W. 2013. Polymorph Identification and Crystal Structure Determination by a Combined Crystal Structure Prediction and Transmission Electron Microscopy Approach. **19**(24), pp.7874-7882.
- Egerton, R.F. 2005. *Physical principles of electron microscopy: An introduction to TEM, SEM, and AEM*.
- Egerton, R.F. 2013. Control of radiation damage in the TEM. *Ultramicroscopy*. **127**, pp.100-108.
- Egerton, R.F. 2019. Radiation damage to organic and inorganic specimens in the TEM. *Micron*. **119**, pp.72-87.
- Egerton, R.F., Li, P. and Malac, M. 2004. Radiation damage in the TEM and SEM. *Micron*. **35**(6), pp.399-409.
- Elbaum, M., Seifer, S., Houben, L., Wolf, S.G. and Rez, P. 2021. Toward Compositional Contrast by Cryo-STEM. *Accounts of Chemical Research*. **54**(19), pp.3621-3631.
- European Medicines Agency. 2018. *Assessment report: Lokelma*.

- Faller, B. and Ertl, P. 2007. Computational approaches to determine drug solubility. *Advanced Drug Delivery Reviews*. **59**(7), pp.533-545.
- Farias, M. and Carneiro, R. 2014. Simultaneous quantification of three polymorphic forms of carbamazepine in the presence of excipients using Raman spectroscopy. *Molecules*. **19**(9), pp.14128-14138.
- Farzan, M., Roth, R., Schoelkopf, J., Huwyler, J. and Puchkov, M. 2023. The processes behind drug loading and release in porous drug delivery systems. *European Journal of Pharmaceutics and Biopharmaceutics*. **189**, pp.133-151.
- Ferrari, M. 2005. Cancer nanotechnology: opportunities and challenges. *Nature Reviews Cancer*. **5**(3), pp.161-171.
- Ferreira, P., Ferreira, A., Rocha, J. and Soares, M.R. 2001. Synthesis and Structural Characterization of Zirconium Silicates. *Chemistry of Materials*. **13**(2), pp.355-363.
- Feth, M.P., Jurascheck, J., Spitzenberg, M., Dillenz, J., Bertele, G. and Stark, H. 2011. New Technology for the Investigation of Water Vapor Sorption Induced Crystallographic Form Transformations of Chemical Compounds: A Water Vapor Sorption Gravimetry Dispersive Raman Spectroscopy Coupling. *Journal of Pharmaceutical Sciences*. **100**(3), pp.1080-1092.
- Flicker, F., Eberle, V.A. and Betz, G. 2011. Variability in commercial carbamazepine samples – Impact on drug release. *International Journal of Pharmaceutics*. **410**(1), pp.99-106.
- Freundlich, M.M. 1963. Origin of the Electron Microscope. *Science*. **142**(3589), pp.185-188.
- Friedrich, H. 2021. “No-dose” imaging. *Microscopy and Microanalysis*. **27**(S1), pp.2620-2622.
- Fryer, J.R. 1987. The effect of dose rate on imaging aromatic organic crystals. *Ultramicroscopy*. **23**(3), pp.321-327.
- Fucke, K., McIntyre, G.J., Wilkinson, C., Henry, M., Howard, J.A.K. and Steed, J.W. 2012. New Insights into an Old Molecule: Interaction Energies of Theophylline Crystal Forms. *Crystal Growth & Design*. **12**(3), pp.1395-1401.
- Gavas, S., Quazi, S. and Karpiński, T.M. 2021. Nanoparticles for Cancer Therapy: Current Progress and Challenges. *Nanoscale Research Letters*. **16**(1), p173.
- Glaeser, R.M., Han, B.-G., Csencsits, R., Killilea, A., Pulk, A. and Cate, J.H.D. 2016. Factors that Influence the Formation and Stability of Thin, Cryo-EM Specimens. *Biophysical Journal*. **110**(4), pp.749-755.
- Goud, N.R., Gangavaram, S., Suresh, K., Pal, S., Manjunatha, S.G., Nambiar, S. and Nangia, A. 2012. Novel furosemide cocrystals and selection of high solubility drug forms. *Journal of Pharmaceutical Sciences*. **101**(2), pp.664-680.
- Griesser, U.J. 2006. The Importance of Solvates. *Polymorphism*. pp.211-233.

- Hadjittofis, E., Isbell, M.A., Karde, V., Varghese, S., Ghoroi, C. and Heng, J.Y.Y. 2018. Influences of Crystal Anisotropy in Pharmaceutical Process Development. *Pharmaceutical Research*. **35**(5), p100.
- Hami, Z., Amini, M., Ghazi-Khansari, M., Rezayat, S.M. and Gilani, K. 2014a. Synthesis and in vitro evaluation of a pH-sensitive PLA-PEG-folate based polymeric micelle for controlled delivery of docetaxel. *Colloids and Surfaces B: Biointerfaces*. **116**, pp.309-317.
- Hami, Z., Amini, M., Ghazi-Khansari, M., Rezayat, S.M. and Gilani, K. 2014b. Doxorubicin-conjugated PLA-PEG-Folate based polymeric micelle for tumor-targeted delivery: Synthesis and in vitro evaluation. *DARU Journal of Pharmaceutical Sciences*. **22**(1), p30.
- Han, J., Michel, A.R., Lee, H.S., Kalscheuer, S., Wohl, A., Hoyer, T.R., McCormick, A.V., Panyam, J. and Macosko, C.W. 2015. Nanoparticles Containing High Loads of Paclitaxel-Silicate Prodrugs: Formulation, Drug Release, and Anticancer Efficacy. *Molecular Pharmaceutics*. **12**(12), pp.4329-4335.
- Hare, J.I., Lammers, T., Ashford, M.B., Puri, S., Storm, G. and Barry, S.T. 2017. Challenges and strategies in anti-cancer nanomedicine development: An industry perspective. *Advanced Drug Delivery Reviews*. **108**, pp.25-38.
- Haruta, M. and Kurata, H. 2012. Direct observation of crystal defects in an organic molecular crystals of copper hexachlorophthalocyanine by STEM-EELS. *Scientific Reports*. **2**(1), p252.
- Healy, A.M., Worku, Z.A., Kumar, D. and Madi, A.M. 2017. Pharmaceutical solvates, hydrates and amorphous forms: A special emphasis on cocrystals. *Advanced Drug Delivery Reviews*. **117**, pp.25-46.
- Herdiana, Y., Wathoni, N., Shamsuddin, S. and Muchtaridi, M. 2022. Scale-up polymeric-based nanoparticles drug delivery systems: Development and challenges. *OpenNano*. **7**, p100048.
- Holder, C.F. and Schaak, R.E. 2019. Tutorial on Powder X-ray Diffraction for Characterizing Nanoscale Materials. *ACS Nano*. **13**(7), pp.7359-7365.
- Hu, Q., Gao, X., Gu, G., Kang, T., Tu, Y., Liu, Z., Song, Q., Yao, L., Pang, Z., Jiang, X., Chen, H. and Chen, J. 2013. Glioma therapy using tumor homing and penetrating peptide-functionalized PEG-PLA nanoparticles loaded with paclitaxel. *Biomaterials*. **34**(22), pp.5640-5650.
- Ilett, M., Bamiduro, F., Matar, O., Brown, A., Brydson, R. and Hondow, N. 2017. Cryo-STEM-EDX spectroscopy for the characterisation of nanoparticles in cell culture media. *Journal of Physics*. **902**.
- Ilett, M., Brydson, R., Brown, A. and Hondow, N. 2019. Cryo-analytical STEM of frozen, aqueous dispersions of nanoparticles. *Micron*. **120**, pp.35-42.

- Ilett, M., S'Ari, M., Freeman, H., Aslam, Z., Koniuch, N., Afzali, M., Cattle, J., Hooley, R., Roncal-Herrero, T., Collins, S.M., Hondow, N., Brown, A. and Brydson, R. 2020. Analysis of complex, beam-sensitive materials by transmission electron microscopy and associated techniques. *Philosophical Transactions. Series A, Mathematical, Physical, and Engineering Sciences*. **378**(2186), p20190601.
- Isaacson, M.S., Langmore, J., Parker, N.W., Kopf, D. and Utlaut, M. 1976. The study of the adsorption and diffusion of heavy atoms on light element substrates by means of the atomic resolution stem. *Ultramicroscopy*. **1**(3), pp.359-376.
- Ishizuka, K., Eilers, P.H.C. and Kogure, T. 2018. Optimal Noise Filters in High-Resolution Electron Microscopy. *Microscopy Today*. **15**(5), pp.16-21.
- Jale, S.R., Ojo, A. and Fitch, F.R. 1999. Synthesis of microporous zirconosilicates containing ZrO₆ octahedra and SiO₄ tetrahedra. *Chemical Communications*. (5), pp.411-412.
- Jasim, A.M., He, X., Xing, Y., White, T.A. and Young, M.J. 2021. Cryo-ePDF: Overcoming Electron Beam Damage to Study the Local Atomic Structure of Amorphous ALD Aluminum Oxide Thin Films within a TEM. *ACS Omega*. **6**(13), pp.8986-9000.
- Johnstone, D.N., Allen, C.S., Danaie, M., Copley, R.C.B., Brum, J., Kirkland, A.I. and Midgley, P.A. 2019. Low-Dose Scanning Electron Diffraction Microscopy of Mechanochemically Nanostructured Pharmaceuticals. *Microscopy and Microanalysis*. **25**(S2), pp.1746-1747.
- Jones, L., Varambhia, A., Beanland, R., Kepaptsoglou, D., Griffiths, I., Ishizuka, A., Azough, F., Freer, R., Ishizuka, K., Cherns, D., Ramasse, Q.M., Lozano-Perez, S. and Nellist, P.D. 2018. Managing dose-, damage- and data-rates in multi-frame spectrum-imaging. *Microscopy*. **67**(suppl_1), pp.i98-i113.
- Jones, W. and Thomas, J.M. 1979. Applications of electron microscopy to organic solid-state chemistry. *Progress in Solid State Chemistry*. **12**(2), pp.101-124.
- Jönsson, C. 1961. Elektroneninterferenzen an mehreren künstlich hergestellten Feinspalten. *Zeitschrift für Physik*. **161**(4), pp.454-474.
- Jørgensen, A.C., Airaksinen, S., Karjalainen, M., Luukkonen, P., Rantanen, J. and Yliruusi, J. 2004. Role of excipients in hydrate formation kinetics of theophylline in wet masses studied by near-infrared spectroscopy. *European Journal of Pharmaceutical Sciences*. **23**(1), pp.99-104.
- Jurczak, E., Mazurek, A.H., Szeleszczuk, Ł., Pisklak, D.M. and Zielińska-Pisklak, M. 2020. Pharmaceutical Hydrates Analysis-Overview of Methods and Recent Advances. *Pharmaceutics*. **12**(10).

- Kabova, E.A., Blundell, C.D., Murny, C.A., Whitehead, G.F.S., Vitorica-Yrezabal, I.J., Ross, M.J. and Shankland, K. 2022. SDPD-SX: combining a single crystal X-ray diffraction setup with advanced powder data structure determination for use in early stage drug discovery. *CrystEngComm*. **24**(24), pp.4337-4340.
- Kamaly, N., Yameen, B., Wu, J. and Farokhzad, O.C. 2016. Degradable Controlled-Release Polymers and Polymeric Nanoparticles: Mechanisms of Controlling Drug Release. *Chemical Reviews*. **116**(4), pp.2602-2663.
- Kawabata, Y., Wada, K., Nakatani, M., Yamada, S. and Onoue, S. 2011. Formulation design for poorly water-soluble drugs based on biopharmaceutics classification system: basic approaches and practical applications. *International Journal of Pharmaceutics*. **420**(1), pp.1-10.
- Ke, X., Zhang, M., Zhao, K. and Su, D. 2022. Moiré Fringe Method via Scanning Transmission Electron Microscopy. *Small Methods*. **6**(1), p2101040.
- Keyser, E.A. 2015. *US Patent Application Publication US 2015/0359821 A1*.
- Khaleque, A., Alam, M.M., Hoque, M., Mondal, S., Haider, J.B., Xu, B., Johir, M.A.H., Karmakar, A.K., Zhou, J.L., Ahmed, M.B. and Moni, M.A. 2020. Zeolite synthesis from low-cost materials and environmental applications: A review. *Environmental Advances*. **2**, p100019.
- Khivantsev, K., Derewinski, M.A. and Szanyi, J. 2023. Novel and emerging concepts related to cationic species in zeolites: Characterization, chemistry and catalysis. *Microporous and Mesoporous Materials*. **358**, p112378.
- Khoo, J.Y., Williams, D.R. and Heng, J.Y.Y. 2010. Dehydration Kinetics of Pharmaceutical Hydrate: Effects of Environmental Conditions and Crystal Forms. *Drying Technology*. **28**(10), pp.1164-1169.
- Kim, G., Sousa, A., Meyers, D., Shope, M. and Libera, M. 2006. Cryo-STEM EELS Mapping of Polymer Nanocolloids Preserved in Amorphous Ice. *Microscopy and Microanalysis*. **12**(S02), pp.1384-1385.
- Kishimoto, S. 2012. Electron Moiré method. *Theoretical and Applied Mechanics Letters*. **2**(1), p011001.
- Klang, V., Valenta, C. and Matsko, N.B. 2013. Electron microscopy of pharmaceutical systems. *Micron*. **44**, pp.45-74.
- Kobayashi, Y., Ito, S., Itai, S. and Yamamoto, K. 2000. Physicochemical properties and bioavailability of carbamazepine polymorphs and dihydrate. *International Journal of Pharmaceutics*. **193**(2), pp.137-146.

- Kondo, Y., Fukunaga, K., Okunishi, E. and Endo, N. 2017. Way to Reduce Electron Dose in Pseudo Atomic Column Elemental Maps by 2D STEM Moire Method. *Microscopy and Microanalysis*. **23**(S1), pp.1790-1791.
- Kondo, Y. and Okunishi, E. 2014. Magnified pseudo-elemental map of atomic column obtained by Moiré method in scanning transmission electron microscopy. *Microscopy*. **63**(5), pp.391-395.
- Koniuch, N., Ilett, M., Collins, S.M., Hondow, N., Brown, A., Hughes, L. and Blade, H. 2023. Structure of polymeric nanoparticles encapsulating a drug - pamoic acid ion pair by scanning transmission electron microscopy. *Heliyon*. **9**(6), pe16959.
- Kraljević Pavelić, S., Simović Medica, J., Gumbarević, D., Filošević, A., Pržulj, N. and Pavelić, K. 2018. Critical Review on Zeolite Clinoptilolite Safety and Medical Applications in vivo. *Frontiers in Pharmacology*. **9**.
- Kumar, M., Gupta, D., Singh, G., Sharma, S., Bhat, M., Prashant, C.K., Dinda, A.K., Kharbanda, S., Kufe, D. and Singh, H. 2014. Novel polymeric nanoparticles for intracellular delivery of peptide Cargos: antitumor efficacy of the BCL-2 conversion peptide NuBCP-9. *Cancer Research*. **74**(12), pp.3271-3281.
- Kuo, I.A.M. and Glaeser, R.M. 1975. Development of methodology for low exposure, high resolution electron microscopy of biological specimens. *Ultramicroscopy*. **1**(1), pp.53-66.
- Labhasetwar, V., Song, C. and Levy, R.J. 1997. Nanoparticle drug delivery system for restenosis. *Advanced Drug Delivery Reviews*. **24**(1), pp.63-85.
- Leapman, R.D. and Sun, S. 1995. Cryo-electron energy loss spectroscopy: observations on vitrified hydrated specimens and radiation damage. *Ultramicroscopy*. **59**(1), pp.71-79.
- Leijten, Z.J.W.A., Keizer, A.D.A., de With, G. and Friedrich, H. 2017. Quantitative Analysis of Electron Beam Damage in Organic Thin Films. *The Journal of Physical Chemistry C*. **121**(19), pp.10552-10561.
- Lim Soo, P., Cho, J., Grant, J., Ho, E., Piquette-Miller, M. and Allen, C. 2008. Drug release mechanism of paclitaxel from a chitosan–lipid implant system: Effect of swelling, degradation and morphology. *European Journal of Pharmaceutics and Biopharmaceutics*. **69**(1), pp.149-157.
- Linder, K.E., Krawczynski, M.A. and Laskey, D. 2016. Sodium Zirconium Cyclosilicate (ZS-9): A Novel Agent for the Treatment of Hyperkalemia. *Pharmacotherapy*. **36**(8), pp.923-933.
- Lucas, G., Burdet, P., Cantoni, M. and Hébert, C. 2013. Multivariate statistical analysis as a tool for the segmentation of 3D spectral data. *Micron*. **52-53**, pp.49-56.

- Macrae, C.F., Sovago, I., Cottrell, S.J., Galek, P.T.A., McCabe, P., Pidcock, E., Platings, M., Shields, G.P., Stevens, J.S., Towler, M. and Wood, P.A. 2020. Mercury 4.0: from visualization to analysis, design and prediction. *Journal of Applied Crystallography*. **53**(Pt 1), pp.226-235.
- Mahapatro, A. and Singh, D.K. 2011. Biodegradable nanoparticles are excellent vehicle for site directed in-vivo delivery of drugs and vaccines. *Journal of Nanobiotechnology*. **9**, p55.
- Mahdavi, Z., Rezvani, H. and Keshavarz Moraveji, M. 2020. Core-shell nanoparticles used in drug delivery-microfluidics: a review. *RSC Advances*. **10**(31), pp.18280-18295.
- Mahl, D., Diendorf, J., Meyer-Zaika, W. and Epple, M. 2011. Possibilities and limitations of different analytical methods for the size determination of a bimodal dispersion of metallic nanoparticles. *Colloids and Surfaces A: Physicochemical and Engineering Aspects*. **377**(1), pp.386-392.
- Matsuda, Y. and Tatsumi, E. 1990. Physicochemical characterization of furosemide modifications. *International Journal of Pharmaceutics*. **60**(1), pp.11-26.
- Matsumura, Y. and Maeda, H. 1986. A New Concept for Macromolecular Therapeutics in Cancer Chemotherapy: Mechanism of Tumoritropic Accumulation of Proteins and the Antitumor Agent Smancs1. *Cancer Research*. **46**(12_Part_1), pp.6387-6392.
- Matsuo, K. and Matsuoka, M. 2007. Solid-State Polymorphic Transition of Theophylline Anhydrate and Humidity Effect. *Crystal Growth & Design*. **7**(2), pp.411-415.
- Mayoral, A., Anderson, P.A. and Diaz, I. 2015. Zeolites are no longer a challenge: Atomic resolution data by Aberration-corrected STEM. *Micron*. **68**, pp.146-151.
- Moseson, D.E. and Taylor, L.S. 2018. The application of temperature-composition phase diagrams for hot melt extrusion processing of amorphous solid dispersions to prevent residual crystallinity. *International Journal of Pharmaceutics*. **553**(1-2), pp.454-466.
- Murakami, Y., Sasaki, T.T., Ohkubo, T. and Hono, K. 2015. Strain measurements from Nd₂Fe₁₄B grains in sintered magnets using artificial moiré fringes. *Acta Materialia*. **101**, pp.101-106.
- Newman, A. and Zografi, G. 2014. Critical considerations for the qualitative and quantitative determination of process-induced disorder in crystalline solids. *Journal of Pharmaceutical Sciences*. **103**(9), pp.2595-2604.
- Newman, A.W. and Byrn, S.R. 2003. Solid-state analysis of the active pharmaceutical ingredient in drug products. *Drug Discovery Today*. **8**(19), pp.898-905.
- Nicholls, D., Lee, J., Amari, H., Stevens, A.J., Mehdi, B.L. and Browning, N.D. 2020. Minimising damage in high resolution scanning transmission electron microscope images of nanoscale structures and processes. *Nanoscale*. **12**(41), pp.21248-21254.

- Nielsen, L.H., Gordon, S., Holm, R., Selen, A., Rades, T. and Müllertz, A. 2013. Preparation of an amorphous sodium furosemide salt improves solubility and dissolution rate and leads to a faster T_{max} after oral dosing to rats. *European Journal of Pharmaceutics and Biopharmaceutics*. **85**(3 Pt B), pp.942-951.
- Nimesh, S., Manchanda, R., Kumar, R., Saxena, A., Chaudhary, P., Yadav, V., Mozumdar, S. and Chandra, R. 2006. Preparation, characterization and in vitro drug release studies of novel polymeric nanoparticles. *International Journal of Pharmaceutics*. **323**(1), pp.146-152.
- Nunes, C., Mahendrasingam, A. and Suryanarayanan, R. 2006. Investigation of the multi-step dehydration reaction of theophylline monohydrate using 2-dimensional powder X-ray diffractometry. *Pharmaceutical Research*. **23**(10), pp.2393-2404.
- Ohta, M. and Buckton, G. 2004. Determination of the changes in surface energetics of cefditoren pivoxil as a consequence of processing induced disorder and equilibration to different relative humidities. *International Journal of Pharmaceutics*. **269**(1), pp.81-88.
- Okunishi, E., Endo, N. and Kondo, Y. 2014. Atomic Column Elemental Mapping by STEM-Moire Method. *Microscopy and Microanalysis*. **20**(S3), pp.586-587.
- Olson, I.A., Shtukenberg, A.G., Kahr, B. and Ward, M.D. 2018. Dislocations in molecular crystals. *Reports on Progress in Physics. Physical Society*. **81**(9), p096501.
- Otsuka, M., Kaneniwa, N., Kawakami, K. and Umezawa, O. 1990. Effect of Surface Characteristics of Theophylline Anhydrate Powder on Hygroscopic Stability. *Journal of Pharmacy and Pharmacology*. **42**(9), pp.606-610.
- Otsuka, M., Kaneniwa, N., Kawakami, K. and Umezawa, O. 1991. Effects of Tableting Pressure on Hydration Kinetics of Theophylline Anhydrate Tablets. *Journal of Pharmacy and Pharmacology*. **43**(4), pp.226-231.
- Pagels, R.F., Edelstein, J., Tang, C. and Prud'homme, R.K. 2018. Controlling and Predicting Nanoparticle Formation by Block Copolymer Directed Rapid Precipitations. *Nano Letters*. **18**(2), pp.1139-1144.
- Paiva, E.M., Li, Q., Zaczek, A.J., Pereira, C.F., Rohwedder, J.J.R. and Zeitler, J.A. 2021. Understanding the Metastability of Theophylline FIII by Means of Low-Frequency Vibrational Spectroscopy. *Molecular Pharmaceutics*. **18**(9), pp.3578-3587.
- Pal, R., Bourgeois, L., Weyland, M., Sikder, A.K., Saito, K., Funston, A.M. and Bellare, J.R. 2021. Chemical Fingerprinting of Polymers Using Electron Energy-Loss Spectroscopy. *ACS Omega*. **6**(37), pp.23934-23942.

- Patra, J.K., Das, G., Fraceto, L.F., Campos, E.V.R., Rodriguez-Torres, M.d.P., Acosta-Torres, L.S., Diaz-Torres, L.A., Grillo, R., Swamy, M.K., Sharma, S., Habtemariam, S. and Shin, H.-S. 2018. Nano based drug delivery systems: recent developments and future prospects. *Journal of Nanobiotechnology*. **16**(1), p71.
- Pennycook, S.J. and Nellist, P.D. 2011. *Scanning transmission electron microscopy: imaging and analysis*. Springer Science & Business Media.
- Perrier, P. and Byrn, S.R. 1982. Influence of crystal packing on the solid-state desolvation of purine and pyrimidine hydrates: loss of water of crystallization from thymine monohydrate, cytosine monohydrate, 5-nitouracil monohydrate, and 2'-deoxyadenosine monohydrate. *The Journal of Organic Chemistry*. **47**(24), pp.4671-4676.
- Perry, A.R., Lazenby, R.A., Adobes-Vidal, M., Peruffo, M., McKelvey, K., Snowden, M.E. and Unwin, P.R. 2015. Hopping intermittent contact-scanning electrochemical microscopy (HIC-SECM) as a new local dissolution kinetic probe: application to salicylic acid dissolution in aqueous solution. *CrystEngComm*. **17**(41), pp.7835-7843.
- Phadnis, N.V. and Suryanarayanan, R. 1997. Polymorphism in Anhydrous Theophylline - Implications on the Dissolution Rate of Theophylline Tablets. *Journal of Pharmaceutical Sciences*. **86**(11), pp.1256-1263.
- Pham, S.T., Koniuch, N., Wynne, E., Brown, A. and Collins, S.M. 2023. Microscopic crystallographic analysis of dislocations in molecular crystals. *arXiv preprint*. **arXiv:2308.16589**.
- Piepenbrock, C., Mayr, S. and Buchner, A. 2014. Positive Display Polarity Is Particularly Advantageous for Small Character Sizes: Implications for Display Design. **56**(5), pp.942-951.
- Pustulka, K.M., Wohl, A.R., Lee, H.S., Michel, A.R., Han, J., Hoye, T.R., McCormick, A.V., Panyam, J. and Macosko, C.W. 2013. Flash Nanoprecipitation: Particle Structure and Stability. *Molecular Pharmaceutics*. **10**(11), pp.4367-4377.
- Qiu, Y., Chen, Y., Zhang, G.G.Z., Yu, L.X. and Mantri, R.V. 2017. *Developing solid oral dosage forms : pharmaceutical theory & practice*. Second edition ed. London, UK: Elsevier Academic Press London, UK.
- Rabanel, J.-M., Faivre, J., Tehrani, S.F., Lalloz, A., Hildgen, P. and Banquy, X. 2015. Effect of the Polymer Architecture on the Structural and Biophysical Properties of PEG-PLA Nanoparticles. *ACS Applied Materials & Interfaces*. **7**(19), pp.10374-10385.
- Rafique, Z., Peacock, W.F., LoVecchio, F. and Levy, P.D. 2015. Sodium zirconium cyclosilicate (ZS-9) for the treatment of hyperkalemia. *Expert Opinion on Pharmacotherapy*. **16**(11), pp.1727-1734.
- Ren, S., Nian, F., Chen, X., Xue, R. and Chen, F. 2023. Routes of Theophylline Monohydrate Dehydration Process Proposed by Mid-Frequency Raman Difference Spectra. *Journal of Pharmaceutical Sciences*.

- Ricarte, R.G., Lodge, T.P. and Hillmyer, M.A. 2015. Detection of pharmaceutical drug crystallites in solid dispersions by transmission electron microscopy. *Molecular Pharmaceutics*. **12**(3), pp.983-990.
- Riley, T., Heald, C.R., Stolnik, S., Garnett, M.C., Illum, L., Davis, S.S., King, S.M., Heenan, R.K., Purkiss, S.C., Barlow, R.J., Gellert, P.R. and Washington, C. 2003. Core-Shell Structure of PLA-PEG Nanoparticles Used for Drug Delivery. *Langmuir*. **19**(20), pp.8428-8435.
- Rodríguez-Hornedo, N., Lechuga-Ballesteros, D. and Hsiu-Jean, W. 1992. Phase transition and heterogeneous/epitaxial nucleation of hydrated and anhydrous theophylline crystals. *International Journal of Pharmaceutics*. **85**(1), pp.149-162.
- S'ari, M., Blade, H., Cosgrove, S., Drummond-Brydson, R., Hondow, N., Hughes, L.P. and Brown, A. 2021. Characterization of Amorphous Solid Dispersions and Identification of Low Levels of Crystallinity by Transmission Electron Microscopy. *Molecular Pharmaceutics*. **18**(5), pp.1905-1919.
- S'ari, M., Koniuch, N., Brydson, R., Hondow, N. and Brown, A. 2020. High-resolution imaging of organic pharmaceutical crystals by transmission electron microscopy and scanning moiré fringes. *Journal of Microscopy*. **279**(3), pp.197-206.
- S'ari, M., Blade, H., Brydson, R., Cosgrove, S.D., Hondow, N., Hughes, L.P. and Brown, A. 2018. Toward Developing a Predictive Approach To Assess Electron Beam Instability during Transmission Electron Microscopy of Drug Molecules. *Molecular Pharmaceutics*. **15**(11), pp.5114-5123.
- S'ari, M., Cattle, J., Hondow, N., Brydson, R. and Brown, A. 2019. Low dose scanning transmission electron microscopy of organic crystals by scanning moiré fringes. *Micron*. **120**, pp.1-9.
- Sader, K., Brown, A., Brydson, R. and Bleloch, A. 2010. Quantitative analysis of image contrast in phase contrast STEM for low dose imaging. *Ultramicroscopy*. **110**(10), pp.1324-1331.
- Sadler, P.J. 1991. Inorganic Chemistry and Drug Design. In: Sykes, A.G. ed. *Advances in Inorganic Chemistry*. Academic Press, pp.1-48.
- Saleki-Gerhardt, A., Ahlneck, C. and Zograf, G. 1994. Assessment of disorder in crystalline solids. *International Journal of Pharmaceutics*. **101**(3), pp.237-247.
- Sangwal, K. 2012. *Etching of Crystals. Theory, Experiment and Application*. Elsevier Science.
- Sanii, R., Patyk-Kaźmierczak, E., Hua, C., Darwish, S., Pham, T., Forrest, K.A., Space, B. and Zaworotko, M.J. 2021. Toward an Understanding of the Propensity for Crystalline Hydrate Formation by Molecular Compounds. Part 2. *Crystal Growth & Design*. **21**(9), pp.4927-4939.
- Schneider, C.A., Rasband, W.S. and Eliceiri, K.W. 2012. NIH Image to ImageJ: 25 years of image analysis. *Nature Methods*. **9**(7), pp.671-675.

- Sekhon, B.S. and Gandhi, L.J.R. 2006. Medicinal uses of inorganic compounds - 1. **11**, pp.75-89.
- Shalgunov, V., Zaytseva-Zotova, D., Zintchenko, A., Levada, T., Shilov, Y., Andreyev, D., Dzhumashev, D., Metelkin, E., Urusova, A., Demin, O., McDonnell, K., Troiano, G., Zale, S. and Safarova, E. 2017. Comprehensive study of the drug delivery properties of poly(L-lactide)-poly(ethylene glycol) nanoparticles in rats and tumor-bearing mice. *Journal of Controlled Release*. **261**, pp.31-42.
- Shariare, M.H., Altamimi, M.A., Marzan, A.L., Tabassum, R., Jahan, B., Reza, H.M., Rahman, M., Ahsan, G.U. and Kazi, M. 2019. In vitro dissolution and bioavailability study of furosemide nanosuspension prepared using design of experiment (DoE). *Saudi Pharmaceutical Journal*. **27**(1), pp.96-105.
- Shekunov, B.Y. and York, P. 2000. Crystallization processes in pharmaceutical technology and drug delivery design. *Journal of Crystal Growth*. **211**(1), pp.122-136.
- Shrestha, D.B., Budhathoki, P., Sedhai, Y.R., Baniya, R., Cable, C.A., Kashiouris, M.G., Dixon, D.L., Kidd, J.M., Adhikari, Y., Marasini, A. and Bhandari, S. 2021. Patiromer and Sodium Zirconium Cyclosilicate in Treatment of Hyperkalemia: A Systematic Review and Meta-Analysis. *Current Therapeutic Research*. **95**, p100635.
- Singh, V.B. 2015. Spectroscopic signatures and structural motifs in isolated and hydrated theophylline: a computational study. *RSC Advances*. **5**(15), pp.11433-11444.
- Skoyles, G., McKay, G. and Fisher, M. 2017. Sodium zirconium cyclosilicate. **34**(8), pp.294-295a.
- Smeets, S., Zou, X. and Wan, W. 2018. Serial electron crystallography for structure determination and phase analysis of nanocrystalline materials. *Journal of Applied Crystallography*. **51**(Pt 5), pp.1262-1273.
- Song, Y.H., Shin, E., Wang, H., Nolan, J., Low, S., Parsons, D., Zale, S., Ashton, S., Ashford, M.B., Ali, M., Thrasher, D., Boylan, N.J. and Troiano, G. 2016. A novel in situ hydrophobic ion pairing (HIP) formulation strategy for clinical product selection of a nanoparticle drug delivery system. *Journal of Controlled Release*. **229**, pp.106-119.
- Stavros, F., Yang, A., Leon, A., Nuttall, M. and Rasmussen, H.S. 2014. Characterization of Structure and Function of ZS-9, a K⁺ Selective Ion Trap. *PLOS ONE*. **9**(12), pe114686.
- Su, D. and Zhu, Y. 2010. Scanning moiré fringe imaging by scanning transmission electron microscopy. *Ultramicroscopy*. **110**(3), pp.229-233.
- Suzuki, E., Shimomura, K. and Sekiguchi, K. 1989. Thermochemical Study of Theophylline and Its Hydrate. *Chemical and Pharmaceutical Bulletin*. **37**(2), pp.493-497.
- Swalin, R.A. and Arents, J. 1962. Thermodynamics of Solids. *Journal of The Electrochemical Society*. **109**(12), p308C.

- Tang, N., Wang, X., Du, W., Zhang, L., Xiang, J., Wang, S., Cheng, P., Zhu, L. and Yin, Q. 2019. Conformational Flexibility and Crystallization: The Case of Furosemide. *Crystal Growth & Design*. **19**(4), pp.2050-2059.
- Tang, Y., Wang, X., Li, J., Nie, Y., Liao, G., Yu, Y. and Li, C. 2019. Overcoming the Reticuloendothelial System Barrier to Drug Delivery with a “Don't-Eat-Us” Strategy. *ACS Nano*. **13**(11), pp.13015-13026.
- Tantry, J.S., Tank, J. and Suryanarayanan, R. 2007. Processing-induced phase transitions of theophylline—implications on the dissolution of theophylline tablets. *Journal of Pharmaceutical Sciences*. **96**(5), pp.1434-1444.
- Taylor, L.S., Braun, D.E. and Steed, J.W. 2021. Crystals and Crystallization in Drug Delivery Design. *Crystal Growth & Design*. **21**(3), pp.1375-1377.
- Thakral, S., Garcia-Barriocanal, J. and Thakral, N.K. 2019. Effect of processing conditions and excipients on dehydration kinetics of sodium naproxen hydrate in formulation. *International Journal of Pharmaceutics*. **557**, pp.221-228.
- Tian, C., Feng, J. and Prud'homme, R.K. 2020. Adsorption dynamics of polymeric nanoparticles at an air-water interface with addition of surfactants. *Journal of Colloid and Interface Science*. **575**, pp.416-424.
- Torchilin, V.P. 2006. Multifunctional nanocarriers. *Advanced Drug Delivery Reviews*. **58**(14), pp.1532-1555.
- van der Meel, R., Lammers, T. and Hennink, W.E. 2017. Cancer nanomedicines: oversold or underappreciated? *Expert Opinion on Drug Delivery*. **14**(1), pp.1-5.
- van Vreeswijk, S.H. and Weckhuysen, B.M. 2022. Emerging analytical methods to characterize zeolite-based materials. *National Science Review*. **9**(9).
- Vasilchenko, M.A., Shakhtshneider, T.P., Naumov, D.Y. and Boldyrev, V.V. 1999. The Morphology of Etch Pits During Thermal Treatment of Drugs and its Dependence on the Features of Their Crystallochemical Structure. *Journal of Thermal Analysis and Calorimetry*. **57**(1), pp.157-164.
- Velazco, A., Béché, A., Jannis, D. and Verbeeck, J. 2022. Reducing electron beam damage through alternative STEM scanning strategies, Part I: Experimental findings. *Ultramicroscopy*. **232**, p113398.
- Vippagunta, S.R., Brittain, H.G. and Grant, D.J. 2001. Crystalline solids. *Advanced Drug Delivery Reviews*. **48**(1), pp.3-26.
- von Harrach, H.S., Klenov, D., Freitag, B., Schlossmacher, P., Collins, P.C. and Fraser, H.L. 2010. Comparison of the Detection Limits of EDS and EELS in S/TEM. *Microscopy and Microanalysis*. **16**(S2), pp.1312-1313.

- Vora, K.L., Buckton, G. and Clapham, D. 2004. The use of dynamic vapour sorption and near infra-red spectroscopy (DVS-NIR) to study the crystal transitions of theophylline and the report of a new solid-state transition. *European Journal of Pharmaceutical Sciences*. **22**(2-3), pp.97-105.
- Wade, R.H. and Pelissier, J. 1982. The temperature dependence of the electron irradiation resistance of crystalline paraffin. *Ultramicroscopy*. **10**(3), pp.285-290.
- Wadhawan, A., Singh, J., Sharma, H., Handa, S., Singh, G., Kumar, R., Barnwal, R.P., Pal Kaur, I. and Chatterjee, M. 2022. Anticancer Biosurfactant-Loaded PLA-PEG Nanoparticles Induce Apoptosis in Human MDA-MB-231 Breast Cancer Cells. *ACS Omega*. **7**(6), pp.5231-5241.
- Wallace, S.J., Li, J., Nation, R.L. and Boyd, B.J. 2012. Drug release from nanomedicines: Selection of appropriate encapsulation and release methodology. *Drug Delivery and Translational Research*. **2**(4), pp.284-292.
- Wang, S.X., Wang, L.M. and Ewing, R.C. 2000. Electron and ion irradiation of zeolites. *Journal of Nuclear Materials*. **278**(2), pp.233-241.
- Weinberger, P. 2006. Revisiting Louis de Broglie's famous 1924 paper in the Philosophical Magazine. *Philosophical Magazine Letters*. **86**(7), pp.405-410.
- Weinert, F. 2009. Davisson—Germer Experiment. In: Greenberger, D., et al. eds. *Compendium of Quantum Physics*. Berlin, Heidelberg: Springer Berlin Heidelberg, pp.150-152.
- Weiss, A.-V., Koch, M. and Schneider, M. 2019. Combining cryo-TEM and energy-filtered TEM for imaging organic core-shell nanoparticles and defining the polymer distribution. *International Journal of Pharmaceutics*. **570**, p118650.
- Whittaker, E. 1949. The structure of Bolivian crocidolite. *Acta Crystallographica*. **2**(5), pp.312-317.
- Williams, D.B. and Carter, C.B. 2009. *Transmission Electron Microscopy*. New York: Plenum Press.
- Wolf, S.G. and Elbaum, M. 2019. Chapter 10 - CryoSTEM tomography in biology. In: Müller-Reichert, T. and Pigino, G. eds. *Methods in Cell Biology*. Academic Press, pp.197-215.
- Wren, S., Collins, L., Hughes, L.P. and Jones, I. 2021. Measuring the Rate of In-vitro Drug Release From Polymeric Nanoparticles by ¹⁹F Solution State NMR Spectroscopy. *Journal of Pharmaceutical Sciences*. **110**(11), pp.3546-3549.
- Xiao, R.Z., Zeng, Z.W., Zhou, G.L., Wang, J.J., Li, F.Z. and Wang, A.M. 2010. Recent advances in PEG-PLA block copolymer nanoparticles. *International Journal of Nanomedicine*. **5**, pp.1057-1065.

- Xu, Q., Ensign, L.M., Boylan, N.J., Schön, A., Gong, X., Yang, J.C., Lamb, N.W., Cai, S., Yu, T., Freire, E. and Hanes, J. 2015. Impact of Surface Polyethylene Glycol (PEG) Density on Biodegradable Nanoparticle Transport in Mucus ex Vivo and Distribution in Vivo. *ACS Nano*. **9**(9), pp.9217-9227.
- Yakovlev, S. and Libera, M. 2008. Dose-limited spectroscopic imaging of soft materials by low-loss EELS in the scanning transmission electron microscope. *Micron*. **39**(6), pp.734-740.
- Zhang, Z., Dai, S., Fan, X., Blom, D.A., Pennycook, S.J. and Wei, Y. 2001. Controlled Synthesis of CdS Nanoparticles inside Ordered Mesoporous Silica Using Ion-Exchange Reaction. *The Journal of Physical Chemistry B*. **105**(29), pp.6755-6758.
- Zhu, H., Yuen, C. and Grant, D.J.W. 1996. Influence of water activity in organic solvent + water mixtures on the nature of the crystallizing drug phase. 1. Theophylline. *International Journal of Pharmaceutics*. **135**(1), pp.151-160.
- Zielińska, A., Carreiró, F., Oliveira, A.M., Neves, A., Pires, B., Venkatesh, D.N., Durazzo, A., Lucarini, M., Eder, P., Silva, A.M., Santini, A. and Souto, E.B. 2020. Polymeric Nanoparticles: Production, Characterization, Toxicology and Ecotoxicology. *Molecules*. **25**(16).